2022

The Cavity-Embedded Cooper Pair Transistor as a Charge Detector Operating in the Nonlinear Regime

Bhargava Thyagarajan
Bhargava.Thyagarajan.GR@Dartmouth.edu

THE CAVITY-EMBEDDED COOPER PAIR TRANSISTOR AS A CHARGE DETECTOR OPERATING IN THE NONLINEAR REGIME

A Thesis

Submitted to the Faculty

in partial fulfillment of the requirements for the

degree of

Doctor of Philosophy

in

Physics and Astronomy

by

Bhargava Thyagarajan

Guarini School of Graduate and Advanced Studies

Dartmouth College

Hanover, New Hampshire

May 2022

Examining Committee:

Alexander J. Rimberg, Chair

Miles P. Blencowe

Chandrasekhar Ramanathan

Archana Kamal

F. Jon Kull, Ph.D.
Dean of the Guarini School of Graduate and Advanced Studies

Abstract

The cavity-embedded Cooper pair transistor (cCPT) has been shown to be a nearly quantum limited charge detector operating with only a single intracavity photon[1]. Here, we use the inherent Kerr nonlinearity to demonstrate a dispersive charge sensing technique inspired by the Josephson bifurcation amplifier. Operating in the bistable regime close to a bifurcation edge, the cCPT is sensitive to charge shifts of $0.09e$ in a single-shot readout scheme with a detection time of 3 μs and a detection fidelity of 94%. The readout is implemented with only $\sim$ 25 intracavity photons in the high oscillation amplitude state, still several orders of magnitude lower than drives used in state-of-the-art radio frequency single electron transistors (rf-SETs). We find that a major limitation to the charge sensitivity of the device is fluctuation-induced switching between the metastable oscillation states in the bistable region. We study the lifetimes of these states across the gate and flux range of the cCPT and find that the switching properties depend on the strength of the Kerr nonlinearity at the cCPT bias point.

We also explore a second nonlinear detection scheme where we parametrically pump the cCPT using a time-varying flux close to twice its resonance frequency to induce parametric oscillations. Flux pumping at a detuning on the edge of the parametric oscillation threshold makes the amplitude of oscillations sensitive to the charge environment. With no input drive, we are able to distinguish charge states $\sim 0.1e$ apart in a measurement time of 1 μs with a fidelity of 83%.

The cCPT is a rich nonlinear system in which we observe sub-harmonic oscillations and phase coherent degenerate parametric amplification which could potentially be used to enhance the dispersive charge sensing of the device operating with a single intracavity photon level drive.

Acknowledgements

I would like to thank all my committee members for taking the time to serve on it. First and most importantly, I would like to thank my advisor, Alex Rimberg for always being by my side through this journey. He never failed to make the time to pass on bits of his vast expanse of experimental cryogenic and electronics knowledge. His ability to unerringly cut through the details to get to the crux of an issue is something I hope to master some day. His methodical working and ability to make quick back-of-the-envelope estimates are traits I hope I have begun to inculcate. Last, but definitely not the least, was his aid in dealing with malfunctioning pieces of equipment, which happened more often than I care to remember. Miles Blencowe has been an incredible resource throughout my time here. His unfinished, forthcoming book on nanomechanical systems that he kindly shared with me is a very pedagogical text that will aid grad students in that field for decades to come. Talking physics with him in Wilder and on the mountains of New Hampshire was always a delight. Chandrasekhar (Sekhar) Ramanathan taught two excellent courses on condensed matter in my first few years in grad school. Since then, he has been a great part-time fellow-basement-dweller to talk to about both technical issues and physics. All three have always been tremendous mentors in shaping my professional and personal life. I would like to thank Archana Kamal for agreeing to be on my committee. Though I haven't interacted directly with her yet, her work has been instrumental in aiding my understanding of the cCPT.

Huge shout-out to all my past labmates. Joel Stettenheim was a post-doc in the lab when I began working here, and he showed me the ropes of fabrication. Juliang Li and Chunyang Tang were the senior grad students in the lab, and they taught me everything I know about keeping the lab running. Jules' resourcefulness in dealing with lab equipment will never cease to amaze me. I am also particularly indebted to him for the cCPT sample that forms the bulk of this thesis. Billy Braasch was my partner in working on the cCPT-NR fabrication, and made long hours in the lab quite pleasant with his camaraderie, maintaining a keen interest in the project even after he had moved on from it. Be it in the lab, or in the apartment building we shared, he was usually just a flimsy wall away. I also cherish the time I spent outdoors with Billy. Ben Brock and Sisira Kanhirathingal were my partners while working with the cCPT. We learnt and figured out a lot of the experimental details together. Ben's methodical work on the cCPT was inspirational and guided a lot of my thinking about the system. Sisira and Miles' incredible calculations on the cCPT provided a strong foundation to understand this system. The companionship Ben and Sisira provided in the office we shared in pre-COVID times will be cherished.

Members of my cohort at Dartmouth - Jesse Evans, Hui Wang, Rob Sims, Yanping Cai, Salini Karuvade, McKinley Brumback, Meghan Harrington, Michelle Stephens and Katie Weil all made my first few years of grad school very enjoyable, both in Wilder and outside. Thanks are owed to all my fellow basement dwellers over the years - Whitey Adams, Chris Grant, Jeff Renk, Lihuang Zhu, Daniel Allman, Parth Sabharwal, Ethan Williams and Linta Joseph. The last few years discussing his spin physics, life and everything else with Ethan have been enriching and relaxing, just like the hours we spent on the Connecticut river. Whitey and Chris in the machine shop and Jeff in the electronics shop have all been instrumental in making new pieces of equipment and helping mend malfunctioning equipment, always well before schedule.

It is safe to say the Rimberg lab wouldn't be standing without them. Thanks also to the regulars on the 'grad soccer superstars', often a few hours of RR through a packed week that would help me unwind.

My gratitude to Charles (Chuck) Daghlian who was succeeded by Maxime Guinel at the Dartmouth electron microscope facility for their support when I had to diagnose and fix things on the SEM. Maxime's dry sense of humour could always be counted on to serve up a laugh.

Many thanks to everyone in the Wilder community who make the department of Physics and Astronomy such a vibrant place to be in, and especially to Judy Lowell, Tressy Manning, Meg Whitlock and Jean Blandin for handling all the administrative tasks (including those I had no idea they were doing on my behalf). Special thanks to Alan Goldblatt, David Enriquez and Ray Aubut who have made TA-ing undergraduate labs a very smooth experience over the years.

Lastly, but quite importantly, to my parents who have been by my side the last thirty years, always gently guiding me and aiding me when necessary, while giving me the freedom to pursue my own path, I owe my gratitude. I haven't spent nearly as much time as I would have liked to with them over the course of this PhD, but our weekly video calls where they would enthrall me with stories of their new life living on a farm back home in India have been something to look forward to every week. My extended family - Raghu and Lata, Ravi and Jamuna (who also read and edited my introduction, for which they have my thanks), Tom and Raju could always be counted on to encourage and distract. My partner, Kelly Tanguay, has been a rock over the last few years - encouraging, consoling, commiserating, cheering me as required. The fantastic times we have had in my not inconsiderable time at Dartmouth will be cherished memories forever. For her thorough editing of this thesis, reducing the number of typos and grammatical errors severalfold, she has my gratitude.

Contents

Abstract ii

Acknowledgements iv

1 Introduction **1**

2 The cavity-embedded Cooper pair transistor - theory **7**

2.1 The classical $\lambda/4$ cavity 8

2.1.1 Classical infinite transmission line 8

2.1.2 The shorted $\lambda/4$ transmission line 11

2.1.3 Lumped element parallel LCR circuit 13

2.1.4 Capacitively coupled shorted $\lambda/4$ cavity 14

2.1.5 Classical S_{11} for the shorted $\lambda/4$ cavity 17

2.2 Quantum mechanical model for $\lambda/4$ resonator 20

2.2.1 Quantum infinite transmission line 20

2.3 Input-output theory 27

2.3.1 The $\lambda/4$ microwave cavity coupled to a semi-infinite transmission line 30

2.4 The Cooper pair transistor (CPT) 33

2.4.1 The Josephson junction 34

2.4.2 The Cooper pair transistor (CPT) 39

2.4.3 The CPT as a tunable inductor 43

2.5 The cavity-embedded Cooper pair transistor (cCPT) 45
2.5.1 Resonant frequency tuned by Josephson inductance 46
2.5.2 cCPT Hamiltonian 47

3 Experimental setup and techniques 56
3.1 The cCPT sample 56
3.1.1 Fabrication process 57
3.1.2 PCB and sample box 65
3.2 Fridge RF and DC wiring 67
3.2.1 RF wiring 67
3.2.2 DC wiring 70
3.3 Experimental methods 71
3.3.1 S_{11} measurement and analysis 72
3.3.2 Quasiparticle Poisoning (QP) and effect on S_{11}. 74
3.3.3 Estimating the attenuation on the input line 84
3.3.4 Amplifier chain calibration 86
3.3.5 Heterodyne measurement 89

4 Charge sensing using the cCPT as a cavity Bifurcation Amplifier 97
4.1 Kerr cavity theory 98
4.1.1 Metastable oscillation states 108
4.2 Experiments 111
4.2.1 Hysteresis 113
4.2.2 Charge sensing in the bistable region 118
4.2.3 Average lifetimes of metastable states 132
4.3 Discussion 138

5 Charge sensing driving the cCPT into parametric oscillations 141

5.1 Theory . . . 141

5.1.1 Pump induced detuning . . . 145

5.2 Experimental data . . . 146

5.2.1 Charge sensing . . . 149

5.3 Conclusion . . . 152

6 Summary and future directions 154

6.1 Future directions . . . 155

6.1.1 Strong single-photon-phonon coupling of the cCPT-NR . . . 155

6.1.2 Progress in fabrication . . . 159

6.1.3 Non-linear charge sensing before bifurcation . . . 166

6.1.4 On-chip parametric amplification while performing linear charge sensing . . . 167

A Parametric amplification in the cCPT operating below the parametric threshold 168

A.1 Theory . . . 169

A.2 Experiments . . . 179

A.2.1 Subharmonic oscillations, multi-photon resonances and phase space crystals . . . 180

References 182

Chapter 1

Introduction

Transporting and measuring electron charge is ubiquitous in modern day technology. We have come a long way from Millikan's oil-drop experiment that measured the charge-to-mass ratio of an electron. Each smartphone in people's pockets comes with a camera based on a charge-coupled-device (CCD) [2]. These convert photons to electrons in small pixels, each of which is read out to obtain information about the incident light. The scanning electron microscope, a workhorse of the semiconductor industry and playing a monumental albeit background role in this thesis, is based on the detection of electrons to gain information about the surface topography and composition of a sample. These tasks are typically performed by measuring several thousands of electrons.

The past few decades have witnessed a tremendous push to use quantum computers [3, 4] to perform tasks that would be pratically impossible on a classical computer [5]. Though superconducting qubits based on transmons [6] are the furthest-along technology thus far, phosphorous donor spin qubits in silicon [7] are a promising technology for a number of reasons. With the decades' worth of expertise from the Si-based semiconductor industry, these qubits are scalable with high precision atomic level scanning tunneling microscopy (STM) based fabrication capabilities [8, 9]; fast

[10, 11], implementing single and two-qubit gates on the order of ns; and stable, exhibiting T_1 times of the order of seconds and T_2 times of the order of a few hundred μs [9, 12, 13].

Though the actual qubit is the spin of the electron in the Phosphorous donor, the tiny magnetic moment of a single electron spin makes it very challenging to readout directly. Usually, some form of spin-to-charge conversion is performed [14, 15], where energy levels across a quantum dot are tuned such that in a magnetic field, certain spin states can tunnel, while others cannot. The change in the electrostatic field induced by this single tunneling electron is readout by a charge sensitive device [12] which is capable of measuring such a single electron tunneling event. Such fast and sensitive electrometry is important for the readout of these spin-based qubits [16], for detecting signs of dark matter [17], for the detection of Majorana zero modes in nanowires [18], and for the detection of electrons tunneling in quantum dots [19].

The weak-link based single electron transistor (SET) [20, 21] first demonstrated the measurement of a fraction of an electronic charge. SETs have been used to measure electron lifetimes in a single electron trap [22], used to map static electric fields with 100 nm spatial resolution [23] and to observe macroscopic charge quantization [24]. However, the typical junction resistance of an SET is of the order of 100 kΩ, so designed to ensure charging effects are visible [25], and combined with stray capacitances of the order of 1 nF, this corresponds to a frequency bandwidth of about 1 kHz. The rf-SET [26] embeds the SET in a high-frequency tank circuit and readout is accomplished by monitoring the change in the reflected power from this tank circuit as the SET modulates the effective impedance as it goes into and out of Coulomb blockade. This increases the instantaneous bandwidth of the device to about 100 MHz operating with a charge sensitivity of 1.9 $\mu e/\sqrt{Hz}$ [27]. Electron shot-noise is the major limiting factor for the rf-SET operating at cryogenic temperatures, since

this device still operates in the voltage-biased branch. The Cooper pair transistor (CPT) [28] when current biased on the supercurrent branch, circumvents this issue (though quasiparticles still play a role [29]). A cavity-embedded Cooper pair transistor (cCPT) moves from the dissipative operation of the rf-SETs to a dispersive regime where the resonant frequency of the resonant circuit encodes the charge information, allowing us to move closer to the quantum-limit for charge detection demonstrating a charge sensitivity of 14 $\mu e/\sqrt{\text{Hz}}$ [1, 30] while operating in the single-photon regime, compared to the hundreds of thousands of photons employed by rf-SETs. Other devices based on dispersive SETs achieving 30 $\mu e/\sqrt{\text{Hz}}$ sensitivity have been demonstrated [31, 32].

The cCPT is a rich nonlinear system [33]. It has an inherent tunable Kerr nonlinearity which is comparable to the system linewidth. This puts it in an interesting, not-too-well understood 'mesoscopic' parameter regime between that of the JBAs, which can be described as a classical Duffing oscillator [34, 35], and the two-level transmons [6] which require full quantum description [36, 37]. The JBAs have been used to perform single-shot readout of a qubit [38, 39]. Devices with Kerr exceeding the system linewidth have been studied since the mid 20th century in optical systems [40], where they have been used to create squeezed states [41], in frequency conversion [42], in the generation of ultra-fast pulses [43], as a single-photon source [44] and could be used to implement quantum non-demolition measurements [45]. In the microwave regime, such systems have usually been realised using arrays of Josephson junctions (JJs) [46, 47] and have been used to demonstrate generation of cat states [48] and to create a 'Kerr-cat' qubit. The Kerr nonlinearity has also been used to implement parametric amplifiers operating in the four-wave-mixing scheme [49, 50, 51] and the broadband traveling wave parametric amplifiers (TWPA) [52]. Ref. [53] studies a device with a tunable Kerr term as it transitions from the classical Duffing oscillator

to a Kerr parametric oscillator in the single-photon Kerr regime.

Another interesting nonlinearity that appears in the cCPT is that which gives rise to three-wave-mixing upon pumping the cCPT flux line at twice the resonant frequency. Such systems have been shown to perform phase-sensitive amplification [54, 55] and have been used to perform single-shot readout of a flux qubit [56]. Parametric oscillations [57, 58] and the dynamical Casimir effect [59, 60] have been observed in such systems. Parametric oscillations have also been used to perform a dispersive readout of the state of a superconducting transmon [61].

In this thesis, we use the inherent nonlinearities in the cCPT [33] to demonstrate a novel charge sensing scheme based on the bifurcation between the bistable and the monostable region induced by the Kerr nonlinearity [34, 35]. We demonstrate a single-shot readout of $0.09e$ of charge in $3\,\mu$s with 94% readout fidelity, with fewer than 25 intracavity photons. Operating at such low powers ensures minimal back-action on the system being measured [62]. Low power operation also aids in the integration of these cCPT detectors with state-of-the-art first stage amplifiers such as TWPAs [52], without running into the danger of hitting their 3 dB compression point. Such fast, high fidelity readout is comparable to the current state-of-the-art for semiconductor spin qubits [16].

In another charge sensing scheme using the parametric oscillations induced in the cCPT, in order to distinguish between two charge states $0.08e$ apart, we choose a set of flux pump parameters such that one of the states causes no oscillations in the cCPT, while the other generates finite-amplitude parametric oscillations which can be read out in a time of $1\,\mu$s with a fidelity of 83%. A similar idea was demonstrated with lower charge resolution at room temperature in a nonlinear MoS_2 mechanical resonator [63].

We find that the limiting factor in these measurements is not the readout elec-

tronics, but is the fluctuations-induced spontaneous switching between the metastable states in the bistable regime. We perform a study of the dependence of the population ratios of the two states on system and drive parameters and qualitatively compare them to a well-understood semiclassical quantum activation model [64]. This work studies the variation of the lifetimes and steady-state populations as the strength of the Kerr and the drive parameters are varied, and could be important in better understanding the dynamics of these mescoscopic systems along with the crossover from the classical to the quantum regime.

We structure this thesis as follows: in chapter 2, we go through some of the underlying theory behind modelling microwave systems. We then derive the Hamiltonian for the cCPT as a flux and charge tunable nonlinear oscillator. In chapter 3, we describe the cCPT sample, its fabrication (done entirely by Juliang Li [65]) and the measurement setup. We also go through some common measurements on the cCPT, and discuss the effects of quasiparticle poisoning [66], which limits the operation of the cCPT. In chapter 4, we first go through the semiclassical dynamics of a Kerr cavity and discuss the semiclassical theory of switching between metastable states in the bistable regime. We then look at some experimental data from the cCPT operating in this regime, including hysteresis, switching probabilities and their dependence on system parameters. We then describe and perform the optimal charge sensing experiment. In chapter 5, we introduce the semiclassical theory of parametric oscillations and show some data showing the existence of a parametric oscillation region in the cCPT. We then demonstrate a proof-of-principle unoptimised charge detection measurement. In chapter 6, we conclude and present some possibilities for the future. In Appendix A, we derive the Hamiltonian and the dynamics for the operation of the cCPT as a parametric amplifier, and produce some data of its working as a phase-coherent degenerate parametric amplifier. We present some data for the emer-

gence of period tripling in the cCPT upon driving the flux line at thrice the resonant frequency.

Chapter 2

The cavity-embedded Cooper pair transistor - theory

The workhorse of this thesis is a cavity-embedded Cooper pair transistor (cCPT) [33, 65, 67]. The cCPT consists of two main components - (i) a quarter wavelength ($\lambda/4$) coplanar waveguide (CPW) superconducting microwave resonator (which we interchangeably refer to as the cavity) and (ii) the Cooper pair transistor [28], [68], [69]. In this chapter, we go through the theoretical background for each of these separately and derive the Hamiltonian for the composite system. Ref. [67] is an excellent pedagogical resource to understand these systems. In section 2.1.1, we go through the classical description of an infinite transmission line; in section 2.1.2, we obtain the input impedance of a shorted $\lambda/4$ transmission line such as the CPW; and in section 2.1.3 we draw a parallel between a parallel LCR circuit and the $\lambda/4$ cavity and derive the damping rates for this cavity when capacitively coupled to a feedline in section 2.1.4. Once we have all this, we can finally derive the reflection parameter (S_{11}) using this classical model which we do in section 2.1.5. In section 2.2.1, we then develop a quantum mechanical model of the transmission line resonator and having established the basics of input-output theory in section 2.3, show that the same S_{11}

is obtained using this quantum mechanical approach in section 2.3.1.

Section 2.1

The classical $\lambda/4$ cavity

In this section, we follow chapter 2 of *Microwave Engineering* by Pozar [70], which is the standard text for microwave systems in the classical regime. Starting with Kirchoff's laws for a generic transmission line, we derive the input impedance for a $\lambda/4$ cavity.

2.1.1. Classical infinite transmission line

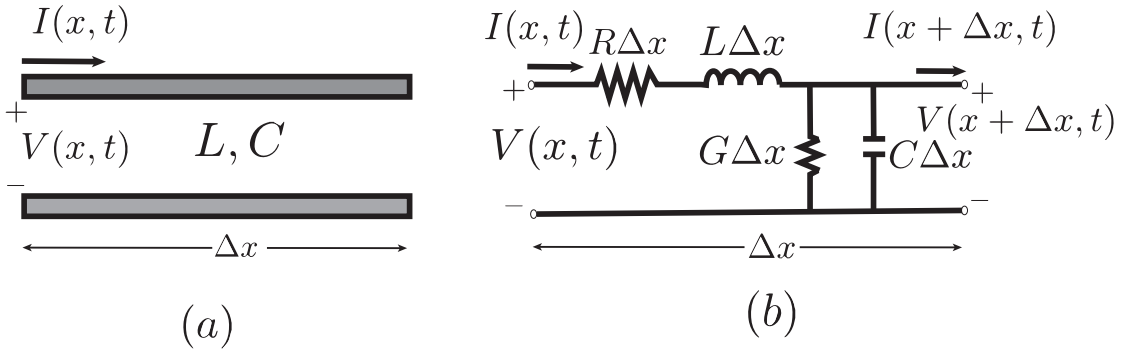

Figure 2.1: Schematic of a transmission line (a) showing the two conductors and the voltages and currents, (b) lumped element equivalent circuit.

Fig. (2.1) shows a schematic of a transmission line operating in the TEM mode (like our $\lambda/4$ cavity) which typically requires two conductors (the center line and the ground plane of the CPW) shown in Fig. (2.1a). Each infinitesimal section of the transmission line can be viewed as consisting of the equivalent lumped elements shown in Fig. (2.1b), where L is an inductance per unit length, C is a capacitance per unit length, G is a shunt conductance per unit length through the dielectric between the center line and the ground plane of the CPT and R represents the resistive loss

per unit length in the transmission line. R is typically negligible when the CPW goes superconducting as we cool our sample to dilution fridge temperatures, but we retain it here for completeness. The voltage $V(x,t)$ and the current $I(x,t)$ denote the position dependence of the voltage and current along the transmission line. It is critical to keep track of this in microwave systems, since the electrical wavelength in this region of the electromagnetic spectrum is comparable to the length of the system being studied. This is in contrast to much lower frequencies, where the corresponding wavelength is so large that the variation across typical system lengths is negligible. The other extreme is that of systems operating near optical frequencies where the wavelengths involved are so small that their description can be reduced to that of geometric optics.

For the section of transmission line shown in Fig. (2.1b), we can apply Kirchoff's voltage law and we obtain

$$V(x,t) - R\Delta x I(x,t) - L\Delta x \frac{\partial I(x,t)}{\partial t} - V(x+\Delta x,t) = 0, \tag{2.1a}$$

while Kirchoff's current law gives

$$I(x,t) - G\Delta x V(x+\Delta x,t) - C\Delta x \frac{\partial V(x+\Delta x,t)}{\partial t} - I(x+\Delta x,t)0 = 0. \tag{2.1b}$$

Dividing Eqn.(2.1a) and Eqn.(2.1b) by Δx and taking the limit $\Delta x \to 0$, we get the well known Telegrapher's equations

$$\frac{\partial V(x,t)}{\partial x} = -RI(x,t) - L\frac{\partial I(x,t)}{\partial t}, \tag{2.2a}$$

and,

$$\frac{\partial I(x,t)}{\partial x} = -GV(x,t) - C\frac{\partial V(x,t)}{\partial t}. \tag{2.2b}$$

Writing $V(x,t) = V(x)e^{i\omega t}$, we have

$$\frac{dV(x)}{dx} = -(R + i\omega L)I(x),, \tag{2.3a}$$

and,

$$\frac{dI(x)}{dx} = -(G + i\omega C)V(x). \tag{2.3b}$$

Taking the derivative of 2.3a and 2.3b w.r.t x, using Eqn.(2.3b) in Eqn.(2.3a) and vice versa, we get

$$\frac{d^2V(x)}{dx^2} - \gamma^2 V(x) = 0, \tag{2.4a}$$

and,

$$\frac{d^2I(x)}{dx^2} - \gamma^2 I(x) = 0. \tag{2.4b}$$

where $\gamma = \alpha + i\beta = \sqrt{(R + i\omega L)(G + i\omega C)}$. These equations admit traveling wave solutions of the form

$$V(x) = V_0^+ e^{-\gamma x} + V_0^- e^{\gamma x}, \tag{2.5a}$$

$$I(x) = \frac{V_0^+}{Z_0} e^{-\gamma x} - \frac{V_0^-}{Z_0} e^{\gamma x}. \tag{2.5b}$$

where $Z_0 = \sqrt{\frac{R+i\omega L}{G+i\omega C}}$ is the characteristic impedance of the transmission line and $V_0^{+(-)}$ is the complex voltage of the forward (backward) traveling component at $x = 0$. For our case of a superconducting CPW with low dielectric loss, $R \ll \omega L$ and $G \ll \omega C$, we have $Z_0 = \sqrt{\frac{L}{C}}$ for the characteristic impedance similar to that of a lossless transmission line.

Reintroducing the time dependence, we have for the voltage

$$V(x,t) = \left|V_0^+\right| \cos\left(\omega t - \beta x + \phi^+\right) e^{-\alpha x} + \left|V_0^-\right| \cos\left(\omega t + \beta x + \phi^-\right) e^{\alpha x} \tag{2.6}$$

where $\phi^{\pm}$ is the phase of the corresponding wave, and the wave number β is related to the wavelength λ by $\beta = 2\pi/\lambda = \omega/v_p$ with v_p being the propagation velocity in the TEM mode of a transmission line. This depends on the dielectric constant ϵ_r and is given by $v_p = \frac{c}{\epsilon_r}$, where c is the speed of light in vacuum.

To estimate the dielectric loss in our TEM mode transmission line, we use the fact that $\alpha_d = \frac{GZ_0}{2} = \frac{\beta \tan\delta}{2}$ Np/m from chapter 3 in [70], where α_d is the contribution of the dielectric loss to the total loss, α, and $\tan\delta = 0.004$ is the loss tangent for the silicon substrate at 300 K, which is only expected to decrease at cryogenic temperatures. This yields a $G/\omega C = 0.0054 \ll 1$ at a frequency $\omega/2\pi = 5$ GHz (estimated for our $C = 0.17$ nF/m) [33]. We also note here that $\alpha_d l = \frac{\beta l \tan\delta}{2} = \frac{\pi \tan\delta}{4} \ll 1$ for a $\lambda/4$ cavity with a silicon dielectric.

2.1.2. The shorted $\lambda/4$ transmission line

Now that we know the form of the voltage and current waves in an infinite transmission line which is a good approximation for the long (relative to the wavelength of the microwave drives) coaxial cables which we use to connect our microwave instruments to the $\lambda/4$ cavity at the mixing chamber of a dilution fridge, we can consider a transmission line of finite length l terminated with a load Z_L at $x = 0$ as show in

Fig. (2.2). For our specific case of a $\lambda/4$ CPW, $l = \lambda/4$ and $Z_L = 0$.

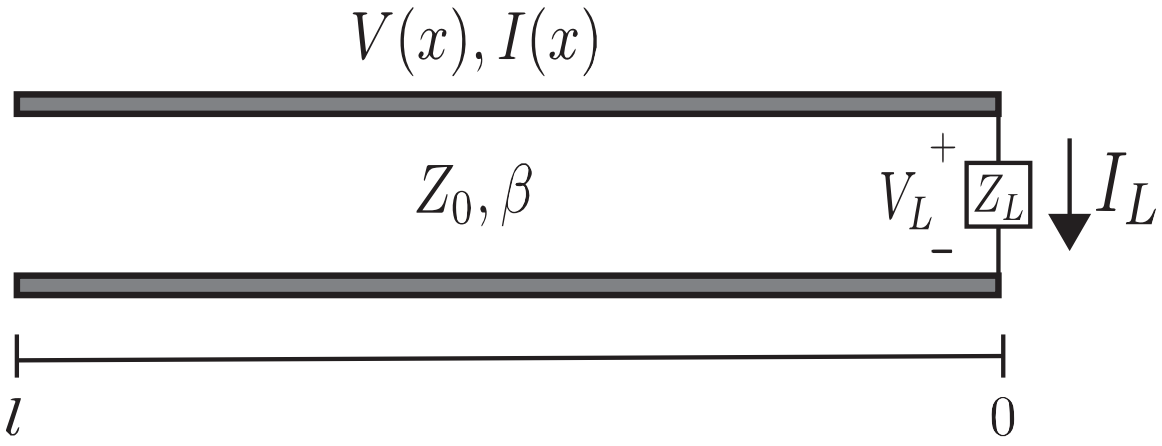

Figure 2.2: Schematic of a transmission line loaded with a load impedance Z_L.

At $x = 0$, using Eqns. (2.5a) and (2.5b), we now have

$$Z_L = \frac{V(0)}{I(0)} = \frac{V_0^+ + V_0^-}{V_0^+ - V_0^-}, \tag{2.7}$$

which gives us the reflection coefficient Γ,

$$\Gamma = \frac{V_0^-}{V_0^+} = \frac{Z_L - Z_0}{Z_L + Z_0}. \tag{2.8}$$

The input impedance of the transmission line at $x = -l$ is thus

$$Z_{\text{in}} = \frac{V(-l)}{I(-l)} = \frac{V_0^+[e^{\gamma l} + \Gamma e^{-\gamma l}]}{V_0^+[e^{\gamma l} - \Gamma e^{-\gamma l}]} Z_0 = Z_0 \frac{(Z_L + Z_0 \tanh \gamma l)}{(Z_0 + Z_L \tanh \gamma l)}. \tag{2.9}$$

For the case of our shorted $\lambda/4$ CPW, $Z_L = 0$ and this becomes

$$\begin{aligned} Z_{\text{in}} &= Z_0 \tanh \gamma l \\ &= Z_0 \tanh (\alpha + i\beta) l \\ &= Z_0 \frac{\tanh \alpha l + i \tan \beta l}{1 + i \tan \beta l \tanh \alpha l}. \end{aligned} \tag{2.10}$$

Further, we define the fundamental resonant frequency as the frequency ω_0 which has a corresponding wavelength λ_1 such that $l = \lambda_1/4$ (we will see later that this is the frequency at which the input impedance as seen by a feedline to the cavity is purely real) and we write $\omega = \omega_0 + \Delta$ in terms of the detuning Δ. This gives us

$$\beta l = \frac{\omega_0 l}{v_p} + \frac{\Delta l}{v_p} = \frac{\pi}{2} + \frac{\pi\Delta}{2\omega_0}, \tag{2.11}$$

since $\omega_0\lambda_1/v_p = 2\pi$, and,

$$\cot\beta l = \cot\big(\frac{\pi}{2} + \frac{\pi\Delta}{2\omega_0}\big) = -\tan\frac{\pi\Delta}{2\omega_0} \approx \frac{-\pi\Delta}{2\omega_0}. \tag{2.12}$$

We note that this holds only close to the resonant frequency ($\Delta \ll \omega_0$). Also using $\tanh\alpha l \approx \alpha l$ for small loss, we have

$$Z_{\text{in}} \approx Z_0\frac{1 + i\alpha l\Delta/2\omega_0}{\alpha l + i\pi\Delta/2\omega_0} \approx \frac{Z_0}{\alpha l + i\pi\Delta/2\omega_0} \tag{2.13}$$

where we have used the fact that $\alpha l\pi\Delta/2\omega_0 \ll 1$.

2.1.3. Lumped element parallel LCR circuit

The input impedance $Z_{\text{in}}^{\text{LCR}}$ of a lumped element parallel LCR circuit shown in Fig. (2.3) is given by

$$Z_{\text{in}}^{\text{LCR}} = \big(\frac{1}{R_{\text{LCR}}} + \frac{1}{i\omega L_{\text{LCR}}} + i\omega C_{\text{LCR}}\big)^{-1}. \tag{2.14}$$

Writing $\omega = \omega_0 + \Delta$ as in sec. (2.1.2), working close to $\omega_0 = \frac{1}{\sqrt{L_{\text{LCR}}C_{\text{LCR}}}}$ at which frequency $Z_{\text{in}}^{\text{LCR}}$ is purely real, and Taylor expanding the inductive impedance to first order around ω_0, we have

$$Z_{\text{in}}^{\text{LCR}} \approx \left(\frac{1}{R_{\text{LCR}}} + \frac{1}{i\omega_0 L_{\text{LCR}}} - \frac{\Delta}{i\omega_0^2 L_{\text{LCR}}} + i\omega_0 C_{\text{LCR}} + i\Delta C_{\text{LCR}}\right)^{-1}$$

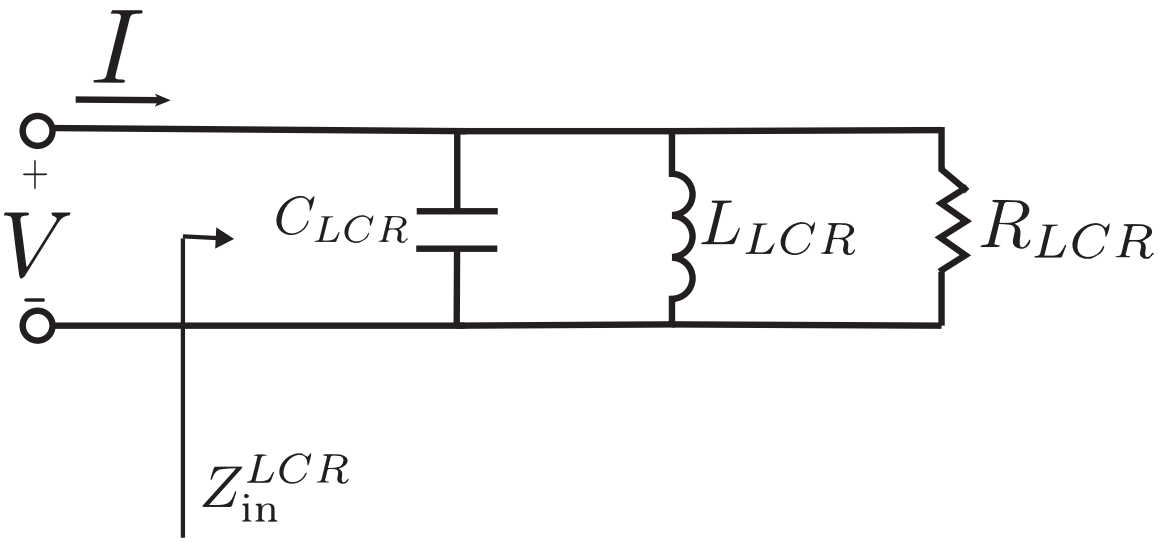

Figure 2.3: Schematic of a parallel LCR circuit.

$$
\begin{aligned}
&= \left(\frac{1}{R_{\text{LCR}}} + \frac{i\Delta}{\omega_0^2 L_{\text{LCR}}} + i\Delta C_{\text{LCR}} \right)^{-1} \\
&= \left(\frac{1}{R_{\text{LCR}}} + 2i\Delta C_{\text{LCR}} \right)^{-1} \\
&= \frac{1}{(1/R_{\text{LCR}}) + 2i\Delta C_{\text{LCR}}}.
\end{aligned} \tag{2.15}
$$

Comparing Eqns. (2.13) and (2.15), we see that close to its fundamental resonance at ω_0, the $\lambda/4$ cavity behaves as a parallel LCR circuit with effective lumped element parameters

$$R_{\text{LCR}} = \frac{Z_0}{\alpha l}, \tag{2.16a}$$

$$C_{\text{LCR}} = \frac{\pi}{4\omega_0 Z_0}, \tag{2.16b}$$

$$L_{\text{LCR}} = \frac{4Z_0}{\pi\omega_0}. \tag{2.16c}$$

2.1.4. Capacitively coupled shorted $\lambda/4$ cavity

Now that we have a classical model for the standalone cavity itself, we are in a position to study what happens when this cavity is capacitively coupled through a capacitance

C_c to an external setup through a matched feedline which also has a characteristic impedance Z_0 as in Fig. (2.4a).

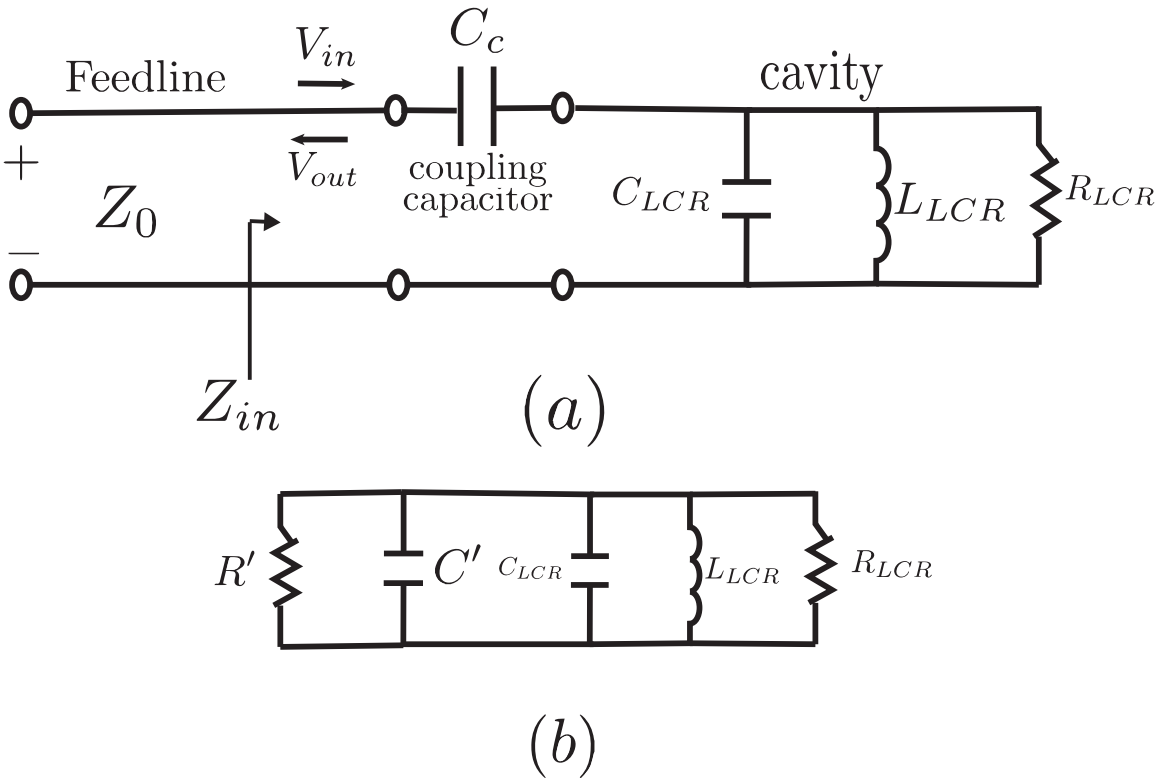

Figure 2.4: (a) Schematic of a $\lambda/4$ cavity capacitively coupled to a feedline with characteristic impedance Z_0. (b) Equivalent lumped element circuit.

As in [71], we replace this series combination of Z_0 and C_c with a parallel combination of R' and C' as in Fig. (2.4b). To find R' and C', we use

$$Z_0 - \frac{i}{\omega C_c} = \left(\frac{1}{R'} + i\omega C'\right)^{-1}. \tag{2.17}$$

Equating the real and imaginary parts on both sides, we find

$$\begin{aligned} C' &= \frac{C_c}{1+\omega^2 Z_0^2 C_c^2} \\ &\approx C_c, \end{aligned} \tag{2.18a}$$

$$R' = Z_0\left(1 + \frac{1}{\omega^2 Z_0^2 C_c^2}\right) \approx \frac{1}{\omega_0^2 C_c^2 Z_0}, \tag{2.18b}$$

where we have used the fact that $\Delta \approx 0$ for drive tones close to resonance to write $\omega \approx \omega_0$ and the fact that $\omega_0 Z_0 C_c = 0.0144 \ll 1$ for our $\lambda/4$ cavity with parameters $C_c = 7.95$ fF, $\omega_0/2\pi \approx 5.76$ GHz, $Z_0 = 50\Omega$, corresponding to $C_{\mathrm{LCR}} = 434$ fF, $L_{\mathrm{LCR}} = 1.76$ nH.

With the circuit in the form of Fig.(2.4b), we are in a position to determine the internal and external quality factors (Qs) of the cavity. As defined in chapter 6 of [70], the Q is given by

$$Q = \omega \frac{\text{average energy stored}}{\text{energy loss/second}}. \tag{2.19}$$

Looking at Fig. (2.4b), we see that there are two loss mechanisms in the driven cavity. The first (with a corresponding Q_{int}) is due to the intrinsic loss in the cavity, which is related to dielectric loss and is modelled by the loss through the resistor R_{LCR}. The second (with a corresponding Q_{ext}) is due to the external circuitry as energy leaks into and out of the cavity through the coupling capacitor C_c as we probe the cavity. This is modelled by the loss through the resistor R'. The total energy stored in the circuit in Fig. (2.4b) is the sum of the energy stored in the capacitors (C_{LCR} and C') and the energy stored in the inductor (L_{LCR}). On resonance, these energies are equal. For a drive voltage of amplitude V_{in}, we have

$$\text{Energy stored in LC circuit} = 2 \times \frac{1}{2} \times (C_{\mathrm{LCR}} + C')|V_{\mathrm{in}}|^2, \tag{2.20a}$$

$$\text{Energy loss through } R_{\mathrm{LCR}}/\text{second} = \frac{|V_{\mathrm{in}}|^2}{R_{\mathrm{LCR}}}, \tag{2.20b}$$

$$\text{Energy loss through } R'/\text{second} = \frac{|V_{\mathrm{in}}|^2}{R'}, \tag{2.20c}$$

where the factor of 2 in energy stored accounts for both the capacitive and the inductive energies, we then have

$$Q_{\text{int}} = \omega \frac{\text{energy stored in LC circuit}}{\text{energy loss through } R_{\text{LCR}}/\text{second}} = (C_{\text{LCR}} + C_c) R_{\text{LCR}} \omega_0, \tag{2.21a}$$

$$Q_{\text{ext}} = \omega \frac{\text{energy stored in LC circuit}}{\text{energy loss through } R'/\text{second}} = (C_{\text{LCR}} + C_c) R' \omega_0 \tag{2.21b}$$

$$= \frac{(C_{\text{LCR}} + C_c)}{\omega_0 Z_0 C_c^2}. \tag{2.21c}$$

Re-writing the above equations in terms of the parameters of the $\lambda/4$ cavity,

$$Q_{\text{int}} = \frac{\pi}{4\alpha l}, \tag{2.22a}$$

$$Q_{\text{ext}} = \frac{\pi}{4\omega_0^2 Z_0^2 C_c^2}, \tag{2.22b}$$

where we used the fact $C_c \ll C_{\text{LCR}}$ based on the above design parameters. Defining the cavity internal and external damping rates as $\kappa_{\text{int(ext)}} = \frac{\omega_0}{Q_{\text{int(ext)}}}$, we have

$$\kappa_{\text{int}} = \frac{4\omega_0 \alpha l}{\pi}, \tag{2.23a}$$

$$\kappa_{\text{ext}} = \frac{4\omega_0^3 Z_0^2 C_c^2}{\pi}. \tag{2.23b}$$

For our experimental devices, we typically want to be in the regime where $\kappa_{\text{ext}} > \kappa_{\text{int}}$. Heurisitcally, this can be thought of as saying that we want any information leaking out of the cavity to be accessible, as opposed to being lost through some internal lossy channel.

2.1.5. Classical S_{11} for the shorted $\lambda/4$ cavity

In order to calculate the reflection coefficient we change notation here from the previous Γ to S_{11} to make contact with the fact that this measurement is done with a

vector network analyzer (VNA) for which it is common to talk about the scattering (S) matrix of the device under test (DUT). We follow appendix B of [72] for this section. The reflection coefficient S_{11} at the point where the feedline drives the coupling capacitor as depicted in Fig. (2.4a), using Eqn. (2.8) is given by

$$S_{11} = \frac{Z_{\text{cav}} - Z_0}{Z_{\text{cav}} + Z_0}, \tag{2.24}$$

where, (dropping the 'LCR' subscript for brevity)

$$\begin{aligned} Z_{\text{cav}} &= \frac{1}{i\omega C_c} + \left(\frac{1}{R} + \frac{1}{i\omega L} + i\omega + C\right)^{-1} \\ &= \frac{i\omega L + R - R\omega^2 LC - \omega^2 RLC_c}{i\omega C_c(i\omega L + R - R\omega^2 LC)}. \end{aligned} \tag{2.25}$$

We then have

$$S_{11} = \frac{1 - \omega^2[L(C_c + C) - \frac{Z_0 C_c L}{R}] + i\omega\left[\frac{L}{R} - Z_0 C_c(1 - \omega^2 LC)\right]}{1 - \omega^2[L(C_c + C) + \frac{Z_0 C_c L}{R}] + i\omega\left[\frac{L}{R} + Z_0 C_c(1 - \omega^2 LC)\right]}. \tag{2.26}$$

Since $\frac{Z_0}{R} = \alpha l \ll 1$ (see section 2.1.1 and Eqn. (2.16a)), and writing $y = \frac{\omega}{\omega_0}$ where the cavity resonant frequency, ω_0 is defined as

$$\omega_0 = \frac{1}{\sqrt{L(C_c + C)}} \approx \frac{1}{\sqrt{LC}}, \tag{2.27}$$

for $C_c \ll C$, we have

$$S_{11} = \frac{1 - y^2 + iy\omega_0\left[\frac{L}{R} - Z_0 C_c(1 - y^2\omega_0^2 LC)\right]}{1 - y^2 + iy\omega_0\left[\frac{L}{R} + Z_0 C_c(1 - y^2\omega_0^2 LC)\right]}. \tag{2.28}$$

Eliminating R and Z_0 for Q_{int} and Q_{ext} from Eqns. (2.22a and 2.22b), we have

$$S_{11} = \frac{1 - y^2 + iy\left[\frac{1}{Q_{\text{int}}} - \frac{C+C_c}{Q_{\text{ext}}C_c}\left(1 - y^2\frac{C}{C+C_c}\right)\right]}{1 - y^2 + iy\left[\frac{1}{Q_{\text{int}}} + \frac{C+C_c}{Q_{\text{ext}}C_c}\left(1 - y^2\frac{C}{C+C_c}\right)\right]}. \tag{2.29}$$

We now use the fact that we are driving close to resonance again. So, we write $y = 1 + \delta y$ where $\delta y = \frac{\Delta}{\omega_0}$ and expand to first order in δy and make use of the fact that $C_c/(C_c + C) \ll 1$, to get

$$S_{11} = \frac{-2\delta y + i\left[\frac{1}{Q_{\text{int}}} - \frac{1}{Q_{\text{ext}}}\right]}{-2\delta y + i\left[\frac{1}{Q_{\text{int}}} + \frac{1}{Q_{\text{ext}}}\right]}. \tag{2.30}$$

Multiplying throughout by ω_0 and using the definitions of κ_{ext} and κ_{int}, we have

$$S_{11}(\omega) = \frac{(\omega - \omega_0) + i(\kappa_{\text{ext}} - \kappa_{\text{int}})/2}{(\omega - \omega_0) + i\kappa_{\text{tot}}/2}. \tag{2.31}$$

where we defined the total damping rate $\kappa_{\text{tot}} = \kappa_{\text{int}} + \kappa_{\text{ext}}$.

In section 2.5, we see that the introduction of the CPT in the $\lambda/4$ cavity gives us the ability to tune the resonant frequency ω_0 using the DC gate voltage and the flux through the cavity. Eqn. (2.31) is the model we use to extract the damping rates and the resonant frequency across the bias range of the cCPT when operated at low drive powers, which in turn is used to model the nonlinear behaviour of the cCPT in chapters 4 and 5. In section 3.7, we will see a few examples of how we extract these cavity parameters in the presence of noise in the bias parameter as described in [33, 67, 73].

Section 2.2

Quantum mechanical model for $\lambda/4$ resonator

In this section, we show that the infinite transmission line admits traveling wave solutions in both directions. This is essentially an infinite number of harmonic oscillator modes which we quantize by introducing canonical commutation relations. We then turn to the the $\lambda/4$ cavity and by introducing boundary conditions show that the cavity Hamiltonian is the sum of discrete harmonic oscillator modes. We will then introduce input-output theory in section 2.3 [74], [75] which is a standard model to describe systems coupled to a Bosonic bath such as a transmission line in section 2.3 and re-derive the scattering parameter S_{11} using this formalism.

2.2.1. Quantum infinite transmission line

We begin with the same lumped element model for an infinitesimal section of an infinite transmission line as in section 2.1.1 and Fig. (2.1), reproduced here in Fig. (2.5) but assume it to be lossless with $G = R = 0$. We will see that we can re-introduce the effect of loss using input-output theory in section 2.3. Here, we follow the treatment in appendices C and D of [76]. Ref.[77] is also a very accessible resource that deals with these concepts.

We define a branch flux variable [78] as

$$\phi(x,t) = \int_{-\infty}^{t} d\tau V(x,\tau). \tag{2.32}$$

In terms of the energy stored in the capacitor, which by convention behaves like a kinetic energy, and the energy in the inductor, which by the same convention plays the role of a potential energy in this infinitesimal section of the transmission line, the

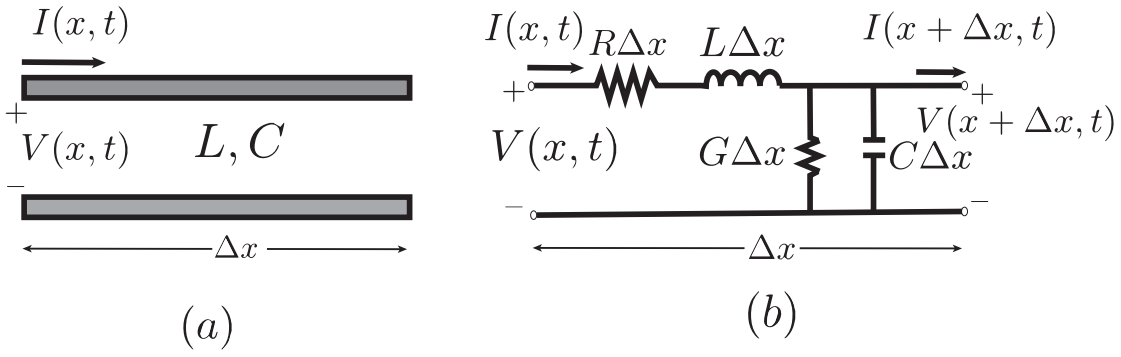

Figure 2.5: Schematic of a transmission line (a) showing the two conductors and the voltages and currents, (b) lumped element equivalent circuit.

Lagrangian density is then given by,

$$\mathscr{L}(x,t) = \frac{C}{2}\dot{\phi}^2(x,t) - \frac{1}{2L}\big(\partial_x\phi(x,t)\big)^2. \tag{2.33}$$

where we used the fact that the current through the inductor is related to the voltage dV across it by $L\dot{I} = dV$ and used the definition of the branch flux Eqn. (2.32) to write $I = \frac{1}{L}\partial_x\phi(x,t)$. The conjugate momentum to this branch flux is the canonical charge $q(x,t)$ given by

$$q(x,t) = \frac{\partial\mathscr{L}}{\partial\dot{\phi}} = C\dot{\phi}(x,t). \tag{2.34}$$

We can then write down the Hamiltonian density as

$$\mathscr{H} = \frac{1}{2C}q^2(x,t) + \frac{1}{2L}\big(\partial_x\phi(x,t)\big)^2. \tag{2.35}$$

Using the Euler-Lagrange equations in ϕ, $\phi' = \partial_x\phi$ and $\dot{\phi} = \partial_t\phi$, we obtain the wave equation

$$\partial_t^2\phi(x,t) = v_p^2\partial_x^2\phi(x,t) \tag{2.36}$$

where $v_p = 1/\sqrt{LC}$ is the phase velocity as before. We note that this wave equation can also be obtained from the Telegrapher's equations, Eqn.(2.3a) and (2.3b), by writing $V(x,t)$ and $I(x,t)$ in terms of $\phi(x,t)$ as above.

We now quantize $\mathscr{H}$ by promoting q and ϕ to operators $\hat{q}$ and $\hat{\phi}$, and impose the equal time canonical commutation relations,

$$\begin{aligned}
\left[\hat{\phi}(x,t), \hat{q}(x',t)\right] &= i\hbar\delta(x-x'), \\
\left[\hat{q}(x,t), \hat{q}(x',t)\right] &= 0, \\
\left[\hat{\phi}(x,t), \hat{\phi}(x',t)\right] &= 0.
\end{aligned} \tag{2.37a}$$

The general solution to the wave equation Eqn. (2.36) can be written as the sum of a right propagating and a left propagating wave, which in turn can be expanded in their normal modes $a_R(\omega)$ and $a_L(\omega)$ respectively. We then have (dropping hats for brevity) [30],

$$\phi(x,t) = \sqrt{\frac{\hbar Z_0}{4\pi}} \int_0^\infty \frac{d\omega}{\sqrt{\omega}} \left(e^{-i\omega(t+x/v_p)} a_L(\omega) + e^{-i\omega(t-x/v_p)} a_R(\omega) \right) + h.c., \tag{2.38a}$$

$$q(x,t) = -iC\sqrt{\frac{\hbar Z_0}{4\pi}} \int_0^\infty d\omega \sqrt{\omega} \left(e^{-i\omega(t+x/v_p)} a_L(\omega) + e^{-i\omega(t-x/v_p)} a_R(\omega) \right) + h.c. \tag{2.38b}$$

In order to obtain the mode operators $a_L(\omega)$ ($a_R(\omega)$), we multiply Eqn.(2.38b) by $\frac{1}{-iC\omega} e^{i\omega(t\pm x/v_p)}$ and Eqn.(2.38a) by $e^{i\omega(t\pm x/v_p)}$ respectively and integrate the sum over all space dx. Using the definition of the Dirac-delta function

$$\int_{-\infty}^{\infty} e^{i(\omega-\omega')x/v_p} dx = 2\pi v_p \delta(\omega-\omega') \tag{2.39}$$

we get,

$$a_L(\omega) = \frac{1}{v_p}\sqrt{\frac{\omega}{4\pi\hbar Z_0}}\int_{-\infty}^{\infty}\left(\phi(x,t) + \frac{i}{\omega C}q(x,t)\right)e^{i\omega(t+x/v)}dx, \tag{2.40a}$$

$$a_R(\omega) = \frac{1}{v_p}\sqrt{\frac{\omega}{4\pi\hbar Z_0}}\int_{-\infty}^{\infty}\left(\phi(x,t) + \frac{i}{\omega C}q(x,t)\right)e^{i\omega(t-x/v)}dx. \tag{2.40b}$$

We can then use this and the canonical commutation relation Eqn.(2.37a) to derive the commutation relations of the mode operators to be

$$\left[a_{L(R)}(\omega), a^{\dagger}_{L(R)}(\omega')\right] = \delta(\omega - \omega'), \tag{2.41}$$

with all other commutators being zero. We note here that using $q = CV$ and $\phi = LI$, we can write

$$V(x,t) = -i\sqrt{\frac{\hbar Z_0}{4\pi}}\int_0^{\infty} d\omega\sqrt{\omega}\left(e^{-i\omega(t+x/v_p)}a_L(\omega) + e^{-i\omega(t-x/v_p)}a_R(\omega)\right) + h.c., \tag{2.42a}$$

$$I(x,t) = \frac{1}{L}\sqrt{\frac{\hbar Z_0}{4\pi}}\int_0^{\infty}\frac{d\omega}{\sqrt{\omega}}\left(e^{-i\omega(t+x/v_p)}a_L(\omega) + e^{-i\omega(t-x/v_p)a_R(\omega)}\right) + h.c. \tag{2.42b}$$

In order to express the Hamiltonian in Eqn.(2.35) in terms of these mode operators, we first write $\phi'(x,t)$ in Eqn.(2.35) as

$$\phi'(x,t) = \frac{-i}{v_p}\sqrt{\frac{\hbar Z_0}{4\pi}}\int_0^{\infty}\frac{d\omega}{\sqrt{\omega}}\Big(e^{-i\omega(t+x/v_p)}a_L(\omega) - e^{-i\omega(t-x/v_p)}a_R(\omega) - e^{i\omega(t+x/v_p)}a^{\dagger}_L(\omega) + e^{i\omega(t+x/v_p)}a^{\dagger}_R(\omega)\Big). \tag{2.43}$$

Using Eqns.(2.43) and (2.38b) in the Hamiltonian density, and integrating over

all space dx to obtain the Hamiltonian, we have

$$H = \int_0^\infty \hbar\omega\big(a_R^\dagger(\omega)a_R(\omega) + a_L^\dagger(\omega)a_L(\omega)\big), \tag{2.44}$$

where we have used the mode operator commutation relations Eqn.(2.41).

By associating the left-moving modes with negative frequencies, and the right-moving modes with positive frequencies as in appendix C of [76], we then finally have for the Hamiltonian of the infinite transmission line

$$H = \int_{-\infty}^{\infty} d\omega\hbar\omega a^\dagger(\omega)a(\omega) \tag{2.45}$$

The quantum $\lambda/4$ transmission line

Having dealt with the case of an infinite transmission line such as the coax cables running the length of our dilution fridge to the cCPT sample, we will now look at the case of the $\lambda/4$ microwave cavity forming the cCPT itself. The Lagrangian density for this system is the same as in Eqn.(2.33), but holds only for the space between $x = 0$ and $x = l = \frac{\lambda_1}{4}$ (where l is the length of the cavity and λ_1 is the wavelength of the fundamental mode of the cavity). The wave equation Eqn.(2.36) is still satisfied in this region, and we impose the additional boundary conditions

$$\frac{\partial\phi(x,t)}{\partial t}|_{x=0} = 0, \tag{2.46a}$$

$$\phi(l,t) = 0. \tag{2.46b}$$

which are tantamount to the voltage at the shorted end of the cavity being zero and the current at the open end of the cavity being zero. Applying these boundary

conditions, the general solution to the wave equation can be conveniently written as

$$\begin{aligned}\phi(x,t) &= \sum_k A_k \cos(kx+\alpha_k)\cos(kv_p t+\beta_k),\\ &= \sum_{n=1}^{\infty} \Phi_n(t)\cos(k_n x),\\ \because \alpha_k &= 0\ \forall\ k,\ k\in\left\{k_n = \frac{(2n-1)\pi}{2l},\ n\in\mathbb{N}\right\}\end{aligned} \tag{2.47}$$

where $\Phi_n(t) = A_n\cos(k_n v_p t+\beta_n)$ are the normal modes of the cavity. We see that the boundary conditions give rise to a superposition of standing waves, each corresponding to a normal mode of the cavity, as opposed to the traveling wave solutions in the infinite transmission line earlier. To obtain the Lagrangian of this cavity, we use Eqn.(2.47) in the Lagrangian density of the system Eqn.(2.33) and integrating over the limits $x=0$ and $x=l$, we have

$$L = \sum_{n=1}^{\infty}\left[\frac{lC}{4}\dot{\Phi}_n^2 - \frac{lk_n^2}{4L}\Phi_n^2\right]. \tag{2.48}$$

The Lagrangian of a single mode bears close resemblance to that of a lumped element LC circuit [67], and thus we can conclude that the cavity behaves as a collection of modes, each effectively an LC circuit with effective mode inductance $L_n = 2L/lk_n^2$ and effective mode capacitance $C_n = lC/2$.

As before, we can now find the momentum conjugate to the canonical position Φ_n and use that in a Legendre transform to obtain the Hamiltonian of this system. The momentum conjugate to the flux is the charge q, given by,

$$q_n = \frac{\partial\mathcal{L}}{\partial\dot{\Phi}_n} = C_n\dot{\Phi}_n, \tag{2.49}$$

which gives the Hamiltonian

$$H = \sum_{n=1}^{\infty} \left[\frac{q_n^2}{2C_n} + \frac{\Phi_n^2}{2L_n} \right]. \tag{2.50}$$

As before, we quantize this Hamiltonian by promoting q_n's and Φ_n's to operators (immediately dropping the hats) so that they obey the canoncical commutation relations

$$\begin{aligned} \big[\Phi_m, q_n\big] &= i\hbar\delta_{mn}, \\ \big[\Phi_m, \Phi_n\big] &= 0, \\ \big[q_m, q_n\big] &= 0. \end{aligned} \tag{2.51}$$

Introducing the creation and annihilation (ladder) operators defined by

$$\begin{aligned} a_n &= \sqrt{\frac{1}{2\hbar Z_n}}(\Phi_n + iZ_n q_n), \\ a_n^\dagger &= \sqrt{\frac{1}{2\hbar Z_n}}(\Phi_n - iZ_n q_n), \end{aligned} \tag{2.52}$$

where $Z_n = \sqrt{L_n/C_n}$ is the mode impedance of the nth mode, and these satisfy the usual commutation relations,

$$\begin{aligned} \big[a_m, a_n^\dagger\big] &= \delta_{mn}, \\ \big[a_m, a_n\big] &= 0, \\ \big[a_m^\dagger, a_n^\dagger\big] &= 0, \end{aligned} \tag{2.53}$$

we have for the Hamiltonian of the $\lambda/4$ cavity,

$$H = \sum_{n=1}^{\infty} \hbar\omega_n \left(a_n^\dagger a_n + \frac{1}{2} \right), \tag{2.54}$$

where $\omega_n = 1/\sqrt{L_n C_n}$ is the resonant frequency of the nth cavity mode which matches with our classical derivation Eqn.(2.27) for the fundamental cavity mode with resonant frequency ω_0.

Section 2.3

Input-output theory

In this section, we will see how input-output theory [74] is a versatile theory to model how a system such as the microwave cavity oscillator described in section 2.1.4 couples to its environment. This will be used to model how the (nonlinear) cCPT couples to the external microwave signals which we use to both drive the system and to probe the dynamics of the system. We follow the text of Gardiner and Zoller [75] here, in particular, sections (3.1), (3.2) and (5.3). Chapter 1 of [79] is also an excellent concise reference for modelling such open quantum system dynamics.

The quantum Langevin equation, which is the quantum analog of the Langevin equation describing the motion of a Brownian particle in a viscous medium and a given potential, is at its heart based on the Heisenberg equation of motion. It describes a system (we will assume a single degree of freedom here) linearly coupled to a thermal bath assumed to be a Bosonic harmonic oscillator bath with a dense spectrum of oscillator frequencies. This linear coupling is a good model for electromagnetic radiation such as exists in our cavity and cCPT. We will also make the first Markov approximation at the outset, which ensures the coupling strength between the bath and the system is independent of the frequency of the bath mode, also equiv-

alent to saying that the bath is memoryless and correlations are very short-lived. We thus have the following total Hamiltonian

$$H = H_{\text{sys}} + H_{\text{bath}} + H_{\text{int}}, \tag{2.55}$$

where the system Hamiltonian will remain arbitrary for now, with the associated single degree of freedom being represented by the mode operator a and $a^\dagger$. Further,

$$\begin{aligned} H_{\text{bath}} &= \int_{-\infty}^{\infty} d\omega \hbar\omega b^\dagger(\omega) b(\omega), \\ H_{\text{int}} &= -i\hbar \int_{-\infty}^{\infty} d\omega \sqrt{\frac{\kappa}{2\pi}} \left[b^\dagger(\omega) a - a^\dagger b(\omega) \right], \end{aligned} \tag{2.56}$$

where κ is the strength of the coupling between the bath and the system, $b(\omega)$ is the bath operator associated with the bath mode with frequency ω, satisfying the commutation relation,

$$\left[b(\omega), b^\dagger(\omega') \right] = \delta(\omega - \omega'),$$

and all other commutators are zero. This form of the bath is exactly that of the infinite transmission line Hamiltonian in Eqn.(2.45), and shows that the coupling between the transmission line and the cavity can be modelled by considering the transmission line to be a loss channel to the microwave cavity. This form of the interaction Hamiltonian has implicitly made the rotating wave approximation (RWA), which justifies extending the lower limit of integration in the H_{int} to $-\infty$. The RWA essentially says that given that $a(\omega, t) = a(\omega, 0)e^{-i\omega t}$ (and that the h.c. evolves similarly), Hamiltonian terms that are not stationary in the rotating frame will evolve rapidly (oscillation period on the order of ns for microwave systems), and will average to zero over any experimentally relevant measurement time.

The Heisenberg equations of motion for the system and bath operator a and b

respectively are then

$$\dot{b}(\omega,t) = -i\omega b(\omega,t) - \sqrt{\frac{\kappa}{2\pi}}a(t), \tag{2.57a}$$

$$\dot{a}(t) = -\frac{i}{\hbar}\big[a(t), H_{\text{sys}}\big] + \sqrt{\frac{\kappa}{2\pi}}\int_{-\infty}^{\infty} d\omega b(\omega,t). \tag{2.57b}$$

We now solve Eqn.(2.57a) by adding a particular solution to the solution of the homogeneous equation, and we have (dropping explicit time-dependent notation),

$$b(\omega) = e^{-i\omega(t-t_0)}b_0(\omega) - \sqrt{\frac{\kappa}{2\pi}}\int_{t_0}^{t} e^{-i\omega(t-t')}a(t')dt', \tag{2.58}$$

where $b_0(\omega) = b(\omega, t_0)$. We now define an 'in' field with appropriate commutation relations as

$$b_{\text{in}}(t) = \frac{1}{\sqrt{2\pi}}\int_{-\infty}^{\infty} d\omega e^{-i\omega(t-t_0)}b_0(\omega), \tag{2.59}$$

$$\big[b_{\text{in}}(t), b_{\text{in}}(t')\big] = \delta(t-t'), \tag{2.60}$$

where we can derive Eqn.(2.60) from the fact that the bath operators obey the commutation relation $\big[b(\omega), b(\omega')\big] = \delta(\omega-\omega')$. Plugging this into the integral over all bath modes of Eqn.(2.58), we have

$$\sqrt{\frac{\kappa}{2\pi}}\int_{-\infty}^{\infty} b(\omega)d\omega = \sqrt{\kappa}b_{in}(t) - \frac{\kappa}{2}a(t), \tag{2.61}$$

where the factor of 2 in the last term comes from the fact that the peak of the delta function is at the limit of the interval of integration. Plugging this back into the differential equation for the system operator $a(t)$, Eqn.(2.57b), we have

$$\dot{a}(t) = -\frac{i}{\hbar}\big[a(t), H_{\text{sys}}\big] + \sqrt{\kappa}b_{\text{in}}(t) - \frac{\kappa}{2}a(t). \tag{2.62}$$

This shows that the system dynamics in this input-output model is similar to that due to the closed system dynamics, along with a damping term proportional to $\kappa/2$ and a driving field which couples in with strength $\sqrt{\kappa}$.

Instead of the 'in' field in Eqn.(2.59), if we instead defined an 'out' field for times $t_1 > t$ as

$$b_{\text{out}}(\omega, t) = \frac{1}{\sqrt{2\pi}} \int_{-\infty}^{\infty} d\omega e^{-i\omega(t-t_1)} b_1(\omega), \tag{2.63}$$

where $b_1(\omega) = b(\omega, t_1)$. The Heisenberg equation for the system operator becomes

$$\dot{a}(t) = -\frac{i}{\hbar}\big[a, H_{\text{sys}}\big] + \frac{\kappa}{2} a(t) + \sqrt{\kappa} b_{\text{out}}(t). \tag{2.64}$$

Equating Eqn.(2.62) and Eqn.(2.64), we obtain a boundary condition

$$b_{\text{out}}(t) - b_{\text{in}}(t) = -\sqrt{\kappa} a(t), \tag{2.65}$$

which relates the input and output (microwave) fields to the cavity (cCPT). We note that our input-output relation Eqn.(2.65) differs from [75] by a sign because of the different sign we used for the interaction Hamiltonian H_{int} defined in Eqn.(2.56).

2.3.1. The $\lambda/4$ microwave cavity coupled to a semi-infinite transmission line

In this section, we aim to re-derive the scattering parameter S_{11} for a linear $\lambda/4$ microwave as in section 2.1.5, but using the input-output formalism just described. We saw that the coupling between the transmission line Hamiltonian is exactly that of the Bosonic baths considered in input-output theory, and so we model this coupling as one of the two baths in the environment of the system oscillator, as shown in Fig.(2.6). The other bath is an internal lossy port, which is attributed classically to the dielectric and resisitve losses as in section 2.1.1. These two baths are assumed to

be uncorrelated. We consider only the fundamental mode of the cavity for clarity. All other modes will couple similarly with the loss channels, albeit with different coupling constants $\kappa_{1,2}$.

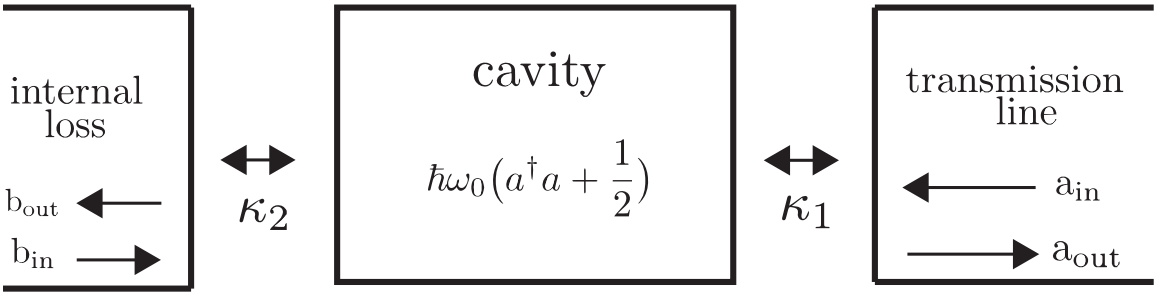

Figure 2.6: Schematic of a microwave cavity coupled to two ports - a transmission line and an internal loss channel.

Our system Hamiltonian $H_{\rm sys}$ here is given by Eqn.(2.54), with n = 0 corresponding to the fundamental mode. Using this in Eqn.(2.62), we have

$$\dot{a}(t) = -i\omega_0 a - \frac{\big(\kappa_1 + \kappa_2\big)}{2} a(t) + \sqrt{\kappa_1} a_{\rm in}(t) + \sqrt{\kappa_2} b_{\rm in}(t). \tag{2.66}$$

We solve this equation by taking the Fourier transform. In doing so, we note that

$$\begin{aligned} \dot{a}(\omega) = \mathscr{F}\big\{\dot{a}(t)\big\} &= \int_{-\infty}^{\infty} \dot{a}(t) e^{-i\omega t} dt \\ &= -\int_{-\infty}^{\infty} i\omega a(t) e^{i\omega t} dt \\ &= -i\omega a(\omega), \end{aligned} \tag{2.67}$$

where $a(\omega) = \mathscr{F}\big\{a(t)\big\}$. Eqn.(2.66) gives us

$$a(\omega) = \frac{\sqrt{\kappa_1} a_{\rm in}(\omega) + \sqrt{\kappa_2} b_{\rm in}(\omega)}{\big((\kappa_1 + \kappa_2)/2 - i\Delta\big)}, \tag{2.68}$$

where $\Delta = \omega - \omega_0$ as before. Using this solution for $a(\omega)$ in the input-output relation

Eqn.(2.65) for each loss channel separately, we have

$$a_{\text{out}}(\omega) = a_{\text{in}}(\omega) - \frac{\kappa_1 a_{\text{in}}(\omega) + \sqrt{\kappa_1\kappa_2}b_{\text{in}}(\omega)}{\big((\kappa_1+\kappa_2)/2 - i\Delta\big)}, \tag{2.69a}$$

$$b_{\text{out}}(\omega) = b_{\text{in}}(\omega) - \frac{\sqrt{\kappa_1\kappa_2}a_{\text{in}}(\omega) + \kappa_2 b_{\text{in}}(\omega)}{\big((\kappa_1+\kappa_2)/2 - i\Delta\big)}. \tag{2.69b}$$

Since we only have experimental access to the transmission line and not the internal loss port, we only concern ourselves with extracting the reflection measurements at the transmission line (we notate this with S_{11}). As detailed in [67], since the reflection coefficient acts on quadrature operators (and hence the mode operators) by changing the magnitude and rotating in phase space (and not just a multiplicative phase), the corresponding S_{11} equation is given by

$$\begin{aligned} a_{\text{out}} &= S_{11}^* a_{\text{in}}, \\ a_{\text{out}}^\dagger &= S_{11} a_{\text{in}}^\dagger. \end{aligned} \tag{2.70}$$

Also, experimentally we measure only the classical expectation value of these operators. The internal loss channel is in a thermal state with $\langle b_{\text{in(out)}}\rangle = 0$ while we use a coherent tone with power $|\alpha_{\text{in}}|^2$ on the transmission line to probe the cCPT. Eqn.(2.69a) then becomes

$$\alpha_{\text{out}} = \frac{\Delta + i(\kappa_2-\kappa_1)/2}{\Delta + i(\kappa_1+\kappa_2)/2}\alpha_{\text{in}}. \tag{2.71}$$

Comparing this to Eqn.(2.70), we see that

$$S_{11} = \frac{\Delta - i(\kappa_2-\kappa_1)/2}{\Delta - i(\kappa_1+\kappa_2)/2}. \tag{2.72}$$

This matches up with Eqn.(2.31) if we recognize $\kappa_{\text{ext}} = \kappa_1$ and $\kappa_{\text{int}} = \kappa_2$. Generalizing

this to a system Hamiltonian which could be nonlinear in the single degree of freedom, we write down the quantum Langevin equation for the system operator and the input-output relation for the two loss channels to be

$$\dot{a}(t) = -\frac{i}{\hbar}\big[a, H_{\rm sys}\big] - \frac{\big(\kappa_{\rm ext} + \kappa_{\rm int}\big)}{2} a(t) + \sqrt{\kappa_{\rm ext}}\, a_{\rm in}(t) + \sqrt{\kappa_{\rm int}}\, b_{\rm in}(t), \tag{2.73a}$$

with,

$$a_{\rm out}(t) = a_{\rm in}(t) - \sqrt{\kappa_{\rm ext}}\, a(t), \tag{2.73b}$$

$$b_{\rm out}(t) = b_{\rm in}(t) - \sqrt{\kappa_{\rm int}}\, a(t). \tag{2.73c}$$

We will see in the coming sections that the cCPT can be treated as a flux- and gate-tunable nonlinear oscillator. Eqns.(2.73a) and (2.73b) will be our primary tools in modelling and analyzing the dynamics of the system and to extract parameters such as the resonant frequency ω_0, and the internal and external damping rates $\kappa_{\rm int}$ and $\kappa_{\rm ext}$.

Section 2.4

The Cooper pair transistor (CPT)

The second component of the cCPT is the Cooper pair transistor. The building block of the CPT itself is the Josephson junction (JJ). A JJ consists of two superconducting electrodes interrupted by a 'weak link' [80]. In this section, we will treat the JJs phenomenologically starting from the Josephson equations. We will use the branch flux formalism we used for the infinite transmission line to derive the Hamiltonian of the JJ. We will then see how the CPT consists of two JJs forming a superconducting island and how this behaves as a charge- and flux-tunable inductor.

2.4.1. The Josephson junction

We derive the Hamiltonian for a single JJ here following chapter 6 of Tinkham [81]. The JJ is described by an RCSJ (resistively and capacitively shunted) model as shown in Fig.(2.7b). The current in the supercurrent channel is described by the DC Josephson effect

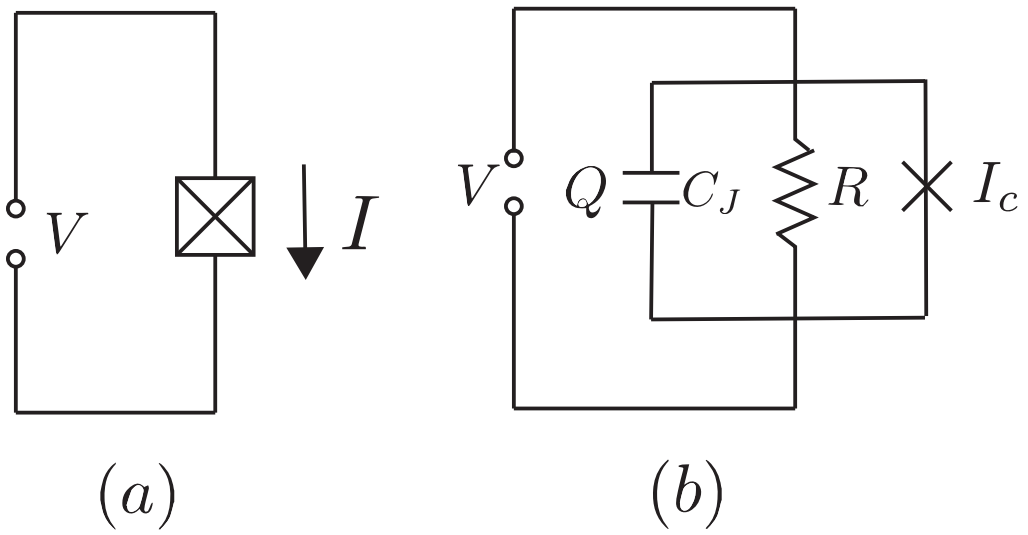

Figure 2.7: (a) A voltage biased Josephson junction denoted by the boxed cross. (b) Equivalent circuit in the RCSJ model.

$$I = I_c \sin\phi, \tag{2.74}$$

where I_c is the critical current of the junction and ϕ is the difference in phase of the Ginzburg-Landau order parameter across the junction. This current flows through the junction even at $V = 0$. The resistive branch accounts for transport due to quasiparticle tunneling across the JJ. The resistance $R \approx R_N$ close to T_c where R_N is the normal state resistance of the JJ. It goes exponentially at lower temperatures T as $R = R_N e^{\Delta/k_B T}$ where Δ is the superconducting gap, and k_B is the Boltzmann constant, and we neglect this term for our operating temperatures well below T_c of aluminium JJs. The capacitive channel describes the displacement current arising from the geometric capacitance between the two electrodes forming the JJ. The critical

current I_c of the JJ is related to its normal state resistance R_N by the Ambegaokar-Baratoff formula [82]

$$\begin{aligned} I_c R_N &= \frac{\pi\Delta}{2e} \tanh \frac{\Delta}{2k_B T} \\ &\approx \frac{\pi\Delta(0)}{2e}, \end{aligned} \tag{2.75}$$

where the approximation holds for $T \ll T_c$.

When a voltage $V \neq 0$ is applied to the JJ, the phase difference across the JJ evolves according to the AC Josephson equation

$$V = \frac{\Phi_0}{2\pi} \frac{d\phi}{dt}, \tag{2.76}$$

where $\Phi_0 = h/2e = 2.067 \times 10^{-15}$ Wb is the magnetic flux quantum. Since ϕ is not gauge invariant and can't describe a physical quantity such as the current I, we now define a gauge invariant phase difference $\varphi \equiv \phi - (2\pi/\Phi_0) \int \mathbf{A}.\mathbf{ds}$ where $\mathbf{A}$ is the vector potential integrated between the two electrodes forming the weak link and rewrite the Josephson equations in terms of this quantity.

One way to proceed is to write down Kirchoff's laws for the RCSJ model and to recognize that this corresponds to a particle with mass $(\hbar/2e)^2 C_J$ moving in an effective potential as in [81, 69] which can then be quantized, but we follow the approach of [67] here instead.

Kirchoff's laws for the circuit in Fig.(2.7b) can be written as (neglecting the R as mentioned above)

$$V = \frac{Q}{C_J} = \frac{\Phi_0}{2\pi} \frac{d\varphi}{dt}, \tag{2.77a}$$

$$I = -\dot{Q} = I_c \sin\varphi. \tag{2.77b}$$

Combining these equations, we have

$$C_J \frac{\Phi_0}{2\pi} \frac{d^2\varphi}{dt^2} + I_c \sin\varphi = 0. \tag{2.78}$$

Introducing a branch flux Φ_J using the definition in Eqn.(2.32), we have

$$\Phi_J = \frac{\Phi_0}{2\pi}\varphi(t), \tag{2.79}$$

which has units of magnetic flux. We can then write Eqn.(2.78) as

$$C_J \ddot{\Phi}_J + I_c \sin\left(\frac{2\pi\Phi_J}{\Phi_0}\right) = 0. \tag{2.80}$$

This equation of motion is found to satisfy the Lagrangian

$$L = \frac{1}{2} C_J \dot{\Phi}^2 + \frac{\Phi_0}{2\pi} I_c \cos\left(\frac{2\pi\Phi_J}{\Phi_0}\right). \tag{2.81}$$

The charge q_J conjugate to Φ_J is given by

$$q_J = \frac{\partial L}{\partial \dot{\Phi}_J} = C_J \dot{\Phi}_J, \tag{2.82}$$

and performing the Legendre transformation, the Hamiltonian reads

$$H = \frac{q_J^2}{2C_J} - E_J \cos\left(\frac{2\pi\Phi_J}{\Phi_0}\right), \tag{2.83}$$

where we defined the Josephson energy $E_J = I_c\Phi_0/2\pi$. We now quantize this Hamiltonian as before by imposing the canonical commutation relations on these charge and flux variables (we immediately drop the hats)

$$\left[\Phi_J, q_J\right] = i\hbar. \tag{2.84}$$

Anticipating using the excess number of Cooper pair on the CPT island as our variable in forthcoming sections, we define a charge number variable $N = q_J/2e$. Using the dimensionless gauge-invariant phase difference across the JJ, and defining the charging energy, $E_C = e^2/2C_J$, which is the energy required for an electron to be added to the capacitor plate, we have

$$H = 4E_C N^2 - E_J \cos\varphi, \tag{2.85}$$

where N and φ now satisfy this commutation relation

$$\big[\varphi, N\big] = i. \tag{2.86}$$

So we see that the JJ Hamiltonian consists of two terms. The first is, as mentioned above, the classical electrostatic cost of adding an electron to the electrode of the JJ. C_J behaves like a parallel plate capacitor whose capacitance can be estimated to be

$$C_J = \frac{\epsilon A}{d}, \tag{2.87}$$

where ϵ is the dielectric constant of the material between the two electrodes of the JJ (Al_2O_3 in the case of our cCPT, as shall be seen), A is the area of the electrodes forming the JJ, and d is the thickness of the dielectric. The second Josehpson coupling energy term is a tunneling term between neighbouring charge states. Joyez [68] draws a nice analogy to the tight binding model of a 1D lattice where the charging energy plays the role of the atomic orbitals, and the Josephson term that of the hopping between nearest neighbours.

We will now follow [69] to express the Hamiltonian in Eqn.(2.85) in the charge basis. The Hamiltonian can be solved exactly in the phase basis in terms of Mathieu

functions as in the reference above, but we choose to work in the charge basis instead. We will see that solving for the eigenvalues in this basis requires a truncation of the Hilbert space, but note that for our charge-sensitive CPT working in the $E_J/E_C < 1$ regime, a few (< 10) dimensional Hilbert space is sufficient [68, 67]. In order to express φ in the charge basis, we first note the cyclic property of the phase operator (single-valuedness of phases separated by 2π). Using this in tandem with the fact that the operator N is the generator of translations in φ based on the commutation relation Eqn.(2.86), we have

$$|\varphi + 2\pi\rangle = e^{i2\pi N} |\varphi\rangle = |\varphi\rangle \,, \tag{2.88}$$

which tells us that the eigenvalues of N have to be integers with associated eigenkets. Conversely, φ is the generator of translations in N, and we have

$$|N + 1\rangle = e^{i\varphi(1)} |N\rangle \,. \tag{2.89}$$

Applying this operator on an infinite superposition of number eigenbras $\sum_{N\in\mathbb{Z}} \langle N|$, this gives us

$$2\cos\varphi = e^{i\varphi(1)} + e^{i\varphi(-1)} = \sum_{N\in\mathbb{Z}} \Big(|N+1\rangle \langle N| + |N\rangle \langle N+1| \Big), \tag{2.90}$$

using which we can write the total JJ Hamiltonian Eqn.(2.85) in the charge basis as

$$H = 4E_C \sum_{N\in\mathbb{Z}} N^2 |N\rangle \langle N| - \frac{E_J}{2} \sum_{N\in\mathbb{Z}} \Big(|N\rangle \langle N+1| + |N\rangle \langle N+1| \Big) \tag{2.91}$$

which makes the identification of the Josephson energy as a tunneling term linking neighbouring charge states more apparent.

2.4.2. The Cooper pair transistor (CPT)

We now turn to the analysis of the Cooper pair transistor which consists of two JJs in series, forming a superconducting island, which is gated by an electrode biased with a voltage. The schematic for this device is shown in Fig.(2.8). We will see in section 2.5 that I corresponds to the current in the $\lambda/4$ cavity due to the cavity flux. For now, this notation serves in understanding the dynamics of the system.

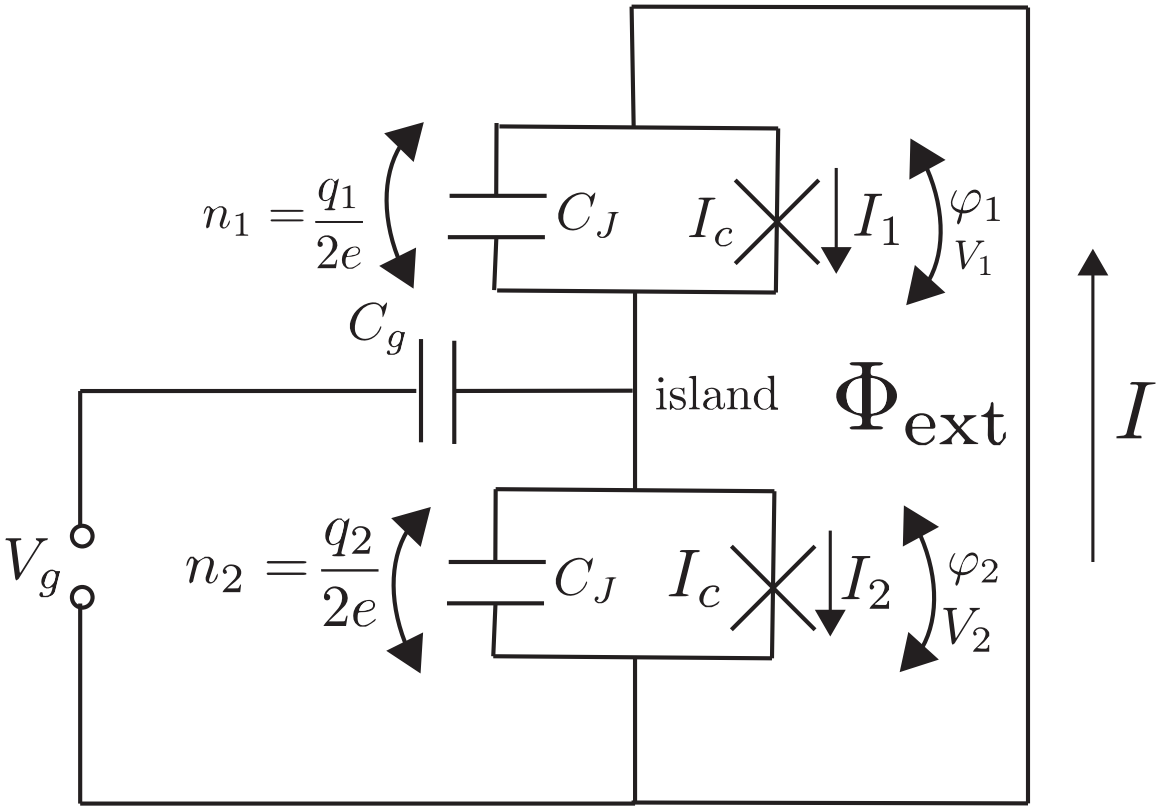

Figure 2.8: Schematic of a Cooper pair transistor with the island formed by two JJs in series, gated by a capacitance C_g and Φ_{ext} is the flux threading the CPT circuit. We assume that the CPT is embedded in a superconducting loop, as is the case for the cCPT which we consider in the next section.

We assume here that the two JJs are identical. Ref.[69] deals with asymmetry between the two junctions, but we ignore this here since the asymmetry in our experimental device is found to be quite small [30]. The JJs have a capacitance C_J and a critical current I_c. The charge on the junction capacitances is denoted by q_1 and

q_2 respectively, corresponding to a voltage drop V_1 and V_2. I_1 and I_2 are the currents through each of the junctions. We denote the phase across each junction to be φ_1 and φ_2 respectively. Applying Kirchoff's current law through each JJ separately, we have

$$\begin{aligned} I &= I_1 + \frac{\Phi_0}{2\pi} C_J \frac{d^2\varphi_1}{dt^2} \\ &= I_c \sin\varphi_1 + \frac{\Phi_0}{2\pi} C_J \frac{d^2\varphi_1}{dt^2}, \end{aligned} \tag{2.92a}$$

$$\begin{aligned} I + C_g\dot{V}_g - \frac{\Phi_0}{2\pi} C_g \frac{d^2\varphi_2}{dt^2} &= I_2 + \frac{\Phi_0}{2\pi} C_J \frac{d^2\varphi_2}{dt^2} \\ \Rightarrow I &= I_c \sin\varphi_2 + \frac{\Phi_0}{2\pi}\big(C_J + C_g\big)\frac{d^2\varphi_2}{dt^2} - C_g\dot{V}_g, \end{aligned} \tag{2.92b}$$

where we have used the two Josephson's equations (2.74) and (2.76) and the fact that the voltage of the island is $V_{\text{island}} = \frac{\Phi_0}{2\pi}\frac{d\varphi_2}{dt}$, which is the voltage across JJ number 2. Further, given the fact that $\mathbf{A} = (\Phi_0/2\pi)\nabla\phi$ (where ϕ is the difference in the phase of the Ginzburg-Landau order parameter across the JJ) and the fact that the phase has to be single-valued, we obtain for the superconducting loop encompassing the 2 JJs enclosing the flux Φ_{ext} (as in chapter 6 of [81]),

$$\varphi_1 + \varphi_2 = \frac{2\pi\Phi_{\text{ext}}}{\Phi_0} (\text{mod } 2\pi) \tag{2.93}$$

As in [68, 69], since n_1, n_2, φ_1 and φ_2 are not good quantum numbers, we now introduce the phase coordinates $\bar{\varphi}$ and $\delta\varphi$ which have conjugate variables $\bar{n}$ and N where

$$\begin{aligned} \bar{\varphi} &= \frac{\varphi_1 + \varphi_2}{2} = \frac{\pi\Phi_{\text{ext}}}{\Phi_0}, \\ \delta\varphi &= \frac{\varphi_1 - \varphi_2}{2}, \\ \bar{n} &= \frac{n_1 + n_2}{2}, \end{aligned}$$

$$N = \frac{n_1 - n_2}{2}. \tag{2.94a}$$

Here, $\bar{n}$ can be interpreted as the total number of Cooper pairs having passed through the entire transistor, and N as the number of Cooper pairs on the superconducting island. Using these new coordinates in Eqns.(2.92a and 2.92b) and adding and subtracting the two resulting equations, we have

$$C_J \frac{\Phi_0}{2\pi} \ddot{\bar{\varphi}} + I_c \sin \bar{\varphi} - \frac{C_g \dot{V}_g}{2} = I, \tag{2.95a}$$

$$C_J \frac{\Phi_0}{2\pi} \delta\ddot{\varphi} + 2I_c \cos \bar{\varphi} \sin \delta\varphi + C_g \dot{V}_g = 0. \tag{2.95b}$$

where we have made the assumption that $C_g \ll C_J$ ($C_g \approx 7$ aF and $C_J \approx 200$ aF for our sample). We now introduce the branch flux $\Phi_J = \big(\Phi_0/2\pi\big)\delta\varphi$ as we did for the single JJ, and Eqn.(2.95b) becomes

$$2C_J \ddot{\Phi}_J + 2I_c \cos\left(\frac{\pi\Phi_{\text{ext}}}{\Phi_0}\right) \sin\left(\frac{2\pi\Phi_J}{\Phi_0}\right) + C_g \dot{V}_g = 0. \tag{2.96}$$

We immediately see that this equation of motion can be derived from the Lagrangian

$$L = C_J \dot{\Phi}_J^2 + 2\frac{\Phi_0 I_c}{2\pi} \cos\left(\frac{\pi\Phi_{\text{ext}}}{\Phi_0}\right) \cos\left(\frac{2\pi\Phi_J}{\Phi_0}\right) + C_g V_g \dot{\Phi}_J. \tag{2.97}$$

The conjugate momentum to this branch flux Φ_J is found as before to be the charge variable q_J, which is given by,

$$q_J = \frac{\partial L}{\partial \dot{\Phi}_J} = 2C_J \dot{\Phi}_J + C_g V_g. \tag{2.98}$$

Performing a Legendre transformation as before, the Hamiltonian is found to be

$$H = \frac{1}{4C_J}\big(q_J - C_g V_g\big)^2 + 2E_J \cos\left(\frac{\pi\Phi_{\text{ext}}}{\Phi_0}\right) \cos\left(\frac{2\pi\Phi_J}{\Phi_0}\right), \tag{2.99}$$

where $E_J = \frac{\Phi_0 I_c}{2\pi}$ denotes the Josephson energy as before. The operators q_J and Φ_J are quantized again, and obey the commutation relations,

$$\big[\Phi_J, q_j\big] = i\hbar. \tag{2.100}$$

As for a single JJ, we define $N = \big(1/2e\big)q_J$ with the corresponding commutation relation $\big[\delta\varphi, N\big] = i$, defining the charging energy $E_C = e^2/2C_\Sigma$ where $C_\Sigma = \big(2C_J + C_g\big) \approx 2C_J$, and the gate charge $n_g = C_g V_g/e$, we have,

$$H = 4E_C\left(N - \frac{n_g}{2}\right)^2 - 2E_J \cos\left(\frac{\pi\Phi_{\text{ext}}}{\Phi_0}\right)\cos\delta\varphi \tag{2.101}$$

Expressing this in the charge basis using Eqn.(2.90) as for a single JJ, we finally have,

$$H = 4E_C \sum_{N\in\mathbb{Z}} \left(N - \frac{n_g}{2}\right)^2 |N\rangle\langle N| - E_J \cos\left(\frac{\pi\Phi_{\text{ext}}}{\Phi_0}\right) \sum_{N\in\mathbb{Z}} \Big(|N\rangle\langle N+1| + |N+1\rangle\langle N| \Big). \tag{2.102}$$

Looking at this Hamiltonian, we note that in addition to being able to tune the CPT into and out of Coulomb blockade using the gate, the CPT embedded in a superconducting loop gives us the ability to tune the Josephson energy with an applied external magnetic flux, Φ_{ext}.

Fig.(2.9) shows the ground and first excited state energies of a CPT with E_J =14.8 GHz and E_C =54.1 GHz computed numerically using an eigensolver. The Hilbert space was truncated to 9 charge states which produces a good approximation of the eigenstates obtained from the exact solutions to the Mathieu equation for our $E_J/E_C < 1$.

In order to observe single Cooper pair tunneling phenomena through a JJ, two conditions need to be met. First, the normal state resistance (R_N) of the tunnel

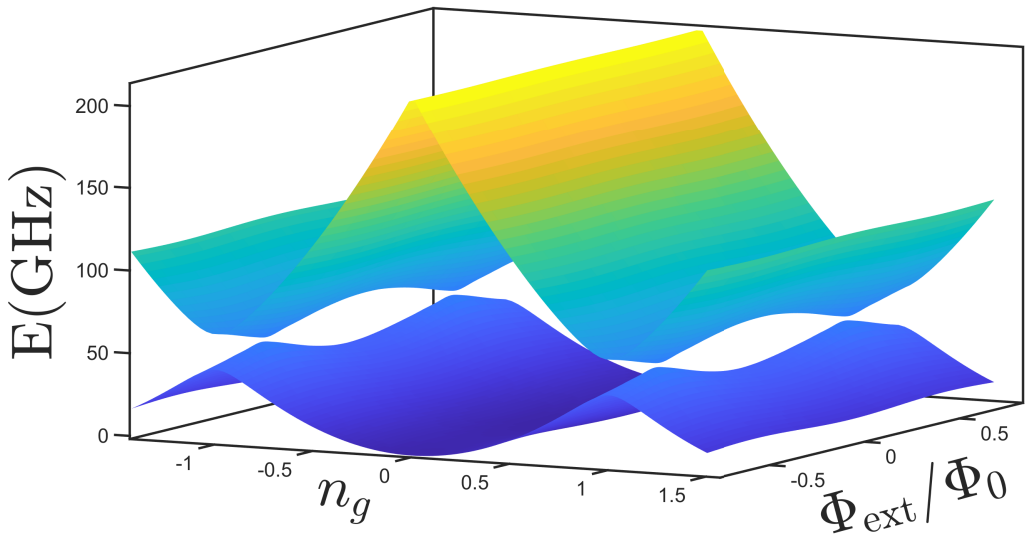

Figure 2.9: First two energy states of a CPT with $E_J = 14.8$ GHz and $E_C = 54.1$ GHz as a function of the gate charge (n_g) and the external flux Φ_{ext}. The energies are in frequency units.

junction forming the JJ must be larger than the resistance quantum for Cooper pairs - $R_N \gg R_K/4 = 6.4\,k\Omega$. This ensures that the Cooper pair wavefunction is localized on the island of the CPT. The second, is that the charging energy is large enough that thermal fluctuations are not sufficient to add an electron to the CPT island. This gives us $E_C \gg k_B T$, which considering the fact that even ultrasmall junctions typically have capacitances larger than a few 100 aF, requires the operation of these devices at mK temperatures in a dilution fridge. Chapters 1 and 2 in [25] go through these concepts in much more detail.

We will see in the next section that the CPT behaves as an inductor which can be tuned using the voltage gating the island and by the flux threading the superconducting loop.

2.4.3. The CPT as a tunable inductor

Following chapter 5 in [71], we will now see how the CPT behaves as a charge and flux tunable nonlinear inductance. This will admit a simple description of the cCPT as

a parallel LCR circuit (the cavity) as in section 2.1 along with a tunable inductance (the CPT) in parallel. In order to view this as a tunable inductance $L_J(\varphi)$, we first follow this procedure to view a single JJ as a nonlinear inductor, write it in terms of the derivative w.r.t φ of the energy stored in an inductor and then generalise this procedure to the CPT. We compare the AC Josephson equation Eqn.(2.76) to the typical voltage relation for an inductor L_J which is $V = L_J\dot{I}$. Also using the DC Josephson equation Eqn.(2.74), we have

$$\begin{aligned} V = L_J\dot{I} &= \frac{\Phi_0}{2\pi}\dot{\varphi}, \\ \Rightarrow L_J = \frac{\Phi_0}{2\pi I_c \cos\varphi} &= \frac{L_J^{(0)}}{\cos\varphi} = \frac{L_J^{(0)}}{\sqrt{1-\left(I/I_c\right)^2}}, \end{aligned} \tag{2.103}$$

where

$$L_J^{(0)} = \frac{\Phi_0}{2\pi I_c}. \tag{2.104}$$

In analogy with the equation for energy stored in an inductor, we have

$$E = \frac{\Phi_J^2}{2L_J}, \tag{2.105}$$

$$\Rightarrow L_J = \left(\frac{d^2E}{d\Phi_J^2}\right)^{-1}, \tag{2.106}$$

for this form of the energy, but this can be generalised to a non-quadratic form for the energy (such as the CPT) by Taylor expanding and evaluating the second derivative about the equilibrium point for the energy function. Formally, this means that for the CPT Hamiltonian Eqn.(2.102), we can write the Josephson inductance as

$$L_J(n_g, \Phi_{\text{ext}}) = \left(\frac{\Phi_0}{2\pi}\right)^2 \left(\frac{\partial^2 E_0^{\text{CPT}}(n_g,\varphi)}{\partial\varphi^2}\right)^{-1}\Bigg|_{\varphi=2\pi\Phi_{\text{ext}}/\Phi_0}, \tag{2.107}$$

where this is now tunable with both the gate charge and the loop flux.

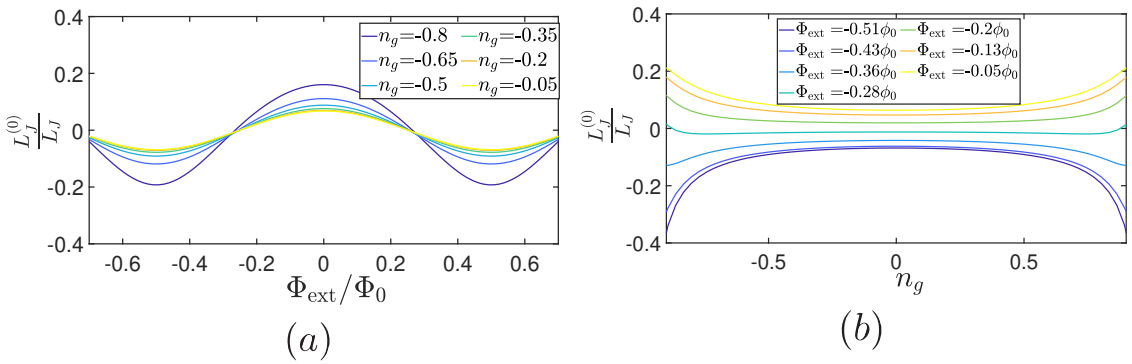

Figure 2.10: $L_j^{(0)}$ vs (a) flux at different gates (b) gate for different fluxes for a CPT with $E_J = 14.8$ GHz and $E_C = 54.1$ GHz.

Fig.(2.10) shows the variation of the Josephson inductance for nominal values of E_J and E_c. It's to be noted that the Josephson inductance spans positive as well as negative values depending on the curvature of the ground state at a given bias point. We will see that this enables us to tune the resonant frequency above and below the bare cavity frequency, and also the Kerr coefficient of the cCPT.

Section 2.5

The cavity-embedded Cooper pair transistor (cCPT)

The cCPT is formed by hooking up a CPT across the center line and the ground plane at the voltage anti-node of a $\lambda/4$ cavity as shown in Fig.(2.11). It is gated with a voltage V_g across a capacitance C_g and is threaded by a flux Φ_{ext}.

In this section, we first describe the cCPT using the equivalent model in Fig.(2.11b), where the tunable Josephson inductance L_J allows for tuning of the resonant frequency of the effective LC system. We will then present the Hamiltonian of the cCPT as the sum of that of its parts - (i) the $\lambda/4$ cavity and (ii) the CPT, and see how the superconducting SQUID loop formed by the pair of systems gives rise to a

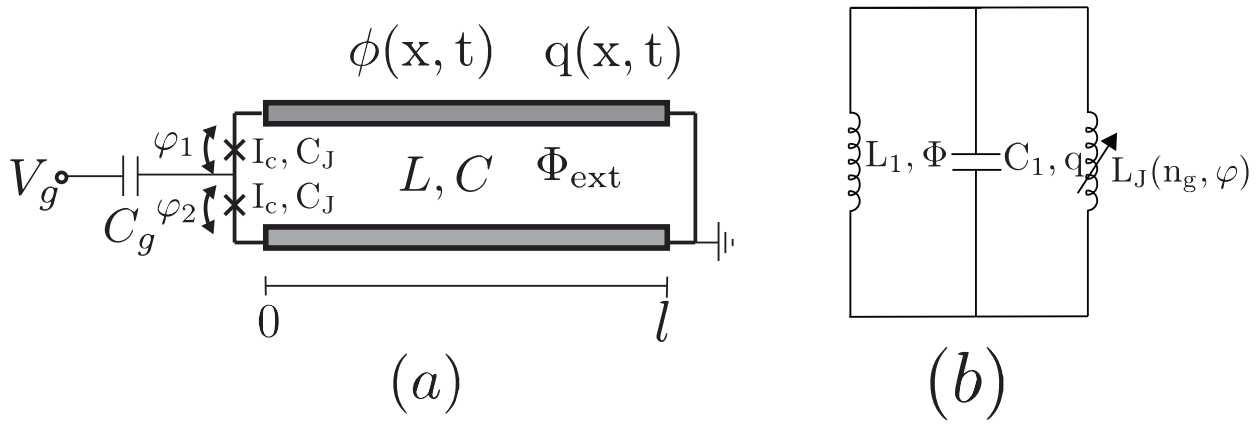

Figure 2.11: Schematic of the cCPT where (a) the CPT is shown to be hooked up at the voltage anti-node of a shorted $\lambda/4$ cavity (b) The equivalent circuit where the CPT behaves as a tunable inductance in parallel with the equivalent LC circuit corresponding to the fundamental mode of the $\lambda/4$ cavity.

flux quantization constraint similar to the one in section 2.4. Then performing an adiabatic approximation, since all relevant energy scales are much less than the energy required to cause transitions between the ground state and the first excited state (see Fig.(2.9)), we can approximate the CPT to remain in its ground state throughout the dynamics of the cCPT, and derive an effective Hamiltonian for the system. This is not a derivation from first principles, for that see [30], where the modification of the cavity modes (as in section 2.2) by the CPT and the coupling capacitor C_c is treated in detail using scattering analysis, along with the system's coupling to a transmission line. We follow here the approach described in [33].

2.5.1. Resonant frequency tuned by Josephson inductance

Close to its resonant frequency (we consider only the fundamental mode for now), we saw in section 2.1.3 that the cavity behaves as an LCR circuit. Hooked up at its voltage anti-node, the CPT appears in parallel with this LCR circuit as a tunable

inductor as shown in Fig.(2.11). The resonant frequency of this circuit is then

$$\omega_0(n_g,\varphi) = \sqrt{\frac{1}{C_0}\left(\frac{1}{L_J(n_g,\varphi)} + \frac{1}{L_1}\right)} \tag{2.108}$$

$$= \omega_0^{\lambda/4}\sqrt{\left(1 + \frac{L_1}{L_J(n_g,\varphi)}\right)}, \tag{2.109}$$

where $\omega_0(n_g,\varphi)$ is the (tunable) resonant frequency of the cCPT, and $\omega_0^{\lambda/4} = 1/\left(\sqrt{L_1 C_1}\right)$ is the resonant frequency of the fundamental mode of the cavity before the CPT was hooked up. Since $L_1 \ll L_J(n_g,\varphi)$, this can be written to first order in L_1/L_J as,

$$\begin{aligned}\omega_0(n_g,\varphi) &= \omega_0^{\lambda/4}\left(1 + \frac{L_1}{2L_J(n_g,\varphi)}\right) \\ &= \omega_0^{\lambda/4}\left(1 + L_1\left(\frac{2\pi}{\Phi_0}\right)^2 \frac{\partial^2 E_0^{\mathrm{CPT}}(n_g,\varphi)}{\partial\varphi^2}\right),\end{aligned} \tag{2.110}$$

and so we see that the Josephson inductance pulls the resonant frequency of the cCPT in either direction of that of the bare cavity depending on the sign of the curvature of the ground state energy of the CPT. We will see in the next section that the resonant frequency variation derived above by modelling the system as a parallel LC oscillator with a tunable inductor matches with the frequency shift obtained by considering the Hamiltonian of the system.

2.5.2. cCPT Hamiltonian

The Hamiltonian of the cCPT can be written as the sum of its parts

$$\begin{aligned}H_{\mathrm{cCPT}} =& H_{\mathrm{cavity}} + H_{\mathrm{CPT}} \\ =& \sum_{n=1}^{\infty}\left[\frac{q_n^2}{2C_n} + \frac{\Phi_n^2}{2L_n}\right]\end{aligned} \tag{2.111}$$

$$+ 4E_C \sum_{N\in\mathbb{Z}} \left(N - \frac{n_g}{2}\right)^2 |N\rangle\langle N| - E_J \cos\bar{\varphi} \sum_{N\in\mathbb{Z}} \Big(|N\rangle\langle N+1| + |N+1\rangle\langle N| \Big), \tag{2.112}$$

where we have used Eqn.(2.50) and Eqn.(2.102) for the respective Hamiltonians.

Given the quantization of the flux in the superconducting SQUID loop in Fig.(2.11a) we have

$$\begin{aligned} &\frac{\Phi_0}{2\pi}\big(\varphi_1 + \varphi_2\big) - \phi(0,t) = 2\pi m\Phi_0 + \Phi_{\text{ext}};\ m \in \mathbb{Z}, \\ &\frac{\Phi_0}{2\pi}\big(\varphi_1 + \varphi_2\big) - \sum_{n\in\mathbb{N}} \Phi_n = \Phi_{\text{ext}}. \end{aligned} \tag{2.113}$$

where we have used Eqn.(2.47) for $\phi(0,t)$, and absorbed the constant into Φ_{ext}. We see that this equation couples the cavity degrees of freedom with that of the CPT. We find the Hamiltonian of the full system to be

$$\begin{aligned} H_{\text{cCPT}} =& \sum_{n=1}^{\infty} \left[\frac{q_n^2}{2C_n} + \frac{\Phi_n^2}{2L_n}\right] + 4E_C \sum_{N\in\mathbb{Z}} \left(N - \frac{n_g}{2}\right)^2 |N\rangle\langle N| \\ &- E_J \cos\left(\frac{\pi}{\Phi_0}\sum_{n\in\mathbb{N}} \Phi_n + \Phi_{\text{ext}}\right) \sum_{N\in\mathbb{Z}} \Big(|N\rangle\langle N+1| + |N+1\rangle\langle N| \Big). \end{aligned} \tag{2.114}$$

We next make an adiabatic approximation to say that the CPT remains in its ground state throughout its dynamic evolution. To justify this approximation, we see from Fig.(2.9) that the energy spacing between the ground and first excited state is of the order of a few tens of GHz at all bias points away from the charge degeneracy point ($n_g = 1$) at $\Phi_{\text{ext}} = \pm 0.5\Phi_0$. As long as we stay away from the region $|1 - n_g| < 0.15$, the energy spacing is several factors larger than the fundamental frequency of our cCPT sample ($\omega_0^{\lambda/4} \approx 5.76$ GHz). As long as we are only driving the fundamental mode of the cavity, none of our input tones should be able to drive the qubit transition. Additionally, our sample is mounted at the mixing chamber of a dilution fridge with

a temperature of 30 mK. Since $k_B T \equiv 600$ MHz at 30 mK, the thermal fluctuations are unable to drive the transitions too. It should be noted that the cavity is designed to operate at 5.76GHz where the thermal occupation of the cavity is nearly that of the vacuum state.

Making this approximation, we then write the Hamiltonian in terms of the ground state energy E_0^{CPT} which is of course the expectation value of the cCPT Hamiltonian for the ground state $|g\rangle$, i.e. $E_0^{\mathrm{CPT}} = \langle g| H_{\mathrm{cCPT}} |g\rangle$. The cCPT Hamiltonian then becomes

$$\begin{aligned} H_{\mathrm{cCPT}} &= \sum_{n=1}^{\infty} \frac{q_n^2}{2C_n} + V_{\mathrm{eff}} \\ &= \sum_{n=1}^{\infty} \frac{q_n^2}{2C_n} + \sum_{n=1}^{\infty} \frac{\Phi_n^2}{2L_n} + E_0^{\mathrm{CPT}}. \end{aligned} \tag{2.115}$$

We now consider the CPT Hamiltonian to be a perturbation to the simple harmonic potential of the cavity modes, and Taylor expand the effective potential V_{eff} about the equilibrium point of the potential $\Phi^{(eq)}$. As shown in [67] using a bounding argument, $\Phi^{(eq)} \leq 0.035 \ll 1$. Defining $\phi = \frac{2\pi}{\Phi_0}\Phi_{\mathrm{ext}}$ which is a dimensionless flux, we then arrive at the Hamiltonian,

$$H_{\mathrm{cCPT}} = \sum_{n=1}^{\infty} \left[\frac{q_n^2}{2C_n} + \frac{\Phi_n^2}{2L_n} \right] + \sum_{k=2}^{\infty} \frac{1}{k!} \frac{\partial^k E_0^{\mathrm{CPT}}(n_g, \phi)}{\partial \phi^k} \left(\frac{2\pi}{\Phi_0} \sum_{n=1}^{\infty} \Phi_n \right)^k, \tag{2.116}$$

where we neglect $k = 0$ as just an additive constant, and the $k = 1$ term is zero at the equilibrium point around which we are performing the Taylor expansion.

We now focus on the fundamental mode of the cavity $n = 1$ and drop all terms $n \geq 2$ along with the mode index n. We note here that in addition to neglecting dynamics of higher order modes of the cCPT whose direct readout is experimentally inaccessible, this immediately ignores all cross-mode effects such as cross-Kerr terms

[36, 47] and non-degenerate parametric amplification terms [83, 84]. For the fundamental frequency at ω_0, the next higher order mode fo the $\lambda/4$ cavity will have resonant frequency $3\omega_0$. This means that as long as we are driving the cavity close to ω_0, the rotating wave approximation (RWA) implies that these higher order modes will not affect the dynamics of the fundamental mode. However, they could come into play when applying a parametric drive to the cavity.

We now recognise the $k = 2$ term to be proportional to the $L_J(n_g, \phi)$ defined in Eqn.(2.107) and we define as in section 2.5.1

$$\frac{1}{L_{\text{tot}}(n_g, \phi)} = \left(\frac{1}{L_1} + \frac{1}{L_J(n_g, \phi)}\right), \tag{2.117}$$

and the Hamiltonian becomes

$$H_{\text{cCPT}} = \frac{q^2}{2C} + \frac{\Phi^2}{2L_{\text{tot}}(n_g, \phi)} + \sum_{k=3}^{\infty} \frac{1}{k!} \frac{\partial^k E_0^{\text{CPT}}(n_g, \phi)}{\partial \phi^k} \left(\frac{2\pi}{\Phi_0}\Phi\right)^k. \tag{2.118}$$

where we have dropped non-stationary terms (a^2 and $a^{\dagger 2}$) under the RWA assuming only a near resonant drive. We will see later that these terms become important when applying parametric drives to the cCPT. We already recognise the first two terms of the other Hamiltonian to be that of an LC oscillator tunable with the gate voltage and loop flux, but introduce creation annihilation operators to write the total Hamiltonian in the familiar form for an oscillator as in Eqn.(2.54). We define

$$a = \sqrt{\frac{1}{2\hbar Z_{\text{tot}}}}\big(\Phi + iZ_{\text{tot}}q\big), \tag{2.119a}$$

$$a^\dagger = \sqrt{\frac{1}{2\hbar Z_{\text{tot}}}}\big(\Phi - iZ_{\text{tot}}q\big), \tag{2.119b}$$

where $\left[a, a^\dagger\right] = 1$, $Z_{\text{tot}} = \sqrt{L_{\text{tot}}/C}$ and we can write the inverse transformations

$$\Phi = \Phi_{\rm zp}\big(a + a^\dagger\big) = \sqrt{\frac{\hbar Z_{\rm tot}}{2}}\big(a + a^\dagger\big), \tag{2.120a}$$

$$q = iq_{\rm zp}\big(a^\dagger - a\big) = i\sqrt{\frac{\hbar}{2Z_{\rm tot}}}\big(a^\dagger - a\big). \tag{2.120b}$$

We then find the familiar form of the Hamiltonian (dropping constants)

$$H_{\rm cCPT} = \hbar\omega_0(n_g, \Phi_{\rm ext})a^\dagger a + \sum_{k=3}^{\infty}\frac{1}{k!}\left(\frac{2\pi}{\Phi_0}\sqrt{\frac{\hbar Z_{\rm tot}}{2}}\right)^k \frac{\partial^k E_0^{\rm CPT}(n_g,\phi)}{\partial\phi^k}\big(a + a^\dagger\big)^k, \tag{2.121}$$

where $\omega_0(n_g, \Phi_{\rm ext}) = 1/\sqrt{L_{\rm tot}(n_g, \Phi_{\rm ext})C}$.

We refer to the Hamiltonian of the cCPT with RWA applied for a drive close to resonance and neglecting terms with $k > 2$ as the linear cCPT Hamiltonian. A detailed characterization of the linear behaviour of the cCPT has been carried out in [33]. It is worth noting here that the relative strengths of the higher order terms in the Hamiltonian in Eqn.(2.125) are decided by the factor $\phi_{\rm zp} = \big(2\pi/\Phi_0\big)\Phi_{\rm zp}$ which is a dimensionless form of the zero point flux fluctuations in Eqn.(2.120a) since the n-th derivative of the CPT ground state energy switches between a sine and cosine dependence for even and odd n's respectively. To evaluate $\Phi_{\rm zp}$, we have

$$\begin{aligned}
\Phi_{\rm zp} &= \sqrt{\frac{\hbar Z_{\rm tot}}{2}} = \sqrt{\frac{\hbar}{2}\sqrt{\frac{L_{\rm tot}}{C}}} \\
&= \sqrt{\frac{\hbar}{2}\sqrt{\frac{1}{C}\left(\frac{1}{L_J(n_g,\Phi_{\rm ext})} + \frac{1}{L_1}\right)}} \\
&\approx \sqrt{\frac{\hbar Z}{2}}\left(1 - \frac{L_1}{4L_J(n_g,\Phi_{\rm ext})}\right) \qquad (2.122) \\
&\approx \sqrt{\frac{\hbar Z}{2}} = 0.028\Phi_0, \qquad (2.123)
\end{aligned}$$

where we have made the empirically justified assertion that $L_1 \ll L_J$ again and

$Z = \sqrt{\frac{\mathbb{L}}{\mathbb{C}}}$ is the characteristic impedance of the cavity ($\mathbb{L}$ and $\mathbb{C}$ are the inductance per unit length and conductance per unit length respectively, see section 2.2.1), as before and is $\approx 50\Omega$ for our sample (since $\sqrt{L_1/C_1} = (4/\pi)(\sqrt{\mathbb{L}/\mathbb{C}}) = Z_0 = (4/\pi)Z$). This gives us the dimensionless quantity

$$\phi_{\text{zp}} = \frac{2\pi}{\Phi_0}\Phi_{\text{zp}} \approx 0.176. \tag{2.124}$$

The final Hamiltonian can then be re-written as

$$H_{\text{cCPT}} = \hbar\omega_0(n_g, \Phi_{\text{ext}})a^\dagger a + \sum_{k=3}^{\infty} \frac{1}{k!}(\phi_{\text{zp}})^k \partial_\phi^k E_0^{\text{CPT}}(n_g, \Phi_{\text{ext}})\big(a + a^\dagger\big)^k, \tag{2.125}$$

where we have defined

$$\partial_\phi^k E_0^{\text{CPT}}(n_g, \Phi_{\text{ext}}) = \frac{\partial^k E_0^{\text{CPT}}(n_g, \phi)}{\partial\phi^k}\bigg|_{\phi=2\pi\Phi_{\text{ext}}/\Phi_0}, \tag{2.126}$$

as in [33].

Also, using the definitions Eqn.(2.123) and Eqn.(2.124) in the equation for the tunable resonant frequency Eqn.(2.110), we have

$$\omega_0(n_g, \Phi_{\text{ext}}) = \omega_0^{\lambda/4} + \frac{\phi_{\text{zp}}^2}{\hbar}\partial_\phi^2 E_0^{\text{CPT}}(n_g, \Phi_{\text{ext}}), \tag{2.127}$$

which is plotted in Fig.(2.12) for the parameters of our cCPT device.

The next higher order term in the above Hamiltonian that contributes to the stationary dynamics of the cCPT when driven near resonance is the Duffing term ($k = 4$). We will discuss the dynamics of the system in more detail in chapter 4, but for now, we show that this term contributes an intracavity photon number resonant frequency shift of the cCPT, which we see will be used to determine the input attenuation of the dilution fridge circuitry in chapter 3. Expanding the k =4

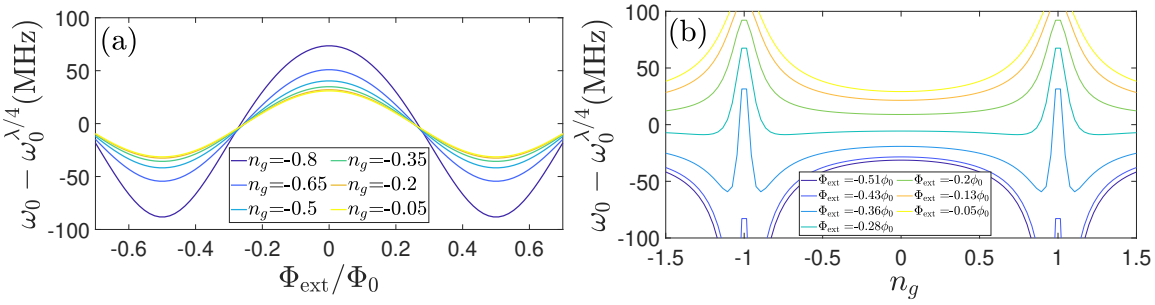

Figure 2.12: resonant frequency shift vs (a) flux at different gates and (b) gate for different fluxes for a cCPT with $E_J = 14.8$ GHz and $E_C = 54.1$ GHz.

term in powers of the creation/annihilation operators, applying the commutation relations, and the RWA, we obtain for the Duffing Hamiltonian

$$\begin{aligned} H_{\text{Duff}} &= \frac{1}{4}\phi_{\text{zp}}^4 \partial_\phi^4 E_0^{\text{CPT}}(n_g, \Phi_{\text{ext}})\big(a^\dagger a + 1\big)a^\dagger a \\ &= \frac{\hbar}{2}K(n_g, \phi_{\text{ext}})\big(a^\dagger a + 1\big)a^\dagger a \\ &= \frac{\hbar}{2}K(n_g, \phi_{\text{ext}})\big(n + 1\big)a^\dagger a, \end{aligned} \tag{2.128}$$

where we have defined the intracavity photon number $n = a^\dagger a$ and the Kerr coefficient K as

$$K = \frac{1}{2\hbar}\phi_{\text{zp}}^4 \partial_\phi^4 E_0^{\text{CPT}}(n_g, \Phi_{\text{ext}}). \tag{2.129}$$

So we see that if we drive the cavity with a large enough power to cause $nK > \kappa_{\text{tot}}$ (typically for $3 < n < 10$ for our cCPT system), we will see a resonant frequency shift larger than the cavity linewidth, and this depends linearly on the cavity occupation n. We can then experimentally measure this frequency shift to extract the input attenuation as we shall see in chapter 3.

Fig.(2.13) shows the simulated variation of the Kerr coefficient for our cCPT sample with an $E_J = 14.8$ GHz and an $E_C = 54.1$ GHz. As expected it varies sinusoidally in flux, reaching minimum and maximum at $\Phi_{\text{ext}} = 0$ and $\Phi_{\text{ext}} = 0.5\Phi_0$

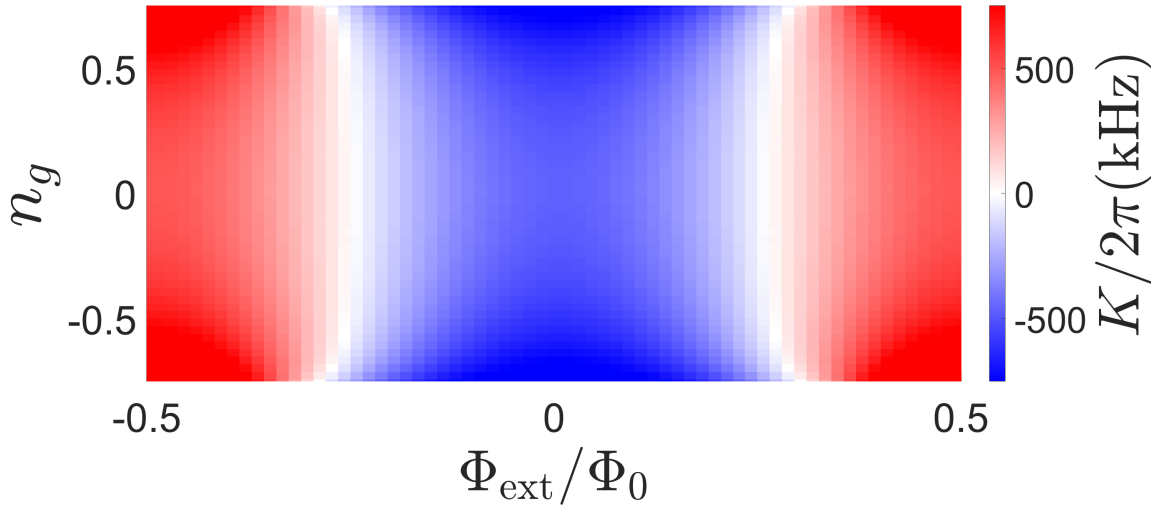

Figure 2.13: Simulated variation of the Kerr coefficient as a function of the gate and flux bias for an $E_J = 14.8$ GHz and an $E_C = 54.1$ GHz.

respectively. An interesting aspect to the Kerr coefficient is that we can tune it to 0 close to $\Phi_{\text{ext}} = 0.25\Phi_0$. We will see in Appendix A that we can implement a degenerate parametric amplifier Hamiltonian using the cCPT Hamiltonian in Eqn.(2.125). It has been studied that the Kerr term is one of the limiting factors for the dynamic range of parametric amplifiers working in both the three and four-wave mixing scheme [85, 86, 87] because of the above Kerr induced resonant frequency shift. As the amplifier does its job and the intracavity photon number increases, the resonant frequency quickly shifts away from the optimum pump detuning, and an equilibrium between amplification and the detuning is reached. Work has been done in engineering the Hamiltonian of devices such as the 'SNAIL' parametric amplifier (SPAs) to minimize the effect of the Kerr term [88, 89]. Similar to these devices, the Kerr can be tuned in-situ in our cCPT using the flux to an optimal working point. We will see in chapter 5 and appendix A that the strength of the parametric pump and the gain depends on the slope of the resonant frequency with respect to flux, and this is maximized at $\Phi_{\text{ext}} = 0.25\Phi_0$, the same bias point at which the Kerr is minimized. We note that the

Kerr also has some tunability with the gate n_g, which we will look at in chapter 4.

We have shown in this chapter that the cCPT is a rich nonlinear system in which different terms in the Hamiltonian, Eqn.(2.125), can be driven into resonance under the RWA, each giving rise to interesting dynamics, some of which we will study in the coming chapters. We have also derived some of the tools such as the reflection coefficient, S_{11}, for the linear cCPT Hamiltonian with which we can probe the dynamics of the cCPT and obtain several useful experimental parameters as we shall see in the following chapters.

Chapter 3

Experimental setup and techniques

In this chapter, in section 3.1 we first briefly describe the cCPT sample fabrication and then discuss the mounting of this chip on a printed circuit board (PCB) inside a sample box which is mounted at the mixing chamber of a dilution fridge. In section 3.2 we discuss some details of the RF and DC dilution fridge circuitry that we use to probe the sample, and some room temperature measurement schemes. In section 3.3, we will then touch upon a few analysis techniques that we regularly use.

Section 3.1

The cCPT sample

The cCPT sample studied in this thesis was made entirely by Juliang Li [65]. We go through the general idea behind the fabrication process, and discuss more details in chapter 6 where we report on our attempts to combine the cCPT with a nanoresonator system (cCPT-NR) to reach the single photon-phonon strong coupling regime of optomechanics. The detailed fabrication of this cCPT device are described in [65].

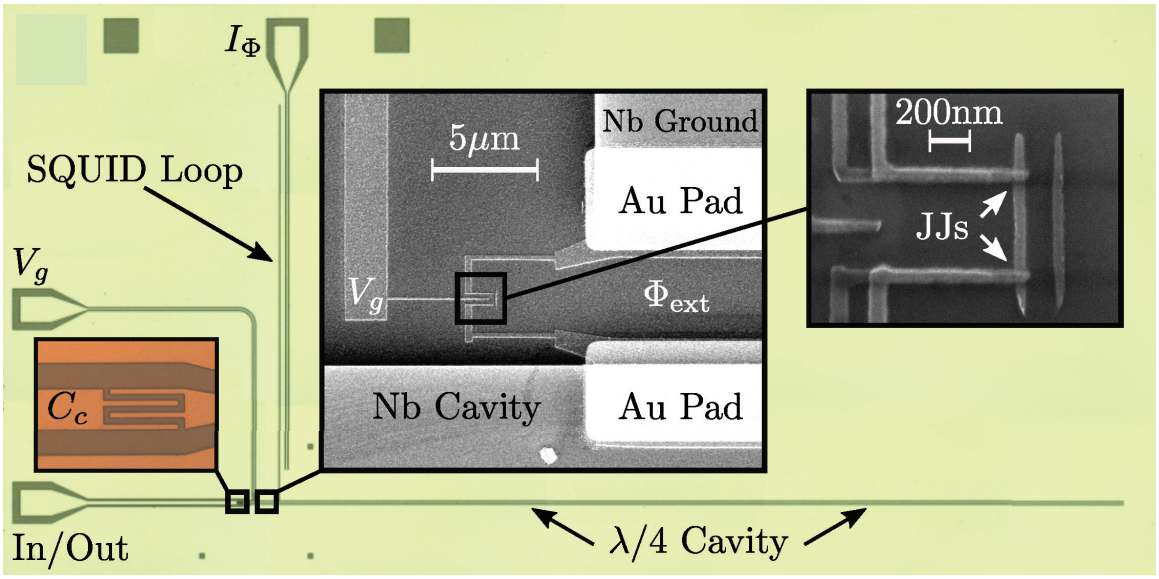

Figure 3.1: Optical microscope image of the cCPT showing the CPW forming the $\lambda/4$ cavity, the coupling capacitor C_c, the gate and flux transmission lines. The insets show a close-up of the interdigitated coupling capacitor, the connection of the cCPT between the ground plane and the center line of the CPW, and a scanning electron micrograph of the two 50 nm x 50 nm JJs forming the superconducting island between them, which is gated by an electrode biased with a voltage V_g. Figure from [33].

3.1.1. Fabrication process

The cCPT sample we used is shown in Fig.(3.1). The first step in the making of the cCPT is to sputter niobium (Nb) on to a silicon wafer. We use an undoped silicon wafer with no oxide layer, but a high intrinsic resistance >20 kΩcm. The co-planar waveguide (CPW) design that will form our $\lambda/4$ cavity is then patterned by photolithography. The coupling capacitor is designed to have a capacitance of ≈ 8 fF, which should yield an overcoupled system ($\kappa_{\text{ext}} > \kappa_{\text{int}}$) (see section 2.4). On the other side of the coupling capacitor is an impedance matched transmission line which will be connected through the PCB and to the fridge electronics denoted 'In/Out' in Fig.(3.1) through which we insert microwave signals into and out of the cCPT to study its response.

The CPW, as its name implies, is a 2D microwave cavity where the center line and

the ground plane forming the two conductors of the transmission are separated by the Si dielectric. The two conductors are shorted at the right end of the transmission line in Fig.(3.1), with a length of 5135 μm between the short and the interdigitated coupling capacitor shown in the enlarged image in Fig.(3.1) corresponding to a resonant frequency of roughly 5.5 GHz. The other important parameter we control on the CPW is the characteristic impedance (see section 2.1.4), which depends on the geometry of the CPW in terms of the ratio of the spacing between the center line and the ground plane; the width of the center line; and the thickness of the substrate. Using the Eqns. in section 3.1.5 of [90], and based on *Sonnet* simulations, we settle upon a center line width = 9.67 μm, and a spacing of 6.6 μm between the center line and the ground plane for our 300 μm thick silicon substrate.

The photolithography step also defines the transmission line denoted 'I_Φ' in Fig.(3.1) which is shorted to the ground plane at its lower extreme and the one denoted 'V_g' which provides a gate bias to the CPT island. The Nb in the negative space defined by the photolithography is then etched using a reactive-ion etch.

Once the Nb has been sputtered, it quickly forms a self-terminating oxide on its surface. Our next step is to make the Al/Al_2O_3 JJs which need to hook up to the ground plane and the center line of the cavity as shown in the inset in Fig.(3.1). In order to facilitate contact between the Al and the oxidized Nb, we lithographically define the rectangular gold (Au) pads shown in the inset. The sample is then placed in a thermal evaporator equipped with an ion mill, pumped to 1×10^{-6} Torr vacuum levels, and the Nb on the exposed Au pad is milled clear of the oxide. A thin 10 nm layer of Au is evaporated onto the rectangular spaces without breaking the vacuum.

The SQUID loop formed by the shorted cavity and the 2 JJs forming the CPT shown schematically in Fig.(2.11) is imperative for the coupling of the CPT to the cavity and hence to the operation of the device. This *thin* Au layer which is part of

that SQUID loop also goes superconducting by virtue of the proximity effect [91].

The wafer is then diced into individual chips which are about 7 mm x 5 mm broad. The JJs are then patterned using ebeam lithography one chip at a time. The important design parameters for the CPT are the charging energy E_C and the Josephson energy E_J. As we saw in section 2.4, in order to see charging effects, we want the charging energy to be quite high. The charging energy is in turn a function of the self-capacitance of the CPT island, which is mostly dominated by the junction capacitances, C_J (section 2.4). Using a parallel plate capacitor model, since the typical thickness of the oxide formed between two Al electrodes is 1 nm, and the relative dielectric constant for Al_2O_3 is 9.34, we shoot for junction sizes of 50 nm x 50 nm which corresponds to capacitances of 206.7 aF. For the CPT consisting of 2 such JJs, this gives an $E_C \approx 47$GHz. The other parameter we control independently (though this also depends on the thickness of the oxide) is the tunneling resistance of the junction which controls the critical current I_c and hence the Josephson energy E_J through the Ambegaokar-Baratoff relation [82] (see section 2.4.1). We will see how we can tune the tunneling resistance once we go through the Dolan bridge or shadow evaporation technique for the CPT fabrication.

We begin the ebeam lithography process by cleaning off the protective photoresist layer on the diced chips with the CPW patterned on it. We do this by putting the chips in an acetone or PG remover bath at 50° c for 15 mins. We then rinse the chip in IPA, blow dry it and sonicate in acetone and subsequently in IPA for 2 mins. Any organic residue is removed by doing an O_2 ash in an RIE for 2 mins at 30 W.

We use a bilayer ebeam resist stack with the bottom layer consisting of Microchem MMA EL(9) spin coated for 45 s at 4000 rpm leading to a layer about 350 nm thick and bake it on a hot plate at 150°c for 1.5 mins. We then pre-expose the chip to UV light for 3 minutes, with a generic store-bought UV light source. The second resist

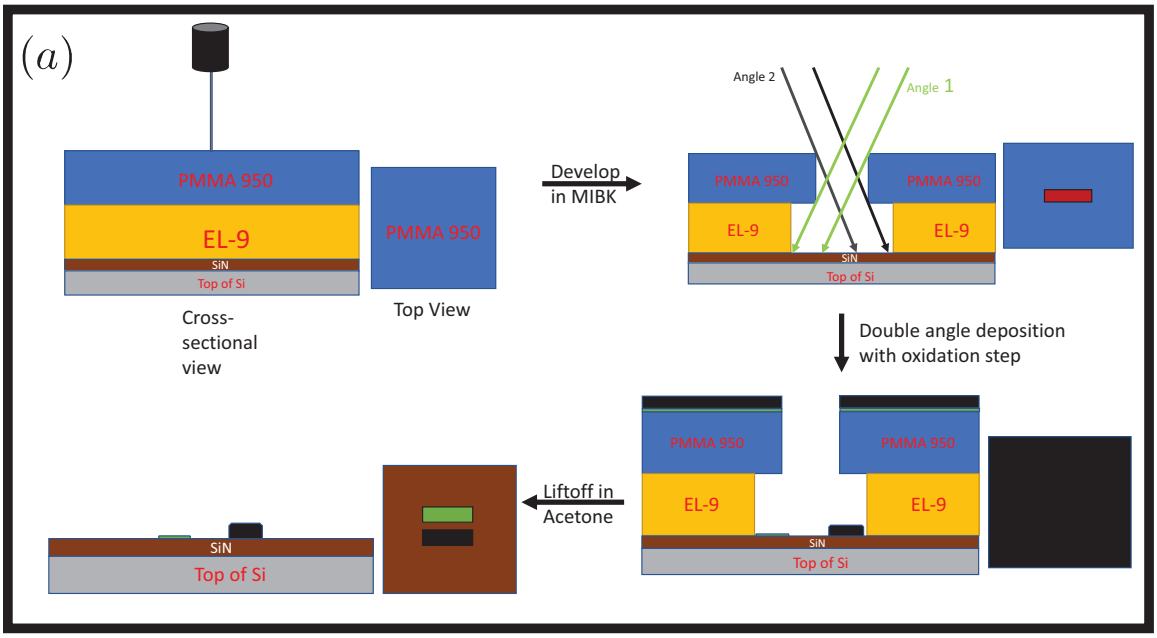

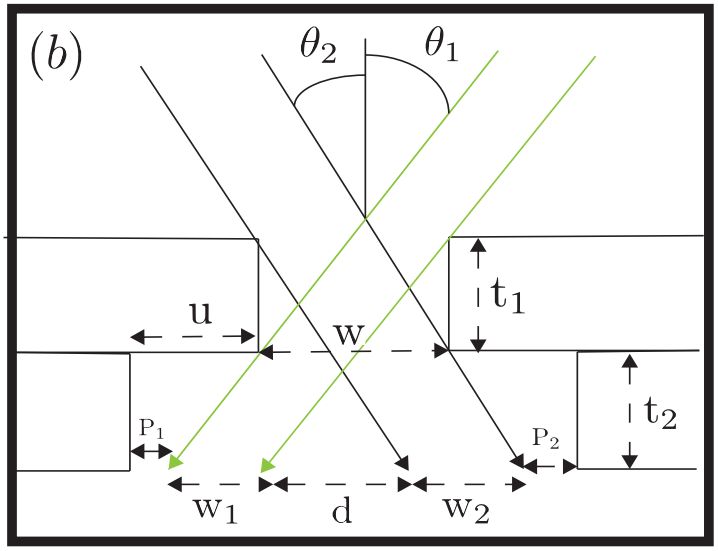

Figure 3.2: (a) Sequence of steps of the shadow evaporation technique showing the patterning of a single rectangular structure. Notice the undercut formed in the resist stack because the EL9 is more sensitive to the ebeam than the 950. The SiN is for the cCPT-NR sample, but the process is identical for the cCPT, though without the SiN. (b) This allows us to form two separated shadows of a single polygon structure when it meets some design constraints (see text). The undercut using a bilayer stack is also used in simple deposition techniques to facilitate liftoff.

layer is a Microchem PMMA 950 A4 layer also spun on at 4000 rpm to a thickness of 200 nm, similarly baked for 1.5mins but at 180° c. The different baking temperatures is as indicated on the datasheets for the respective resists, but doesn't make too much of a difference in practice. We then pattern the desired structure on this ebeam resist using the Dartmouth electron microscopy facility's FEI XL30/Scios2/Helios5 or the Harvard CNS' JEOL JSM 7000 using Joe Nabity's excellent NPGS software. As with high resolution SEM imaging, we use a high accelerating voltage (30 keV, the highest setting on all the above microscopes), and relatively small aperture size yielding a compact spot size for the finest structures (the JJs). An aperture corresponding to the 21 pA beam current setting on the Helios5 worked well to produce sub-50 nm structures.

After patterning, the resist is developed in methyl-isobutyl-ketone(MIBK):IPA::1:3 for 45 s and rinsed in IPA for 30 s. Organic residue on the exposed pieces of substrate was again cleaned using a low power O_2 plasma ash before mounting the chip in the sample holder (stage) of our thermal evaporator. We have mechanical control on the axis of the stage with respect to the evaporation source, and we use 10 rotations of the screw in each direction of the horizontal mounting position (corresponding to about 15° in each direction) for layer 1 and 2 of the deposition respectively. Having loaded 99.999% pure Al pellets 1/8 " dia. x 1/8 " long from Kurt J. Lesker in the two evaporation sources for layer 1 and 2 respectively, we pump the chamber to a high vacuum of $< 1 \times 10^{-6}$ Torr.

The idea behind the double angle technique is that the vertical 'fingers' of the 'π' shaped leads of the CPT (Fig.(3.1)) which form the source and drain of the CPT are patterned to fall a few 100 nm short of the horizontal arm of the 'π' which forms the island. So the 1st layer of deposition with the stage tilted by $+15^o$ will then overlap with the 2nd layer of the vertical fingers and we can perform a controlled oxide growth

on the first layer before the second layer is deposited on top of this oxide. The second layer of the island deposition is visible in Fig.(3.1) as a floating piece of metal.

Fig.(3.2b) shows the geometry of a shadow. Using some simple trigonometry, we have

$$\begin{aligned} \tan\theta_1 &< \frac{u}{t_2} \text{ for } P_1 > 0, \\ \tan\theta_2 &< \frac{u}{t_2} \text{ for } P_2 > 0, \end{aligned} \tag{3.1}$$

where u is the width of the undercut, $\theta_{1(2)}$ are the tilt angles of the stage with respect to the horizontal, and $t_{1(2)}$ are the thicknesses of the respective resist layers. u depends on the chemical properties of the resist stack and the dose delivered to this structure by the ebeam. In order for all of the deposited metal to land on the substrate and not on the sidewall, we need $P_1, P_2 > 0$ and achieve this by attaining the above condition. Deposition on the sidewall causes a slight peeling of that edge of the structure, and is often visible as a bright spot of metal when the device is imaged after processing. Deposition on the sidewall also makes liftoff harder. From Eqns.(3.1), we see that the simplest way to prevent this from happending is by not tilting the sample too much. We will see below that while a high tilt angle will increase the separation d between the two layers, this should be avoided when possible and the increased separation should be achieved in other ways (like controlling resist thicknesses t_1 and t_2 instead, or by reducing the width of the patterned structure w).

We also see that

$$\begin{aligned} w_1 &= w - t_1 \tan\theta_1, \\ w_2 &= w - t_2 \tan\theta_2, \end{aligned} \tag{3.2}$$

where $w_{1(2)}$ are the widths of the structure deposited on the substrate during layer 1

and layer 2 respectively, given that the width of the structure after development is w on the top layer. We also have for the separation d between the two layers

$$d = \big(\tan\theta_1 + \tan\theta_2\big)\big(t_1 + t_2\big) - w, \tag{3.3}$$

where we see that once the width of the patterned structure is larger than a given value (usually a few 100nms), we don't see any separation between the two layers, which is why the larger structures patterned using the double angle evaporation method appear as one solid piece, though you can see a small step around one edge of a large step if inspected closely.

In practice, these equations above only work as guidelines which tell us which direction to tune a certain parameter to achieve a certain effect, since most of these parameters denoted here are nonlinear functions of control knobs such as the patterned width, the dose delivered, the spin speed for the resist coating and so on, which will all have to be sorted out by trial-and-error. These concerns of separation and width are not crucial to the cCPT system, but we will see in a later chapter that they are very important for the cCPT-NR design being implemented in chapter 6.

For the first layer of deposition which ultimately only forms the superconducting island we put down only 7-10 nm of Al. This is done in order to make sure that any quasiparticles, which are detrimental to the efficient functioning of the cCPT (as we will see in section 3.3.2), are not long-lived on the CPT island. This is done by engineering the superconducting gap of the island to be much higher than that of the connecting leads which are deposited in layer 2. Refs. [92, 93, 94] study the variation of the superconducting gap with thickness and for a thickness of 7nm, the superconducting gap of Al is 300 μeV compared to about 200 μeV in the bulk. The dependence of the island quasiparticle lifetime on the superconducting energies is studied in [66], and will be elaborated in section 3.3.2.

Depositing a thin layer of Al comes with its own challenges in terms of grain size dependence on thickness of deposition [95]. We overcome this by cooling the stage using liquid nitrogen during deposition. This reduces the kinetic energy of the Al hitting the substrate and yields more uniform films.

The formation of the oxide between the superconducting electrodes forming the JJs is done by a controlled introduction of 5% O_2 and 95% Ar. Typical pressures we use are about 54 mTorr for 5 mins to obtain normal state resistances of $R_N \approx 10\,k\Omega$ for each JJ when the size of the junction is nominally 50 nm x 50 nm. As mentioned earlier, both C_J (and hence E_C) as well as R_N (and hence I_c and E_J) depend on the size of the junctions and the thickness of the oxide layer. However, we typically use the size of the junctions to tune E_C, and the oxidation pressure and time to tune the thickness to tune E_J, since C_J only depends weakly on the oxide thickness (which itself depends rather weakly on the the pressure and time of oxidation), but R_N, being a tunneling resistance depends exponentially on the thickness. The oxidation also depends to a small extent on the rate of introduction of the gas and the rate at which it is pumped out. So we tend to develop a procedure which is reproducible in terms of slowly building up the pressure to the required value over a constant interval of time and similarly for the pumping out, and don't vary these aspects of the process too much.

The second layer is then deposited and for the cCPT sample was 65-70 nm of Al. This was sufficient to make contact with the Au on top of the 100 nm Nb because of the sloped CPW sidewalls design described in [65]. We then let the stage which had been cooled with liquid nitrogen warm up for a half hour in vacuum or with some dry N_2 introduced to hasten thermalization, in order to avoid contaminants settling on the cold surface of the substrate. We then liftoff the metal in an acetone bath at 50° c for 10-15 mins, gently squirting acetone from a syringe on to the surface of the chip

to aid liftoff. We then get rid of organic residue again by performing a low power O_2 ash. The sample is now ready to be mounted on the PCB in the sample box.

3.1.2. PCB and sample box

The chip is then mounted in a receptacle on a printed circuit board (PCB) with some paper cement (Fig.(3.3)). The PCB helps launch the microwaves to and from the fridge cabling. The PCB is essentially also a set of CPWs, one for each of the control lines indicated in Fig.(3.1) - the input/output line, the gate, and the flux bias. The fourth transmission line visible in the Fig.(3.3) is for the NR described in chapter 6 and is not used for the cCPT device.

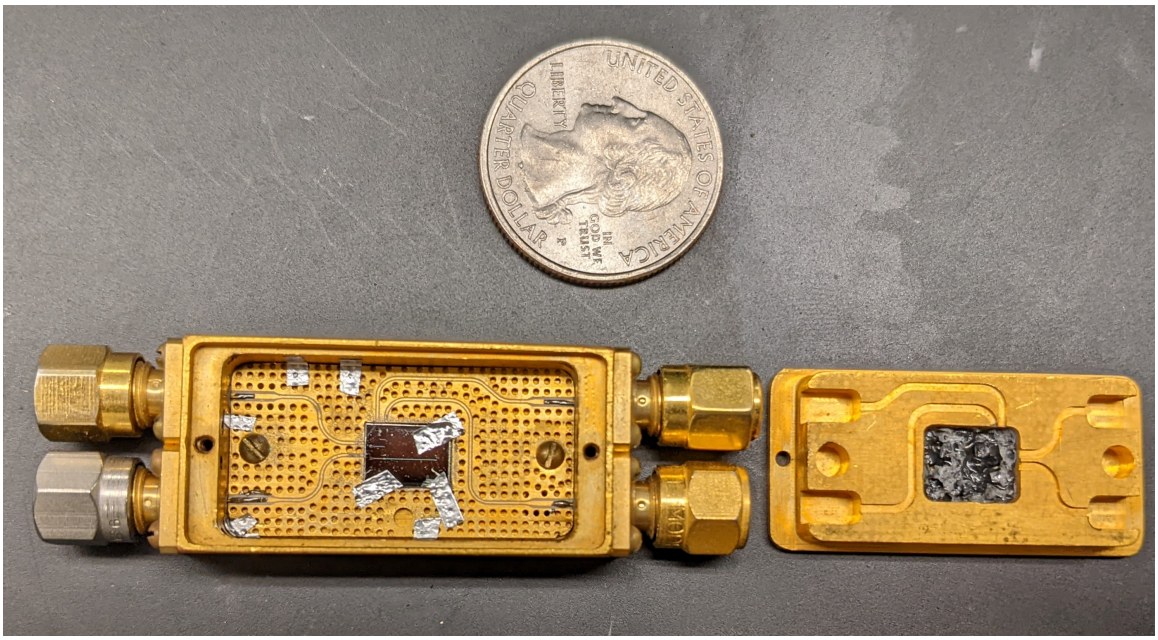

Figure 3.3: Image of the sample box showing the chip seated in a receptacle on the PCB, which is screwed down to the sample box with SMA connectors to hook up to fridge wiring. On the right is the inside of the lid of the sample box, designed to be mode-filling.

The PCB is patterned on an Arlon AD1000 sheet, with vias (the holes in Fig.(3.3)) shunting top and bottom faces regularly along the face of the board. This is done to prevent any parasitic modes between the two ground planes [96]. After being printed,

the PCB is plated with Au, being careful to avoid the Ni based process that is the industry standard and using a soft plating technique instead. This is to avoid any magnetic effects from the Ni. The CPW traces on the PCB line up pretty closely with those on the chip, and only short wire bonds are required to connect the center line of the PCB CPW to that of the chip's. We also fit in 2-3 wire bonds on the PCB of each transmission line on the chip in an effort to lower the effective inductance using the parallel combination of the bonds. To provide an effective uniform ground on the chip, we make as many bonds as possible between the ground plane of the chip and the ground plane of the PCB, all along the edge of the chip. We also connect different sections of the ground plane on chip to equalize potential across its face to suppress parasitic modes. These numerous wire bonds, though thin, also provide a good thermal link between the chip and PCB.

The PCB is screwed down on to a sample box with SMA connectors soldered to the CPWs on the board. The box is made of OFHC (oxygen-free-high-conductivity) copper, which is plated in gold. In order to suppress cross-talk between different transmission lines because of TE/TM modes propagating through the rectangular waveguide like box itself, we use a mode-filling design for the lid of the box [97, 98]. This essentially places the cutoff frequency for the propagation of TE/TM modes in the waveguide well above frequencies we are dealing with. This is especially a concern in transmission mode measurements where you could have spurious signal leakage from the input to output port, bypassing the sample, but could also affect the cCPT which operates in reflection mode by coupling parametric or modulation signals between the gate and flux port. The space in the lid above the sample is filled with an absorptive material (black in Fig.(3.3)) made of silica, silicon carbide and Stycast 1266 [99], to prevent both Cooper pair-breaking IR radiation as well as stray microwave radiation from getting to the sample. The entire sample box is also

enclosed in a magnetic shield made of Cryoperm 10 when mounted on the mixing chamber of the dilution fridge.

Section 3.2

Fridge RF and DC wiring

In this section, we discuss the setup of both the microwave and DC wiring in the dilution fridge that we use to study the cCPT sample. We will go through some of the considerations in the setup illustrated in Fig.(3.4).

3.2.1. RF wiring

Two important considerations in any kind of cryogenic circuitry are i) how much heat is being transferred by any piece of wire between two stages at different temperatures ii) how much electrical noise is being carried by it.

The electrical noise we are largely concerned about is the Johnson noise [100], quantified by Nyquist [101, 102] which says that the noise power spectral density in a resistor at temperature T is

$$S(\omega) = \frac{\hbar\omega}{e^{(\hbar\omega)/(k_B T)} - 1}, \tag{3.4}$$

which is a one-dimensional form of the Planck blackbody law. At high temperatures, this takes the familiar frequency independent form of the Johnson noise $P = k_B BT$ over a bandwidth B. As we saw in section 2.4, the cCPT needs to work at low temperatures where the thermal noise is quite minimal. The way this is typically achieved in cryogenic circuitry is by attenuating the input wires to the fridge to thermalize the noise at each temperature stage. This is the job of the 20dB attenuators at various stages in Fig.(3.4). To equate the noise at two different temperatures T_1 and T_2, the amount of attenuation needed is the ratio of their power spectral densities.

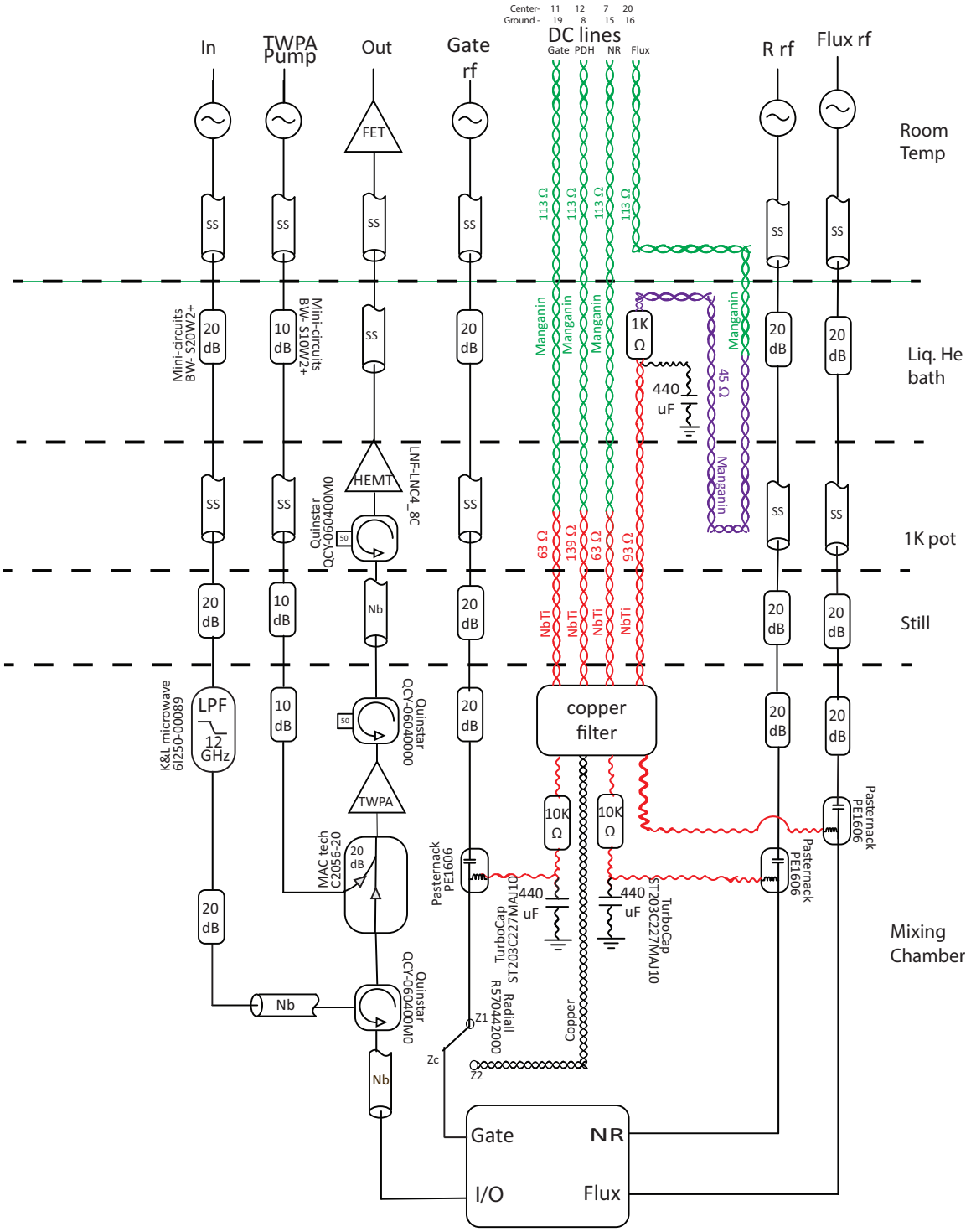

Figure 3.4: Wiring schematic of different temperature stages of the Oxford Kelvinox 400 dilution fridge used to measure the cCPT sample. Nb represents superconducting niogium cabling, while SS represents stainless steel.

$$A(f) = -10 \log \left(\frac{e^{(\hbar\omega)/(k_B T_1)} - 1}{e^{(\hbar\omega)/(k_B T_2)} - 1} \right), \tag{3.5}$$

which for a temperature gradient from 300 K to 30 mK requires an attenuation of about 70 dB. Too much attenuation also dissipates lots of heat, and should be avoided. The stainless steel (SS) semi-rigid coaxial cables themselves also have some additional loss, which all aid in the reduction of input noise. We will see in section 3.3.3 that the total input attenuation on the input line is measured to be about 83dB. This ensures that the power spectral density of the noise at the mixing chamber is less than 0.5 photons/Hz around the tunable frequency range of the cCPT.

The SS coax cables are a little more lossy than other materials such as copper, but are poorer conductors of heat, which is also an important consideration for wires between different temperature stages. The RF gate and flux lines combine with the corresponding DC bias at a bias tee, before the combined RF+DC signal is fed to the appropriate port of the sample. This allows us to easily tune the gate and flux working point of the cCPT using DC voltages and currents, while also leaving open the possibility to modulate the gate/flux as is done in [1] or to introduce parametric tones at $2\omega_0$ as we will see in chapter 5.

Since the cCPT works in reflection mode, the circulator at the mixing chamber separates the input and the output signal. The reflected output signal is then carried by superconducting zero-loss Nb cables to the first stage traveling wave parametric amplifier (TWPA) [52] made at the MIT Lincoln lab. The TWPA acts close to the quantum-limit of added noise, and we shall see the characterization of the added noise of the amplifier chain in section 3.3.4. The output of the TWPA is connected to a Low Noise Factory LNF LNC4_8C high electron mobility transistor (HEMT) by another Nb cable through two isolators to minimize any back-action of the HEMT on the TWPA.

It is important to note that any attenuation also adds noise at the physical temperature of the attenuator[96]. This arises from the commutation relations, similar to the added noise from a phase insensitive amplifier [103, 76]. While this means that no noise is added by a lossy line at the same physical temperature as the noise temperature of the signal passing through it, the signal will undergo attenuation, reducing the signal-to-noise-ration (SNR). This is why we use Nb even between the sample and the TWPA which is at the same temperature stage. Nb is also a poor conductor of heat, which means we don't have to worry about it conducting heat down to the mixing chamber when used between the HEMT and the TWPA.

The TWPA works on the principle of four-wave mixing and requires a pump tone around 6.7 GHz. After undergoing appropriate attenuation, this pump tone is coupled into the input port of the TWPA along with the sample signal using a directional coupler.

All RF lines are thermally anchored at each stage of the dilution fridge by wrapping solder wick between the body of the coax and anchor posts on the fridge, all held in place by Lakeshore GE varnish which is a good thermal conductor, but poor electrical conductor.

3.2.2. DC wiring

The DC wires running the length of the dilution fridge are either 2-pair or 4-pair twisted looms, 100 μm dia. The wiring down to the 1K pot stage of the cryostat is made of Manganin, to minimize the heat transfer from room temperature to 4K, which is the largest thermal gradient. Manganin has a poor thermal conductivity (and also low thermal coeffiecient) compared to other commonly used materials like copper. All of the DC wiring goes through a copper powder filter to filter out RF signals [104]. It also passes through RC low pass filters. The gate line draws no current and the filtering is straightforward, using an $R = 10\,k\Omega$ and a $C = 440\,\mu$F at room

temperature (which drops by a factor of ≈ 10 upon cooling to base temperature), which gives an LPF with a cutoff around 2.5 Hz. The flux line is typically biased with currents of $\approx 50\,\mu$A which corresponds to the Φ_0 periodicity of our SQUID loop, and a 10 kΩ resistor at the mixing chamber would produce 250 μW of power at the mixing chamber, while the cooling power of the Kelvinox 400 is (unsurprisingly) 400 μW at 95mK. To avoid undue heat stress on the dilution fridge, the flux line is thus filtered by an $R = 1\,k\Omega$ at the 1K pot stage which can tolerate this heat load, and superconducting cables run from that resistor to the mixing chamber (see Fig.(3.4)). This yields a cutoff frequency of about 25 Hz for that line.

Similar to the RF cables, the DC looms are also thermally anchored using GE varnish at all temperature stages of the dilution fridge.

In addition to the in-fridge wiring, we use an RC low pass filter with a cutoff frequency of 200Hz at each of the gate and flux DC bias inputs at room temperature. The resistor of the LPF on the flux line along with the 1k Ω resistor at the 1K pot stage on the DC flux line serve to current bias the flux port of the cCPT.

Section 3.3

Experimental methods

In this section, we look at some common setups used in the experiments described in the following chapters, and some of the analysis tools we use to extract useful parameters and information from these measurements. In section 3.3.1 we describe what is usually the first step in any experiment - to characterize the linear resonance at a given cCPT bias point. This includes extracting the resonant frequency (ω_0), and the internal and external damping rates (κ_{int} and κ_{ext}) based on the reflection coefficient S_{11} derived in section 2.1.5. We will see how this quantity is changed by the presence of noise in the tunable parameters - gate and flux as described in [73, 33].

We will then see how we can use the Kerr induced photon number dependent resonant frequency shift described in section 2.5.2 to quantify the attenuation of the input line of the dilution fridge in section 3.3.3. In section 3.3.4, we then use this to determine the added noise at the input to the amplifier chain as a function of the pump frequency and pump power of the TWPA, and find the optimal parameters which minimize the added noise at the input, thereby maximizing the signal-to-noise-ratio (SNR) of our measurement. Finally, in section 3.3.5 we describe our setup to generate shaped pulses followed by subsequent heterodyne measurement of the reflected signal to learn about the dynamics of the system.

3.3.1. S_{11} measurement and analysis

We use a vector network anaylzer (VNA), the Agilent E5071C, to obtain the reflection coefficient S_{11} of our tunable cCPT. We work here in the low input drive limit, where the Kerr and higher order effects can be neglected, so the Hamiltonian of the system looks like that of Eqn.(2.125) with all terms with $k \geq 3$ set to 0. In addition to the S_{11} of the cavity, the measurement includes the attenuation of the input line ($\eta(\omega)$) and the gain of the amplifier chain ($G(\omega)$) which are both also complex coefficients. So the VNA measures

$$S_{21}^{\mathrm{VNA}}(\omega) = \sqrt{\frac{|G(\omega)|}{|\eta(\omega)|}} e^{i\theta(\omega)} S_{11}(\omega), \tag{3.6}$$

where we have absorbed the phases of $G(\omega)$ and $\eta(\omega)$ into one phase $\theta(\omega)$. The VNA measures this reflection coeffiecnt across two different ports because of the separation of the input and output signals by the circulator in Fig. (3.4). We use the method described in [67] where we average the reflected $S_{21}^{\mathrm{VNA}}(\omega)$ across a range of cCPT flux biases to quantify the pre-factor to $S_{21}(\omega)$ in Eqn.(3.6) which we call the 'background gain profile' and use this to extract the $S_{11}(\omega)$ at the sample. We can then fit this to

our model Eqn.(2.31) to extract the parameters of the cavity at a given bias point.

We also include the effect of Gaussian resonant frequency fluctuations [73, 33]. These occur because of changes to the charge environment caused by TLSs on the substrate of the CPT [105, 106] and by flux noise from unpaired surface spins [106, 107]. These fluctuations get averaged into the measured $S_{11}(\omega)$, and we will see later that the standard deviation of these resonant frequency fluctuations sets an error bar on the precision with which we can drive the cCPT at a desired detuning. The modified $S_{11}(\omega, \sigma_{\omega_0})$ then becomes [73]

$$\overline{S_{11}}(\Delta) = 1 - \sqrt{\frac{\pi}{2}} \frac{\kappa_{\text{ext}}}{\sigma_{\omega_0}} w\left(\frac{(i\kappa_{\text{tot}} - 2\Delta)}{2\sqrt{2}\sigma_{\omega_0}}\right), \tag{3.7}$$

where $w(z) = e^{-z^2}\text{erfc}(-iz)$ is the Faddeeva function, σ_{ω_0} is the standard deviation

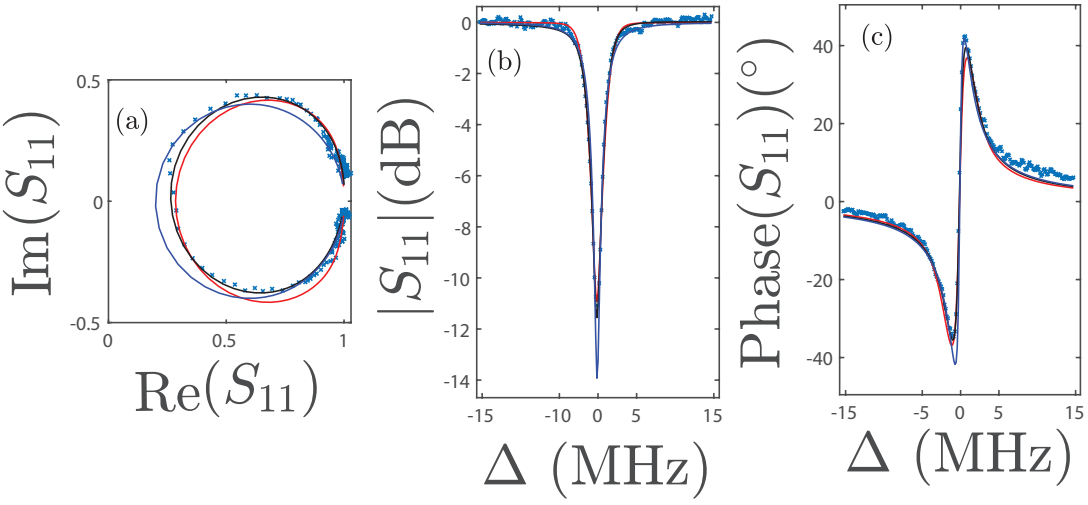

Figure 3.5: Reflection coefficient $S_{11}(\omega)$ for a cCPT bias point $(n_g, \Phi_{\text{ext}}) = (0.65, 0.11)$. The x's represent data, the blue solid line is a fit to Eqn.(2.31), the red to Eqn.(3.7), and the black is with the rotation correction described in [108]. (a) is the polar plot of $S_{11}(\Delta)$, (b) is the magnitude of $(S_{11}(\Delta))$ as a function of detuning and (c) is the phase of the reflection coefficient.

of the resonant frequency fluctuations, and $\Delta = \omega - \omega_0$ is the detuning as before. In addition to this correction to the measured reflection coefficient, we also see a rotation of the measured S_{11} about the off-resonant point. This often arises as a result of impedance mismatches between the sample and the biasing circuitry [108]. We account for this by fitting a model that shifts the entire polar plot of the measured $\overline{S_{11}}(\Delta)$ such that the off-resonant detuning falls at $(0, 0)$. We then perform an $SO(2)$ rotation followed by shifting the off-resonant detuning back to $(1, 0)$. Fig. (3.5) shows the obtained data and the fits corresponding to the model with no resonant frequency fluctuations, with frequency fluctuations but no impedance mismatch, and the model with impedance mismatch respectively. It can be seen that the fit without frequency fluctuations cannot account for the squashing of the S_{11} in Fig.(3.5a) which is taken care of by the fluctuations model. The rotation of about 4.15° is necessary to correctly extract all other parameters, yielding $\omega_0/2\pi = 5.7967$GHz, $\kappa_{\text{int}}/2\pi = 1.01$MHz, $\kappa_{\text{ext}}/2\pi = 0.99$MHz and $\sigma_{\omega_0}/2\pi = 0.75$MHz respectively.

3.3.2. Quasiparticle Poisoning (QP) and effect on S_{11}.

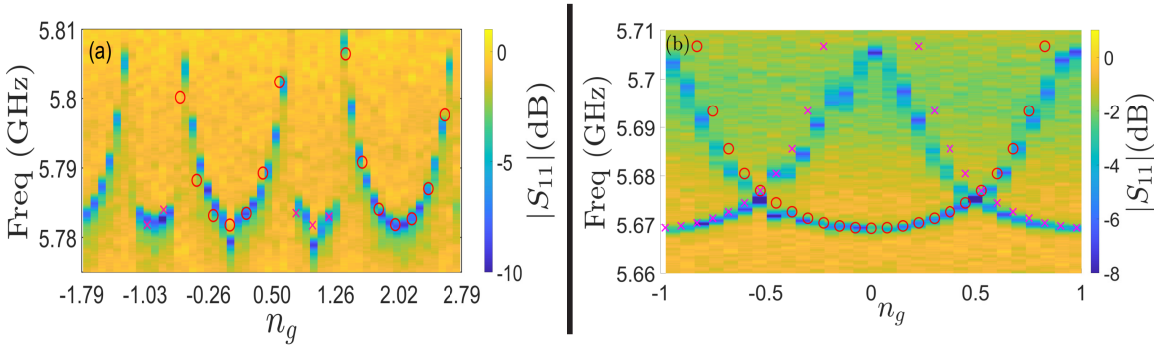

Figure 3.6: Gate variation of resonant frequency for (a) cCPT sample with $E_J = 14.8$ GHz and $E_C = 54.1$ GHz (b) cCPT - NR sample described in chapter 6 with $E_J = 9$ GHz and $E_C = 27$ GHz. Each sample shows different levels of quasiparticle poisoning. The crosses and circles are the simulated values for the odd and even bands respectively for corresponding parameters.

We saw in Fig.(2.12b) that we expect to see a clean periodic variation in the linear

resonant frequency of the cCPT with a period of 2 gate electrons. In real systems, this picture is often distorted by the fact that quasiparticles can tunnel to and from the CPT island. Each time a quasiparticle tunnels on to the island, the effective gate charge goes to $n_g' \to 1 - n_g$, where n_g is the desired gate bias of the cCPT corresponding to an applied voltage at room temperature. The resonant frequency shifts accordingly, shifting back when the quasiparticle tunnels off the island. These 'poisoning' and 'ejection' rates are typically of the order of 1-100 kHz [66, 109]. So during an acquisition of S_{11} using a VNA as described above, the instrument averages over both resonant frequencies (when biased away from $n_g = 0.5$), and the result looks as shown in Fig.(3.6) where the smaller values of the colour plot (bluer hues), represent a dip in the S_{11} and a corresponding resonance at that frequency. We sometimes see resonances corresponding to n_g values in the even band (explained below), sometimes resonances corresponding to n_g' in the odd band, and sometimes both, when the switching times are much less than the measurement times.

We see that the scans from the cCPT sample, Fig.(3.6a) shows two resonances only for a small range of n_g values around $n_g = 0.7$. As in [66], we refer to the 'odd band' as the manifold where a quasiparticle exists on the island and the 'even band' as the manifold where there isn't one. If the system is perfectly shielded from Cooper pair-breaking radiation, no quasiparticles are generated, and this section becomes moot, but assuming a quasiparticle is created, we can have two possible configurations - (i) the quasiparticle lives on the island (odd parity) and (ii) the quasiparticle lives on the lead (even parity). Following [66], the energies of the system in each of these configurations is

$$E_{\text{even}}^{\text{CPT}}(n_g, \Phi_{\text{ext}}) = E_0^{\text{CPT}}(n_g, \Phi_{\text{ext}}) + \Delta_l, \tag{3.8a}$$

$$E_{\text{odd}}^{\text{CPT}}(n_g, \Phi_{\text{ext}}) = E_0^{\text{CPT}}(n_g + 1, \Phi_{\text{ext}}) + \Delta_i, \tag{3.8b}$$

where $\Delta_{\mathrm{l(i)}}$ is the superconducting energy gap in the leads and island of the CPT respectively, and so Eqn.(3.8a) represents the energy of the system when a quasiparticle is created on one of the leads of the CPT, which doesn't change the parity and the CPT remains in the even band. Eqn.(3.8b) represents the energy of the system when a quasiparticle is created on the island and this does change the parity. As long as the energy difference $\Delta E(n_g, \Phi_{\mathrm{ext}}) = E^{\mathrm{CPT}}_{\mathrm{even}}(n_g, \Phi_{\mathrm{ext}}) - E^{\mathrm{CPT}}_{\mathrm{odd}}(n_g, \Phi_{\mathrm{ext}}) > 0$, it is energetically favourable for the quasiparticle to reside on the island, and we are more likely to be in the odd band. The ejection out of the island is then an activated thermal process with an energy barrier ΔE. Similarly, if $\Delta E < 0$, a quasiparticle on the leads is more likely. This keeps the CPT in an even parity, and the poisoning of the island which would drive us into the odd band is an activated event with a barrier ΔE [66]. ΔE is, of course, a function of the CPT band structure and varies with n_g. We see in Fig.(3.6a) that the crossover from $\Delta E < 0$ close to $n_g = 0$ to $\Delta E > 0$ happens around $n_g = 0.73$. Close to that gate bias, the activation energy ΔE is small enough that we see hopping back and forth between the two states within the measurement timescales of the VNA. Far away from this region, one or the other parity state is more probable and we live completely in the even band for $n_g < 0.7$ and completely in the odd band for $n_g > 0.81$. Note that this means that the cCPT cannot be operated effectively at gate points close to charge degeneracy ($n_g = 1$) where the slope of the ω_0 vs n_g curve is largest and the system is most sensitive to charge.

Eqns.(3.8a) and (3.8b) explain why we chose to decrease the thickness of the island (and hence increase Δ_i) - this will help reduce ΔE and ensure that we stay in the even parity across a larger range of n_g. Simulating the energy bands for the CPT parameters for both figures in Fig.(3.6), we plot Fig.(3.7). In Fig.(3.7a), we mark the lines corresponding to $n_g = \pm 0.71$ where we empirically begin seeing QP. This

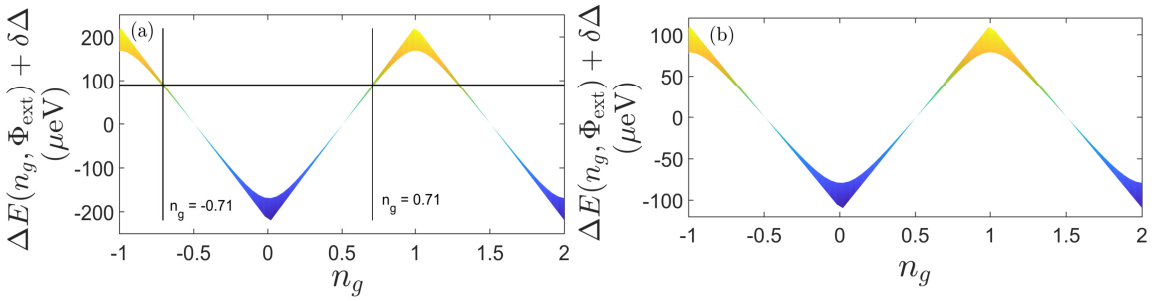

Figure 3.7: Gate variation of $\Delta E(n_g, \Phi_{\text{ext}})$ simulated for (a) cCPT sample with $E_J =$ 14.8 GHz and $E_C = 54.1$ GHz(b) cCPT - NR sample described in chapter 6 with $E_J = 9$ GHz and $E_C = 27$ GHz. The spread of each curve is for different Φ_{ext}, and we see that there isn't much variation with the flux, which we ignore here.

corresponds to the $\delta\Delta = \Delta_i - \Delta_l$ =80 - 90μeV (we'll probably start seeing switching when ΔE is a little less than 0).

Based on the model in [66] which assumes that quasiparticles are created only on the leads with a creation (destruction) rate $\Gamma_{\text{c(d)}}$, using detailed balance we have

$$\mathscr{R}(n_g, \Phi_{\text{ext}}) \equiv \frac{p_{\text{even}}}{p_{\text{odd}}} = \left(1 + \frac{\Gamma_d}{\Gamma_c}\right) e^{-\Delta E(n_g, \Phi_{\text{ext}})/(k_B T_{\text{eff}})}, \tag{3.9}$$

where $p_{\text{even(odd)}}$ is the probability of being in the even(odd) band respectively and T_{eff} is the effective electron temperature that provides the energy kick to transition across the activation barrier.

Fig. (3.8) shows the range of gates over which we see QP at a flux bias of $\Phi_{\text{ext}} = 0$. We see that as we move across from lower to higher gate values, the even band resonance (larger spread of resonances at higher frequencies), becomes smaller (less probable) and the opposite effect is observed for the odd band resonances at lower frequencies. The larger spread of the even band compared to the odd is because of the fact that it is more sensitive to charge at these gate values. From the empirical fact that we see both even and odd band resonances between $n_g = 0.71$ and $n_g = 0.81$ (Fig.(3.8)) and from Fig.(3.7a) we have $\delta\Delta E = \Delta E(0.81, 0) - \Delta E(0.71, 0) = 35\mu$eV,

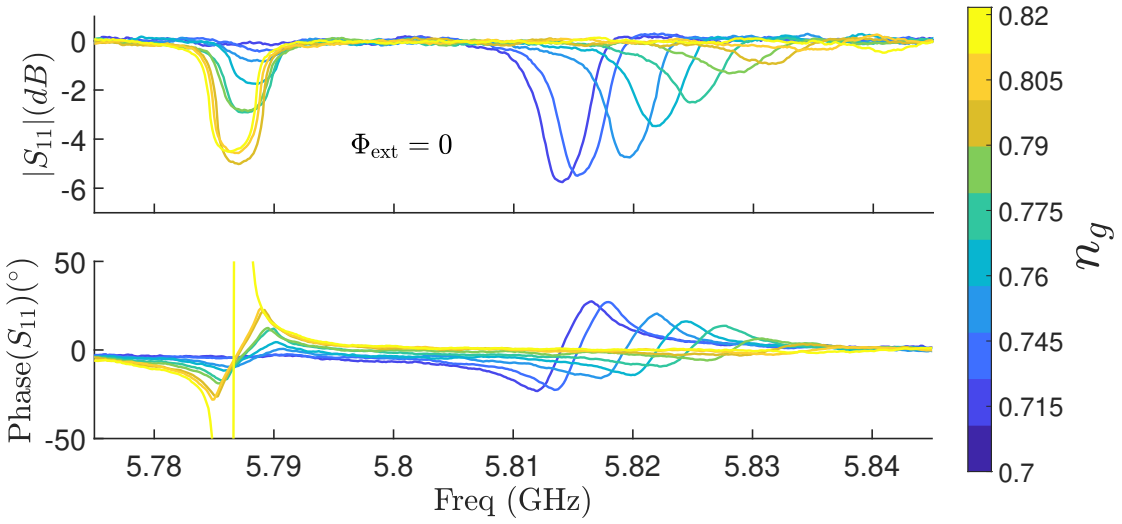

Figure 3.8: S_{11} of the even and odd resonances for the cCPT sample for flux = 0 at a range of gate biases where the lifetime in both bands is comparable.

between these two gate points, and estimating that $p_{\text{even(odd)}} = 0.9(0.1) \to 0.1(0.9)$ in that range (this is a little hand-wavy, but we will describe a technique which could potentially be used to quantify this in the next section), we can extract an estimate for the effective temperature that the quasiparticle is seeing to be

$$\frac{\mathscr{R}(0.71, 0)}{\mathscr{R}(0.8, 0)} = e^{\delta\Delta E/(k_B T_{\text{eff}})}, \tag{3.10}$$

$$\implies T_{\text{eff}} = \frac{\delta\Delta E}{k_B \ln 81} = 92\,\text{mK}. \tag{3.11}$$

Like we said above, this is only a rough upper limit given the fact that the values of 0.9 and 0.1 we used are not exact, but this is a reasonable estimate since the less probable resonance is essentially invisible on a VNA measurement at these points.

We now estimate $\delta\Delta = 90\ \mu$eV based on chapter 6 of [92] for the fabricated thicknesses of 7 nm and 65 nm for the island and leads respectively. Using this and from Fig.(3.7a), we have $\Delta E(0.71, 0) \approx 0$. Plugging this back into Eqn.(3.9), using the T_{eff} we estimated, we have $\Gamma_d/\Gamma_c = 8$ for this cCPT device. The origin of the

quasiparticles is not well understood. For this device, the destruction rate outweighs the creation rate by an order of magnitude.

In the cCPT-NR device in Fig.(3.6b), we see QP across all n_g values. In fact we see this sort of behaviour across all devices fabricated with the cCPT-NR design that we will discuss in 6. To begin, the variation between the extreme values of ΔE (Fig.(3.7)) is much smaller for these devices, for which the charging energy E_C is smaller. This is because the self-capacitance of the CPT when the NR is included is much higher than the cCPT device. This automatically means that the trap height for escape from odd to even or even to odd parity (depending on the sign of ΔE) is much smaller across all n_g. Both the cCPT and the cCPT-NR device were fabricated with an island thickness of 7 nm and leads 60-65 nm. We can assume that they had similar $\delta\Delta = 90\,\mu$eV.

We do not attempt to quantify the effective temperature for this device since we don't have a good sense of the ratio $\mathscr{R}(n_g, \Phi_{\text{ext}})$, but we expect a higher effective temperature and/or a smaller ratio for Γ_d/Γ_c given the fact that we see both bands across all n_g values.

Reflection coefficient in the presence of QP

Similar to section 3.7 where we saw that the S_{11} changes as a function of Gaussian noise on the gate and flux, we can now see how the S_{11} changes due to QP. In this case, we have a Poisson process, and expect to see an S_{11} that is a weighted average of the S_{11}'s corresponding to the even and the odd bands at a given n_g, where the weight is set by p_{even}. So we expect for the Poisson weighted $\overline{S_{11}^{\text{qp}}}(\Delta)$

$$\overline{S_{11}^{\text{qp}}}(\Delta) = p_{\text{even}}\overline{S_{11}^{\text{even}}}(\Delta) + p_{\text{odd}}\overline{S_{11}^{\text{odd}}}(\Delta), \tag{3.12}$$

where $\overline{S_{11}^{\text{even}}}(\Delta)$ is the reflection coefficient defined in Eqn.(3.7) for a particular gate value n_g, and $\overline{S_{11}^{\text{odd}}}(\Delta)$ is that which corresponds to the value $1 - n_g$.

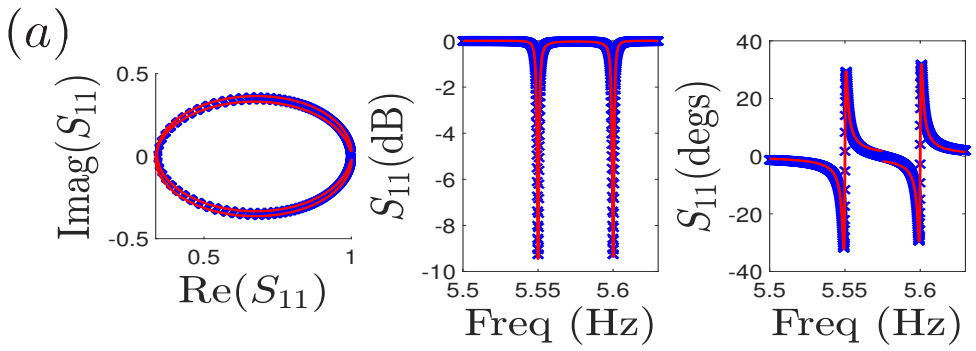

(a)	ω_0(GHz)	κ_{int}(MHz)	κ_{ext}(MHz)	σ_{ω_0}(MHz)	$\theta^{(\circ)}$
Even	5.55	1.330	0.784	0.399	-2.90
Odd	5.60	1.234	0.766	0.456	2.71

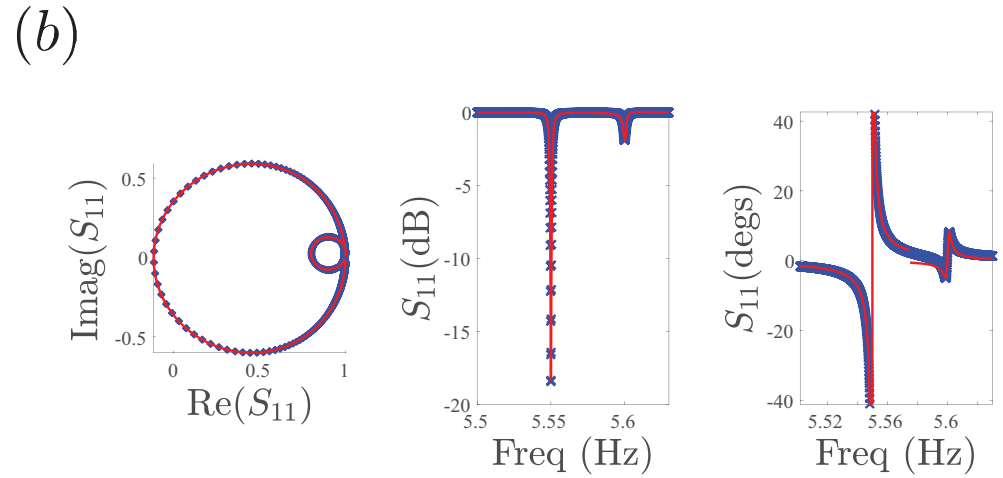

(b)	ω_0(GHz)	κ_{int}(MHz)	κ_{ext}(MHz)	σ_{ω_0}(MHz)	$\theta^{(\circ)}$
Even	5.55	0.65	1.285	0.484	-0.52
Odd	5.60	2.33	0.265	0.1	14.80

Figure 3.9: Simulated S_{11} for $\omega_0^{(\text{even})} = 5.55$ GHz, $\omega_0^{(\text{odd})} = 5.6$GHz, $\kappa_{\text{int}}^{(\text{even})} = \kappa_{\text{int}}^{(\text{odd})} = 0.4$ MHz, $\kappa_{\text{ext}}^{(\text{even})} = \kappa_{\text{ext}}^{(\text{odd})} = 1.5$ MHz , $\sigma_{\omega_0}^{(\text{even})} = \sigma_{\omega_0}^{(\text{odd})} = 0.5$ MHz with (a) $p_{\text{even}} = 0.5$ and (b) $p_{\text{even}} = 0.85$.

We simulate this reflection coefficient for some nominal values of cavity parameters in Fig.(3.9). We see that if we fit to each of the even and odd band resonances without taking into account the weighted effective S_{11}, we wind up with values for the damping rates such that both κ_{tot} and the coupling ratio $\kappa_{\text{int}}/\kappa_{\text{ext}}$ [73] go up. The $\overline{S_{11}}^{(\text{odd})}(\Delta)$ gets rotated one way and the $\overline{S_{11}}^{(\text{even})}(\Delta)$ in the other direction.

We observe this effect in data around the bias points where both bands are visible during a VNA S_{11} measurement. Two such plots and fits are presented in Fig.(3.10). The data at such high n_g values makes it hard to distinguish between internal damping and frequency fluctuations (which have the a similar effect [73] on the q-cirlces), but notwithstanding this deviation, we can still see good fits, and that the two effects described above are clearly visible.

We also see a frequency dependent variation in damping rates [33] in this cCPT sample. To distinguish that effect from the QP induced apparent change in damping parameters, we perform these measurements at n_g which results in a finite probability in both bands, and then move to two different bias point where the resonant frequency matches up with either the even or odd band resonance of our first test. We ensure that we stay entirely in the even band at these latter two bias points, by ensuring that $|1 - n_g| > 0.3$. This is shown in Fig.(3.11) where we see different damping rates and rotation angles for similar resonant frequencies.

In addition to this weighting effect which arises because of the switching statistics of the CPT, quasiparticles also have a detrimental effect on the κ_{tot} of any microwave cavity [99]. Where possible, every shielding precaution should be taken to keep out Cooper-pair breaking radiation [99, 110]. This was one major setback that needs to be resolved in the fabrication of the cCPT-NR devices discussed in chapter 6.

We were unable to reliably fit the Poissonian weight model to QP data to extract meaningful values for the actual damping rates along with appropriate probabilities.

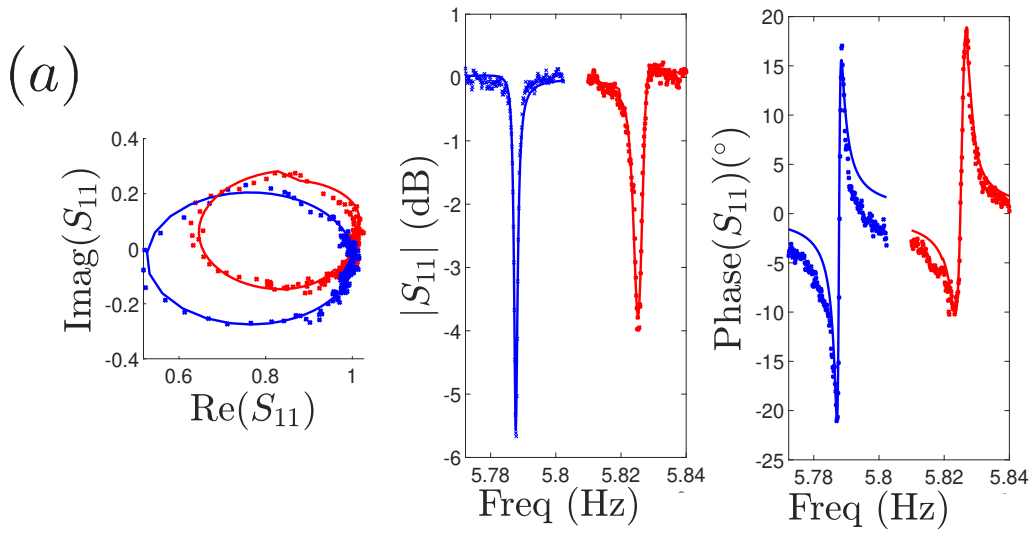

(a)	ω_0(GHz)	κ_{int}(MHz)	κ_{ext}(MHz)	σ_{ω_0}(MHz)	$\theta^{(\circ)}$
Even	5.8254	0.12	0.46	1.39	13.76
Odd	5.7876	1.35	0.43	0.1	-8.53

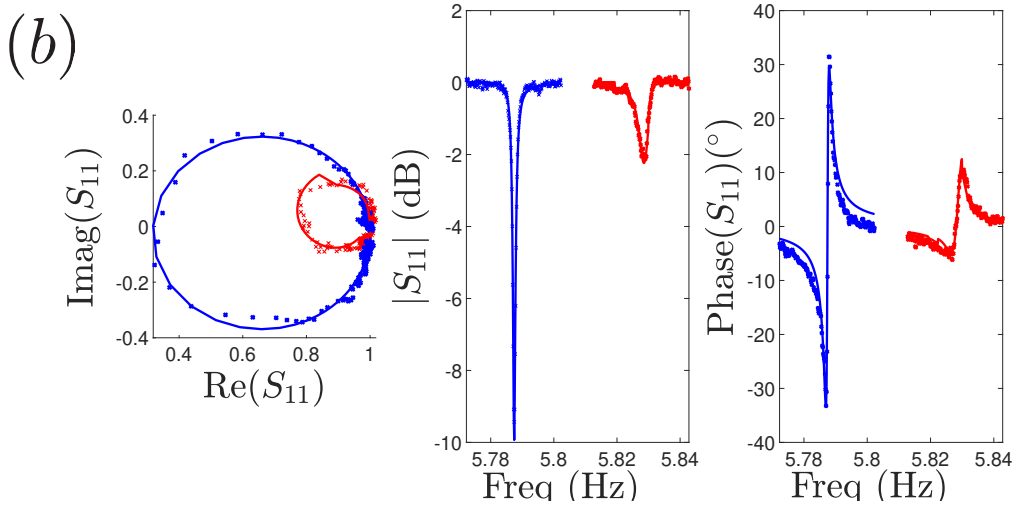

(b)	ω_0(GHz)	κ_{int}(MHz)	κ_{ext}(MHz)	σ_{ω_0}(MHz)	$\theta^{(\circ)}$
Even	5.829	0.1	0.37	1.98	23.66
Odd	5.7874	2.11	0.60	0.14	-3.88

Figure 3.10: Data and fits agnostic to the effects of QP weighting. Fitting separately to the even (red) and odd (blue) band resonances for two different bias points of the cCPT device. In (a) $(n_g, \Phi_{\text{ext}}) = (0.775, 0)$ and (b) $(n_g, \Phi_{\text{ext}}) = (0.790, 0)$.

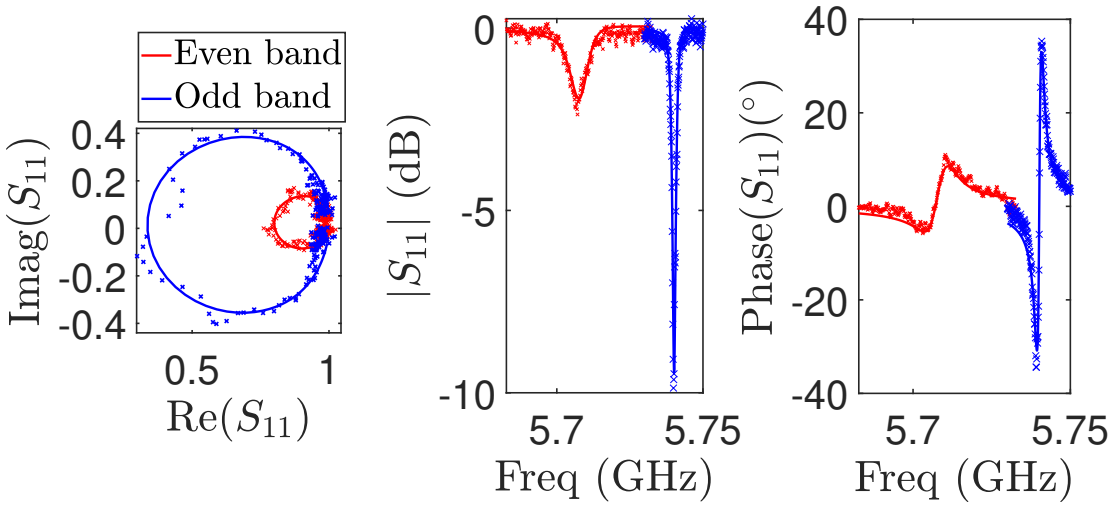

(a)	ω_0(GHz)	κ_{int}(MHz)	κ_{ext}(MHz)	σ_{ω_0}(MHz)	$\theta^{(\circ)}$
Even	5.7082	4.62	0.71	1.87	15.08
Odd	5.7402	0.64	0.64	0.62	-2.697

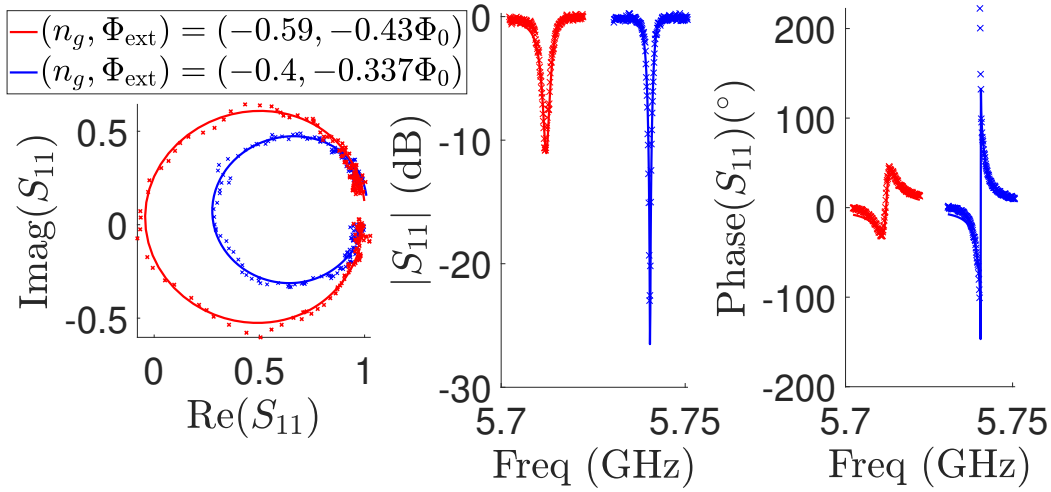

(b)	ω_0(GHz)	κ_{int}(MHz)	κ_{ext}(MHz)	σ_{ω_0}(MHz)	$\theta^{(\circ)}$
(-0.59, -0.43)	5.7127	1.78	1.49	0.96	13.06
(-0.4, -0.337Φ_0)	5.7406	0.61	1.27	0.62	4.75

Figure 3.11: (a) Even and odd band resonances at $(n_g, \Phi_{\text{ext}}) = (0.8, 0.35\Phi_0)$. The even and odd band resonances are at $\omega_0^{\text{even(odd)}} = 5.7082$ GHz and 5.7402 GHz respectively. (b) Two different bias points as indicated, with similar resonance frequncies to the dips in (a). We see considerably different damping rates between the two plots which is the effect of the Poissonian weighting between the even and odd states in (a).

Such a model consists of 9 free parameters even if we fix the resonant frequencies to be the minima of S_{11}, and this becomes an overfitted model.

3.3.3. Estimating the attenuation on the input line

We use the idea described in [33] to characterise the attenuation of the input line of the fridge (see Fig.(3.4)). As we drive the cCPT at different input drive strengths, we use the intracavity photon number dependent Kerr mediated resonant frequency shift to estimate the number of intracavity photons and hence the photon flux in the input transmission line. This should depend linearly on the power output by the signal source with the slope linearly related to the attenuation of the input line of the dilution fridge along with other parameters such as the linear damping rates.

First, we relate the intracavity photon number to the power in the transmission line. In order to do this, we assume that the Hamiltonian of the system is that of a linear cavity, which is a good approximation at the low powers we work at for this measurement (the Kerr shift is less than the cavity linewidth, typically corresponding to < 3 intracavity photons). So, we have for the cCPT Hamiltonian $H_{\mathrm{cCPT}} = \hbar\omega_0 a^\dagger a$ where we have assumed that we are working at a fixed flux and gate bias point with corresponding resonant frequency ω_0. The quantum Langevin equation Eqn.(2.66) then gives us

$$\dot{a} = \left(-i\omega_0 - \frac{\kappa_{\mathrm{tot}}}{2} \right) a + \sqrt{\kappa_{\mathrm{ext}}} a_{\mathrm{in}}(t) + \sqrt{\kappa_{\mathrm{int}}} b_{\mathrm{in}}(t). \tag{3.13}$$

Since the input tone is a pure sine wave at frequency ω_d of the form $a_{in} = \alpha_{in} e^{-i\omega_d t}$. We expect the steady state response of the cavity to be at this drive frequency. We thus make the ansatz $a = \alpha e^{-i\omega_d t}$, $\dot{a} = -i\omega_d \alpha e^{-i\omega_d t}$ and the average cavity occupation

$n = |\alpha|^2 = a^\dagger a$. Plugging this ansatz into Eqn. (3.13) we obtain

$$\begin{aligned}\big[-i\Delta + \frac{\kappa_{\rm tot}}{2}\big]\alpha &= \sqrt{\kappa_{\rm ext}}\alpha_{\rm in},\\ \big[i\Delta + \frac{\kappa_{\rm tot}}{2}\big]\alpha^* &= \sqrt{\kappa_{\rm ext}}\alpha^*_{\rm in}.\end{aligned} \tag{3.14}$$

where $\Delta = \omega_d - \omega_0$ again. Multiplying the above two equations together, we have for the intracavity photon number n

$$n = |\alpha|^2 = \frac{\kappa_{\rm ext}|\alpha_{\rm in}|^2}{\Delta^2 + \kappa_{\rm tot}^2/4} \tag{3.15}$$

For an on-resonant drive, and defining $P_{\rm in} = \hbar\omega_0\alpha_{\rm in}^2$, we have

$$n = \frac{\kappa_{\rm ext}P_{\rm in}/\hbar\omega_0}{\Delta^2 + \kappa_{\rm tot}^2/4} \tag{3.16}$$

This $P_{\rm in}$ is the input power in the transmission line at the coupling capacitor of the cCPT. This is related to the power put out by the signal generator $P_{\rm sg}$ by $P_{\rm in} = \eta(\omega)P_{\rm sg}$. Using this in the cCPT Hamiltonian above, but including the Kerr term in Eqn.(2.128), we have for the resonant frequency

$$\omega_0^{\rm Kerr} = \omega_0 + Kn = \omega_0 + \frac{K\kappa_{\rm ext}\eta(\omega_0)P_{\rm sg}/\hbar\omega_0}{\kappa_{\rm tot}^2/4}, \tag{3.17}$$

where $\omega_0^{\rm Kerr}$ is the shifted resonant frequency in the presence of n intracavity photons.

Fig.(3.12) shows this measurement for two different bias points. We obtain the input attenuation of the input line of the fridge to be 82.9 dB with less than 1 dB variation between 5.7 and 5.85 GHz, the tunable range of the cCPT. This is an important calibration which will help us estimate the intracavity photon number in all our experiments. In addition, this will help us calculate the gain and added noise of our amplifier chain as we will see in the next section. These are important quantities

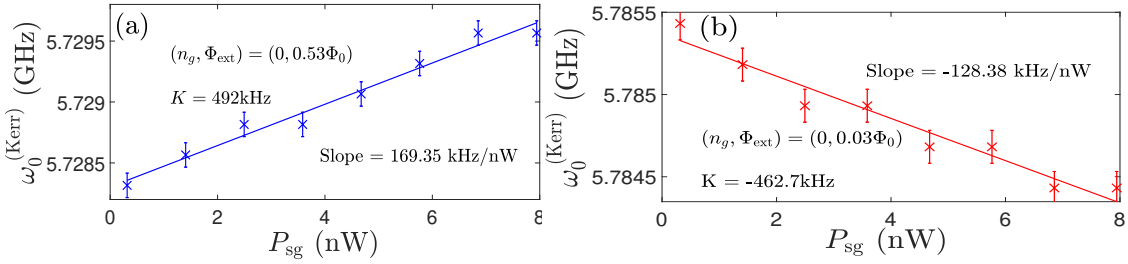

Figure 3.12: Intracavity photon number dependent shift of the resonant frequency for two different cCPT bias points. (a) $(n_g, \Phi_{\text{ext}}) = (0, 0.53\Phi_0)$ (b) $(n_g, \Phi_{\text{ext}}) = (0, 0.03\Phi_0)$ with corresponding $K = 492$ kHz and -462.7 kHz respectively.

because they determine the signal-to-noise-ratio (SNR) of our measurements, and require some optimization over the pump parameters of the TWPA.

3.3.4. Amplifier chain calibration

Knowing the attenuation of the input line of the dilution fridge, we now use the technique described in [67] to obtain the gain $G(\omega)$ and added noise n_{add} of the amplifier chain both of which will be referred to the input of the first stage amplifier - the TWPA. We will then use this technique to find $G(\omega)$ and n_{add} for a range of TWPA pump parameters (pump power and pump frequency), and obtain the parameters for optimum SNR.

The first step in this process is to measure the gain $G(\omega)$. Knowing $\eta(\omega)$, this is done directly using a VNA measurement with all the system amplifiers in their desired state and Eqn.(3.6) by ensuring that $S_{11}(\omega)$ is 1. This is the case for any off-resonant point a few linewidths away from the tunable cCPT resonance. In principle, by biasing the cCPT at two flux points on either end of the resonant frequency vs flux sinusoid, we can measure the $G(\omega)$ at all frequency ranges of interest. We then directly have

$$G(\omega) = \sqrt{\eta(\omega)} S_{21}^{\text{VNA}}(\omega), \tag{3.18}$$

where the square root is because the VNA measures the voltage ratio. We will drop

the frequency dependent notation going forward.

Once we have G, with all the amplifiers still in their desired state, we measure the power spectral density from the amplifier chain on a spectrum analyzer (SA) when there is no input drive. The input to the amplifier chain (input to the TWPA) is then the thermalized noise at the mixing chamber, which is essentially the 0.5 photons of quantum noise n_{qu}. At the output of our first stage amplifier which has gain G_1 and adds a noise n_1 referred to its input, we have

$$n_{\mathrm{out}}^{(1)} = G_1\big(n_{\mathrm{qu}} + n_1\big) \tag{3.19}$$

Assuming no attenuation between the first stage TWPA and the second stage HEMT at the 1k pot stage (see Fig.(3.4)), which is a reasonable assumption since the cables are superconducting Nb, and the only loss is in the insertion loss of the two isolators which is typically < 0.5 dB each, we have for the noise at the output of the HEMT $n_{\mathrm{out}}^{(2)}$

$$\begin{aligned} n_{\mathrm{out}}^{(2)} &= G_2(n_{\mathrm{out}}^{(1)} + n_2) \\ &= G_2 G_1\big(n_{\mathrm{qu}} + n_1\big) + G_2 n_2, \end{aligned} \tag{3.20}$$

where n_2 is the added noise of the second stage amplifier (HEMT). The noise at the output of the second stage referred back to the input of the entire amplifier chain $n_{\mathrm{chain,in}}^{(2)}$ is then (we divide by $G_1 G_2$)

$$\begin{aligned} n_{\mathrm{chain,in}}^2 &= n_{\mathrm{qu}} + n_1 + \frac{n_2}{G_1} \\ &\approx n_{\mathrm{qu}} + n_1 \end{aligned} \tag{3.21}$$

where we have made the assumption that $n_2/G_1 \ll 1$, which is justified for our system, where the HEMT has a noise temperature of $\approx$ 4 K$\equiv$ 14.5 photons at 5.8 GHz. The TWPA typically has a gain of 18-20 dB [52] which corresponds to a factor of between 63-100. Eqn.(3.21) is saying that the added noise to the amplifier chain is dominated by the added noise of the first stage amplifier, which is the hallmark of any good amplifier chain design. Using this result, the total output noise at the end of k amplifier stages will be $n^k_{\text{out}} = G_1G_2...G_k\big(n_{\text{qu}} + n_1\big)$, which is the power spectral density (PSD) the SA measures, $P^{\text{SA}}_{\text{no input}}$. The k amplifier stages may include any of the discrete attenuation stages in the output line of the setup too, and the net gain of the amplifier chain we measured earlier is $G = G_1G_2....G_k$. So we then have

$$n_{\text{qu}} + n_1 = n_{\text{add}} = \frac{P^{\text{SA}}_{\text{no input}}}{G}. \tag{3.22}$$

We typically measure the power spectrum over a small span with resolution bandwidth on the SA set to 1 Hz and a 1 Hz frequency spacing, so that the power spectrum is the same as the PSD. We can then directly convert this PSD which is in dBm/Hz to photons/Hz and also to an equivalent noise temperature.

We perform these gain and noise measurements for a range of pump powers and pump frequency close to the edge of the dispersive feature that marks the resonance of the resonance phase matching circuitry in the TWPA [52]. The surface plots of the average gain and average added noise of our amplifier chain at two discrete frequencies 5.7 and 5.8 GHz which lie in our cCPT tunable range are shown in Fig.(3.13). We perform a coarser scan of pump parameters before narrowing down to the range of pump parameters shown here, and finally settle upon a pump frequency of 6.767 GHz and a power setting of -2.25 dBm of a dedicated signal generator. The average gain G at this setting is 86 dB, and the mean added noise is $n_{\text{add}} = 4.67$ photons which is close to the quantum limit of phase-insensitive amplification of 1 photon [103]. This

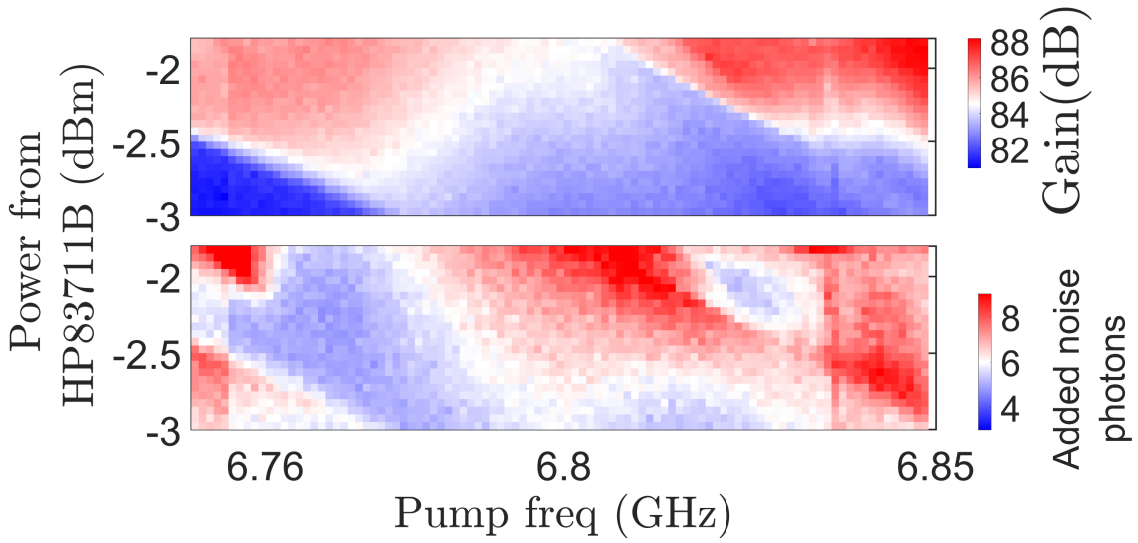

Figure 3.13: Gain and added noise of the amplifier as a function of the pump power and pump frequency to the first stage TWPA.

corresponds to a noise temperature of 1.2 K.

We note that as long as the TWPA gain is sufficient to justify the approximation in Eqn.(3.21), minimising the added noise n_{add} by the process described above is the primary indicator of high SNR as opposed to large gain as is some times mistakenly the goal.

3.3.5. Heterodyne measurement

Most modern digital instruments that are measuring an analog sinusoidal signal are doing some variation of the same thing. They have an analog-to-digital-converter (ADC) that samples the incoming sine wave several times during its period, creating a digital output value for each of those time points. They can then do all kinds of processing on this signal to obtain the required information. In the microwave band (5.8 GHz corresponds to a time period of 170 ps) that we are working in, however, modern electronics isn't fast enough to sample the waveform multiple times in a single period, and attempting to read out a 5.8 GHz waveform with a 1 GS/s device will

lead to severe aliasing. Most devices use an intermediate step where the sine wave of interest is mixed to a lower 'intermediate frequency (IF)' which can then be sampled multiple times per waveform. This is done with the use of a mixer, which in its essence is a diode with a nonlinear I-V relationship which gives rise to sum and difference frequencies of the frequencies input to it while working in the analog world. It uses a 'local oscillator' (LO) tone which is multiplied to the signal of interest, the RF. The difference is typically the IF, and the higher (sum) frequencies are filtered out before being sampled by the ADC. Such a process of mixing down to lower frequency and digitizing is known as a super-heterodyne measurement, homodyne when the mixing is down to the baseband.

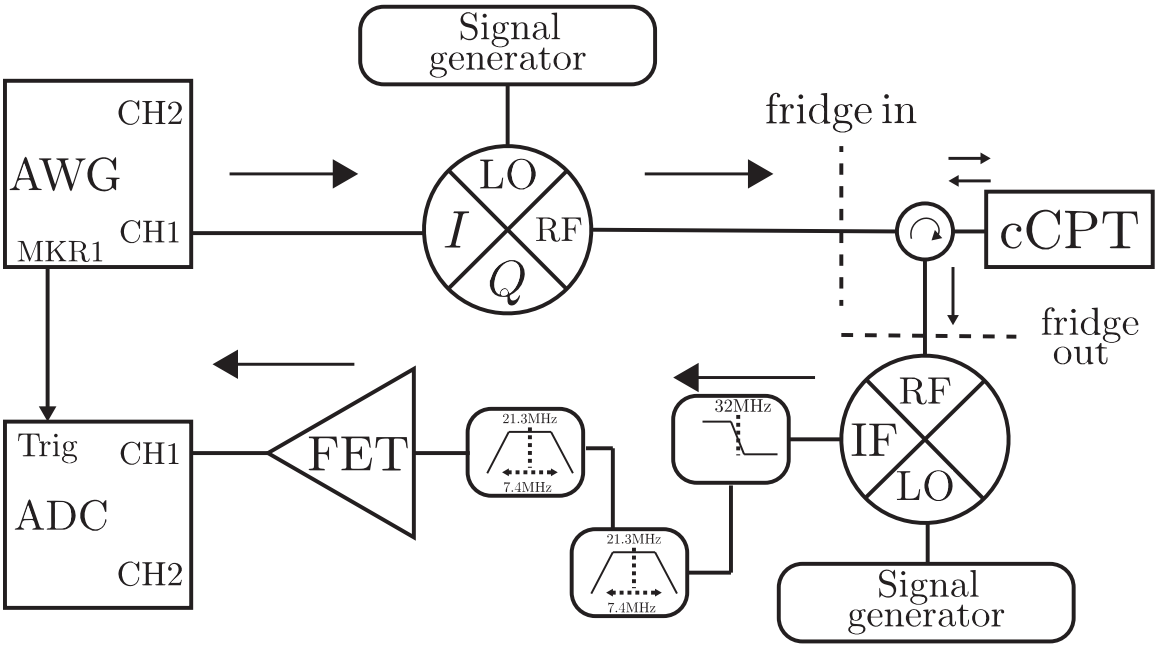

Figure 3.14: Schematic for a pulsed heterodyne measurement. The input stage consists of a mixer whose output can be shaped by the AWG. The output stage consists of a heterodyne measurement operating at an $\omega_{\mathrm{IF}}/2\pi = 21$ MHz.

The VNA and the SA mentioned previously at some level both work by mixing down the RF while ramping an LO across the desired span of the measurement. While the VNA is also capable of performing a heterodyne measurement at a given frequency

as a function of time, we are interested in performing these measurements using pulses whose amplitude envelope as well as frequency are shaped. We also need to perform measurements precisely triggered in time in order to match the phases across different pulse trains. For these reasons, we use the circuitry shown in Fig.(3.14).

Since the bandpass filters we use, as illustrated in Fig.(3.14) have a pass band between 19.6 and 23.4 MHz, we choose to work with an IF at 21 MHz on the output ($\omega_{\mathrm{IF}}^{(\mathrm{out})}$). Though people do work the AWG at baseband with just a modulation envelope which drives the input mixer in Fig.(3.14), this is susceptible to $1/f$ and other low frequency noise such as 60 cycle electrical line noise and so we choose to work with a carrier at $\omega_{\mathrm{IF}}^{(\mathrm{in})} = 84$ MHz instead (we explain this particular choice below, though this exact value drive frequency is not necessary when not performing waveform averaging). We do some times use frequency chirped waveforms to initiate the cCPT in a preferential oscillation state as we shall see in chapter 4, but our steady state drive at the end of the chirp ramp, which is when we actually perform any readout, corresponds to $\omega_{\mathrm{IF}}^{(\mathrm{in})} = 84$MHz on the AWG. We then set our input LO ($\omega_{\mathrm{LO}}^{(\mathrm{in})}$) 84 MHz red detuned to the desired driving frequency, $\omega_{\mathrm{RF}}^{(\mathrm{in})}$, and the right sideband of the mixing output falls at $\omega_{\mathrm{RF}}^{(\mathrm{in})}$. That is to say

$$\omega_{\mathrm{RF}}^{(\mathrm{in})} = \omega_{\mathrm{LO}}^{(\mathrm{in})} + \omega_{\mathrm{IF}}^{(\mathrm{in})}. \tag{3.23}$$

Similarly the output LO at $\omega_{\mathrm{LO}}^{(\mathrm{out})}$ is blue detuned from the drive frequency by $\omega_{(\mathrm{IF})}^{(\mathrm{out})} = 21$ MHz. We then have

$$\omega_{\mathrm{IF}}^{(\mathrm{out})} = \omega_{\mathrm{LO}}^{(\mathrm{out})} - \omega_{\mathrm{RF}}^{(\mathrm{out})} \tag{3.24}$$

where we note that $\omega_{\mathrm{RF}}^{(\mathrm{out})} = \omega_{\mathrm{RF}}^{(\mathrm{in})}$ since the cavity is driven and responds at the same frequency.

By placing the input and output LOs on opposite sides of the drive frequency ($\omega_{\mathrm{RF}}^{(\mathrm{in/out})}$) as in Fig.(3.15), we minimize the chance of a stray mixing product winding up in our output measurement bandwidth, and don't worry about suppressing or filtering the unwanted sideband of the input tone. Some setups also use the same LO for the input and the output side. Though this makes phase-locking easier, we would then have to ensure careful image rejection (or filter out the image, LO and the input IF). This is a valid concern for our cCPT sample since it operates in reflection mode, and any unwanted signals (such as the red sideband of the input mixing product) will be present in the output signal and contribute to $\omega_{\mathrm{IF}}^{(\mathrm{out})}$, but will carry no information about the cCPT dynamics. The sampling rate of the AWG is set at 840 MS/s, and that of the ADC at 168 MS/s which are multiples of 21 and 84, and ensure that we can perform waveform averaging since the ADC would then sample the same phase points on a continuous sinusoidal signal. This ensures that all relevant waveforms in our system will have the same relative phase (and will be sampled at least once, and often more) every $1/21 \times 10^6 = 47.62$ns which could be useful if performing waveform averaging. Whole number (in MHz) frequencies ensure that for an experiment repeat time that is a multiple of 1 μs every individual pulse will have the same phase at the start of each iteration of an experiment.

It is of paramount importance that both LOs are phase locked using a 10 MHz reference from a single signal generator that is distributed by an RF distribution amplifier. Another important idiosyncrasy of our setup is that the AlazarTech ATS 9462 ADC we use has a not-so-good phase locked loop. Feeding it a 10 MHz reference to lock to the other instruments caused discrete jumps in phase over time. The workaround to this was to feed it a fast 800 mVpp clock signal at the desired sampling frequency (168 MS/s) from a separate signal generator that was in turn phase locked using a 10 MHz reference to the LOs of the main setup.

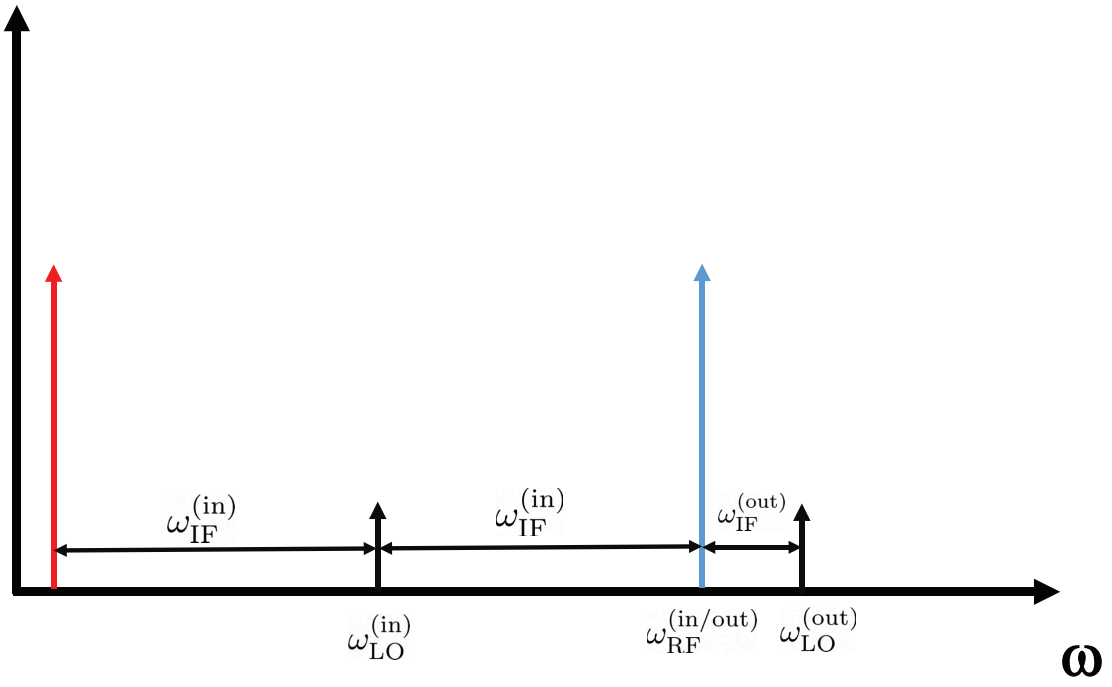

Figure 3.15: Illustration of the involved frequencies in our setup. The local oscillator tones are denote in black. The mixing products of the input tone are shown in red and blue.

The bottom line in a heterodyne measurement is to measure a time-varying signal which has been mixed down to a carrier frequency ω_{IF} so the signal is of the form

$$V(t) = A(t)\sin\left(\omega_{\mathrm{IF}}t + \phi(t)\right) \tag{3.25}$$

$$= I(t)\sin\left(\omega_{\mathrm{IF}}t\right) + Q(t)\cos\left(\omega_{\mathrm{IF}}t\right), \tag{3.26}$$

where $A(t) = \sqrt{I(t)^2 + Q(t)^2}$ and $\phi(t) = \tan^{-1}\left(\frac{I(t)}{Q(t)}\right)$.

The most common way to measure $I(t)$ and $Q(t)$ is to achieve the mixing down using an IQ mixer, which splits the incoming RF into two branches, each of which is mixed down using two branches of the same LO, one of which goes through a quadrature hybrid. The mixed output of each of these branches is then 90° out of phase with each other, and the two channels of the ADC together (or at some times in

the IF period just one of them while the other is 0) contain all the information about $I(t)$ and $Q(t)$ at any sampled time instant. So the bandwidth of the measurement is only constrained by the sampling rate (which is 168 MS/s for us). However, we choose not to use this technique because this requires good calibration to account for imbalances in the two arms of the mixer output. Instead we use what is described in [90] as 'digital heterodyning', which we now describe here.

As we saw earlier, after mixing down with a double-balanced mixer, we have Eqn.(3.25). In order to extract $A(t)$ and $\phi(t)$ or equivalently $I(t)$ and $Q(t)$, we digitally multiply $V(t)$ by $\cos\omega_{\rm IF}t$ and separately by $\sin\omega_{\rm IF}t$, and average each over a full IF period. We then have for the averaged quantities $\overline{I}(t)$ and $\overline{Q}(t)$,

$$\begin{aligned}\overline{I}(t) &= \frac{\omega_{\rm IF}}{2\pi}\int_t^{t+2\pi/\omega_{\rm IF}} d\tau A(\tau)\sin\big(\omega_{\rm IF}\tau+\phi(\tau)\big)\cos\omega_{\rm IF}\tau \\ &= \overline{A}(t)\sin\overline{\phi}(t), \qquad (3.27a)\\ \overline{Q}(t) &= \frac{\omega_{\rm IF}}{2\pi}\int_t^{t+2\pi/\omega_{\rm IF}} d\tau A(\tau)\sin\big(\omega_{\rm IF}\tau+\phi(\tau)\big)\sin\omega_{\rm IF}\tau \\ &= \overline{A}(t)\cos\overline{\phi}(t), \qquad (3.27b)\\ & \qquad (3.27c)\end{aligned}$$

where the over bar represents the average value over a single IF period. To obtain the amplitude and phase of the original signal $V(t)$, we then have $\overline{A}(t)=\sqrt{\overline{I}(t)^2+\overline{Q}(t)^2}$ and $\overline{\phi}(t)=\tan^{-1}\big(\overline{I}(t)/\overline{Q}(t)\big)$.

We see now that at the expense of not having to worry about mismatches between the two arms of an IQ setup, the digital homodyne technique is not sensitive to changes of $A(t)$ and $\phi(t)$ that happen faster than an IF period, i.e., in our case $\omega_{\rm IF}/2\pi = 21$ MHz sets the bandwidth of the measurement. In studying the cCPT sample, the fastest that information about changes in the cCPT can leak out of the microwave cavity is of the order of the cavity linewidth, which is bias point dependent

to a small degree [33], but of the order of 1.5 MHz. So we see that this bandwidth limiting property of the digital heterodyne technique is not really a constraint for us. We perform this averaging as a convolution of the measured voltage signal with a sine and a cosine wave respectively on Matlab.

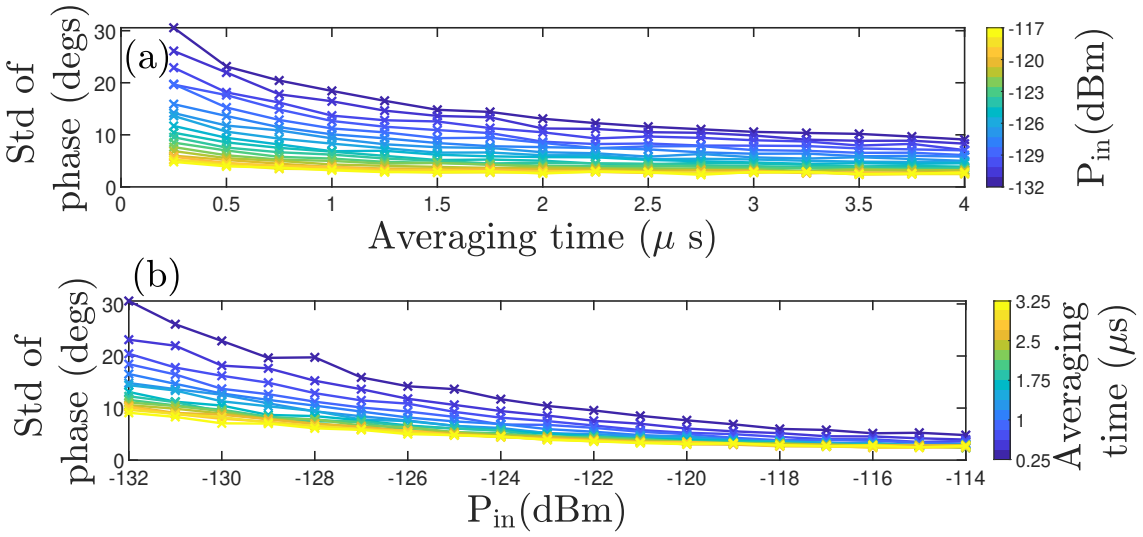

Figure 3.16: Standard deviation of the measured phase for the TWPA pump parameters in section 3.3.4 measured at an off-resonance point just outside the tunable range of the cCPT vs (a) averaging time for different input powers, (b) input power for different averaging times.

To see what kind of phases our setup can resolve, we now input an off-resonance continuous tone at a steady frequency to the cCPT and measure the reflected phase as a function of time. We expect to see a steady phase in the absence of noise, but for this real noisy system (dominated by amplifier noise, see section 3.3.4), we plot in Fig.(3.16) the standard deviation of the phase as a function of averaging time for different input powers, and as a function of input power for different averaging times. We see the expected $1/\sqrt{t}$ behaviour against averaging time. From the measured noise temperature in section 3.3.4, we can calculate the noise power in a bandwidth $B = 10$ MHz around the center of the bandpass filter in Fig.(3.14) using $P_{\text{noise}} = k_B B T_{\text{N}} \equiv -127.8$ dBm where $T_{\text{N}} = 1.2$ K is the noise temperature. We simulate a

pure sine signal at -128 dBm along with noise with a standard deviation of voltage given by 125.87 nVp $\equiv -128$ dBm, and we see a standard deviation in phase of 21.5°, which is for an averaging of $\approx$ 50ns corresponding to the IF period. We see in Fig.(3.16) that for -128 dBm and an averaging time of 250 ns, the measured standard deviation in the phase is 20°, which is in pretty close agreement (within factor of 2 of $\sqrt{\text{averaging time}}$) which inspires confidence in our noise temperature/added photon noise measurement.

Chapter 4

Charge sensing using the cCPT as a cavity Bifurcation Amplifier

In this chapter, we first derive the theory behind the classical dynamics of the cCPT as a Kerr cavity (section 2.5.2) when driven close to its resonant frequency with a drive strength that corresponds to several intracavity photons. In section 4.1, we will see how the cCPT response bifurcates into a bistable regime over a certain frequency range when driven at high enough drive powers and derive the conditions on the input drive tone as a function of the Kerr coefficient and the damping rates neccessary for bistability. We then introduce the idea behind using this bistability to perform sensitive threshold charge detection, similar to the threshold amplifier known as the Josephson bifurcation amplifier (JBA) [34, 35, 38, 39]. In section 4.1.1, we will then see that in the presence of fluctuations which cause spontaneous transitions between the two metstable states in the bistable region, the threshold for detection is broadened because of a non-zero probability of being found in either of the bistable states in a region around what would be the threshold for an ideal non-fluctuating system. This effectively decreases the sensitivity of the detector. We look at experimental data from the cCPT in section 4.2, where we see the first signs of bistability as hys-

teresis in section 4.2.1. In section 4.2.2, we study the populations of the metastable states as a function of a range of relevant parameters, and finally demonstrate resolving two charge states separated by $0.09e$ in a single-shot readout with an input drive corresponding to < 25 intracavity photons with a fidelity of 94%.

Section 4.1

Kerr cavity theory

We begin by rewriting the Hamiltonian of the cCPT retaining non-linear terms to the Duffing order as in section 2.5.2. Applying the RWA for drive tones close to the linear cavity resonance as before, we have

$$H = \hbar\omega_0 a^\dagger a + \frac{1}{2}\hbar K a^{\dagger 2} a^2 \tag{4.1}$$

$$= \hbar(\omega_0 + \frac{K}{2}a^\dagger a)a^\dagger a - \frac{1}{2}\hbar K a^\dagger a \tag{4.2}$$

$$\approx \hbar(\omega_0 + \frac{K}{2}a^\dagger a)a^\dagger a, \tag{4.3}$$

where ω_o is the bias point-dependent resonant frequency, K is the strength of the Kerr term at the bias point, and we neglect the last term in the Hamiltonian because $K < \kappa_{\text{tot}}$ and $K \ll \omega_0$ for our cCPT system across all gate and flux biases.

Writing down the quantum Langevin equation for this Hamiltonian, we get

$$\begin{aligned}\dot{a} &= \frac{1}{i\hbar}\big[a, H\big] - \big[a, a^\dagger\big]\big[\frac{\kappa_{\text{tot}}}{2}a - \sqrt{\kappa_{\text{ext}}}a_{\text{in}}(t) - \sqrt{\kappa_{\text{int}}}b_{\text{in}}(t)\big] \\ &= -\big[i(\omega_0 + Ka^\dagger a\big) + \frac{\kappa_{\text{tot}}}{2}\big]a + \sqrt{\kappa_{\text{ext}}}a_{\text{in}}(t) + \sqrt{\kappa_{\text{int}}}b_{\text{in}}(t),\end{aligned} \tag{4.4}$$

and

$$\dot{a}^\dagger = \frac{1}{i\hbar}\big[a^\dagger, H\big] + \big[\frac{\kappa_{\text{tot}}}{2}a^\dagger - \sqrt{\kappa_{\text{ext}}}a^\dagger_{\text{in}}(t) - \sqrt{\kappa_{\text{int}}}b^\dagger_{\text{in}}(t)\big]\big[a^\dagger, a\big]$$

$$= \big[i(\omega_0 + Ka^\dagger a) - \frac{\kappa_{\text{tot}}}{2}\big]a^\dagger + \sqrt{\kappa_{\text{ext}}}a_{\text{in}}^\dagger(t) + \sqrt{\kappa_{\text{int}}}b_{\text{in}}^\dagger(t), \tag{4.5}$$

where κ_{ext} is the external damping rate because of the coupling to the probe transmission line with the corresponding input bath operator $a_{\text{in}}(t)$, and κ_{int} is the internal damping rate because of the coupling of the resonator to an internal loss channel (typically a thermal bath) with corresponding input operator $b_{\text{in}}(t)$. The total damping rate of the cavity is $\kappa_{\text{tot}} = \kappa_{\text{ext}} + \kappa_{\text{int}}$.

Since the input tone is a pure sine wave at frequency ω_d of the form $a_{\text{in}} = \alpha_{\text{in}}e^{-i\omega_d t}$ we expect the steady state response of the cavity to be at this drive frequency. We thus make the ansatz $a = \alpha e^{-i\omega_d t}$, $\dot{a} = -i\omega_d \alpha e^{-i\omega_d t}$ and the average cavity occupation $n = |\alpha|^2 = a^\dagger a$. Plugging this ansatz into Eqn.(4.4) we obtain

$$\big[-i(\Delta - K|\alpha|^2) + \frac{\kappa_{\text{tot}}}{2}\big]\alpha = \sqrt{\kappa_{\text{ext}}}\alpha_{\text{in}},$$

and,

$$\big[i(\Delta - K|\alpha|^2) + \frac{\kappa_{\text{tot}}}{2}\big]\alpha^* = \sqrt{\kappa_{\text{ext}}}\alpha_{\text{in}}^*, \tag{4.6}$$

where we have defined the detuning $\Delta = \omega_d - \omega_0$

We can now use Eqn.(4.6) and the input-output relation $a_{\text{out}}(t) = a_{\text{in}}(t) - \sqrt{\kappa_{\text{ext}}}a(t)$ [74], [75] to find the reflection coefficient $S_{11}(\Delta)$ (as in section 2.3.1) to be

$$\begin{aligned} S_{11}(\Delta) &= \big(\frac{\alpha_{\text{out}}}{\alpha_{\text{in}}}\big)^* \\ &= \frac{(\Delta - K|\alpha|^2) - i(\kappa_{\text{int}} - \kappa_{\text{ext}})/2}{(\Delta - K|\alpha|^2) - i(\kappa_{\text{int}} + \kappa_{\text{ext}})/2}. \end{aligned} \tag{4.7}$$

We see that this is the exact same form as the reflection coefficient for a linear cavity as in Eqn. 2.72, with the detuning $\Delta \to \Delta - Kn$.

Multiplying the two equations in (4.6), we get a cubic equation in n

$$K^2n^3 - 2K\Delta n^2 + \left(\Delta^2 + \frac{\kappa_{\text{tot}}^2}{4}\right)n = \kappa_{\text{ext}}\frac{P_{\text{in}}}{\hbar\omega_d}, \tag{4.8}$$

where $P_{\text{in}} = n_{\text{in}}\hbar\omega_d$ and $n_{\text{in}} = |\alpha_{\text{in}}|^2$.

Solving this cubic for n and plugging those solutions into Eqn. (4.6), we can write the intracavity field in the form $\alpha = |\alpha|e^{i\phi_\alpha}$, where $|\alpha| = \sqrt{n}$ and $\phi_\alpha = \text{atan2}(\Delta - Kn, \frac{\kappa_{\text{tot}}}{2})$, and plugging n into Eqn.(4.7), we obtain the output amplitude and phase response of the cavity to a given drive.

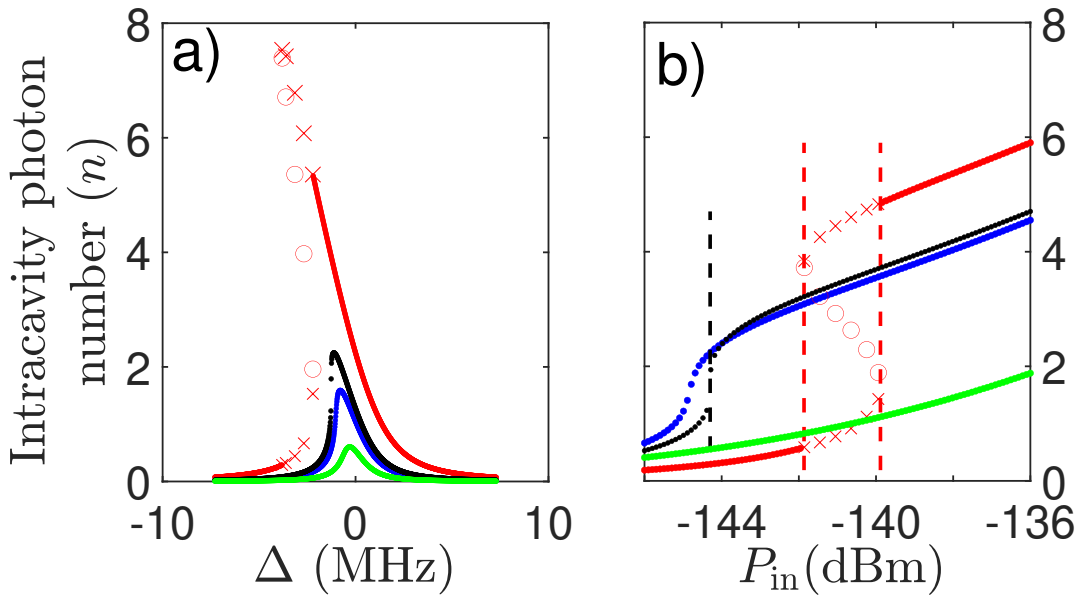

Figure 4.1: (a) Oscillation amplitude as a function of detuning for different input drive powers. The green markers are for an essentially linear cavity with $P_{\text{in}} \ll P_{in_c}$ (see Eqn. (4.13)), blue markers are when driven with a $P_{\text{in}} < P_{in_c}$, the black is when $P_{\text{in}} = P_{in_c}$ and the red is when $P_{\text{in}} > P_{in_c}$. (b) Oscillation amplitude as a function of input power for different detunings. The green markers are for $\Delta > 0$, the blue markers are when $\Delta_c < \Delta < 0$ (see Eqn. (4.12), the black markers are for $\Delta = \Delta_c$ and the red markers are for $\Delta < \Delta_c$. The dots represent monostable solutions, the crosses - bistable solutions, and the unfilled circles represent unstable solutions in both plots. These values are simulated for $K = -0.46$ MHz which occurs at $(n_g, \Phi_{\text{ext}}) = (0, 0)$. $\kappa_{\text{ext}} = 1.23$ MHz, $\kappa_{\text{int}} = 0.23$ MHz and $\omega_0 = 5.7851$ GHz at this bias point.

In the presence of the Kerr non-linearity, the system can exhibit different types of oscillation behaviours as the drive power P_{in} and the detuning Δ are varied. At small drive strengths, when the effect of the non-linearity is small, we see only a monostable oscillation amplitude as for a linear oscillator. As the drive strength is increased, for a certain range of detunings, we see this stable oscillation state bifurcate into two stable higher and lower oscillation states along with an unstable state that is not experimentally observed. The system has bifurcated into a bistable regime (Fig. 4.1). The onset of bistability is marked by the slope of the n vs Δ curve becoming vertical at some value of detuning (black curve in Fig. 4.1a). i.e, $\frac{dn}{d\Delta} = \infty$ for some Δ.

Differentiating Eqn. (4.8) w.r.t n, and setting $\frac{d\Delta}{dn}\big|_{n_c} = 0$, we have

$$3K^2n_c^2 - 4K\Delta n_c - 2Kn_c^2 \left.\frac{d\Delta}{dn}\right|_{n_c} + \Delta^2 + \frac{\kappa_{\text{tot}}^2}{4} + 2\Delta n_c \left.\frac{d\Delta}{dn}\right|_{n_c} = 0 \tag{4.9}$$

$$\implies 3K^2n_c^2 - 4K\Delta n_c + \left(\Delta^2 + \frac{\kappa_{\text{tot}}^2}{4}\right) = 0, \tag{4.10}$$

where n_c is the oscillation number at the onset of bifurcation. Solving this quadratic equation, Eqn. (4.10), we solve for the critical oscillation number obtaining

$$n_c = \frac{2\Delta}{3K}\left(1 \pm \frac{1}{2}\sqrt{1 - \frac{3\kappa_{\text{tot}}^2}{4\Delta^2}}\right). \tag{4.11}$$

This yields real, positive solutions when

$$\begin{aligned} &\Delta < -\frac{\sqrt{3}}{2}\kappa_{\text{tot}} \;\forall\; K < 0, \\ &\Delta > \frac{\sqrt{3}}{2}\kappa_{\text{tot}} \;\forall\; K > 0. \end{aligned} \tag{4.12}$$

To achieve bifurcation at exactly this critical detuning $\Delta_c = \text{sgn}(K)\frac{\sqrt{3}}{2}\kappa_{\text{tot}}$, we see from Eqn. (4.11) that we need a critical cavity occupation number $n_c = \frac{1}{\sqrt{3}}\frac{\kappa_{\text{tot}}}{K}$.

Using these in (4.8), we obtain a critical drive power $P_{\mathrm{in_c}}$. When the cavity is driven by a tone at $\omega_{d_c} = \omega_0 + \Delta_c$ with amplitude exactly $P_{\mathrm{in_c}}$, we see the onset of bistability, where

$$P_{\mathrm{in_c}} = \frac{\sqrt{3}}{9} \frac{\kappa_{\mathrm{tot}}^3}{|K|\kappa_{\mathrm{ext}}} \hbar\omega_{d_c}. \tag{4.13}$$

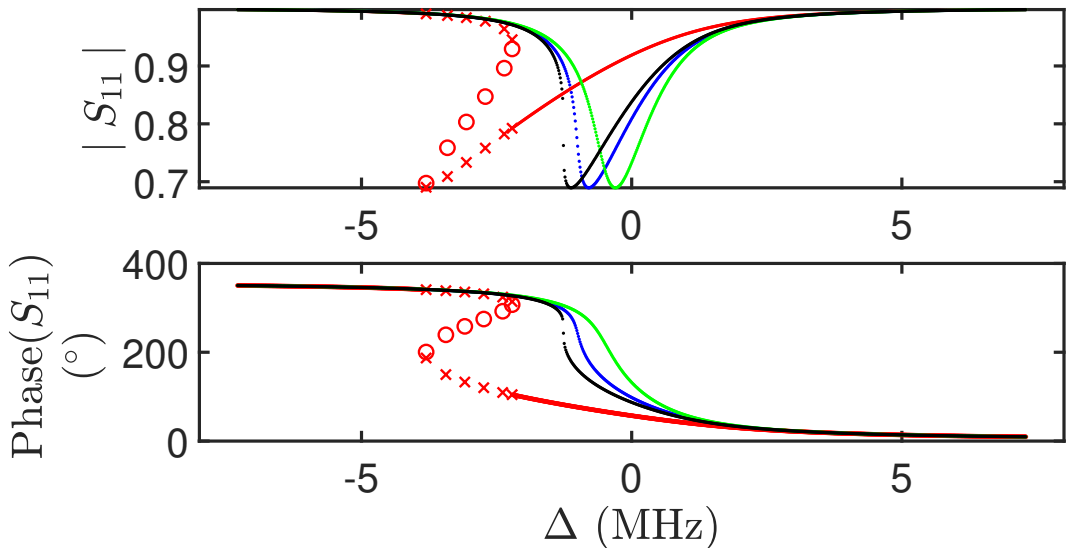

Figure 4.2: Simulated S_{11} as a function of detuning for different input drive powers. The green markers are for an essentially linear cavity with $P_{\mathrm{in}} \ll P_{in_c}$ (see Eqn. (4.13)), blue markers are when driven with a $P_{\mathrm{in}} < P_{in_c}$, the black is when $P_{\mathrm{in}} = P_{in_c}$ and the red is when $P_{\mathrm{in}} > P_{in_c}$. The dots represent monostable solutions, the crosses - bistable solutions, and the unfilled circles represent unstable solutions. These values are simulated for $K = -0.46$ MHz which occurs at $(n_g, \Phi_{\mathrm{ext}}) = (0, 0)$. $\kappa_{\mathrm{ext}} = 1.23$ MHz, $\kappa_{\mathrm{int}} = 0.23$ MHz and $\omega_0 = 5.7851$ GHz at this bias point.

Figs.(4.2) and (4.3), simulated using Eqn.(4.7), show the variation of the reflection coefficient (S_{11}) with detuning and drive power respectively. We clearly see the jump phenomenon in Fig.(4.2). As the detuning is ramped from a value far red-detuned from the linear resonance, S_{11} follows the value corresponding to the monostable solution. Even after the lower bifurcation detuning value at which we first expect to see bistability, it stays on the same branch of the S_{11} corresponding to the low amplitude oscillation state until it reaches the value of the detuning where the second bifurcation occurs. As the detuning is increased past this value, S_{11} has to jump

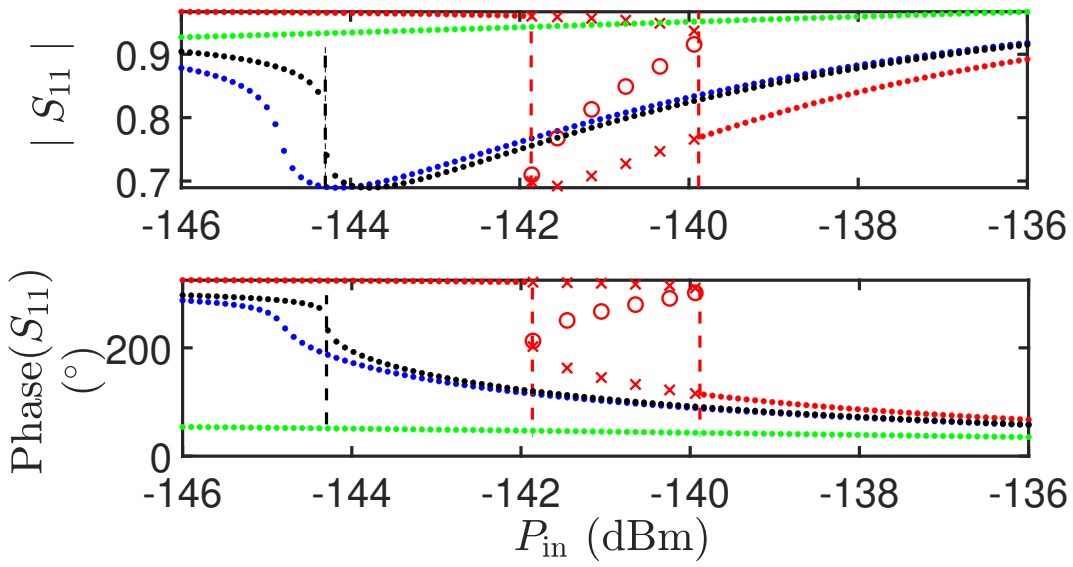

Figure 4.3: Simulated S_{11} as a function of input power for different detunings. The green markers are for a detuning $\Delta > 0$, blue markers are when driven at a detuning $\Delta_c < \Delta < 0$, the black is when $\Delta = \Delta_c$ and the red is when $\Delta < \Delta_c$. The dots represent monostable solutions, the crosses - bistable solutions, and the unfilled circles represent unstable solutions. The dashed lines represent the input powers at the onset of bistability, calculated from Eqn. (4.15). These plots are simulated for $K = -0.46\,\text{MHz}$ which occurs at $(n_g, \Phi_{\text{ext}}) = (0, 0)$. $\kappa_{\text{ext}} = 1.23\,\text{MHz}$, $\kappa_{\text{int}} = 0.23\,\text{MHz}$ and $\omega_0 = 5.7851\,\text{GHz}$ at this bias point.

abruptly to the monostable value on the other side of this upper bifurcation. When the detuning is ramped in the other direction, the S_{11} stays on the branch corresponding to the high amplitude oscillation state, past the upper bifurcation, until it reaches the detuning value at the lower bifurcation. It must then jump abruptly and proceed along the monostable branch of the S_{11} at lower values. This gives rise to a marked hysteresis in the S_{11} curves depending on which way the detuning is ramped as seen in Fig. (4.4). A similar jump phenomenon (Fig. 4.3) and hysteresis is observed as P_{in} is ramped in each direction, as seen in Fig. (4.5).

This sudden jump at the input power bifurcation forms the basis for the operation of the Josephson Bifurcation Amplifier (JBA) [34]. The sensitivity of an amplifier to a change in the drive power is the slope of the phase-input power curve at any point.

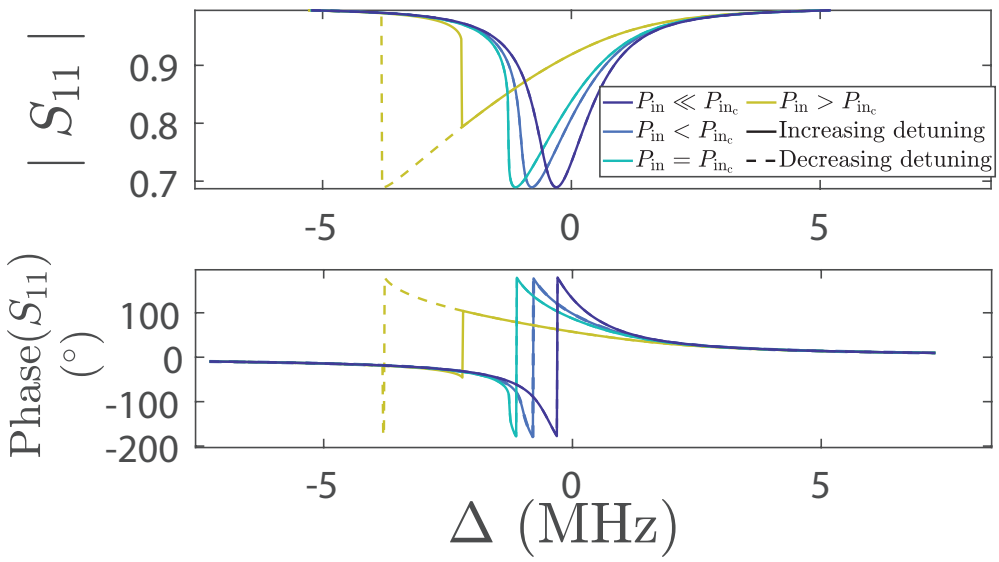

Figure 4.4: Simulated hysteresis in S_{11} as a function of detuning for different input drive powers. Solid traces represent a ramp that sweeps towards increasing detunings, and the dashed ramp toward decreasing detunings. The dashed and solid overlap for $P_{\text{in}} \leq P_{in_c}$. These values are simulated for $K = -0.46\,\text{MHz}$ which occurs at $(n_g, \Phi_{\text{ext}}) = (0, 0)$. $\kappa_{\text{ext}} = 1.23\,\text{MHz}$, $\kappa_{\text{int}} = 0.23\,\text{MHz}$ and $\omega_0 = 5.7851\,\text{GHz}$ at this bias point.

When there is only monostable behaviour, we see that the phase is a linear function of the input power for small variations about any input power bias point. However, by carefully biasing the JBA right at a drive power bifurcation edge, a very small change in the drive power leads to a large shift in the phase response of the amplifier. Monitoring the output phase, we thus have a sensitive measure of very small variations in the input power/current.

In order to find the extent of the bistability region as a function of the input drive strength (for a given detuning Δ), we find the bifurcation points $P_{in_{b_1}}$ and $P_{in_{b_2}}$ where $\frac{dn}{dP_{\text{in}}}\Big|_{P_{in_{b_1}}, P_{in_{b_2}}} = \infty$. Between these points, we expect to see bistability. We thus differentiate Eqn. (4.8) with respect to n and set $\frac{dP_{\text{in}}}{dn}\Big|_{P_{in_{b_1}}, P_{in_{b_2}}} = 0$ yielding

$$n_{P_{in_{b_1}}, P_{in_{b_2}}} = \frac{2}{3}\frac{\Delta}{K}\left[1 \pm \frac{1}{2}\sqrt{(1 - \frac{3\kappa_{\text{tot}}^2}{4\Delta^2})}\right], \tag{4.14}$$

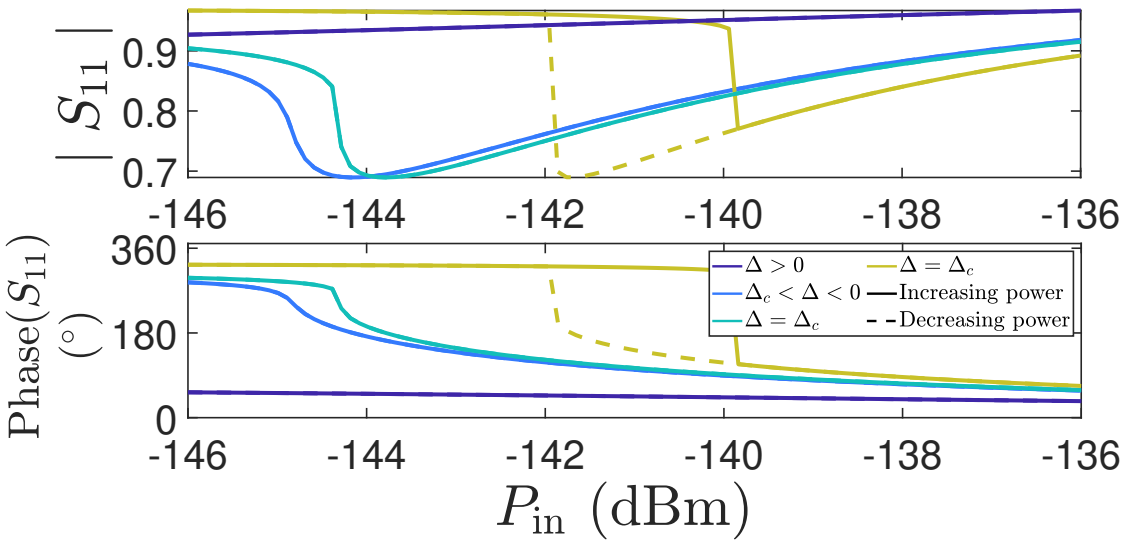

Figure 4.5: Simulated hysteresis in S_{11} as a function of drive power for different detunings. The solid traces represent an increase in drive power with time, and the dashed traces represent a decrease in drive power with time. The dashed and solid curves overlap for $\Delta \geq \Delta_c$. These values are simulated for $K = -0.46$ MHz which occurs at $(n_g, \Phi_{\text{ext}}) = (0, 0)$. $\kappa_{\text{ext}} = 1.23$ MHz, $\kappa_{\text{int}} = 0.23$ MHz and $\omega_0 = 5.7851$ GHz at this bias point.

which is the same as Eqn.(4.11). Using these solutions in Eqn. (4.8), we find the bifurcation points to be

$$P_{\text{in}_{b_1}}, P_{\text{in}_{b_2}} = \frac{2}{27}\frac{\Delta^3}{K}\left[\left(1 + \frac{9\kappa_{\text{tot}}^2}{4\Delta^2}\right) \mp \left(1 - \frac{3\kappa_{\text{tot}}^2}{4\Delta^2}\right)^{3/2}\right]\frac{\hbar\omega_d}{\kappa_{\text{ext}}}, \tag{4.15}$$

which corresponds to Eqn. (2.13) in [51].

Fig.(4.6) shows the variation of the bifurcation powers with detuning for the cCPT biased at $(n_g, \Phi_{\text{ext}}) = (0, 0)$. The point in the $\Delta - P_{\text{in}}$ space where the blue and red curve come together is a singular point, the spinode point [111]. Between the two solid lines, the system is in a bistable state, with transitions between the two states becoming more likely close to the spinode point in analogy to the critical point of a gas-liquid phase transition [111].

Charge sensing using the Kerr cCPT

We envision a charge sensing scheme similar to the power/current readout of the JBA. At a certain drive power, by biasing the cCPT at the edge of a bifurcation in detuning, the output phase should be very sensitive to small changes in the detuning and hence the resonant frequency of the cCPT. This resonant frequency of the cCPT is itself a pretty sensitive function of the gate charge (n_g) of the cCPT [33]. This is illustrated in Fig. (4.7). The blue and red curves represent two different gate cCPT gate points separated by δn_g. This corresponds to a resonant frequency shift $\delta\omega_0$. The dashed line represents the simulated linear reflection coefficient as in Eqn.(2.72), while the solid lines correspond to the Kerr reflection coefficient in Eqn.(4.7). We see that the difference in the phase of the S_{11} ($\delta S_{11}^{(\mathrm{kerr})}$) between the red and the blue solid lines for a drive at a frequency denoted by the black dashed line is much larger than that for the linear curves ($\delta S_{11}^{(\mathrm{lin})}$) for the same separation $\delta\omega_0$. Conversely, by reducing δn_g and bringing the red and blue curves closer together, we still expect to

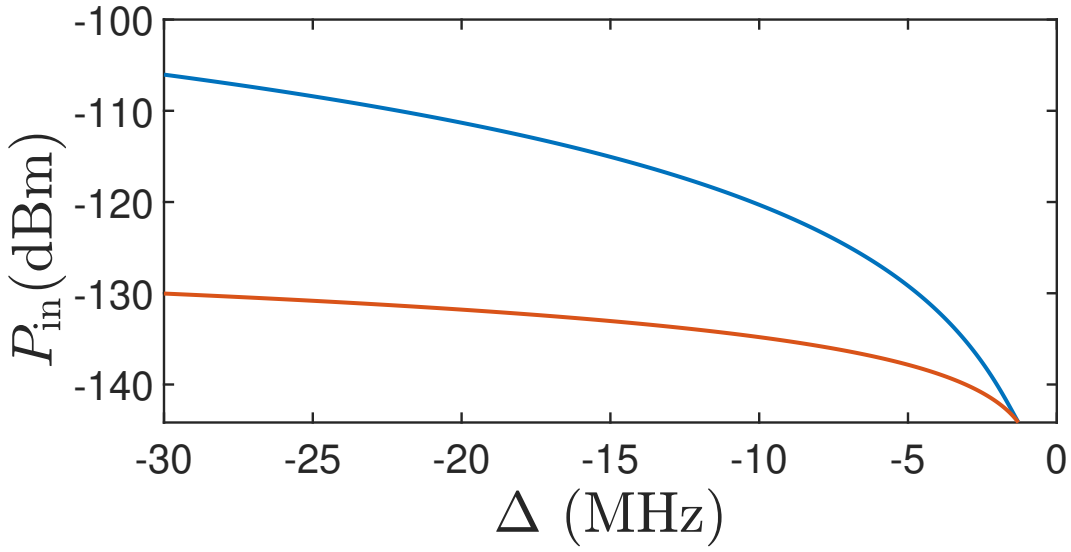

Figure 4.6: Variation of input power at the plane of the sample required for the onset of bifurcation vs detuning. The red (blue) corresponds to the lower (upper) bifurcation point for $K = -0.46\,\mathrm{MHz}$ which occurs at $(n_g, \Phi_{\mathrm{ext}}) = (0, 0)$. $\kappa_{\mathrm{ext}} = 1.23\,\mathrm{MHz}$, $\kappa_{\mathrm{int}} = 0.23\,\mathrm{MHz}$ and $\omega_0 = 5.7851\,\mathrm{GHz}$ at this bias point.

see a considerably large $\delta S_{11}^{(\mathrm{kerr})}$ while $\delta S_{11}^{(\mathrm{lin})}$ shrinks linearly. For a given δS_{11} we can measure, set by the SNR of the system, we see that the Kerr cavity should be able to resolve much smaller values of δn_g. Confounding factors for such a measurement would be : i) the spontaneous hopping between the metastable high and low amplitude states of the cCPT when in a bistable regime as modelled in [51, 112] (section 4.1.1). This can be circumvented by instead measuring the 'S-curves' which are a plot of the probability of being in the low amplitude state as a function of the detuning. The metric for charge sensitivity then becomes the smallest gate charge that causes a perceptible shift in the S-curves, yielding a high contrast between the S-curves for two gate charges separated by δn_g driven at a particular drive frequency ω_d. We note here that a high contrast might still mean poor single-shot readout fidelity because of the lack of separation between the phases of the metastable oscillation states, due to poor SNR. ii) resonant frequency fluctuations as reported in [33]. These could cause the resonant frequency to spontaneously shift due to fluctuations in the charge or flux environment on the cCPT chip, or due to quantum fluctuations in photon number. This can be imagined as causing each S-curve to have an additional finite, non-zero width which is a function of σ_{ω_0} (see Eqn.3.7), and the minimum perceptible change between two S-curves has to be larger than the combined widths of the two. We will see in section 4.2 that the widths of the S-curves we see in the cCPT is typically much larger than the scale of reported frequency fluctuations for the same device, meaning frequency fluctuations are probably not a huge problem. The width of the S-curve is dictated by the energy landscape (in the classical picture) of the oscillator and the effective temperature of the fluctuations (quantum or thermal) that drive them as we shall see in section 4.1.1.

4.1.1. Metastable oscillation states

Switching between metastable states of a nonlinear oscillator near a bifurcation has been the study of much theoretical work since the last decades of the 20th century. In the bistable regime (see Eqn. (4.8)), the two stable solutions form nodes in phase space, and the unstable solution is a saddle-point. In the absence of any fluctuations (or rather small fluctuations), the system spends most of its time around either of the stable nodes. An infrequent large fluctuation drives the oscillator close to the saddle point. Once in the vicinity of the saddle point, the oscillator then moves to the other focus along a 'downhill' trajectory. This complete trajectory forms the 'most probable switching path' [113], [114].

For a system at thermal equilibrium and weakly coupled to a bath, the switching rate out of a stable state takes the form of an activation over an energy barrier and

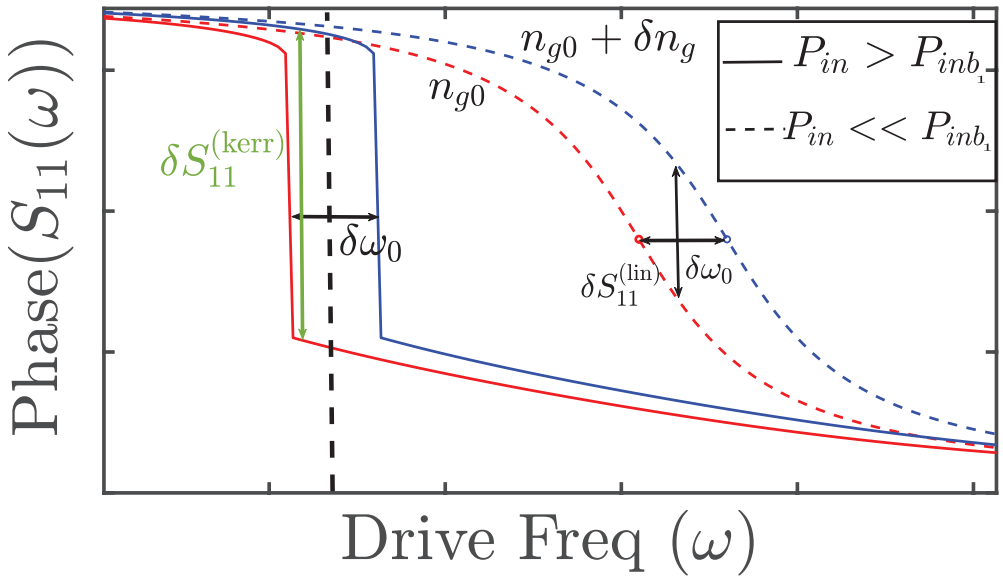

Figure 4.7: Simulated plot of the Phase(S_{11}) vs drive frequency for the case of a Kerr cavity above (solid lines) and well below (dashed lines) the critical power P_{inb_1}. The red and the blue curves represent two different gate biases of the cCPT separated by δn_g which produces a resonant frequency difference of $\delta\omega_0$.

follows Arrhenius' law [115] - the switching rate goes as the exponent of the ratio of the barrier height to the noise (in this case the Boltzmann temperature of the bath). The system we describe above is not in equilibrium because of the periodic drive and cannot be described using a free energy barrier. However, using a variety of methods, [113, 111, 116, 117, 112] show that close to a bifurcation in the presence of Gaussian noise, the switching can still be treated as an activation over a barrier in what is termed 'quantum activation' as opposed to tunneling through the barrier. The escape rate W is given by (chapter 3 in [118])

$$W = W_0 e^{-E_a/I_N^{\text{int}}}, \tag{4.16}$$

where E_a is the barrier height, I_N^{int} is the intrinsic noise intensity, and W_0 is an attempt frequency that also depends on the drive parameters.

Close to the bifurcation point, the motion can be split into fast and slow variables, and under the adiabatic approximation this reduces the 2D system of equations (4.4) and (4.5) to a Langevin equation for a particle in a cubic potential [111, 51]. The minimum of this cubic potential corresponds to the metastable node out of which the oscillator is escaping, and the maximum corresponds to the saddle node. It is apparent that since the curvature of the potential at these points is opposite, as we approach the bifurcation point, this node and the saddle point move towards each other and the potential along the axis connecting these points becomes locally flat. This slows the dynamics of the particle, yielding an overdamped mode. Even in the region close to a bifurcation point, the effect of the 'ghost' of this saddle node leads to slowed-down dynamics [119].

It is shown that at a parameter distance η from a bifurcation point (our parameter can be either the detuning, Δ or the drive strength, P_{in}), the height of the barrier goes as $E_a = k|\eta|^{3/2}$ for some constant k [111], [116], [118]. This scaling is independent of

the system and only depends on the type of bifurcation that occurs. In our case, a saddle-node bifurcation yields a critical exponent $\psi = 3/2$. It was then shown that even further away from $\eta = 0$, though the motion becomes underdamped, the critical exponent $\psi = 3/2$ persists around one of the bifurcation points, with $\psi = 1$ at the other bifurcation point, resulting in a scaling crossover.

In the absence of any additional noise sources, for thermal activation, $I_N^{\text{int}} = k_B T$ when $k_B T > \hbar\omega_0$ (classical, thermal limit) and $I_N^{\text{int}} = \hbar\omega_0$ when $k_B T < \hbar\omega_0$ (quantum limit). Even at T $\rightarrow$ 0, the predominant switching mechanism is quantum activation [112] which is a diffusion over a quasienergy barrier which is more probable than quantum tunneling. The critical exponent remains $\psi = 3/2$ for this mechanism.

This semiclassical quantum activation theory works well for the weak nonlinear regime, where $K \ll \kappa_{\text{tot}}$ which is where most JBAs operate [34, 38]. At $K > \kappa_{\text{tot}}$, the system enters the transmon regime [37] a single intracavity photon shifts the resonant frequency of the cavity to the point where another incoming photon at the same frequency sees the cavity well detuned and cannot enter it until the previous photon has decayed out - the photon blockade effect. This is now effectively a two-level system. In this regime, the oscillator shows no bistability or hysteresis. More recently, [36] showed that for the intermediate 'mesoscopic' regime between these two extreme values for the Kerr is poorly understood, and that the above semiclassical description might not be sufficient to model the switching rates for Kerr nonlinearities in this regime, requiring full quantum master-equation calculations to model the switching which might now be dominated by processes such as quantum tunneling. Ref. [53] recently reported on a device in which the Kerr strength could be tuned from the classical Duffing regime to the Kerr parametric oscillator.

The cCPT lies in a regime where $K/\kappa_{\text{tot}} \sim 0.07$- 0.5, and if the relevant damping rate is just that of the internal channel as in [36], $K/\kappa_{\text{int}} \sim 0.25$ - 2. Quantum effects

might well be important to understand the switching behaviour of the system. We did not perform any quantum analysis of the system here, but point out discrepancies we see in the behaviour of the cCPT as possibly arising from requiring a quantum model.

Section 4.2

Experiments

Our experimental procedure remains similar to our studies for a linear cavity [33]. We send in a probe tone to the sample and collect the reflected, amplified output. The most straightforward experiment is to use a vector network analyzer (VNA) to probe the $S_{11}(\omega)$ of the cCPT as a function of input power. Such a scan for the cCPT biased at $(n_g, \Phi_{\text{ext}}) = (0, 0)$ is shown in Fig. (4.8). The minimum of the reflection coefficient S_{11} follows a logarithmic curve as a function of the logarithmic power scale. This is the linear dependence of resonant frequency on input power (plotted here in dBm) described in section 3.3.3.

In order to observe hysteresis, we set up the VNA to scan forward in frequency and then in the reverse direction and plot the result in Fig. (4.9). At low powers (bluer curves), we are close to the bifurcation edge, and the hysteresis is not very remarkable. At higher powers this becomes more apparent, but is in general a weighted averaged value of the S_{11} corresponding to the two metastable oscillation states due to switching events during the measurement.

To carefully understand and account for the switching between the two metastable states, we use a heterodyne measurement setup to monitor the phase of the output signal at a rate higher than typical switching rates in these systems. As depicted in Fig. (3.14), the generation of the probe tone is slightly modified to facilitate some of the experiments detailed below. We want to be able to probe the sample with

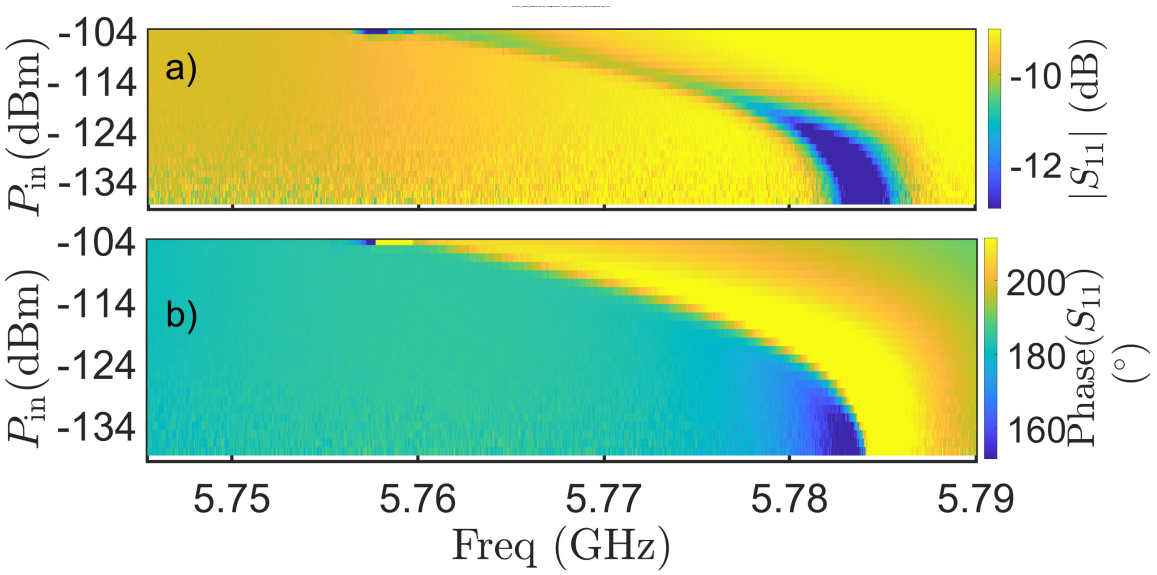

Figure 4.8: $S_{11}(\omega)$ of cCPT measured by a VNA for different input powers at the sample. cCPT biased at $(n_g, \Phi_{\text{ext}}) = (0, 0)$ for which the linear resonance $\omega_0(n_g, \Phi_{\text{ext}}) = 5.7851$ GHz. The dip in the $|S_{11}|$ (bluer hues) and the corresponding transition of the phase as a function of the drive frequency represent the resonant frequency of the oscillator.

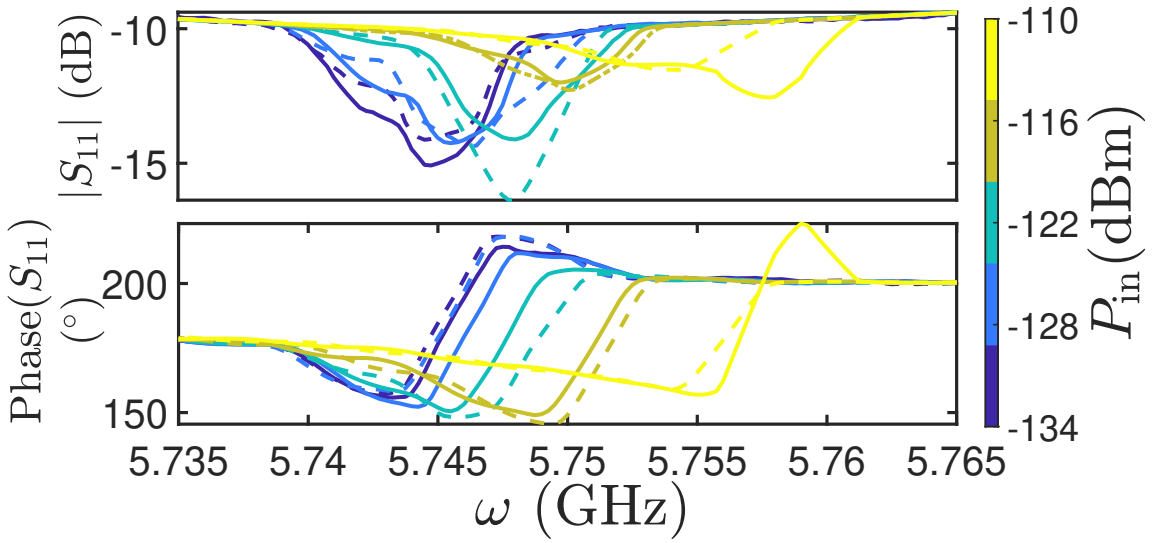

Figure 4.9: $S_{11}(\omega)$ of cCPT measured by a VNA while scanning forward (solid line), and backward (dashed line) in frequency. Input powers of -134, -128, -122, -116, -110 dBm from blue to red curves.

shaped pulses - shaped in terms of both the amplitude of the pulse as a function of time as well as its frequency. Using the AWG, we can design frequency ramps

with both increasing and decreasing frequencies (and powers), but we always use a frequency of 84 MHz for the readout section of the pulse. We then mix this with a local oscillator tone which is 84MHz red detuned from the desired readout detuning, ω_d. The desired pulse is then put into the cCPT, and the reflected signal is mixed down to an IF frequency, $\omega_{\text{IF}} = 21$ MHz. This signal is filtered by a low pass filter, a band pass filter, digitized at a sample rate of 168 MHz using an AlazarTech ATS 9462 and the amplitude and phase of the signal are extracted based on the 'digital homodyne technique' described in section 3.3.5. An AWG marker is used to trigger the digitizer at the start of the readout phase of the pulse.

The shaped pulses let us initiate the experiment in the low or high amplitude oscillation state as desired. Looking at Fig. (4.1a), we see that when we begin at a positive detuning and use a negative ramp to shift the drive frequency into the negative detuning bifrucation regime (as in the red curve when $P_{\text{in}} > P_{in_c}$), the cCPT remains in the high amplitude state until the lower bifurcation point. Similarly, if we started at a large negative detuning and ramped the detuning upwards, it would stay in the low amplitude state until the upper bifurcation point (this is assuming no fluctuations that drive a transition from one metastable state to another). A similar deterministic control on the oscillator state can be achieved using a positive or negative power ramp as is clear from Fig. (4.1b).

4.2.1. Hysteresis

In order to observe the hysteresis in the reflection coefficient as we ramp the input power one way or the other, we design a pulse as pictured in Fig. (4.10). The input tone at the cCPT is a sine wave at the desired detuning whose voltage is linearly ramped from 0 to the desired max value in a time t_r and then ramped back down to 0 in the same time. This pulse repeats every $t_{\text{down}} = 10\,\mu$s. The digitizer samples the output over the $2t_r$ period when the input drive is non-zero and extracts $|S_{11}|$ and

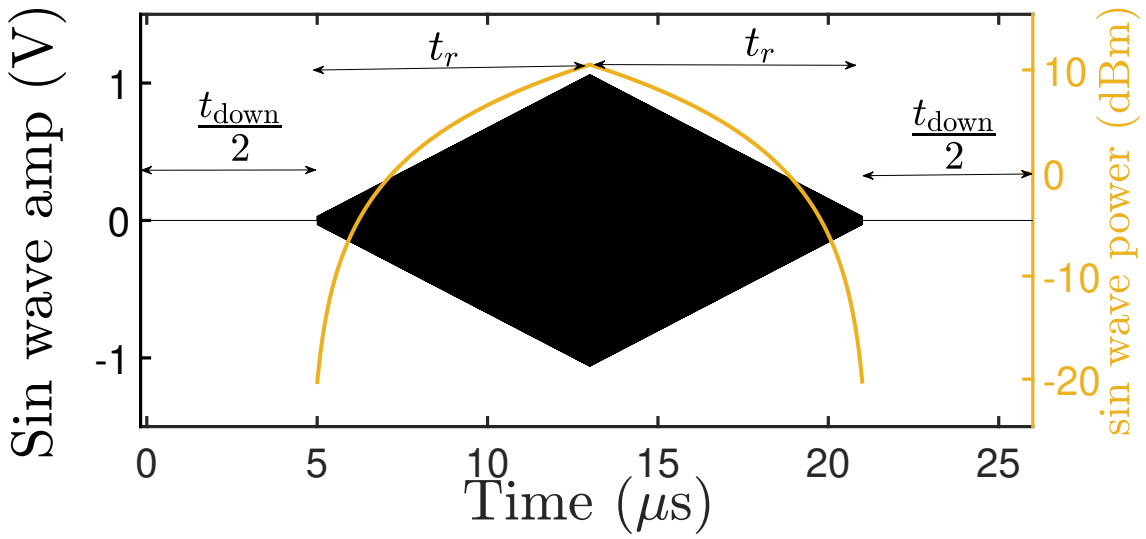

Figure 4.10: IF pulse output by channel 1 on the AWG in Fig.(3.14). The black curve is the actual power chirped sine wave at 84 MHz. The indicated voltage is at the output of the AWG. This then undergoes considerable conversion loss at the input mixing stage along with several orders of cryo attenuation in the dilution fridge insert. The orange curve on the right is the power output by the AWG as a function of time. The voltage is linearly ramped over time. For this illustrated pulse, $t_r = 8\,\mu$s, $t_{\text{down}} = 10\,\mu$s.

Phase(S_{11}) as described in section 3.3.5. Like points for several 1000 acquisitions are then averaged together.

Fig. (4.11) shows the observed hysteresis in the cCPT at the bias point $(n_g, \Phi_{\text{ext}}) = (0, 0)$ for a drive red detuned from the linear resonant frequency ω_0 by 10 MHz. This data was averaged over 5000 pulse sequences. We observe two distinct phases between input powers of -130.5 dBm and -109.5 dBm. The lower and upper bifurcation points from Eqn. (4.15) are calculated to be -131.7 dBm and -118.2 dBm respectively. We put this discrepancy down to the resonant frequency fluctuations in [73], which effectively cause us to work at a a different detuning between different iterations of the pulse sequence, leading to a smearing effect. Another possibility is the ramp rate of the pulse itself causing an error in the estimation of the bifurcation power, because of the slowing down of the dynamics close to the 'ghost' of the saddle-node mentioned

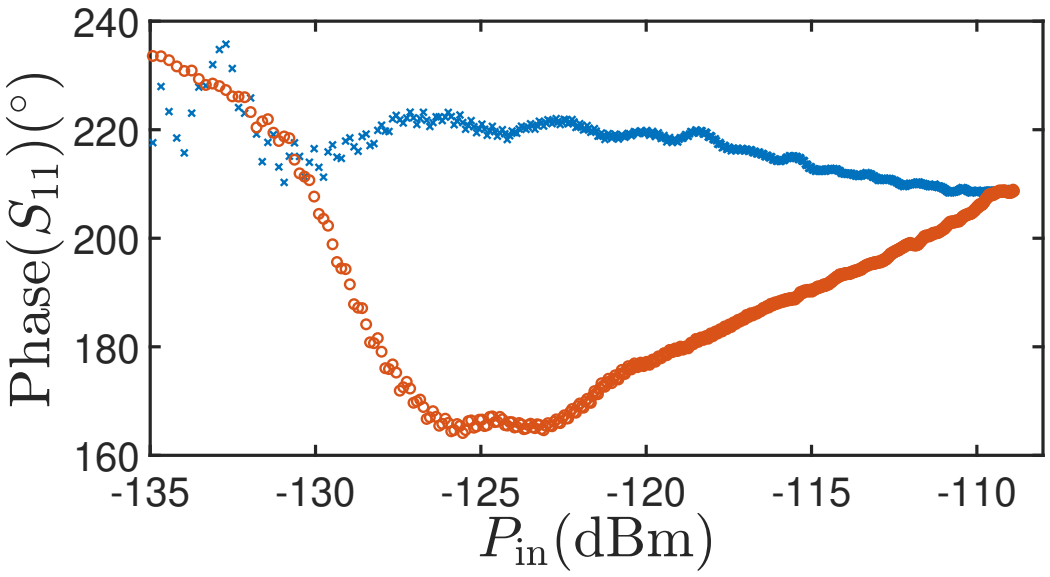

Figure 4.11: Observed hysteresis in Phase(S_{11}) as the power is ramped up and back down in a pulse sequence as shown in Fig.(4.10). The cCPT was biased at $(n_g, \Phi_{\text{ext}}) = (0, 0)$ where the resonance was at $\omega_0 = 5.7851$ GHz. The detuning of the input drive tone, $\Delta = -10$ MHz. The blue curve represents the forward ramp and the red, the reverse ramp. $t_r = 4\,\mu$s and $t_{\text{down}} = 10\,\mu$s for this run, which is more than a factor of 10 of the cavity decay time.

before. [120, 121] estimate the error in the measurement of the bifurcation point for a frequency ramp, but we expect such an effect to carry over for a power ramp as well. Slow adiabatic ramp rates are generally ideal, but as we see in Fig.(4.12), we run into issues of switching between the metastable states even for ramp rates on the order of 2-3 dBm/μs.

As we see in section 4.2.2, we expect to see an increasing separation in the Phase(S_{11}) between the two oscillation amplitude states as we move to lower powers. During the reverse ramp, we expect an abrupt jump from the low to the high oscillation amplitude state at the high power bifurcation point, but instead see a gradual tapering off, which is probably a sign of switching between the metastable states close to the bifurcation edge even for the t_r employed in these pulse sequences.

Fig. (4.12) shows the variation of the hysteresis curves as the ramp time on the

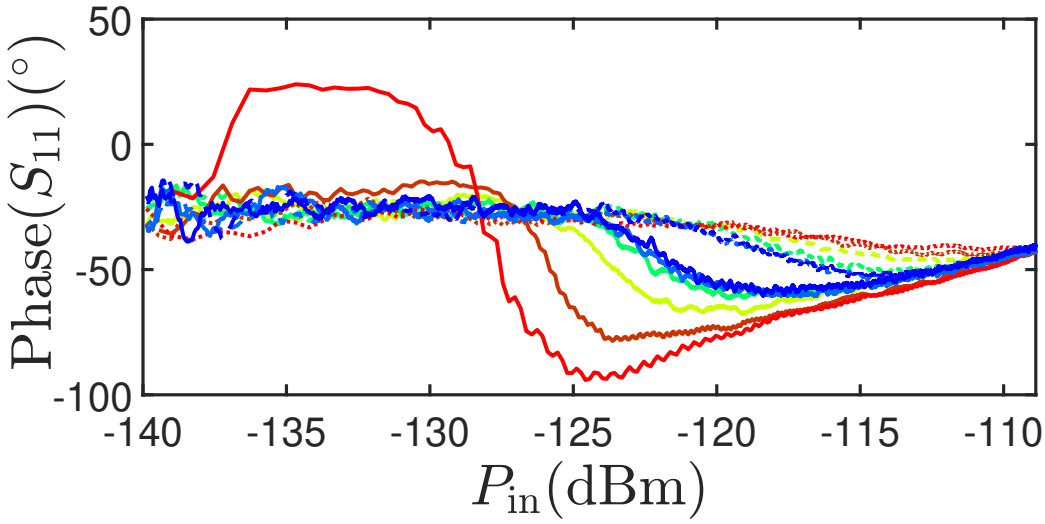

Figure 4.12: Variation of hysteresis curves as as in Fig.(4.11) as the ramp time t_r is varied. For increasingly blue hues, t_r = (2, 4, 8, 16, 24, 28) μs. The dashed lines are the forward ramp and the solid lines are the reverse ramp. The experiment is carried out for $(n_g, \Phi_{\text{ext}}) = (0, 0)$ and $\Delta = -9.5$ MHz.

input pulse of the AWG is varied. As we increase the ramp time (bluer curves), we see that the curves converge to a weighted average value of the phase corresponding to the high and low amplitude state obtained in the shortest ramp $t_r = 2$ μs (red curve). For a given ramp time, the obtained phase value is the weighted mean of the two phases where the weight is given by the probability of being in either oscillation state at each sampled input power (see sec. 4.1.1). This is because the longer the ramp time with respect to the average lifetime of both states, the more likely it is that we see an equilibrium (long time limit) distribution of switching probabilities. The obtained curves appear to reach a saturated mean value at each sampled power for a ramp time of ~ 24 μs, indicating that the average lifetimes of the metastable states are of that order for this cCPT bias point at that detuning. A similar result was recently observed for a non-linear semiconductor microcavity [122].

Fig. (4.13) displays a surface plot where each vertical slice is a scan similar to Fig.(4.11), with each slice at a different detuning Δ. The solid lines indicate the

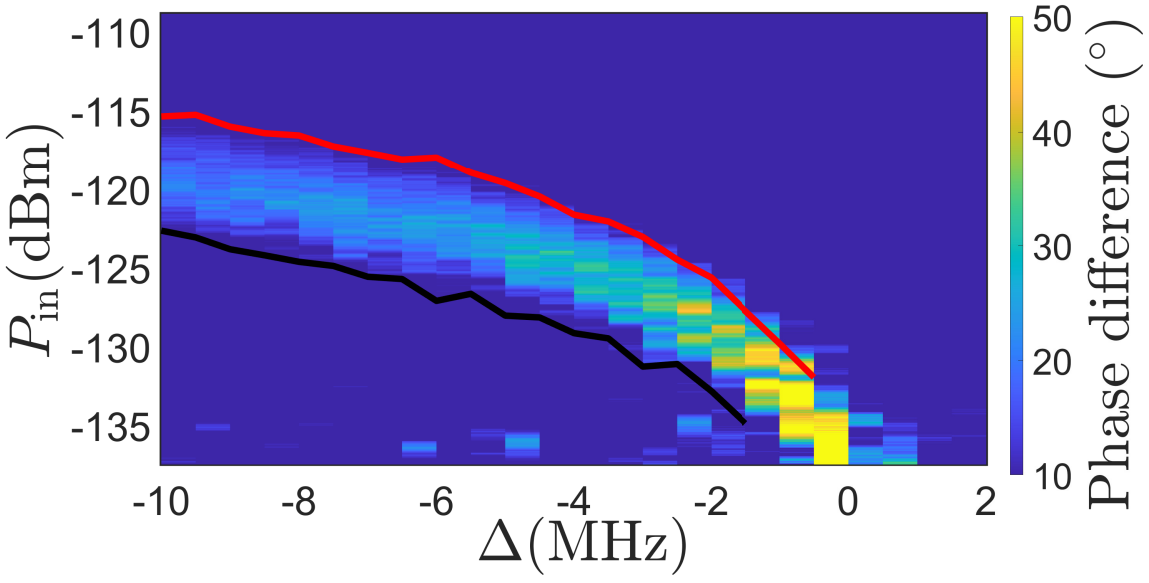

Figure 4.13: Surface plot of phase difference at different sampled powers during a ramp such as in Fig.(4.10) for different detunings with the cCPT biased at $(n_g, \Phi_{\text{ext}}) = (0, 0)$. The red and black lines are a guide to the eye, and denote the points where the phase difference between the forward and reverse ramps changes from less than 5^0 to more than 5^0. They represent the extent of the bistable region. The input pulse had $t_r = 24$ μs, and each phase point is averaged over 5000 repetitions of the pulse.

beginning and end of the bistable region. We expect them to trace out an area similar to that in Fig. (4.6). Though the bifurcation powers do follow an increasing trend at detunings further from resonance as predicted by Eqn. (4.15), we do not see the expected broadening in the bifurcation region at increasing detunings (or conversely narrowing close to the critical detuning as in Eqn. (4.12) with $K < 0$). This could be attributed to the fluctuations in resonant frequency as in [73], [33], but this is at a cCPT bias $(n_g, \Phi_{\text{ext}}) = (0, 0)$, where the standard deviation of the resonant frequency fluctuations due to charge and flux noise are ≈ 30 kHz. If frequency fluctuations are the source of these variations, they must be attributed to quantum fluctuations in photon number causing a shift in cavity resonant frequency through the Kerr effect [73]. We continue to see the bistable region at higher than expected input powers at most detunings similar to Fig.(4.11), which is probably due to the systematic error in

estimating the bifurcation points caused by the ramp rate as mentioned in [120, 121].

4.2.2. Charge sensing in the bistable region

In this section, we study the probability of finding the oscillator in either the high or low amplitude as a function of detuning and as a function of the input power. In order to do so, we use pulses as illustrated in Fig. (4.14).

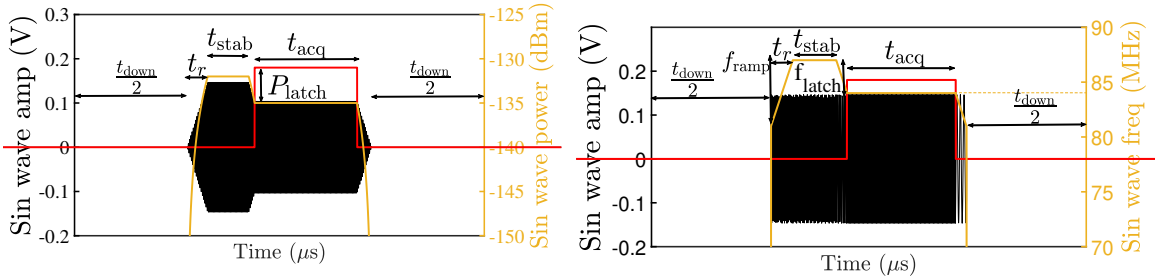

Figure 4.14: Pulses used to obtain the S-curves described in the text as a function of the pulse parameter - (a) Power (b) Detuning respectively. The black sin wave is the actual tone IF tone output by the AWG. The red denotes the acquisition trigger that begins data acquisition for each pulse, and the orange is the value of the pulse parameter at any instant in time. t_r is the time over which the pulse parameter is ramped to it's peak value. The input pulse is then held at this value for t_{stab} to allow the oscillator to settle into one of the two possible oscillation states. The pulse parameter is then ramped down to a latch value P_{latch} (f_{latch}), and the phase of the output signal is acquired for t_{acq}. The entire pulse then repeats after a time t_{down}.

The idea behind ramping up the pulse to its peak value (frequency can be ramped down as well), is to initiate the system preferentially in one oscillation state over the other. The input parameter - input power in Fig. (4.14a) and detuning in Fig. (4.14b), starts out at a value in the monostable regime. As it is ramped into the bistable regime, the oscillator stays in the same oscillation state as in the monostable regime. The system is then subject to a period where the pulse parameter is held constant (t_{stab}). It could potentially switch to the other metastable state in this time, depending on it's transition dynamics at this power and detuning. The pulse parameter is then ramped back down to a value further from the bifurcation point,

where the activation energy barrier to switch from one metastable state to the other is typically much higher. The system is thus 'latched' to the state it was in during the stabilization region of the pulse. This technique allows longer averaging times to improve SNR and has been demonstrated in several non-linear oscillator systems [34], [123], [63]. The pulse then repeats after a reset time t_{down}. The phases during the acquisition section of several 1000 such repetitions are then histogrammed, and the ratio of the counts in the low amplitude oscillation state to the total number of counts gives the probability of being in that state.

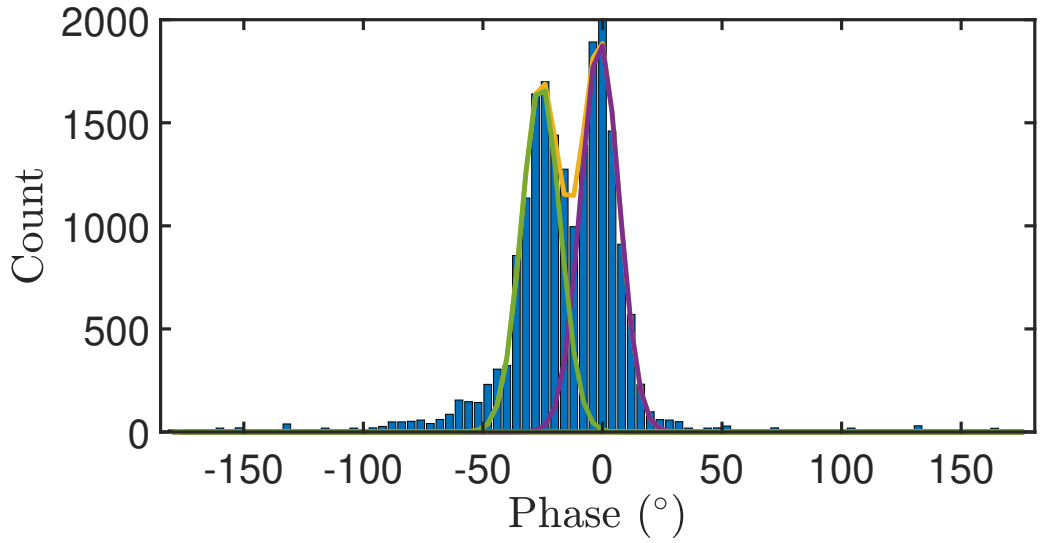

Figure 4.15: Obtained double Gaussian distribution for the cCPT biased at $(n_g, \Phi_{\text{ext}}) = (0, 0)$. $\Delta = -8$ MHz, input drive $P_{\text{in}} = -119$ dBm, using a pulse sequence as in Fig. (4.14a), with $t_r = 200$ ns, $t_{\text{stab}} = 40$ ns, $t_{\text{acq}} = 250$ ns and $P_{\text{latch}} = 0$W. Data is acquired for 20000 repetitions of the sequence. The yellow curve is a best fit to a double Gaussian with mean values -1.07^o and -25.78^o and a system amplifier noise broadening and a standard deviation $\sigma_{\text{fit}} = 8.06^o$ for each Gaussian. The green and purple curves represent the constituent single Gaussians in the double Gaussian fit.

In our experiments, typical values are $t_r = 530$ns, $t_{\text{stab}} = 4.9\mu$s, $t_{\text{acq}} = 250$ns - 2μs (depending on the drive power and the related SNR) and t_{down} of the order of $\sim 5\mu$s for our cavity decay rates of ~ 2MHz. These parameters for t_r and t_{stab} were settled upon after performing QuTip [124] simulations using a master equation solver for the

exact input tone (with frequency and power ramp), and seeing the system through a transient to the steady state. This value of t_r is also close to the nominal value of $5\kappa_{\text{tot}}$ over which transients of oscillating systems are expected to decay, even in the region where switching is observed, where the oscillator dynamics are considerably slowed [36]. Studying the widths and centers of the S-curves (detailed below) as a function of t_r and t_{stab} also showed agreement with the simulations in that they attained a stabilized value for these pulse parameters. In practice, we do not use the latching technique and begin acquisition immediately after the stabilization time. Though we average the acquired phase for a typical time of $0.25 - 3\mu$s depending on the drive power, the separation in phase between the high and low oscillation amplitude states could be small enough that the tails of the noise-broadened Gaussian distributions overlap and distinguishing between the two states by a single-shot measurement becomes murky.

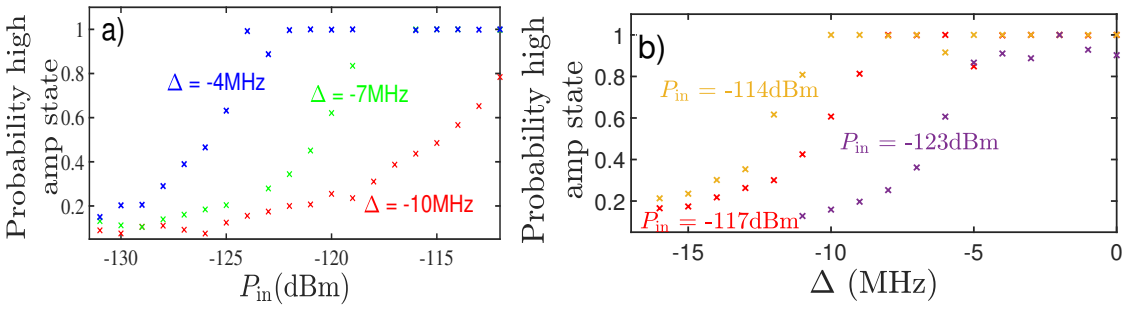

Figure 4.16: Representative s-curves for the cCPT biased at $(n_g, \Phi_{\text{ext}}) = (0, 0)$. a) Using pulse sequence in Fig. (4.14a), b) pulse sequence in Fig. (4.14b). Both sequences had $t_{\text{stab}} = 40$ ns, $t_{\text{acq}} = 250$ ns, $t_{\text{down}} = 10\,\mu$s and $P_{\text{latch}} = 0$ W and $f_{\text{latch}} = 0$ Hz respectively. $t_r = 250$ ns in a) and $t_r = 0$ in b). Each data point is calculated from 20000 repetitions of the pulse sequence.

To find the probability of finding the oscillator in the low amplitude state, we calculate the ratio of the area of the Gaussian best fit curve corresponding to the low amplitude state to the total area of the double Gaussian fit. For the data in Fig. (4.15), this is 0.47. We then repeat this procedure with input pulses in Fig.

(4.14a) and (4.14b) respectively and obtain corresponding s-curves in Fig. (4.16a) and (4.16b).

Looking at these s-curves, it is clear that the picture painted in Fig.(4.7) does not hold in the presence of fluctuations. Even with the appropriate ramp to initiate the oscillator in the desired oscillation amplitude state, we do not see a sharp transition from one state to the other right at the bifurcation point. Instead, we see a gradual transition of the likelihood of the oscillator in the high amplitude state go from $0 \rightarrow 1$ over several cavity linewidths. The ratio of the probability of being in the low amplitude state (ρ_{low}) to being in the high amplitude state (ρ_{high}) can be related to the switching rates $W_{\text{low}\rightarrow\text{high}}$ and $W_{\text{high}\rightarrow\text{low}}$ in Eqn.(4.16) to be [117]

$$\frac{\rho_{\text{low}}}{\rho_{\text{high}}} = \frac{W_{\text{high}\rightarrow\text{low}}}{W_{\text{low}\rightarrow\text{high}}} = \exp\left[\frac{E_a^{(\text{low})} - E_a^{(\text{high})}}{I_N^{\text{int}}}\right], \tag{4.17}$$

where $E_a^{(\text{low})}$ and $E_a^{(\text{high})}$ are the activation energy barriers out of the low and high oscillation amplitude states respectively which depend, along with the effective noise intensity I_N^{int} on the set of drive parameters, particularly Δ and P_{in}. The exponential dependence of the population ratio on the activation energies shows that we expect to find the oscillator either in the high or the low oscillation amplitude state across most of the bistable region, and only in a region where the difference between the two energies becomes comparable to the effective noise intensity, do we expect to see signs of both states co-existing. This is reminiscent again of a kinetic phase tranisition [118], and though these systems are driven and not in equilibrium, supernarrow spectral peaks are predicted because of these fluctuation-induced transitions and have been observed in an analog circuit [125], and in a micromechanical torsional oscillator [126].

Our objective in performing a single-shot charge readout now becomes two-fold. (i) Maximize the contrast denoted by the double-headed arrow in Fig. (4.17) while minimizing δn_g. This will allow us to resolve the two gate charges by performing

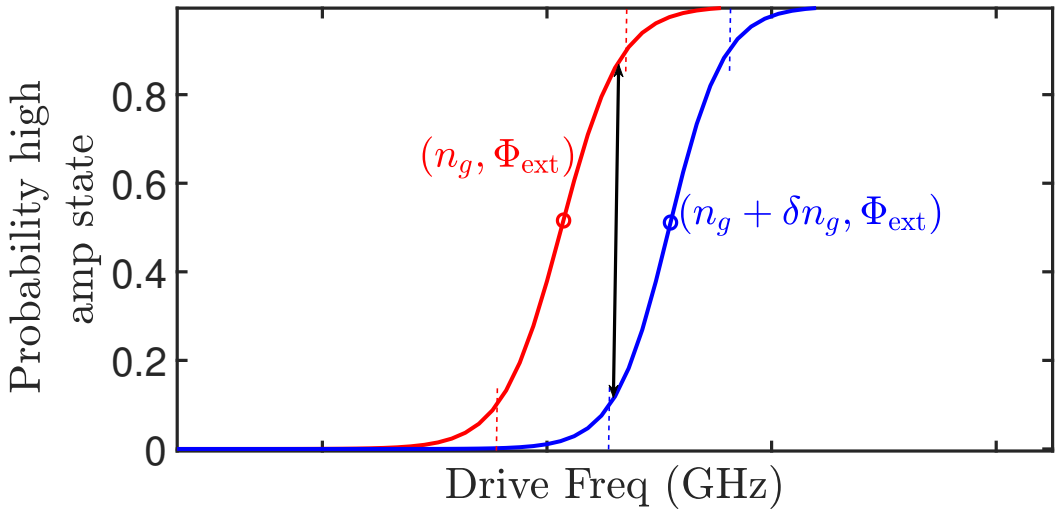

Figure 4.17: Schematic of s-curves for two different charge points (blue and red curves) separated by δn_g.The black double-headed arrow represents the maximum contrast between the two states, and the coloured dashed lines mark the width of the respective s-curve.

an ensemble measurement and calculating the probability, and (ii) maximize the separation between the Gaussian peaks as in Fig.(4.15) at the maximum contrast point in order to enable single-shot readout.

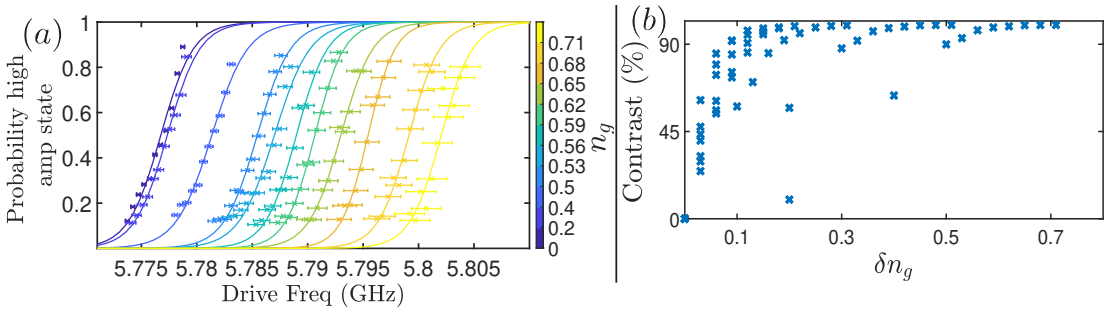

Figure 4.18: (a) S-curves for 11 different gate values with the cCPT flux biased at $\Phi_{\text{ext}} = 0.06\Phi_0$. These are obtained with the pulse sequence in Fig.(4.14b) with $t_r = 530$ ns, $t_{\text{stab}} = 4.5\ \mu$s, $f_{\text{ramp}} = 41$ MHz, $f_{\text{latch}} = 0$, $t_{\text{acq}} = 2\ \mu$s and $t_{\text{down}} = 5\ \mu$s. The crosses are the data points, with error bars representing the extent of frequency fluctuations [33] at that cCPT bias point. The solid line is a sigmoid fit. (b) Maximum contrast for each pair of measured gate points in (a).

Fig.(4.18a) shows the experimentally obtained s-curves for a range of gate values

at cCPT flux bias of $\Phi_{\text{ext}} = 0.06\Phi_0$ while driven with an input tone of $P_{\text{in}} = -128$ dBm and Fig.(4.18b) shows the corresponding maximum contrast value for each pair of gate points. The solid lines are sigmoid fits of the form

$$P(\Delta) = \frac{1}{1 + \exp\left[-\frac{4.3944(\Delta - \Delta_0)}{\gamma}\right]}, \tag{4.18}$$

where Δ_0 is the center of the sigmoid, and γ is the width between $P(\Delta) = 0.1$ and $P(\Delta) = 0.9$.

We see that we should be able to resolve a shift from $n_g = 0.71$ to $n_g = 0.62$ with a contrast of close to 92% for this input power, with a drive tone at 5.7973 GHz. Though the number of intracavity photons depends on the detuning of the drive, we set an upper bound (at the detuning corresponding to the low amplitude bifurcation point) of ~ 50 intracavity photons in the high amplitude oscillation state by solving Eqn.(4.8) with the theoretical value of the Kerr obtained from Eqn.(2.129) for our $E_J = 14.8$ GHz and $E_C = 54.1$ GHz, and using the damping rates obtained from the fits to the linear reflection coefficient Eqn.(3.7) performed with a sub-photon drive VNA measurement. We do not observe much variation of the damping rates with input powers before the onset of bistability [67], and cannot accurately extract the damping rates from a VNA measurement in the bistable regime because of the distortion of S_{11} brought about by the Poissonian switching between the metastable states. In reality, we are working at detunings much closer to the linear resonance than the low amplitude bifurcation point, and expect to have between 8 and 27 intracavity photons in the high amplitude state at the detunings plotted for $n_g = 0.71$ in Fig.(4.18).

In order to optimize the contrast, we need the centers Δ_0 for these gate points to be spaced well apart, and the widths γ to be minimized. Fig.(4.19a) shows the variation of these centers as a function of the gate for various flux values. We see

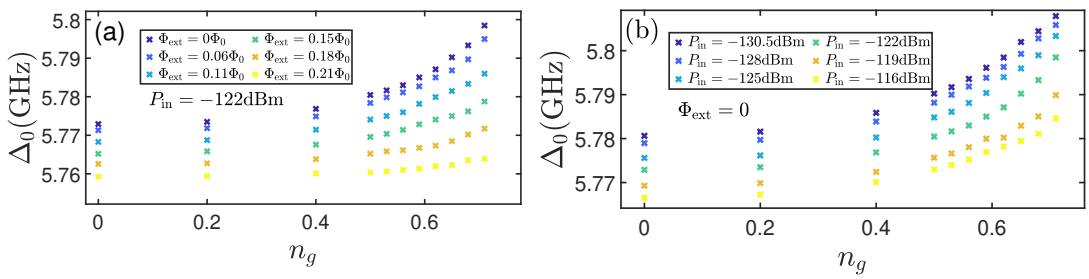

Figure 4.19: Sigmoid center Δ_0 fit vs n_g for (a) range of cCPT flux biases with an input drive strength $P_{\text{in}} = -122$dBm, (b) range of input drives for a cCPT bias $\Phi_{\text{ext}} = 0$. The 95% confidence intervals of the Sigmoid center fits are smaller than the markers.

that these mostly track the resonant frequency of the cavity at the corresponding cCPT bias (including a Kerr shift for this power). As seen here and as expected from Fig.(2.12), flux values closer to $\Phi_{\text{ext}} = 0$ provide larger shifts in resonant frequency and are ideal for charge sensing. This tracking of Δ_0 with the resonant frequency (and hence the Kerr (K), since the two have the same sinusoidal functional form, but differ by a factor $\Phi_{\text{zp}}^2 \sim 0.031$, see section 2.5.2) is clearly demonstrated in Fig.(4.20) for different input powers. We note the variation of the slope of these curves as a function of the input power. Looking at Eqn.(4.17), we see that the center of the sigmoid is expected to fall at the point where $E_a^{(\text{low})} = E_a^{(\text{high})}$. While these energies themselves are expected to scale with the drive amplitude [112], the activation energy of the high-amplitude oscillation state undergoes a scaling crossover as the input drive strength is varied [117]. This change in slope might be indicative of such a crossover. We do, however, also perform longer averaging to extract each phase point for the smaller P_{in} (2 μs as opposed to 250 ns). This might also be giving rise to data points which are averaged over the phases of both low and high oscillation amplitude states as a result of a switch during the averaging time. This is especially more likely at larger K values where the average lifetimes are often down to a few μs at some detunings as we will see in section 4.2.3, though the lifetime values in that section are reported

only for experiments with $P_{\text{in}} = -119$ dBm.

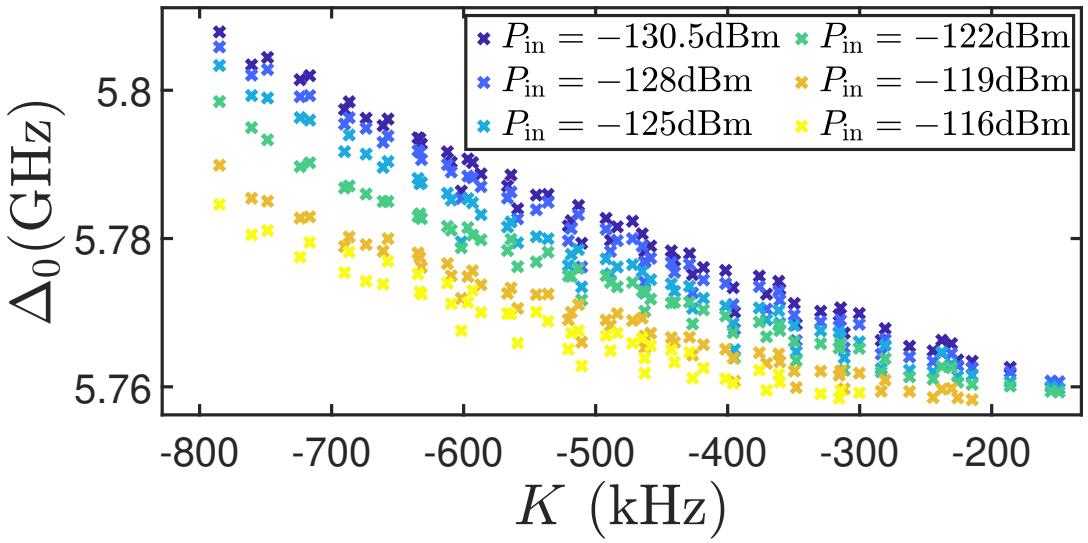

Figure 4.20: Variation of fitted Δ_0 as a function of K for different input powers. The 95% confidence intervals to the sigmoid fits are smaller than the markers.

With regards to our goal of charge sensing, we see from Fig.(4.20) that we obtain a larger separation in the centers while working at smaller drive powers (larger slope). We next consider the widths of the S-curves and plot them directly with K in Fig.(4.21). We see that the width tracks the K again, which is similar to what is predicted in Eqn.(5) of [127], though we do not see sublinear behaviour. We also observe a downturn in the widths of the s-curves at larger magnitudes of K at intermediate drive strengths.

Fig.(4.22) shows the variation of the sigmoid width as a function of the drive strength for three distinct values of the Kerr. We expect to see the width of the s-curve increase with power [47] since the barrier height is decreased with increasing drive amplitude [36, 112] and for the same noise intensity across all powers (for a given Kerr), we expect a substantial escape rate across a larger range of the bistable region for larger drive strengths. This is based on the assumption that the noise intensity only depends on the K and the damping rates [117, 36]. Though we did

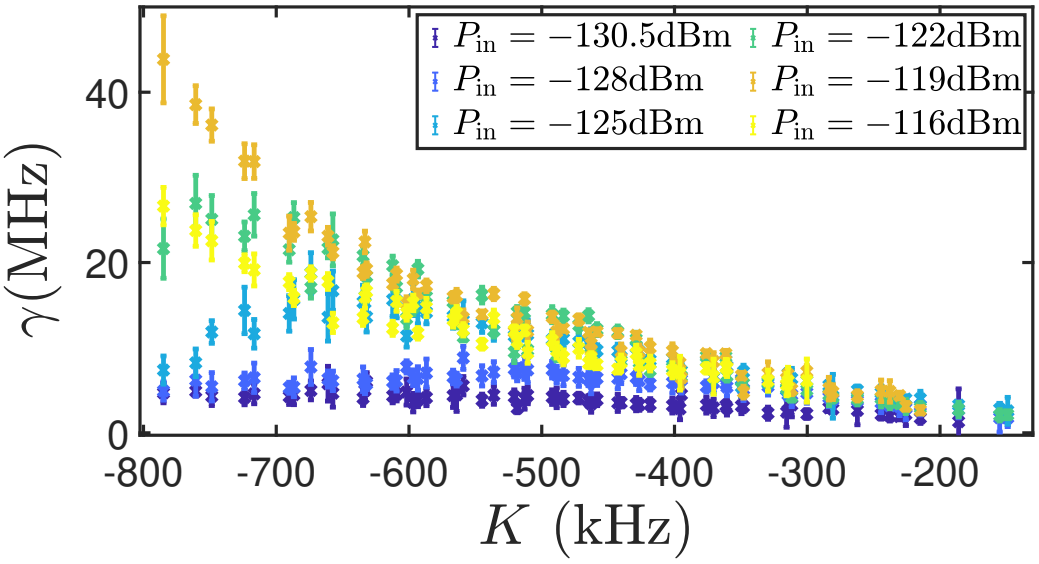

Figure 4.21: Variation of fitted γ as a function of K for different input powers. Error bars are 95% confidence intervals to the sigmoid fits.

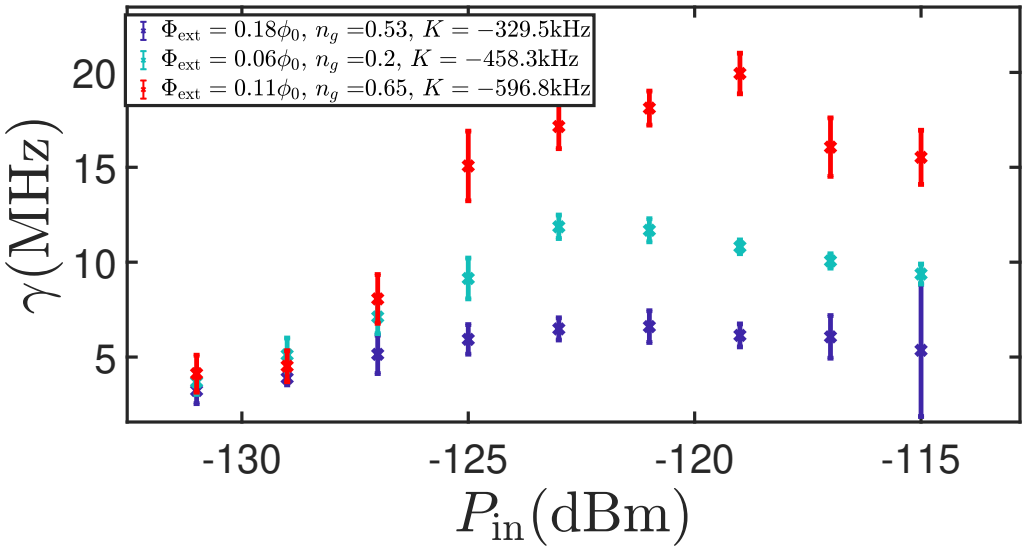

Figure 4.22: Variation of the fitted sigmoid width with input power for three distinct Kerr values in the middle of our tunable Kerr range.

not observe any substantial variation in κ_{int} as the drive strength was increased [67] before bifurcation, other loss mechanisms such as two-photon losses might be playing a role at these substantially higher drive powers [128]. The interplay between this

increased drive dependent loss and the barrier height might be causing this changed behaviour.

Coming back to our goal of charge sensing, Fig.(4.21) suggests that we should work at low powers, or at low Kerr magnitudes to minimize the width of the s-curve and increase sensitivity. Low Kerrs are not ideal since we saw in Figs.(4.19) and (4.20) that that causes the centers of the sigmoids to group together. This indicates that we should be working at high Kerrs ($\Phi_{\text{ext}} = 0$), with low powers. Working at lower powers, with fewer intracavity photons, would also mean less backaction on the system being measured. We will see what this means in terms of SNR below.

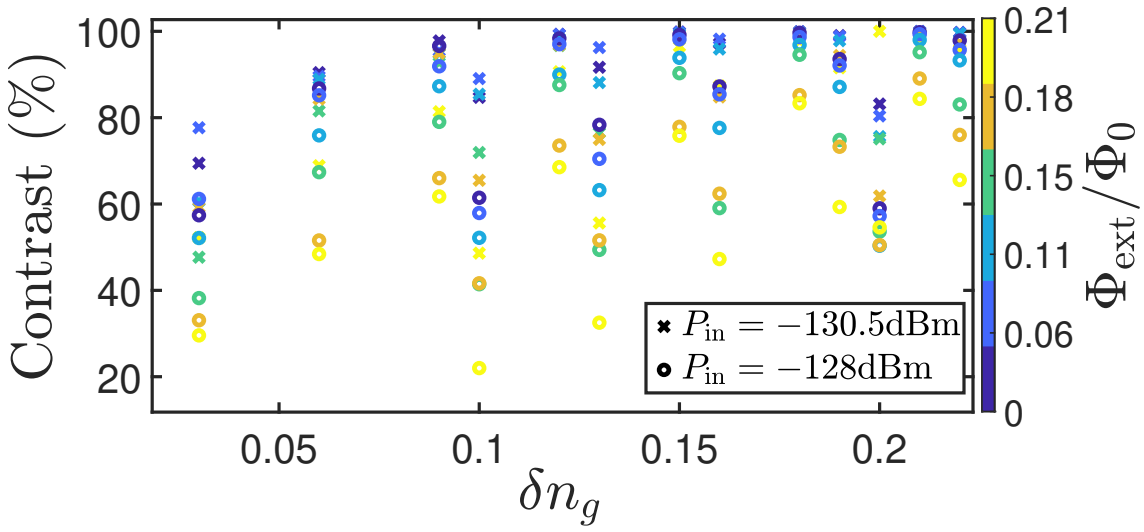

Figure 4.23: Plot of contrast between two gate values separated by δn_g for 6 different flux biases and at the two lowest input powers we consider. The crosses are for $P_{\text{in}} = -130.5$ dBm and the circles for $P_{\text{in}} = -128$ dBm, with the colourbar indicating the value of the flux bias.

Fig. (4.23) shows the obtained contrast at the optimum drive frequency for several pairs of gates separated by δn_g for the smallest powers. We see what we expected - the best contrast for the smallest δn_g occurs close to $\Phi_{\text{ext}} = 0$ reaching a predicted value of 96% in distinguishing between charge states $n_{g1} = 0.62$ and $n_{g2} = 0.71$. However, since we have fit double Gaussians to extract the probability of being in the

high amplitude state at each detuning, this value is agnostic to the overlap between the two Gaussians, which is important in order to perform single-shot measurements.

There are two factors that go into deciding how well resolved the two oscillation states will be. The first is the separation between the means of the two Gaussian peaks, and the second is the standard deviation of these peaks, which is related to the amplifier noise and the averaging time (see section 3.3.5).

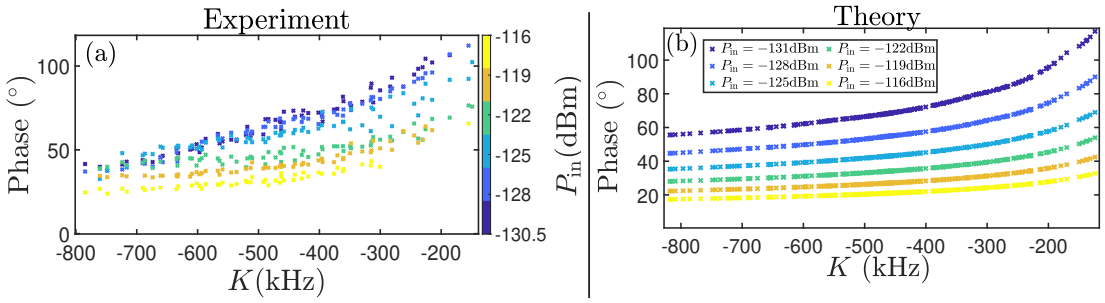

Figure 4.24: (a) Experimental and (b) theory plot of maximum phase difference between the low and high oscillation amplitude states vs Kerr in the detuning region where both states are visible. Each colour represents a different drive power P_{in}.

Fig.(4.24) shows the observed and the expected maximum difference in the Phase(S_{11}) for the high and the low oscillation amplitude states. The theory curves are simulated with a nominal value of $\kappa_{\text{ext}} = 1.2$ MHz and $\kappa_{\text{int}} = 0.4$ MHz in Eqn.(4.7). We see that the trend of higher phase differences arising at lower Kerr magnitudes and lower powers observed in experiments is reproduced by the theoretical model Eqn.(4.7). We understand this as follows.

As we saw in Fig.(4.1a) and reproduce here in Fig.(4.25), the strength of the Kerr nonlinearity of the oscillator causes the hardening/softening of the oscillation amplitude response. The degree of hardening/softening (the bending over of the response curve) is decided by the strength of the non-linearity K. The low oscillation amplitude always stays close to 0 for all drive strengths, and at higher drive strengths, where the region of bistability is much larger, the *total* oscillation number in the high oscillation amplitude state increases with increasing magnitude of Δ, while the slope

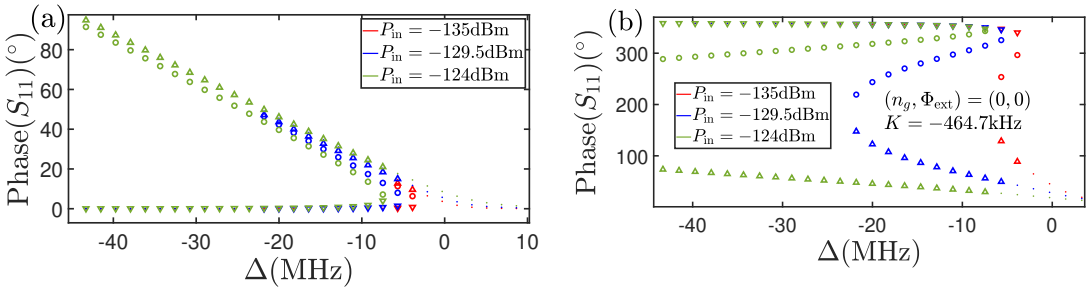

Figure 4.25: Plot of (a) intracavity photon number n and (b) Phase(S_{11}) vs Δ simulated for three different P_{in} for a cCPT bias $(n_g, \Phi_{\text{ext}}) = (0, 0)$ with a $K = -460$ kHz. The upward triangles indicate the high oscillation amplitude state, the downward triangles the low oscillation amplitude state, the circles the unstable state, and the dots the monostable states, respectively, as before.

of the $dn/d\Delta$ line remains practically unchanged across drive strengths. So, as the drive strength increases and the range of Δ over which bistability exists increases, the difference in n between the high and the low oscillation amplitude states increases with Δ. This is what we see in Fig.(4.25a) for the different drive powers.

The Phase(S_{11}) on the other hand is constrained to go from 0 to 2π across the width of the bistable region. So as the width of the bistable region increases, the slope of the S_{11} decreases. At the detunings we work at, where we actually see both oscillation amplitude states co-exist, which is typically $< 15 - 20\kappa_{\text{tot}}$, at higher drive powers (compare black and blue curves in Fig.(4.25b), the separation between the upward and the downward triangles in the bistable region are much smaller (mod 2π) for the higher power curve. The explanation for the reduction in phase difference with an increase in Kerr in Fig.(4.24) is similarly straight-forward as the slope of the Phase(S_{11}) with detuning Δ reduces with the amount of hardening/softening and the corresponding bending of the response curve.

Armed with all this information to perform optimal charge sensing, we choose to work at $(n_{g1}, \Phi_{\text{ext}}) = (0.62, 0)$ and $(n_{g2}, \Phi_{\text{ext}}) = (0.71, 0)$, with an input power $P_{\text{in}} = -128$ or -130.5 dBm. Since the requirement of low Kerr for large phase

separation and high Kerr for larger sensitivity in gate are conflicting, we choose to work at the most sensitive point, at the expense of having to average for a $t_{\text{acq}} = 3\,\mu$s.

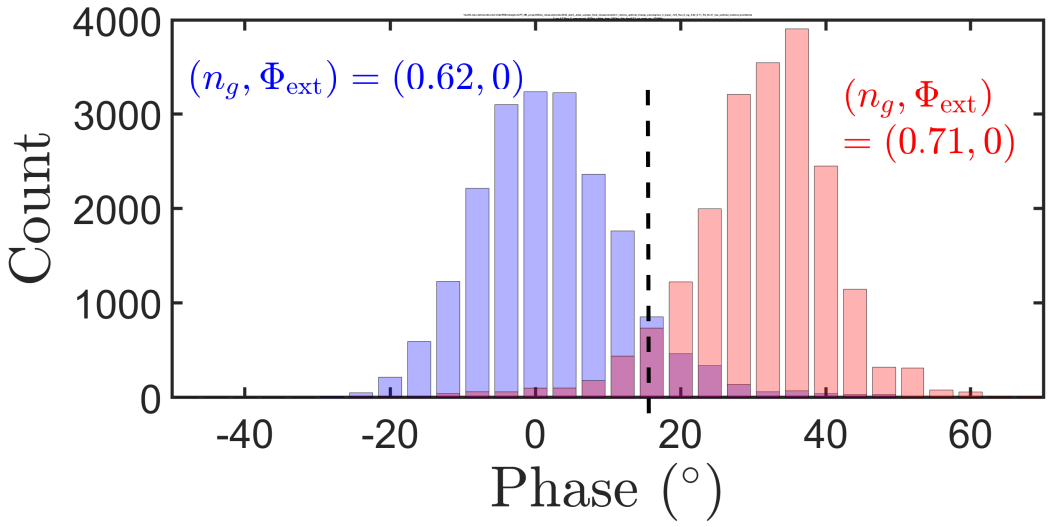

Figure 4.26: Measurement of the phase for 20000 trials each at $(n_g, \Phi_{\text{ext}}) = (0.62, 0)$ in blue, and at $(n_g, \Phi_{\text{ext}}) = (0.71, 0)$ in red for an input drive $P_{\text{in}} = -128$ dBm. The black dashed line indicates the threshold value.

Fig.(4.26) shows the result of such a measurement with drive frequency 5.8003 GHz, close to the predicted maximum contrast at 5.8013 GHz in a plot similar to Fig.(4.18) at $\Phi_{\text{ext}} = 0$. We define the threshold value between the two charge states to be the midpoint between the two Gaussian peaks, denoted by the black dashed line in the figure. We notice a slight asymmetry in each of the Gaussians - the blue curve is slightly broader to the right of its maximum and the red is broader to its left. These are signs of a small possibility of finding the blue in the low and the red in the high oscillation states respectively, showing that we are indeed right at the maximum edge of the contrast window we obtained from the earlier plot. As expected, the phase separation between the two peaks for what are effectively the largest attainable Kerr magnitudes for our cCPT sample, even at these low drive powers is only 36°. The noise broadening at these powers, for the chosen averaging time of 3 μs is in good agreement with Fig.(3.16). This causes an overlap of the tails of the Gaussians.

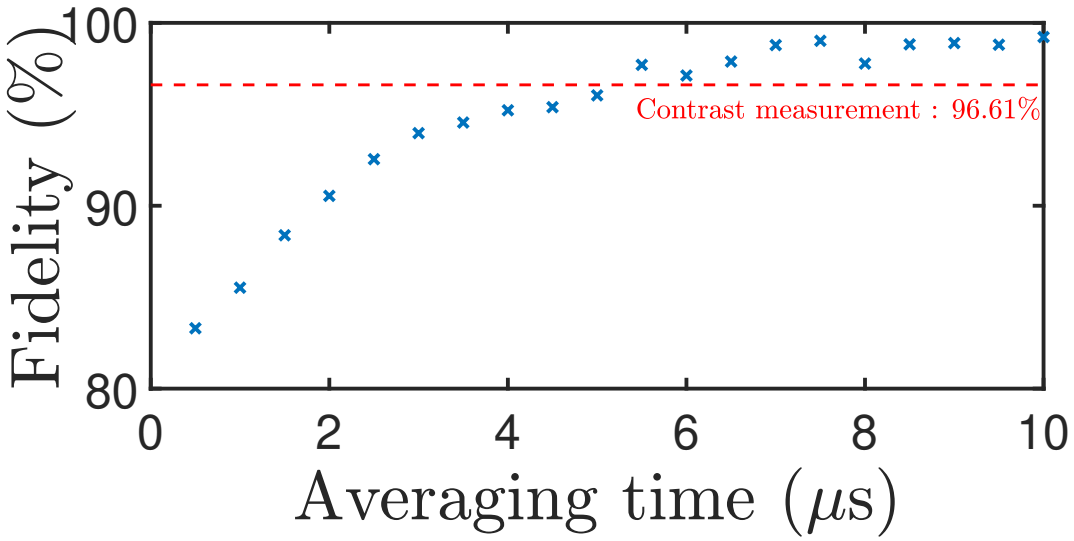

Figure 4.27: Measurement fidelity vs the averaging time to distinguish between $(n_g, \Phi_{\text{ext}}) = (0.62, 0)$ and $(n_g, \Phi_{\text{ext}}) = (0.71, 0)$ with an input drive $P_{\text{in}} = -128$ dBm. Each gate point underwent 20000 trials. The dashed line indicates the measured contrast using the S-curves for these bias points.

The fidelity of a single-shot readout is the measure of accuracy in the process of taking a single obtained phase point in the above plot and sorting it based on the threshold line. We quantify the fidelity of a single-shot readout using a simple fidelity measure

$$\text{fidelity} = 100 \times \left(1 - \frac{\text{false positives}}{\text{total count}}\right), \tag{4.19}$$

which we apply to each of the measured charge states. We obtain a fidelity of 94.21% and 94.97% respectively, and we report a fidelity of at least 94.21% for this measurement. This value is only slightly different from the obtained contrast of 96.61% from our measurement agnostic to the phase separation and amplifier noise. This indicates that for our averaging time, the major limitation is not the measurement setup, but the broadening of the s-curves caused by fluctuation-induced switching between the metastable oscillation states. Using the parameters above in Eqn.(4.8), we find that these drive parameters correspond to 8.1 intracavity photons at $n_g = 0.62$ and 20.94

photons at $n_g = 0.71$, both corresponding to the high amplitude oscillation state. At $n_g = 0.71$, the cCPT resides mostly in the low oscillation amplitude state where the intracavity occupation is of the order of 0.2 photons.

Fig.(4.27) plots the variation of the measured fidelity vs averaging time for the drive parameters in Fig.(4.26). We see that the fidelity saturates at around 94% close to an averaging time of 3μs. At larger averaging times, the fidelity actually exceeds the value predicted by the contrast measurement. We put this down to being because of the fact that at these large averaging times, the less probable states for the two measured gate values almost certainly undergo a switching event out of that state during the averaging time, which in fact increases the contrast for these averaging times.

4.2.3. Average lifetimes of metastable states

In this section, we present some measurements of the average lifetimes in the high and the low oscillation amplitude states of the cCPT in the bistable regime. As mentioned before, the cCPT parameter values lie on the boundary where the semiclassical activation energy model cannot completely describe the switching lifetimes in these mesoscopic systems, and a full quantum approach might be necessary [36]. Though we do not obtain a complete picture of the involved dynamics, we produce some results here which might lead to a better understanding of the cCPT operating in this regime.

The lifetime of switching between metastable states of a Duffing oscillator has been studied theoretically for a while now, as we saw above, but also experimentally, starting with nonlinear mechanical systems [129, 123, 130]. Similar switching has also been observed in parametrically driven systems which also undergo a (supercritical) bifurcation [131] which has been observed in an oscillator system composed of an electron in a Penning trap [132]. In nonlinear systems with JJs or arrays of JJs, these

lifetimes are quantified for systems well in the classical regime [34, 51] and more recently for systems with a slightly stronger non-linearity [47].

In the previous section, we described how we clearly see signs of the existence of two phase states by repeatedly probing the system with a short pulse and studying the probabilities of existence in each of these states at the end of that short pulse. Here, we perform an experiment where we drive the oscillator with a drive tone for a long time (50 ms), and monitor the reflected phase over that time to see signs of switching between the two metastable oscillation states. Fig.(4.28) shows an example of a small section of such a measurement, where we clearly observe (orange curve) a random telegraph signal (RTS) switching between two states. We analyse this noisy time trace by first doing a window averaging for 2 μs for this input power, and then following the iterative algorithm described in [133]. The noise is the amplifier noise as described before. As opposed to setting a simple threshold to determine which state the RTS is in, this algorithm uses an approach where it varies the threshold as a function of time since the last switch, based on an iterative estimate of the average lifetimes, which converges to the appropriate average switching lifetimes in a few iterations of the algorithm. This approach works much better in cleaning up noisy RTS signals such as ours, given the fact that it accounts for the probability that any given time point might mistakenly fall on the wrong side of a fixed threshold, leading to a false switching event or to a missed switching event.

Once we have the clean switching data for a length of time that is long compared to the average switching time, we can obtain the average lifetimes in each of these states by two methods - (i) the average lifetime in a given state is the total length of the acquisition divided by the number of switching events out of the desired state. (ii) since the switching events form a Poisson distribution, we can fit an exponential to the histogram of the switching times, or alternatively a linear plot to the log of

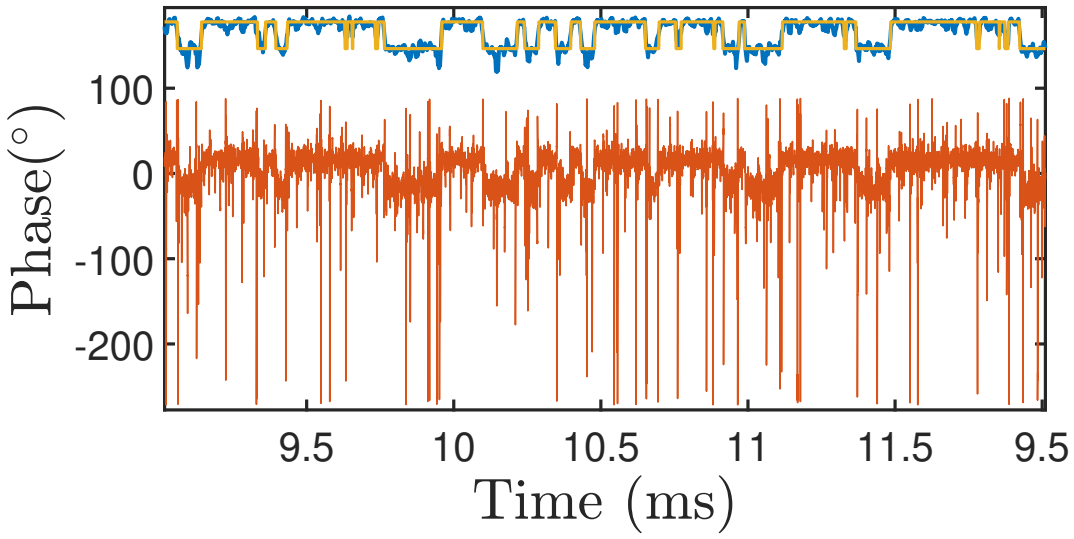

Figure 4.28: Example of the measured phase as a function of time for the cCPT biased at $(n_g, \Phi_{\text{ext}}) = (0.45, 0.11)$ driven at a $\Delta = -24$ MHz for an input drive strength $P_{\text{in}} = -116$ dBm. The orange plot is the noisy phase measured in real time, the blue curve (offset vertically for clarity) is the same trace after performing a window averaging for 2 μs, and the yellow is the cleaned RTS signal, where we used the algorithm described in the text.

the histogram, which is shown in Fig.(4.29).

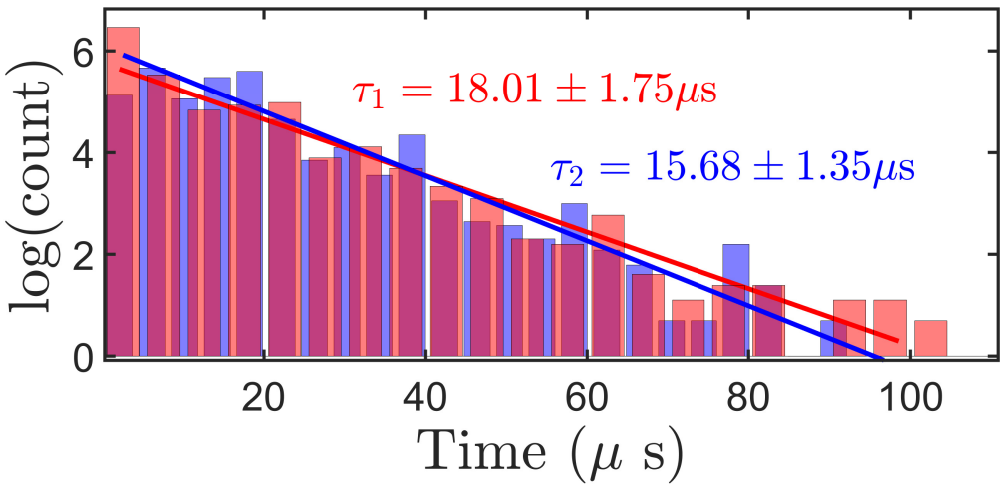

Figure 4.29: Poisson fit to the log of the histogrammed switching data in Fig.(4.28).

We immediately observe that the average lifetimes we obtain for the cCPT is surprisingly short compared to other (both dissimilar and similar systems). [129, 123] see switching events on the order of a few seconds in their micromechanical systems, when injected with additional noise. Once switched from the high to the low oscillation amplitude state, they have to reinitiate the system to the high amplitude state since the low amplitude state is long-lived on experimental time scales. In the JJ array system [47] with $K/\kappa_{\text{int}} \approx 1$, they observe switching lifetimes of the order of seconds too, though their drive tone is of the order of 9 intracavity photons (data in figures above is for several 100 photons in our case) and we have seen that the energy barrier of activation goes down with the drive strength, making switching more likely [36, 112].

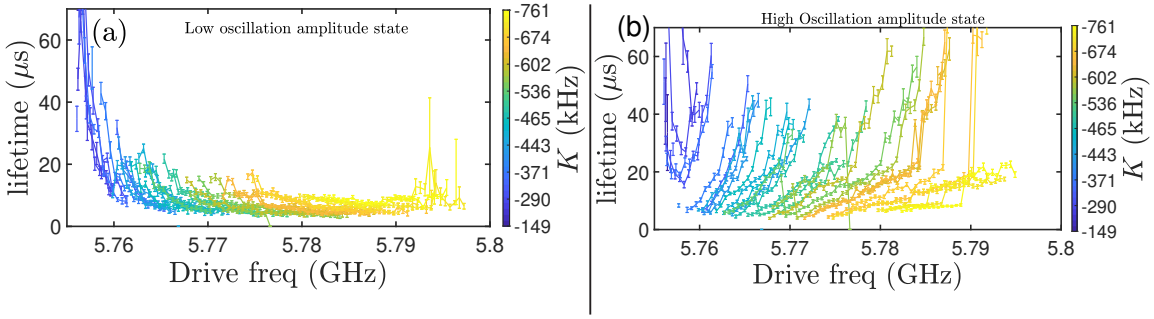

Figure 4.30: Average lifetimes of the high and low oscillation amplitude states as a function of drive frequency plotted for several different Kerr values for a drive strength $P_{\text{in}} = -119$ dBm.

Fig.(4.30) shows the average lifetimes as a function of drive frequency for a range of Kerr values. The high oscillation amplitude state is the one that is long-lived at the bifurcation close to the linear resonant frequency (which is to the right for each curve given our negative Kerr) which is how we identify the recorded phases with their respective oscillation amplitudes since we do not record the amplitude data because of memory constraints while obtaining such large time traces (50ms) of data sampled at 168MS/s. These plots concur with what we observed in the previous

section - larger Kerr values lead to finite lifetimes across a larger region of bistability, while for smaller Kerrs, the co-existence of both states is restricted to a small space in detunings before one or the other becomes long-lived and we barely observe any switching. This ties into Dykman's [112] picture of the Kerr controlling the noise intensity in the semiclassical quantum activated escape model of Eqn.(4.16).

Performing more thorough tests by performing this measurement for different drive strengths in addition to the range of Kerr values on the cCPT might shed some light on the anomalous variation of S-curve width with power in Fig.(4.22).

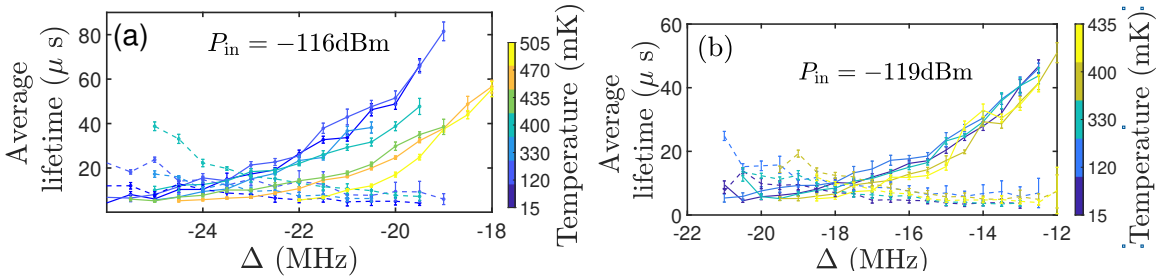

Figure 4.31: Average lifetimes of the high and low oscillation amplitude states as a function of detuning Δ for a range of mixing chamber temperatures for (a) $P_{\text{in}} = -116$ dBm, (b) $P_{\text{in}} = -119$ dBm with the cCPT biased at $(n_g, \Phi_{\text{ext}}) = (0, 0)$.

To get a sense of the barrier height, we perform a temperature dependent measurement of the average lifetimes for two different input powers, shown in Fig.(4.31). For the drive strength of $P_{\text{in}} = -116$ dBm, we see a marked decrease in average lifetimes as the fridge temperature is increased above 400 mK, setting that to be the approximate effective noise temperature driving the fluctuations. Above this temperature, the additional thermal contributions kick the oscillator out of the stable fixed point more often, leading to lower lifetimes. For $\omega_0 = 5.785$ GHz, we expect the switch from the temperature independent quantum limit to where the fluctuations are thermally driven to be at $T = 277$ mK[34], which indicates that there is some additional noise like the quantum activation at work here in addition to simple thermal activation. We do not see any variation with temperature in the lifetimes for $P_{\text{in}} = -119$ dBm,

though we only go up to a temperature of 435 mK at this drive strength.

In order to try to extract the activation energy of escape $E_a^{(\mathrm{low})}$ and $E_a^{(\mathrm{high})}$, as in [123, 129], we try to introduce some additional white noise to the drive tone. When the additional noise dominates over the intrinsic noise temperature, the log of the switching rate will vary linearly with the inverse of the noise intensity, with the slope given by the activation energy (see Eqn.(4.16))

$$\log W = \log W_0 - \frac{E_a}{I_N}, \tag{4.20}$$

where the total noise intensity $I_N = I_N^{\mathrm{int}} + I_N^{\mathrm{add}} \approx I_N^{\mathrm{add}}$ when the added noise intensity $I_N^{\mathrm{add}} \gg I_N^{\mathrm{int}}$.

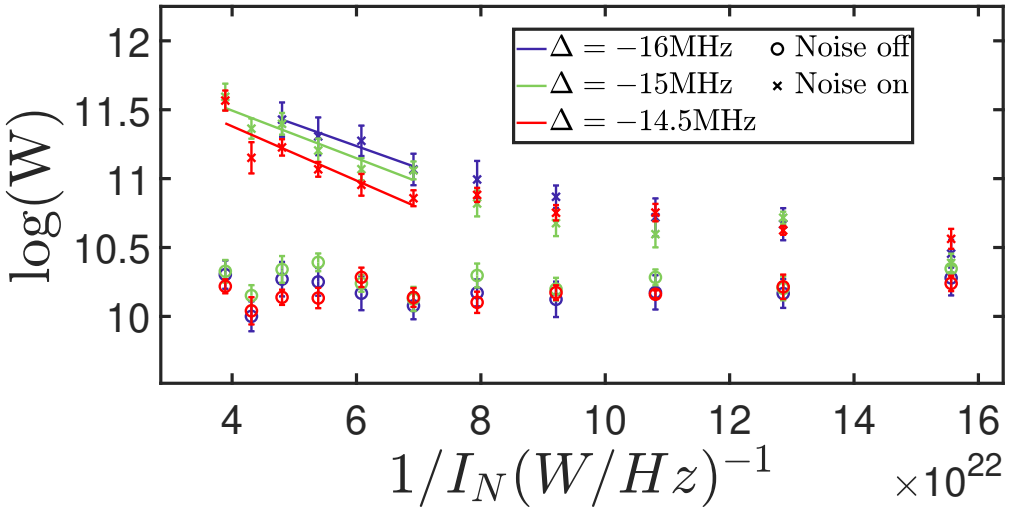

Figure 4.32: Plot of the log of the switching rate vs the inverse added noise intensity for 3 different detunings for $P_{\mathrm{in}} = -119$ dBm with the cCPT biased at $(n_g, \Phi_{\mathrm{ext}}) = (0.45, 0.18)$. The o's are runs with the noise source turned off, and the x's and the corresponding fit lines are with the noise source on.

Fig.(4.31) shows such a measurement for three different detunings alternating between a measurement with the noise source on (x's) and off (∘'s). We see that at the higher noise intensities, the added noise does dominate over the system noise, and we

fit a straight line to that section. We get nominal values for the activation energy, of the order of 1 - 1.5K for these detunings, which is reasonable considering the temperature of the noise we approximated in the temperature dependence measurement in Fig.(4.31).

Since the activation energy itself goes as $E_a = k(\delta\nu)^{3/2}$ where $\delta\nu = \nu - \nu_c$ is the detuning from the critical detuning for that P_{in} and 3/2 is the critical exponent with which the activation energy is expected to scale regardless of the driven oscillator system of consideration, as long as it undergoes a saddle node bifurcation as referenced in section 4.1.1. But the range of detunings over which we see appreciable switching is too small to allow a reasonable logarithmic fit to the data. But this behaviour of the activation energy has been studied in other nonlinear systems in [129, 123, 134], and in parametrically driven systems, this exponent changes to $\psi = 2$ for the supercritical and subcritical bifurcations that such a system undergoes, as we will see in chapter 5.

Section 4.3

Discussion

In this chapter, we have seen that the inherent self-Kerr nonlinearity in the cCPT can be exploited to perform sensitive charge measurements. We demonstrate a resolution of $0.09e$ charge with a fidelity of 94%, in a single-shot readout time of 3 μs. This corresponds to a charge sensitivity of $\delta q\sqrt{t_{\text{acq}}} = 150\,\mu e/\sqrt{Hz}$, comparable to state-of-the art rf-SETs. But this readout is performed with far fewer intracavity photons, $<$ 25 while typical rf-SETs operate with drives that correspond to a few 100,000 photons [26]. The measurement bandwidth of the nonlinear cCPT detector is set by the cavity lifetime, and is of the order of 1MHz. Working in a dispersive readout scheme as opposed to the dissipative technique employed by rf-SETs, we expect minimal back-

action on the system being measured [62]. Based on the application and the system being measured, we could also operate the cCPT at a slightly less sensitive point, but perform a faster readout of the charge state.

We find that the major limitation of this mode of operation of the cCPT is the switching between the metastable oscillation states of the oscillator in the bistable region. The strength of the tunable Kerr nonlinearity in the cCPT lies in an interesting regime where the semiclassical quantum activation description starts breaking down [36], requiring a full quantum mechanical understanding of the system dynamics. We have studied how the switching dynamics between these metastable states depends on some of the parameters of operation of the system, including the strength of the Kerr, the detuning from the linear resonance and the input drive strength. While the semiclassical approach [111, 117, 64]is sufficient to understand some of these trends, behaviour such as the anomalous variation in the width of the s-curve with drive power at a range of Kerr biases might demand a full quantum treatment. This is an important regime as systems are being designed in which the Kerr nonlinearity exceeds the damping rate (but still well outside the transmon regime) [47].

In addition to the switching between the metastable states, other limitations to the operation of the current cCPT device include the quasiparticle poisoning [66] discussed in section 3.3.2, which prevents us from operating the cCPT at more sensitive gate points which would lead to much enhanced charge detection. As we'll see in chapter 6, employing methods such as shielding which are designed to minimize the generation of these quasiparticles might greatly improve the scheme described in this chapter.

Finally, the first stage amplifier in our setup, the TWPA is found to operate with an added noise of about 4 photons/Hz at the pump parameters we are using. The nominal noise temperature of the nearly quantum-limited TWPA is reported to be

closer to 2 photons/Hz [52] and even this particular amplifier has been reported to perform slightly better than the 4 photons/Hz we are seeing [33]. Though we glossed over this in estimating the gain and added noise of the TWPA in section 3.3.4, the added noise and gain of the amplifier chain have a frequency profile. It turns out that the gain is close to a minimum and the noise close to a maximum (as a function of frequency, still quite low as a function of pump parameters, as seen in section 3.22)at around the frequencies we have been working at. An easy solution to this is to just move to flux values between $\Phi_{\text{ext}} = 0.25\Phi_0$ and $0.5\Phi_0$. The resonant frequencies for these fluxes are on the other side of the $\omega_0^{\lambda/4}$ frequency (where the TWPA gain is higher and the added noise lower). Most other system parameters - the damping rates and frequency fluctuations scale the same way as in the flux range 0 to $0.25\Phi_0$. We would see a Duffing hardening as opposed to the softening we have been observing above, but the magnitudes of the Kerr and the behaviour of the system should be comparable.

Chapter 5

Charge sensing driving the cCPT into parametric oscillations

In section 5.1, we will first go through the theory of inducing parametric oscillations by modulating the flux through the cCPT at close to twice its resonant frequency. We will closely follow the work of [135] in deriving the semiclassical dynamics of such a system. In section 5.2, we show some experimental results that conform to the model predicted by theory, validating our three-wave mixing model for the flux-pumped cCPT. Finally, in section 5.2.1, we will then see a proof-of-principle charge detection technique similar to the dispersive qubit state readout scheme described in [61].

Section 5.1

Theory

We begin with the Hamiltonian in Eqn. (2.125). We do not have an input drive to the cavity, but the flux through the SQUID loop is modulated with an amplitude $\delta\Phi$ and at a frequency ω_p such that $\omega_p/2 \approx \omega_0(n_g, \Phi_{\text{ext}})$ where ω_0 is the resonant frequency of the linear tunable cCPT system. The external flux through the SQUID loop is then

described by

$$\Phi_{\text{ext}} \rightarrow \Phi_{\text{ext}} + \delta\Phi \cos\left(\omega_p t + \phi_p\right). \tag{5.1}$$

As described in Eqn. A.13 in Appendix A, this gives rise to a Hamiltonian

$$H_{\text{cCPT}}^{\text{rot}} = \hbar\Delta a^\dagger a + \frac{\hbar K}{2} a^{\dagger 2} a^2 + \frac{\hbar}{2}\left(\epsilon a^2 + \epsilon^* a^{\dagger 2}\right) \tag{5.2}$$

in a frame rotating at $\omega_p/2$, and we define $\Delta = \omega_0 - \frac{\omega_p}{2}$ and $\epsilon = \frac{1}{2}\frac{\partial\omega_0}{\partial\Phi_{\text{ext}}}\delta\Phi e^{i\Phi_p}$ is a measure of the strength of the drive. Note that here we define Δ to be the negative of the convention used in previous chapters of this thesis.

Similar to Eqns.(A.14) and (A.15), the quantum Langevin equations for this Hamiltonian is

$$\dot{a} = -i(\Delta + Ka^\dagger a)a - i\epsilon^* a^\dagger - \frac{\kappa_{\text{tot}}}{2}a + \sqrt{\kappa_{\text{int}}}b_{\text{in}} + \sqrt{\kappa_{\text{ext}}}a_{\text{in}}, \tag{5.3}$$

$$\dot{a}^\dagger = i(\Delta + Ka^\dagger a)a^\dagger + i\epsilon a - \frac{\kappa_{\text{tot}}}{2}a^\dagger + \sqrt{\kappa_{\text{int}}}b_{\text{in}}^\dagger + \sqrt{\kappa_{\text{ext}}}a_{\text{in}}^\dagger. \tag{5.4}$$

Taking the steady state expectation values of Eqns. (5.3) and (5.4), we have

$$\alpha\left(-i(\Delta + Ka^\dagger a) - \frac{\kappa_{\text{tot}}}{2}\right) = i\epsilon^*\alpha^*, \tag{5.5}$$

$$\alpha^*\left(i(\Delta + Ka^\dagger a) - \frac{\kappa_{\text{tot}}}{2}\right) = -i\epsilon\alpha, \tag{5.6}$$

where we have defined the steady state intracavity amplitude to be α and this is independent of time in the rotating frame. Now multiplying Eqns. (5.5) and (5.6), we get

$$|\alpha|^2\left(\frac{\kappa_{\text{tot}}^2}{4} + (\Delta + Ka^\dagger a)^2 - |\epsilon|^2\right) = 0. \tag{5.7}$$

For non-zero roots to this equation, the term in the parentheses in Eqn. (5.7)

should be 0, and we have

$$n = a^\dagger a = |\alpha|^2 = \frac{1}{K}\left(-\Delta \pm \sqrt{|\epsilon|^2 - \frac{\kappa_{\text{tot}}^2}{4}}\right). \tag{5.8}$$

We see that there is a parametric threshold defined by $|\epsilon|^2 > \frac{\kappa_{\text{tot}}^2}{4}$ above which we have a non-zero steady state amplitude in the cavity in addition to the trivial $n = 0$ solution. Above this threshold, there are a three different regimes for steady state solutions. Assuming $K > 0$,

$$n = \begin{cases} 0, & \text{for } \Delta > \sqrt{|\epsilon|^2 - \frac{\kappa_{\text{tot}}^2}{4}} \\ 0,\ \frac{1}{K}\left(-\Delta + \sqrt{|\epsilon|^2 - \frac{\kappa_{\text{tot}}^2}{4}}\right), & \text{for } -\sqrt{|\epsilon|^2 - \frac{\kappa_{\text{tot}}^2}{4}} < \Delta < \sqrt{|\epsilon|^2 - \frac{\kappa_{\text{tot}}^2}{4}} \\ 0,\ \frac{1}{K}\left(-\Delta \pm \sqrt{|\epsilon|^2 - \frac{\kappa_{\text{tot}}^2}{4}}\right), & \text{for } \Delta < -\sqrt{|\epsilon|^2 - \frac{\kappa_{\text{tot}}^2}{4}}. \end{cases} \tag{5.9}$$

As detailed in [135] and looking at Eqn. (5.9) , as we move towards blue detuning ($\Delta < 0$) starting from a highly red detuning, initially, the zero-amplitude state is the only stable steady state. As $|\Delta| \leq \sqrt{|\epsilon|^2 - \frac{\kappa_{\text{tot}}^2}{4}}$, the zero-amplitude state undergoes a supercritical bifurcation and becomes unstable, and a bistable state emerges with an amplitude as in Eqn. (5.9), with the two states separated in phase by π (Eqn. (5.12)). As Δ is further reduced, in addition to the existing bistable same amplitude states above, the zero-amplitude state undergoes another (subcritical) bifurcation, and becomes stable again. It also gives rise to two unstable (and hence experimentally inaccessible) nontrivial states with an amplitude which is the negative solution of the third case in Eqn. (5.9). Thus we have tristability in that region.

Similarly, for $K < 0$, we have

$$n = \begin{cases} 0, & \text{for } \Delta < -\sqrt{|\epsilon|^2 - \frac{\kappa_{\text{tot}}^2}{4}} \\ 0, \frac{1}{K}\left(-\Delta - \sqrt{|\epsilon|^2 - \frac{\kappa_{\text{tot}}^2}{4}}\right), & \text{for } -\sqrt{|\epsilon|^2 - \frac{\kappa_{\text{tot}}^2}{4}} < \Delta < \sqrt{|\epsilon|^2 - \frac{\kappa_{\text{tot}}^2}{4}} \\ 0, \frac{1}{K}\left(-\Delta \pm \sqrt{|\epsilon|^2 - \frac{\kappa_{\text{tot}}^2}{4}}\right), & \text{for } \Delta > \sqrt{|\epsilon|^2 - \frac{\kappa_{\text{tot}}^2}{4}} \end{cases} \quad (5.10)$$

with similar patterns for the stability of the solutions which is plotted in Fig.(5.1.

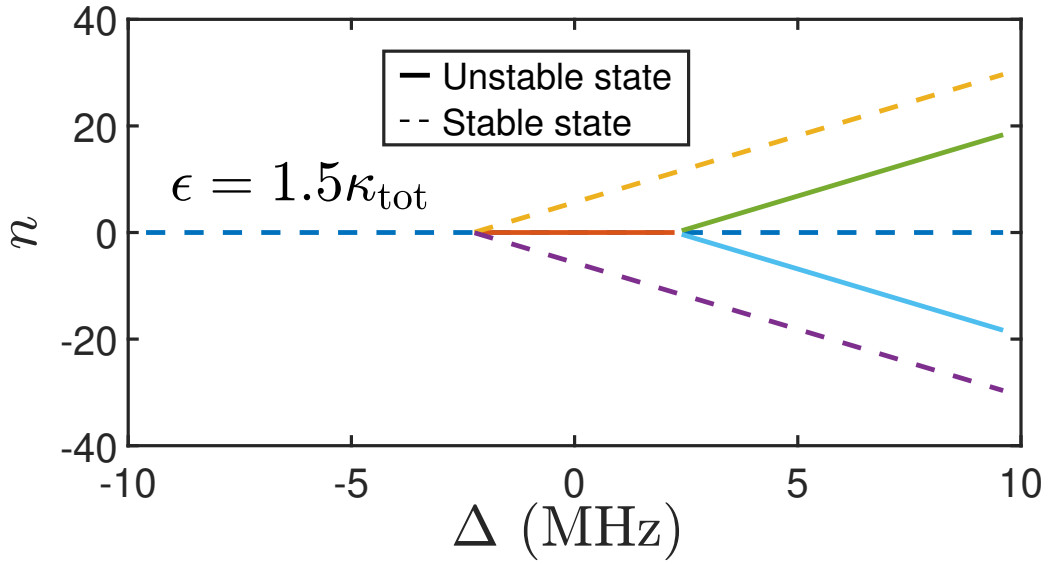

Figure 5.1: Bifurcation diagram of the oscillation response n vs Δ for $K < 0$ at a flux pump strength $\epsilon = 1.5\kappa_{\text{tot}}$. Dashed lines correspond to stable states, and solid lines are unstable states. Negative values of n correspond to states with a phase shifted by π.

To find the phase of the non-zero steady state solution for the bistable (and tristable) case, we plug in the stable steady state cavity occupation number (positive solution to quadratic for $K > 0$ and negative solution for $K < 0$) from (5.8) into Eqn. (5.5), and we get

$$|\alpha|e^{i\theta_\alpha}\left(\mp i\sqrt{|\epsilon|^2 - \frac{\kappa_{\text{tot}}^2}{4}} - \frac{\kappa_{\text{tot}}}{2}\right) = i\epsilon^*|\alpha|e^{-i\theta_\alpha}, \quad (5.11)$$

where $\alpha = |\alpha|e^{i\theta_\alpha}$, the minus is for $K > 0$ and the plus for $K < 0$. Simplifying this,

we get

$$\theta_\alpha = \frac{1}{2}\arcsin\left(\frac{-\kappa_{tot}}{2|\epsilon|}\right) - \frac{\Phi_p}{2},\ \pi - \frac{1}{2}\arcsin\left(\frac{-\kappa_{tot}}{2|\epsilon|}\right) - \frac{\Phi_p}{2}, \tag{5.12}$$

where $2\theta_\alpha + \Phi_p$ lies in the third (and first) quadrant for $K > 0$ and in the fourth (and second) quadrant for $K < 0$. Irrespective of the sign of K, we see that we have two states with the same amplitude, separated by a phase of π.

5.1.1. Pump induced detuning

Because of the large flux pumps required to induce these parametric oscillations, higher order terms in the expansion of the flux drive about its DC value might become important. We will now show that this gives rise to a 'pump induced detuning' as in [58] and [135]. Going back to Eqn. A.3 and expanding to second order in Φ_{ext}, we have an additional term in the Hamiltonian

$$\begin{aligned}
H^{(2)}_{\text{pump}} &= \frac{\delta\Phi^2}{2}\cos^2(\omega_p t + \Phi_p)\frac{\partial^2}{\partial\Phi^2_{\text{ext}}}\left[\sum_{k=0}^{\infty}\frac{1}{k!}\phi^k_{\text{zp}}\partial^k_\phi E_{\text{CPT}}(n_{\text{g}},\Phi_{\text{ext}})(a+a^\dagger)^k\right] \\
&= \frac{\delta\Phi^2}{8}\left(e^{2i\omega_p t}e^{2i\Phi_p} + e^{-2i\omega_p t}e^{-2i\Phi_p} + 1\right)\frac{\partial^2}{\partial\Phi^2_{\text{ext}}}\left[\sum_{k=0}^{\infty}\frac{1}{k!}\phi^k_{\text{zp}}\partial^k_\phi E_{\text{CPT}}(n_{\text{g}},\Phi_{\text{ext}})(a+a^\dagger)^k\right] \\
&= \frac{\delta\Phi^2}{8}\frac{\partial^2}{\partial\Phi^2_{\text{ext}}}\left[\Phi^2_{zp}\partial^2_\phi E_{\text{CPT}}(n_{\text{g}},\Phi_{\text{ext}})\right]a^\dagger a \\
&= \frac{\hbar\delta\Phi^2}{8}\frac{\partial^2\omega_0}{\partial\Phi^2_{\text{ext}}}a^\dagger a,
\end{aligned} \tag{5.13}$$

where we applied an RWA to obtain the third equality, and the fourth equality comes from 2.127. This additional term in the Hamiltonian thus causes a shift in the resonant frequency of the cCPT given by

$$\begin{aligned}
\Delta^{(2)}_{\text{pump}} &= \frac{\delta\Phi^2}{8}\left(\frac{2\pi}{\Phi_0}\right)^2\phi^2_{\text{zp}}\partial^4_\phi E_{\text{CPT}}(n_{\text{g}},\Phi_{\text{ext}}) \\
&= \frac{\delta\Phi^2}{2\hbar Z}K(n_{\text{g}},\Phi_{\text{ext}})
\end{aligned} \tag{5.14}$$

$$= \frac{\delta\Phi^2_{\text{dimless}}\pi^2}{\phi^2_{zp}} K(n_{\text{g}}, \Phi_{\text{ext}}), \tag{5.15}$$

where we have used the definition of the Kerr non-linearity from Eqn. 2.129. We have also used the definitions of Z and ϕ_{zp} from chapter 2. $\delta\Phi_{\text{dimless}}$ is a dimensionless quantity ($\delta\Phi$ in units of Φ_0) between 0 and 1 and is typically $\ll 1$ (see Eqn. A.3).

Looking at the 2nd case in Eqn. (5.9), we see that the boundary of the parametric instability region is defined by the $n = 0$ curve. This gives us a region in Δ-$\delta\Phi$ space defined by $\epsilon^2 = \Delta^2 + \kappa^2_{\text{tot}}/4$ which is symmetric about $\Delta = 0$. In [58] (their Γ = our $\kappa_{\text{tot}}/4$), they show in Eqn. (10) how the flux induced detuning ($\Delta^{(2)}_{\text{pump}}$) of their sample causes $\Delta \to \Delta + \Delta^{(2)}_{\text{pump}} = \Delta - \frac{2\beta\epsilon^2}{\kappa_{\text{tot}}}$ where β is appropriately defined from Eqn. (5.13) and the definition of ϵ. This creates a deformed parametric instability region defined by $\epsilon = \frac{\kappa_{\text{tot}}}{2\sqrt{2}\beta}\left(\sqrt{1 - \frac{4\beta\Delta}{\kappa_{\text{tot}}} \pm \sqrt{1 - 4\beta\left(\frac{2\Delta}{\kappa_{\text{tot}}} + \beta\right)}}\right)$.

Section 5.2

Experimental data

As seen in Fig. (5.2), we do experimentally see an asymmetry about the $\Delta = 0$ axis. However, in estimating the theoretical flux pump induced detuning using Eqn. (5.15), we note that the co-ax line in the dilution fridge used to send RF drives to the flux port of the sample sample box has an attenuation of ≈ 80 dB at room temperature (60 dB intentional attenuation, 20 dB of loss in the coax cables). Since these are stainless steel co-ax lines, we expect little change in the loss even when the fridge is at base temperature. Based on this, we can rescale the flux drive in Fig.(5.2) to range between -88 and -68 dBm at the plane of the sample. This corresponds to a peak voltage of between 12.58 μV and 125.87 μV across the 50 Ω resistance of the on-chip shorted flux transmission line, yielding peak currents of between 251.6 nA

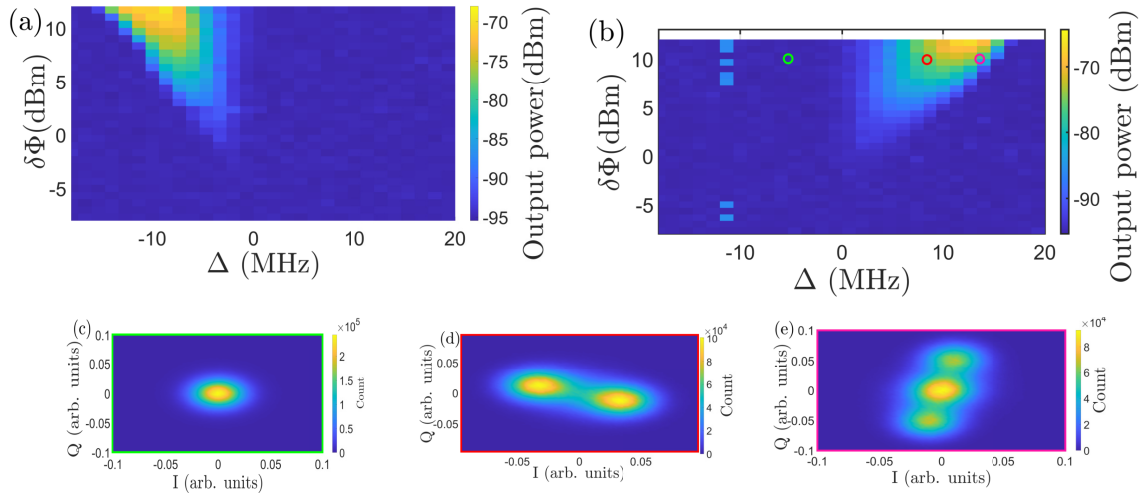

Figure 5.2: Plot of amplitude measured at spectrum analyzer at $\omega_0 - \Delta$ as a function of Δ and strength of flux drive at ω_p at the signal generator. Plots are at $n_g = 0$ and a) $\Phi_{ext} = 3\frac{\Phi_0}{8}$ and b) $\Phi_{ext} = \frac{\Phi_0}{8}$. (c) Histogram of in-phase and quadrature components measured using a heterodyne measurement for the flux pump parameters at the green circle in (b), (d) at the red circle, (e) at the pink circle. The strength of the drive is 10dBm at the source in c, d and e.

and 2.52 μA, which from the empirical DC flux period of $\approx 51\mu$A corresponds to a $\delta\Phi = 0.0049\Phi_0$ and $0.049\Phi_0$ (see Eqn.(A.3)). The flux induced detuning ($\Delta^{(2)}_{pump}$) expected for a $\delta\Phi$ =0.1 is $\approx$ 1.07 MHz $< \kappa_{tot}, \Delta$ for the $(n_g, \Phi_{ext}) = (0, 0.125\Phi_0)$ with a Kerr values of K =-0.33 MHz for our sample and does not account for this assymmetry about the $\Delta = 0$ axis. Using these numbers, the threshold flux wiggle for $\kappa_{tot} = 1.5$MHz is $\delta\Phi_c = .0108\Phi_0$ where we used the definition of ϵ and set that equal to $\kappa_{tot}/2$. This corresponds to a drive $\approx$-1 dBm at the signal generator for the cCPT bias point $(n_g, \Phi_{ext}) = (0, 0.125\Phi_0)$. This matches up with Fig. (5.2a) to within a few dBm, which could easily be attributed to variations in the attenuation of the flux line and to resonant frequency fluctuations [73].

A similar asymmetry is observed in the experiments detailed in [57]. They attribute the asymmetry as arising due to the nature of the bifurcation points described in Eqn. (5.9). For the $K > 0$ case ($(n_g, \Phi_{ext}) = (0, 0.375\Phi_0)$, see Fig. (5.2b)), as we go from $\Delta = 0$ towards the bifurcation at positive detuning, the bistable state disap-

pears and is replaced abruptly by the zero-amplitude state. On the other hand, as we go towards the bifurcation at negative detuning starting at $\Delta = 0$, the oscillations don't die out immediately beyond the bifurcation. There is some shared probability between the zero-amplitude state and the non-zero amplitude states, but the oscillations only die out when the zero-amplitude state probability becomes significant at more negative detunings. Studying the escape probabilities as in [64, 131] might yield a better understanding of what is happening. A similar asymmetry is observed in [84] albeit for a non-degenerate Josephson parametric oscillator system where two modes of a resonator are parametrically driven. As seen in Fig. (3a-d) of this work, the asymmetry between red and blue detuning exists, but is much less pronounced in experiments as compared to the theory.

However, this cannot explain the asymmetry we are seeing either. This explanation requires a non-zero oscillation amplitude on both sides of $\Delta = 0$, with the slope of the $n = 0$ boundary being flatter for $\Delta < 0$ as compared to that for $\Delta > 0$.

We also use our heterodyne detection scheme to try to recreate the 3D histograms as in [57]. With no input drive, Fig. (5.2c, d and e) show the expected zero amplitude state, the bistable non-zero amplitude states and the tri-stable state respectively, as a function of increasing Δ.

Fig.(5.3) shows the observed intracavity photons as a function of detuning, Δ, a range of flux strengths. These are horizontal slices of the surface plot in Fig.(5.2b). From Eqn.(5.10), the slope of the parametric oscillation boundary should correspond to the inverse of the Kerr at the cCPT bias point, and we obtain a value of $K = -286$ kHz close to the theoretically predicted value of -333 kHz. We also notice that the onset of parametric oscillations occurs at the same detuning close to $\Delta = 0$ for all flux pump strengths, which cannot be accounted for by flux pump induced detuning as touched upon above.

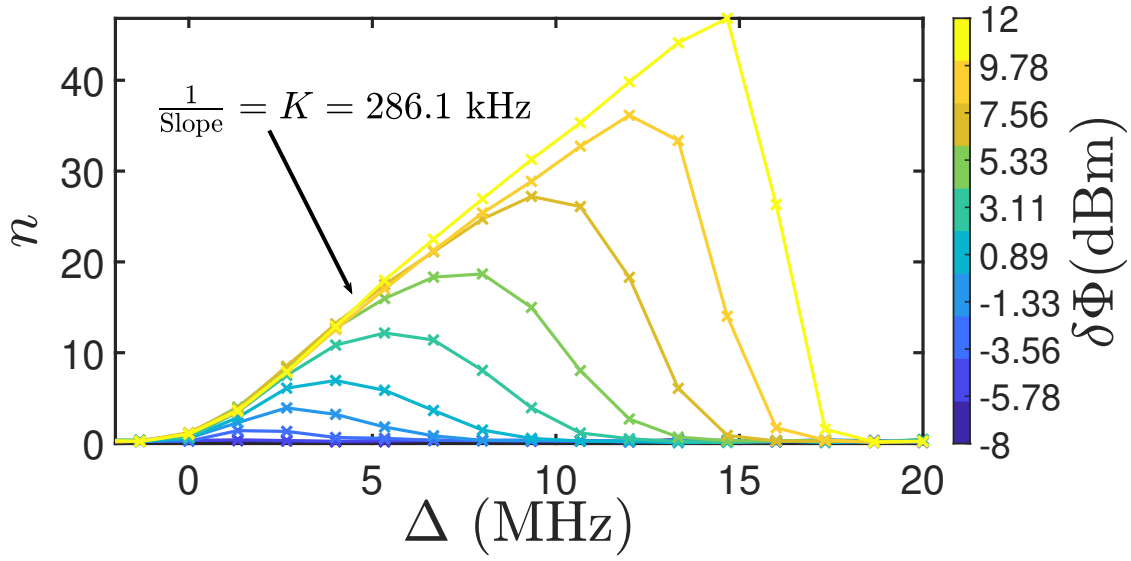

Figure 5.3: Intracavity photon number number vs detuning for a range of flux pump strengths as in Fig.(5.2b) at the same cCPT DC bias of $(n_g, \Phi_{\text{ext}}) = (0, \frac{\Phi_0}{8})$. The x's are data points, and the lines are guides to the eye.

5.2.1. Charge sensing

We now visualise a charge sensing scheme similar to the superconducting qubit state detection scheme in [61]. This is illustrated in Fig.(5.4), where by flux pumping the cCPT at the $\delta\Phi, \Delta$ point denoted in orange, we expect a non-zero amplitude of oscillations for the red gate bias n_{g1} and zero amplitude oscillations for the green gate bias n_{g2}. For a non-zero oscillation amplitude much larger than the amplifier noise broadening, we should be able to resolve these two gate states with high fidelity.

A few considerations have to be taken into account in performing such a measurement, the first being the cCPT bias point. We saw in section 4.2.2 that the cCPT is most sensitive to gate shifts at a flux of $\Phi_{\text{ext}} = 0$. The definition of ϵ in Eqn. (5.2) shows that we need $\frac{\partial\omega_0}{\partial\Phi_{\text{ext}}} \neq 0$, which is not the case at $\Phi_{\text{ext}} = 0$. So it's always going to be a tradeoff between sensitivity and parametric oscillation amplitude at a given $\delta\Phi$. Another factor to take into consideration in picking the cCPT bias are the gate and flux induced fluctuations described in [33]. These will smear out the boundary

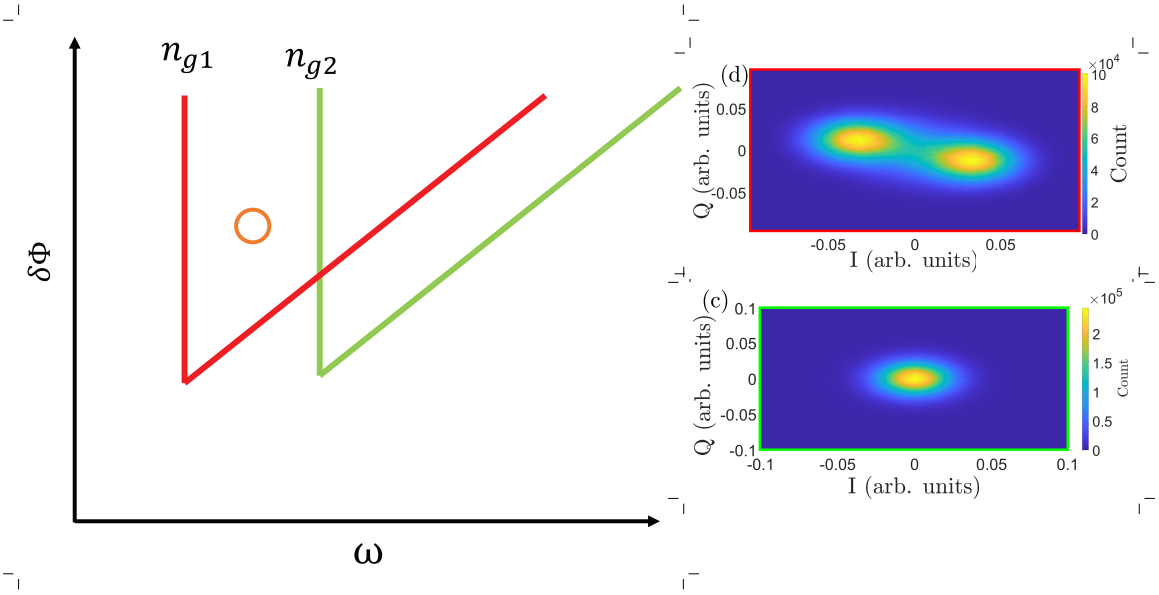

Figure 5.4: Schematic describing the idea behind using parametric oscillations to distinguish charge states. For 2 cCPT bias points $(n_{g1}, \Phi_{\text{ext}})$ and $(n_{g2}, \Phi_{\text{ext}})$ with the corresponding parametric oscillation regions denoted in red and green respectively in $\delta\Phi - \Delta$ space.

between the zero amplitude and the non-zero amplitude states and also depend on the sensitivity to gate and flux, both desirable features for this measurement. Fig.(5.5) shows such a readout for a set of parameters that have not been optimized, but yields a proof of principle measurement to show that two states $0.08e$ apart can be resolved with a fidelity of 83% in a readout time of 1 μs.

Another important consideration that turns out to be the limiting factor for our measurement is the switching between the two π separated non-zero oscillation amplitude states. A switch that occurs during the averaging period of 1 μs will give an averaged value that lies squarely in the non-zero amplitude subspace, and affects the fidelity of our readout. We see that there is a non-zero overlap between the red and the blue plots, partly because the amplitude of the non-zero amplitude state is not large enough to cause sufficient separation from the zero amplitude state in the presence of additional amplifier noise. Larger averaging times is not an option at this

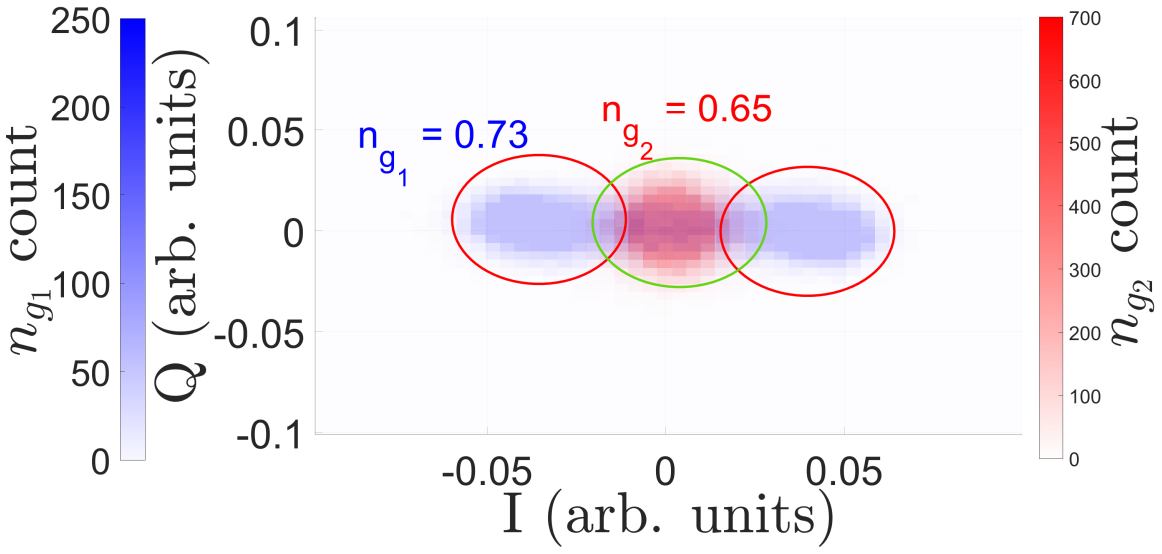

Figure 5.5: Count of I-Q histograms for two cCPT biases $(n_{g1}, \Phi_{\text{ext}}) = (0.65, 0.05\Phi_0)$ in red and $(n_{g2}, \Phi_{\text{ext}}) = (0.73, 0.05\Phi_0)$ in blue. The flux pump was set to $\delta\Phi = 15$ dBm on the signal generator, and $\omega_p = 11.5937$ GHz. Each data point was averaged for 1 μs.

pump parameter point because of the above mentioned switching, which happens more frequently during a single-shot measurement for longer averaging times.

Fig.(5.6) shows the switching between the two π-separated non-zero amplitude states over a time interval of 50μs. Though we don't perform any analysis on this, we see that the lifetime appears to be $< 10\mu$s. Performing a careful characterization of the switching life times and the probabilities as a function of the pump parameters would give us a better idea of optimal drive conditions for charge sensing.

Doing so would also give us a better physical understanding of the energy landscape around this bifurcation point and of the noise driving these transitions. Ref. [131] shows that this switching is a quantum activation process across all temperatures and parameter values.

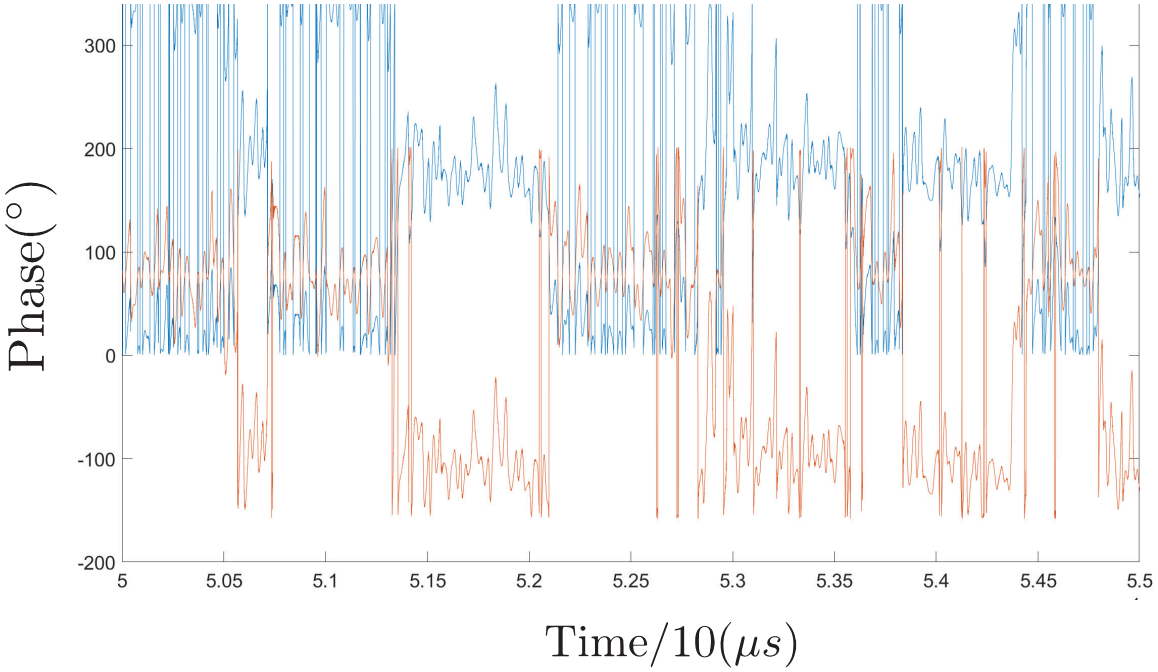

Figure 5.6: Phase measured while flux pumping the cavity with $\Delta = -19$ MHz with a flux pump $\delta\Phi = 15$ dBm on the signal generator, with the cCPT biased at $(n_g, \Phi_{\text{ext}}) = (0.73, 0.05\Phi_0)$. This is one of the bias points in the charge sensitivity measurement in Fig.(5.5). The red line is the real time phase, and the blue is the phase averaged over 2 μs. We clearly see two distinct phase states separated by $\sim 2\pi$.

Section 5.3

Conclusion

In this chapter, we have shown that pumping the flux line of the cCPT gives rise to a three-wave-mixing Hamiltonian. As predicted in [135], we observe parametric oscillations in the cCPT across a range of detunings and flux pump amplitudes above a certain parametric threshold. Operating at a mildly flux sensitive point $\Phi_{\text{ext}} = 0.05\Phi_0$, we provide an unoptimized demonstration of a charge sensing scheme where a small change in the electrostatic environment of the cCPT causes it to switch from a non-zero oscillation amplitude to a finite amplitude oscillation state which can be detected in 1 μs with a fidelity of 83%. We see switching between the metastable finite amplitude oscillation states and recognise this as being the limiting factor in

this charge measurement. A careful characterization of these switching properties across the parametric oscillation regime and over cCPT bias points as we did for the Kerr bifurcation in chapter 4, would help us better locate the optimum bias and drive conditions to perform a potentially faster, more precise charge readout.

Chapter 6

Summary and future directions

The cCPT has been demonstrated to be an ultrasensitive charge detector working in the single-photon regime [1]. In this thesis, we exploit the inherent nonlinearities in the cCPT to implement novel charge sensing schemes. In the first scheme, by driving the cCPT close to a bifurcation edge and monitoring the oscillation amplitude of the device, we are able to detect changes in the electrostatic environment of the cCPT which cause a shift of $0.09e$ on the effective gate of the cCPT island. We are able to perform single-shot readout with 92% fidelity in 3 μs, much faster than the coherence times of spin qubits [13]. We also predict and observe parametric oscillations by flux pumping the cCPT and use this to demonstrate a charge sensing scheme which can distinguish a charge of $0.08e$ in a readout time of 1 μs with 83% fidelity.

Our cCPT system has a tunable K/κ_{tot} which is in the mesoscopic regime between the JBA regime where a purely semiclassical theory describes the switching between metastable states observed in the system, and the transmon regime where a fully quantum mechanical description is required. We study the variation of the switching lifetimes and populations of the metastable states as a function of the cCPT bias and drive parameters, and draw qualitative conclusions based on the semiclassical theory. These observations drawn from the cCPT could be important in guiding understand-

ing of the mesoscopic regime of these devices which is critical in understanding the classical to quantum transition in these Kerr systems.

In the future, one of the most interesting prospects for this device is in using the CPT to enhance the optomechanical (electromechanical) coupling between the microwave cavity described in this thesis and a nanomechanical resonator(NR), as proposed in [136]. This cCPT-NR system should be able to operate in the single-photon-phonon strong coupling regime [137] which has not been experimentally achieved. Achieving this goal would mean we can generate non-classical states of the mechanical resonator [138] by addressing specific transitions in the anharmonic dressed Hamiltonian of a strongly coupled optomechanical system. Doing so in a mesoscopic object with dimensions of the order of 60 nm x 100 nm x 10 μm which corresponds to $\approx 10^8$ atoms of Si_3N_4 would aid in a better understanding of the classical-quantum transition [139].

Section 6.1

Future directions

6.1.1. Strong single-photon-phonon coupling of the cCPT-NR

Optomechanics traces its roots back to the radiation pressure of light experiment of Nichols and Hull [137] (those experiments were performed in the same building as the current work). Modern cavity optomechanics experiments have been demonstrated in a variety of systems (see [137, 79] for a review), but in particular, also in microwave frequency superconducting resonators. The typical optomechanical (OM) Hamiltonian for these systems is written as [79]

$$H_{\mathrm{OM}} = \hbar\omega_0 a^\dagger a + \hbar\omega_m b^\dagger b + \hbar g_0 a^\dagger a\big(b + b^\dagger\big), \tag{6.1}$$

where the photonic cavity and the NR have resonant frequencies $\omega_0(\omega_m)$ with associated creation/annihilation operators $a(b), a^\dagger(b^\dagger)$ respectively, and g_0 is the single photon-phonon coupling strength, which is the shift in the resonant frequency of the cavity by a movement of the NR of the order of its zero point motion, $x_{\rm zp}$.

To achieve strong coupling, systems typically drive the cavity with a large number of photons ($n_{\rm cav}$) (thus not in the single-photon-phonon strong coupling), where they have the effective linearized Hamiltonian

$$H_{\rm OM}^{\rm lin} = \hbar\omega_0 a^\dagger a + \hbar\omega_m b^\dagger b + \hbar g\big(\delta a^\dagger + \delta a\big)\big(b + b^\dagger\big), \tag{6.2}$$

where $g = g_0\sqrt{n_{\rm cav}}$ and $\delta a(\delta a^\dagger)$ are the fluctuations about the steady state large amplitude drive. These systems typically rely on a capacitive coupling of the NR to a plate of a lumped element capacitor [140] or to capacitively change the resonant frequency of a distributed cavity [141], which is typically a small effect ($g_0 = x_{\rm zp}\frac{\omega_0}{2C_1}\frac{\partial C_{\rm NR}}{\partial x}$) and gives rise to g_0 of the order of few 100 Hz[142], where C_1 is the capacitance of the cavity mode with resonant frequency ω_0 (lumped or distributed), $C_{\rm NR}$ is the capacitance of the NR to the cavity, and x is the displacement of the NR with $x = x_{\rm zp}\big(b + b^\dagger\big)$. The enhancement for the proposed cCPT-NR device comes from the fact that the OM coupling (shift in cavity resonance due to NR motion) is not just capacitive, but arises from the variation of the CPT inductance $L_{\rm J}$ (see Fig.(2.10)) as the capacitance on the CPT island due to the NR 'gate' varies because of the motion of the NR. Heuristically, this gives us

$$g_0 = x_{\rm zp}\frac{\partial\omega_0}{\partial x} = x_{\rm zp}\frac{\partial\omega_0}{\partial L_{\rm J}}\frac{\partial L_{\rm J}}{\partial n_g}\frac{\partial n_g}{\partial x} \approx -x_{\rm zp}\frac{\omega_0}{2}\frac{L_1}{L_{\rm J}^2}\frac{\partial n_g}{\partial x}, \tag{6.3}$$

where as before, we assume $L_{\rm J} \gg L_1$. For nominal values of the cavity we have $L_1 = 2$ nH (section 2.1), L_J =50 nH, $\frac{\partial L_J}{\partial n_g}$ =150 nH/electron close to $n_g = 1$ and $\omega_0 = 5$ GHz.

For the NR which is a doubly clamped beam made of a thin film of SiN of thickness 60-70 nm, with a 100 nm layer of Al deposited to apply bias, the mass of the beam is ≈ 0.2 pg. Since the wave velocity for a 'string' made of SiN is 10 m/s, this corresponds to a resonant frequency $\omega_m = 10$MHz (textbook on Nanomechanics, M. P. Blencowe, forthcoming). This yields $x_{\rm zp} = 60$ fm. Using these numbers in Eqn.(6.3), we have $g_0 \approx 4$ MHz. We want to maximize $x_{\rm zp}$ (which goes inversely with mass and resonant frequency of the NR) to the extent possible, while still working with a large resonant frequency (which scales inversely with length and hence mass) to avoid large thermal occupation of the NR. The above numbers are a suitable tradeoff where we expect a few hundred phonons thermal occupation at dilution fridge temperatures, while still preserving a relatively large $x_{\rm zp}$ compared to larger resonators [140].

This would then put us in a regime where $g_0/\kappa_{\rm tot} > 1$ where $\kappa_{\rm tot} \approx 1.5$ MHz is the total cavity linewidth as before. This would mean that motion of the NR of the order of its zero point motion would cause a cavity frequency shift larger than its linewidth, making it detectable. We would also have $2g_0/\omega_m \approx 1$, which means a single photon would cause motion of the order of $x_{\rm zp}$ on the NR. Together these requirements come down to $2g_0^2/\kappa_{\rm tot}\omega_m > 1$.

Going through a more formal derivation as in [30], but including the dynamics of the NR, we have the Hamiltonian

$$\begin{aligned} H_{\rm cCPT-NR} =& a^\dagger a\Big\{\hbar\omega_0^{\lambda/4} + \phi_{\rm zp}^2\partial_{\phi,x}^{(2,0)}E_0^{\rm CPT}(n_g,\Phi_{\rm ext}) + \frac{1}{4}\phi_{\rm zp}^4\partial_{\phi,x}^{(4,0)}E_0^{\rm CPT}(n_g,\Phi_{\rm ext})\big(a^\dagger a+1\big) \\ &+ \frac{1}{6}\partial_{\phi,x}^{(2,2)}E_0^{\rm CPT}(n_g,\Phi_{\rm ext})\phi_{\rm zp}^2 x_{\rm zp}^2\big(b+b^\dagger\big)^2\Big\} \\ &+ b^\dagger b\Big\{\hbar\omega_m + x_{\rm zp}^2\partial_{\phi,x}^{(0,2)}E_0^{\rm CPT}(n_g,\Phi_{\rm ext}) + \frac{1}{4}x_{\rm zp}^4\partial_{\phi,x}^{(0,4)}E_0^{\rm CPT}(n_g,\Phi_{\rm ext})\big(b^\dagger b+1\big)\Big\} \\ &+ \big(b+b^\dagger\big)a^\dagger a\Big\{x_{\rm zp}\phi_{\rm zp}^2\partial_{\phi,x}^{(2,1)}E_0^{\rm CPT}(n_g,\Phi_{\rm ext}) + \frac{1}{4}\phi_{\rm zp}^4 x_{\rm zp}\partial_{\phi,x}^{(4,1)}E_0^{\rm CPT}(n_g,\Phi_{\rm ext}) \\ &+ \frac{3}{10}x_{\rm zp}^3\phi_{\rm zp}^2\partial_{\phi,x}^{(2,3)}E_0^{\rm CPT}(n_g,\Phi_{\rm ext})\big(1+b^\dagger b\big)\Big\} \end{aligned} \tag{6.4}$$

where we defined

$$\partial^{(a,b)}_{\phi,x} E_0^{\mathrm{CPT}}(n_g, \Phi_{\mathrm{ext}}) = \left. \frac{\partial^{(\mathrm{a+b})} E_0^{\mathrm{CPT}}(n_g, \Phi_{\mathrm{ext}})}{\partial \phi^a \partial x^b} \right|_{\phi_{\mathrm{eq}}, x_{\mathrm{eq}}} \tag{6.5}$$

where ϕ_{eq} and x_{eq} are the equilibrium co-ordinates for the effective potential which might be non-zero unlike in section 2.5.2. The first term in curly braces is the cavity frequency renormalization term which as in section 2.5.2 contains the linear frequency shift and the self-Kerr term for the cavity but also has an NR position dependent renormalization which behaves as a cross-Kerr term in the RWA (this could also be written as a cavity dependent NR frequency shift in the 2nd curly brace) which also gets up to a few 100 kHz around charge degeneracy. The second curly braces contain the renormalized NR frequency which also includes the self-Kerr NR term. We identify the 3rd term as the OM coupling term in Eqn.(6.1), and hence have

$$\begin{aligned} g_0(n_g, \Phi_{\mathrm{ext}}) =& \frac{1}{\hbar} \Big[x_{\mathrm{zp}} \phi^2_{\mathrm{zp}} \partial^{(2,1)}_{\phi,x} E_0^{\mathrm{CPT}}(n_g, \Phi_{\mathrm{ext}}) + \frac{1}{4} \phi^4_{\mathrm{zp}} x_{\mathrm{zp}} \partial^{(4,1)}_{\phi,x} E_0^{\mathrm{CPT}}(n_g, \Phi_{\mathrm{ext}}) \\ &+ \frac{3}{10} x^3_{\mathrm{zp}} \phi^2_{\mathrm{zp}} \partial^{(2,3)}_{\phi,x} E_0^{\mathrm{CPT}}(n_g, \Phi_{\mathrm{ext}}) \big(1 + b^\dagger b\big) \Big], \end{aligned} \tag{6.6}$$

where we have defined $E_0^{\mathrm{CPT}}(n_g, \Phi_{\mathrm{ext}})$ as the ground state energy of the CPT as in section 2.5.2. We have also redefined

$$E_C = \frac{e^2 C_\Sigma}{2C_J\big(C_J + C_{\mathrm{NR}}(x)\big)}, \tag{6.7}$$

$$n_g = \frac{C_J}{2eC_\Sigma}\big(C_g V_g + C_{\mathrm{NR}}(x) V_{\mathrm{NR}}\big), \tag{6.8}$$

where we still neglect the standing gate capacitance $C_g \approx 7$ aF in $C_\Sigma = 2C_J + C_g + C_{\mathrm{NR}}$ as before since $C_g \ll C_J$, but we cannot do the same for $C_{\mathrm{NR}} \approx 100$ aF for the NR dimensions above. V_{NR} is a DC bias applied to the NR. Note that C_{NR} is a function of its position x.

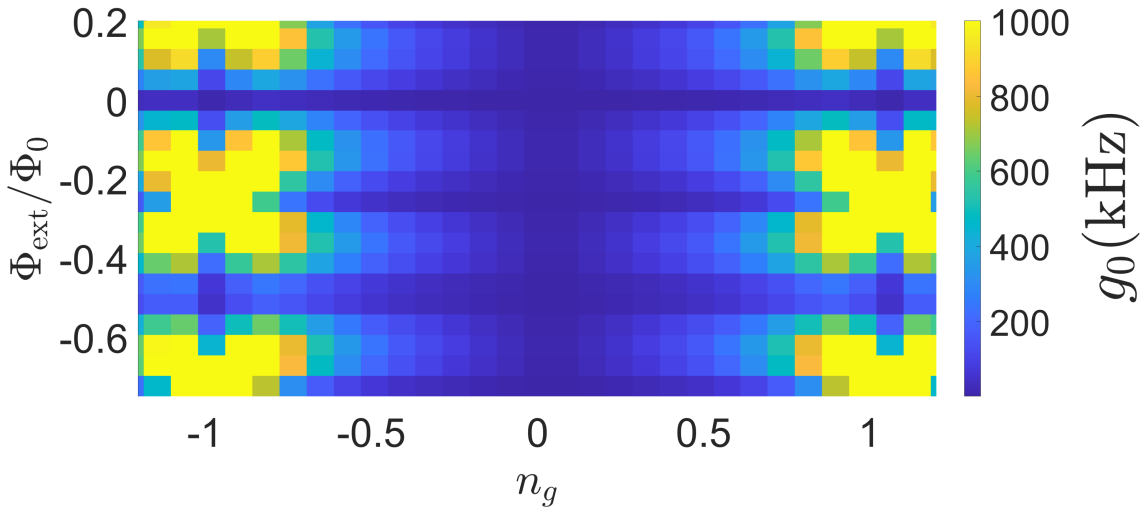

Figure 6.1: Simulated g_0 vs flux and gate for a cCPT-NR device with $E_J = 14.8$ GHz, $C_J = 206.67$ aF, $C_{\text{NR}} = 100$ aF, $V_{\text{NR}} = 10$ V and $x_{\text{zp}} = 60$ fm.

Fig. (6.1) shows the simulated g_0 as a function of a gate and flux for nominal values of the CPT and NR parameters. Close to charge degeneracy, we do see values close to the $g_0 = 4$ MHz we predicted from the heuristic method above.

6.1.2. Progress in fabrication

Here, we discuss some of the progress we made in fabricating a cCPT-NR device, the challenges we are currently facing and some potential solutions.

The cCPT-NR device consists of the same two parts as the cCPT described earlier, but in addition has a doubly-clamped beam SiN nanoresonator. The CPW is designed as before [65], but has one additional transmission line on chip to bias the NR. The main difference involves the fact that we begin with a wafer that has high stress (1100 MPa) SiN of 60 nm thickness grown on it by the Parpia group at Cornell on the same high resisitivity Si wafers as in section 3.1.1. These will eventually form the doubly-clamped beam NR. However, microwave resonators fabricated on Si_3N_4 substrates have not yielded very high Q's (Keith Schwab, personal communication).

So we need to remove the Si_3N_4 everywhere but for a small region between the center line and the ground plane of the microwave resonator, where the NR will be formed. This makes the CPW manufacturing process more complicated than for the cCPT device. Most of the fab of the CPW but for the final etch-stop removal was done by Billy Braasch at the NNIN in Harvard, but we briefly step through the entire process. The thesis by Ndukum [143] is an excellent resource for these processes.

First, a single photo mask with the different designs for various photolithography stages ((i) SiN island/Al etch-stop definition, (ii) Nb mask CPW pattern, (iii) Au contact pads definition) of the fabrication was designed and written with the mask writer tool, each with it's own fiduciary alignment marks. Using a positive photoresist, the section on each die about 2 μm high x 15 μm wide is defined using a stepper tool and 100 nm of Al is deposited in this region. This is the etch-stop to define the SiN island. After liftoff of the Al, the exposed SiN is etched in two seprate steps. The first is a dry etch in an RIE with a plasma of CHF_3 and O_2. This is a relatively fast, coarse etch, etching about 65 nm/min, and is performed until roughly 20 nm of SiN remains. The remaining SiN is then etched using a buffer-oxide-etch which etches about 0.5-1 nm/min and can be controlled much better. This is used to etch through the last of the SiN, periodically checking the thickness of the leftover Nitride using an ellipsometer. A coarse test is that water wets SiN since it is hydrophyllic, but Si is hydrophobic. Optical inspection of the color of the wafer will also give an idea as to the remaining thickness of SiN.

The next step is to put down the Au contact pads that make (superconducting) contact between the Nb and the Al as described in section 3.1.1. The difference here compared to the cCPT sample is that the Au goes under the Nb. It is still < 10 nm thick. We use a positive resist again, and photolitographically define and thermal evaporate the two gold pad structures on the center line and the ground plane of the

CPW.

Nb is then sputtered on the entire wafer by the McDermott group in Wisconsin. The CPW mask is then exposed lithographically again and the defined dielectric gaps between the center line and ground plane are etched free of Nb using an O_2, CF_4 etch. The 100 nm Al etch stop is finally removed using Transene A which etches Al at the rate of about 3 nm/s. This completes the preparation of the Nb CPW while preserving a patch of SiN for the NR to be defined.

As can be seen in Fig.(6.2), this design uses the shadow of the first layer that forms the island of the CPT to form the NR. As we saw above, we need the NR to be about 10 μm long, which means we will have a chunk of metal that long defining the CPT island as well. Before defining the CPT across the voltage anti-node, we test the DC transport properties of such a long island CPT to ensure that we continue seeing coherent transport even for such devices. Fig. (6.3) shows source-drain measurements for such a device with $R_N = 66.2\,k\Omega$ across both junctions. Measured with a setup as in chapter 2 of [144], we obtain the expected I-V characteristics offset by a thermally induced voltage ($\approx$ 7mV). In addition to the supercurrent branch in the middle, we see signs such as the double Josephson quasiparticle tunneling (DJQP) around $V_{\rm ds} = 6.6$ and 7.7 mV, and the Josephson quasiparticle tunneling (JQP) and normal transport above 4Δ, where Δ is the superconducting gap. From the onset of normal transport, we obtain $\Delta = 206\,\mu$eV which in this case would be a value between that of the thin island and the thicker leads. The distance between the small lobes in the middle would be $4E_C$, from which we obtain $E_C = 60$ GHz, which is a factor of 2 larger than we expect. From the periods of the gate variation in Figs.(6.3a and b), we calculate the $C_g = 180$ aF and $C_{\rm NR} = 230$ aF, though there is no way to see if this is $2e$ or a $1e$ periodicity (in which case the capacitances might be halved) due to QP. In any case, this seems to show that the device should work as expected even with a

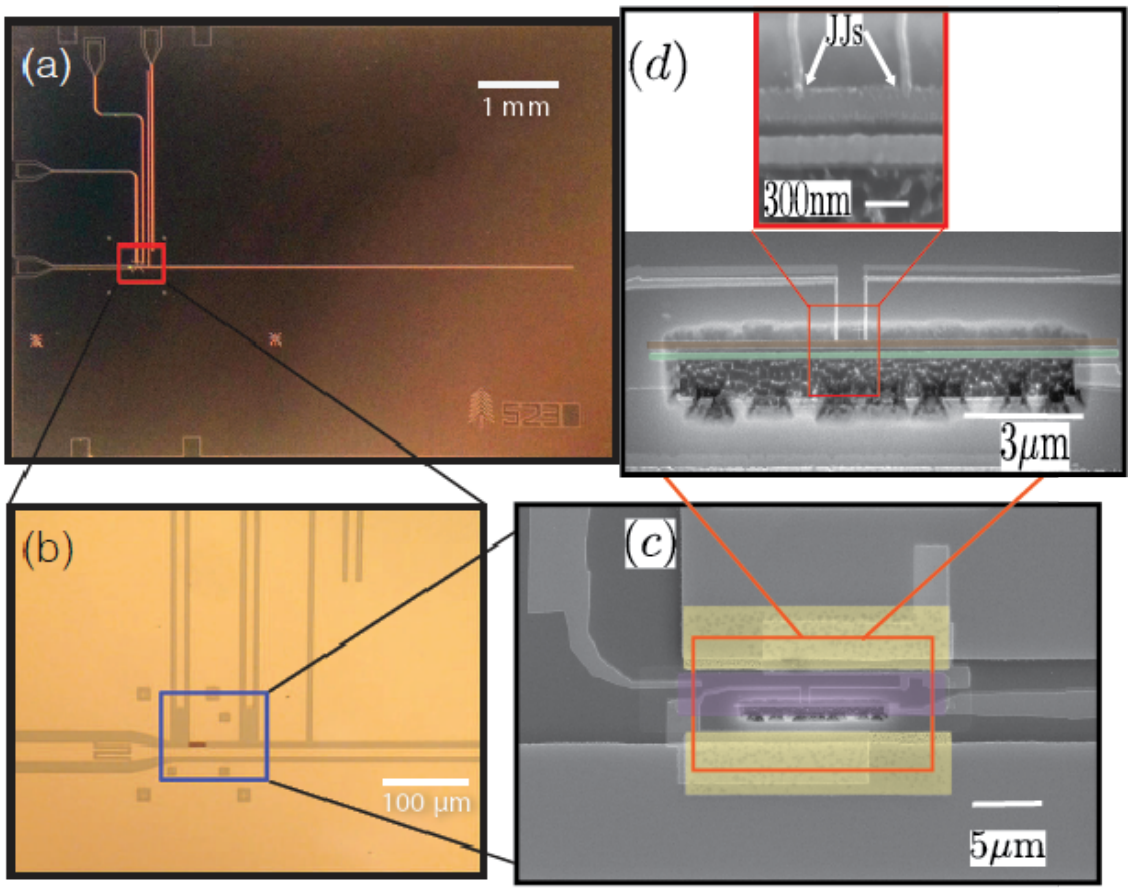

Figure 6.2: (a) false coloured micrograph of the cCPT-NR sample chip showing 4 transmission lines and the $\lambda/4$ CPW. (b) Close up of the voltage anti-node of the CPW showing the island of SiN in purple in the dielectric between the center line and ground plane of the CPW. (c) Scanning electron micrograph of the CPT-NR section of the device at the voltage anti-node. The purple hue indicates the SiN patch and the yellow, the Au. In (d) the false green represents the 10 μm NR, and the brown, the CPT island. In the inset, the sub 50 nm JJs are visible, and the contrast difference of the space above the CPT island to the space between the CPT and the NR shows that the NR is released from the substrate.

long island CPT on a SiN substrate.

We then fabricate the CPT and NR at the voltage anti-node of the CPW using ebeam lithography, as described in section 3.1. We use the geometry derivation in section 3.1 to achieve our desired 100nm width for the CPT island and the NR, and we then play with the positioning of the vertical fingers which overlap the CPT

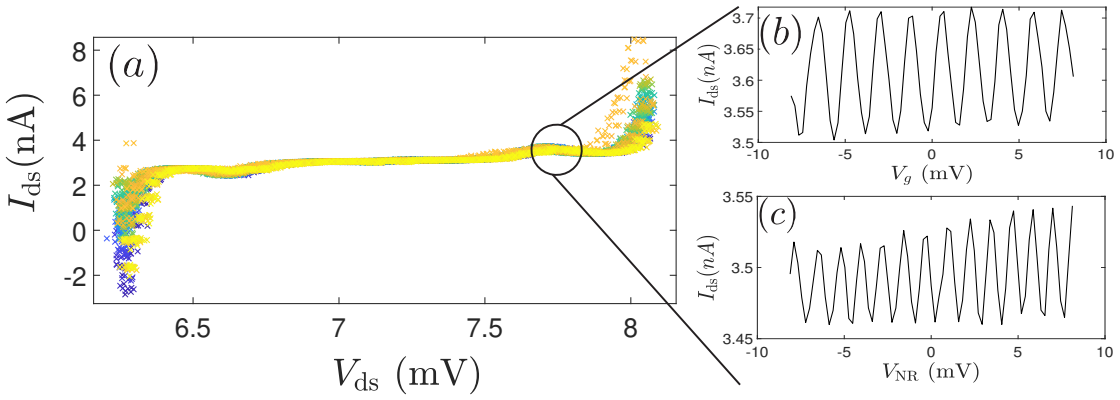

Figure 6.3: DC characterization of a CPT with island length similar to Fig.(6.2d). (a) shows I-V transport properties were measured with the NR line shorted to ground at the mixing chamber of the dilution fridge, with several different gate biases corresponding to several periods. (b) variation of drain-source current as the standing gate voltage V_g is varied while biased at the JQP feature denoted in (a). (c) Varying the NR gate voltage at the same bias point.

island to form the JJs to create an appropriately sized junction. As we saw in the DC characterization, the 100 nm spacing between the island and NR yields a rather high value for the capacitive coupling, but we are somewhat constrained in how large a separation we can reproducibly generate using this shadow technique, and we live with the reduced E_C due to this large capacitive coupling as we saw in the cCPT-NR device in section 3.3.2.

The final step of the fabrication process is to release the NR. This is done using a reactive ion plasma (RIE) etch. The first step is to open up an etch window so we can etch the substrate just around the NR while leaving all other structures tethered to it. We use a hardier (in terms of resistance to the etch) ebeam resist, which can still produce sub 100 nm resolution - GL2000 from GluonLab. The release window is a rectangle the length of the desired NR - 10 μm, whose top lies in the gap between the CPT island and the Al defining the NR subsequent to the CPT fabrication step. We then use a two step etch process - the first being an anisotropic (etches straight into the substrated) CHF_3(50 sccm), CF_4(2 sccm), H_2(15 sccm) in Ar(2 sccm) etch

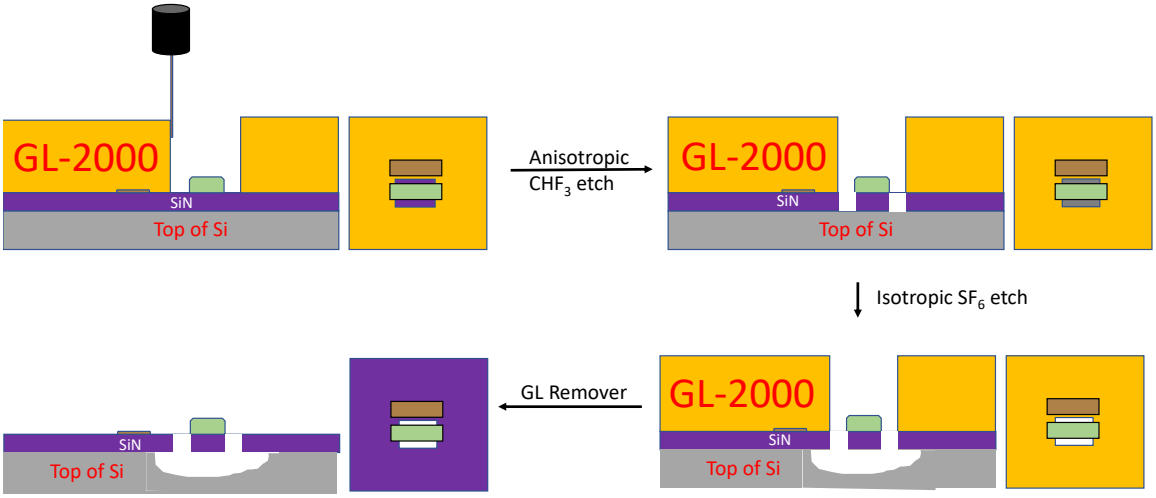

Figure 6.4: Schematic of the steps involved in releasing the NR (top view and cross section at each stage. The purple is the SiN on the gray Si substrate, the release window is the rectangle defined by ebeam lithography and lies between the bottom of the CPT island (brown as before) and the NR (green).

with a total pressure of 10 mTorr etched with a forward power of 800 W for 290 s which etches away the SiN (Fig. (6.4)). This is followed by an isotropic Si etch using SF_6(80 sccm) at a pressure of 20 mTorr and a forward power of 700 W for 35 s. This isotropic etch etches down into the substrate and under the NR to leave it untethered in the middle of the release window as shown in the above figure.

The device described in section 3.3.2 could have been used for some preliminary studies had it had a well-released NR. Even though the QP means that we will be driving the cavity well off-resonance for a good fraction of any input tone, it still had good gate and flux variation.

On subsequent devices, we had to deposit more aluminium (120 nm)to climb the step at the edge of the SiN island, and we started seeing degradation in the cCPT Q for these samples, even accounting for the Poissonian switching detailed in section

3.3.2. We were seeing degradation of the Q akin to what has been observed for microwave cavities and to the degradation of qubit T_1's in such microwave cavities [99] [110] presumably because of the generation of non-equilibrium quasiparticles by Cooper-pair-breaking IR radiation. The degradation was so bad in some samples that the resonance dip was usually of the order of 2 dB, though still tunable with DC bias. However, this degradation was never observed across several 10s of samples on any cavity that did not as yet have the CPT designed already. This seems to point to the origin of the quasiparticles being on the Al leads (or island) which form the CPT and not the Nb which forms the bulk of the cCPT-NR device. This is also borne out by the fact that this problem was exacerbated when we had to deposit more Al to climb the SiN island step. This might also indicate that the frequency of the pair-breaking radiation is between the superconducting bandgap of Al ($T_c = 1.2$ K) and that of Nb ($T_c = 9$ K)

A multi-pronged approach might be required to overcome what appears to primarily be a QP issue. (i) Try to reduce or eliminate the pair breaking radiation by coating the inside of the dilution fridge radiation can with Eccosorb as in [99]. It might be worth considering a setup where the sample is enclosed in a vacuum tight space in the mixing chamber too. (ii) Revisit the design of the sample to minimize the amount of Al. This can be done by patterning the NR in a separate step from the CPT, thereby making the CPT island smaller again, pushing E_C back up, making us less susceptible to QP on the island (section 3.3.2). We could also sputter a small piece of metal (doesn't matter what kind) at every point where a lead has to climb up the SiN island. This way, the Al forming the CPT leads can use the curvature of the sputtered step to climb the SiN island and we can get away with much less Al which is where the quasiparticles appear to be created.

Along the way, it might be worth considering going back to the Au on top of the

Nb technique adopted in the cCPT device. While this is more cumbersome in that ion milling before the Au deposition is required, a close look at Fig.(6.2c) shows that there are what appears to be discontinuities in the Au film. These might be caused by the CF_4 etching through the Nb [145].

In addition to novel applications of the single photon-phonon regime and the interesting quantum physics of mesoscopic objects, the resulting Hamiltonian 6.4 shows that a lot of non-linear terms arise out of this CPT mediated cavity-mechanics interaction, some of which can be tuned into and out of resonance in the RWA by introducing an appropriate drive as we have seen in this thesis, in addition to interesting CPT DC bias points where specific contributions are 0. It has been shown that by simultaneously driving a mechanical oscillator with a Duffing term such as ours with a blue and a red-detuned pump, the NR can be driven to the $n = 2$ Fock state [146]. The cross-Kerr term can be used to directly read out phonon number, performing a quantum non-demolition measurement since this term commutes with the NR Hamiltonian [147].

6.1.3. Non-linear charge sensing before bifurcation

We have used the cCPT as a threshold detector of charge operating in the bistable regime. But looking at the black curve in Fig.(4.2), we see that just before bifurcation, the cCPT still behaves as a continuous charge (and the cCPT-NR correspondingly a position) detector, whose dispersive phase shift with detuning has a much larger slope on the red (blue) detuning side for negative (positive) Kerr coefficients. If we drive the cCPT at a detuning on that sharp edge, we should be a lot more sensitive to charge than was measured in the linear regime in [1]. This has been suggested for a Cooper pair box in [148]. As also mentioned in that paper and observed in [33], resonant frequency fluctuations act as a deterrent in operating the cCPT in this regime. But using the technique described in [149], we might be able to lock

the resonant frequency of the cavity so the input drive is at the targeted detuning throughout the relevant measurement times. Note that an optomechanical system operating in a similar regime - with a Kerr cavity coupled to a mechanical resonator [150, 151] was proposed and has been demonstrated to achieve an order of magnitude better cooling compared to a linear cavity. A similar device has also been proposed in [148].

6.1.4. On-chip parametric amplification while performing linear charge sensing

We saw in appendix A that the cCPT acts as a Josephson Parametric amplifier (JPA), a phase sensitive amplifier when biased at a point that is not insensitive to flux and pumping the flux line at $\omega_p \approx 2\omega_0$ [55]. We could couple this with the linear charge detection scheme in [1] in order to achieve larger SNR at the sidebands at the output of the chip. So far, when operating below the parametric threshold, we only observe parametric gain at half the pump frequency ($\omega_p/2$), and not at the modulated sideband frequencies whose measurement is what constitutes a charge sensor, but we envision performing a charge sensing experiment as in [1] with a single photon level input tone at $\omega_0 \pm \omega_g$, while modulating the gate line with a frequency ω_g of the order of a few hundred kHz, and then flux pumping the cavity at $2\omega_0$, such that one of the sidebands from the gate modulation gets amplified by the phase-coherent degenerate operation, as observed in section A.2.

Appendix A

Parametric amplification in the cCPT operating below the parametric threshold

In section A.1, we derive the Hamiltonian for the flux pumped cCPT and then an expression for the expected gain. We will then show in section A.2 some data that demonstrates the expected behaviour for a phase-coherent degenerate parametric amplifier [152, 55]. We try to demonstrate enhancement in linear charge sensing performed similar to [1] by using the parametric gain to enhance the SNR of the sidebands, and present that data. Then, on a different note, we show some examples of data while pumping the flux line at a frequency $3\omega_0$ generating sub-harmonic oscillations at the fundamental mode of the cavity. Such period tripling has been demonstrated in a SQUID terminated cavity [153]where a $3\omega_0$ drive tone at the input to the cavity drove the fundamental mode using a two-mode subharmonic resonance between the fundamental and the first harmonic mode of the system, opening the path to entanglement between the two modes. Flux pumping the same system at $3\omega_0$ also generated period-tripling [154], similar to what we see in the cCPT, which could

be a path to realising a phase space crystal described in [155].

Section A.1

Theory

Beginning from Eqns. 2.118 and 2.125, the effective cCPT Hamiltonian is given by

$$H_{\mathrm{cCPT}} = \frac{Q^2}{2C} + \frac{\Phi^2}{2L} + \sum_{k=0}^{\infty} \frac{1}{k!} \partial_\phi^k E_{\mathrm{CPT}}(n_g, \Phi_{\mathrm{ext}}) \left(\frac{2\pi\Phi}{\Phi_0} \right)^k \tag{A.1}$$

$$= \frac{Q^2}{2C} + \frac{\Phi^2}{2L} + \sum_{k=0}^{\infty} \frac{\phi_{\mathrm{zp}}^k}{k!} \partial_\phi^k E_{\mathrm{CPT}}(n_g, \Phi_{\mathrm{ext}}) \left(a + a^\dagger \right)^k . \tag{A.2}$$

Modulating the flux through the squid loop such that at a frequency $\omega_p \approx 2\omega_0$, where ω_0 is the resonant frequency of the cCPT for the DC bias point $(n_g, \Phi_{\mathrm{ext}})$

$$\Phi_{\mathrm{ext}} \to \Phi_{\mathrm{ext}} + \delta\Phi \cos\left(\omega_p t + \phi_p\right) \tag{A.3}$$

with a period of Φ_0 and since $\delta\Phi \ll \Phi_{\mathrm{ext}}$, we can Taylor expand the Hamiltonian to first order in $\delta\Phi$ about the equilibrium DC flux Φ_{ext}. By doing so, in addition to the usual tunable linear oscillator and Kerr terms (see eqn. (18) in [33]), we have the term

$$H_{\mathrm{pump}} = \delta\Phi \cos\left(\omega_p t + \phi_p\right) \frac{\partial}{\partial \Phi_{\mathrm{ext}}} \left[\sum_{k=0}^{\infty} \frac{1}{k!} \phi_{\mathrm{zp}}^k \partial_\phi^k E_{\mathrm{CPT}}(n_g, \Phi_{\mathrm{ext}}) (a + a^\dagger)^k \right] \tag{A.4}$$

$$= \frac{\delta\Phi}{2} (e^{i\omega_p t} e^{i\Phi_p} + e^{-i\omega_p t} e^{-i\Phi_p}) \sum_{k=0}^{\infty} (a + a^\dagger)^k \frac{\partial}{\partial \Phi_{\mathrm{ext}}} \left[\frac{1}{k!} \phi_{\mathrm{zp}}^k \partial_\phi^k E_{\mathrm{CPT}}(n_g, \Phi_{\mathrm{ext}}) \right] . \tag{A.5}$$

Since a and $a^\dagger$ oscillate as $a(0)e^{-i\omega_0 t}$ and $a^\dagger(0)e^{i\omega_0 t}$ respectively, we can apply a rotating wave approximation and drop all terms that oscillate fast in a frame rotating

at $\omega_p/2$, giving the modified pump Hamiltonian

$$H_{\text{pump}}^{\text{RWA}} = \frac{\delta\Phi}{2}(e^{i\omega_p t}e^{i\Phi_p}a^2 + e^{-i\omega_p t}e^{-i\Phi_p}a^{\dagger 2})\frac{\partial}{\partial\Phi_{\text{ext}}}\left[\frac{1}{2}\phi_{\text{zp}}^2\partial_\Phi^2 E_{\text{CPT}}(n_g, \Phi_{\text{ext}})\right] \tag{A.6}$$

$$= \frac{\hbar}{4}\frac{\partial\omega_0}{\partial\Phi_{\text{ext}}}\delta\Phi(e^{i\omega_p t}e^{i\Phi_p}a^2 + e^{-i\omega_p t}e^{-i\Phi_p}a^{\dagger 2}), \tag{A.7}$$

where $\hbar\omega_0 = \phi_{\text{zp}}^2\partial_\phi^2 E_{\text{CPT}}(n_g, \Phi_{\text{ext}})$

Taking the RWA of our original cCPT Hamiltonian (A.2) before application of a flux pump as in eqn.(C1) of [33] and adding the above pump Hamiltonian (A.7), we can now write the total Hamiltonian of the cCPT with a parametric flux drive at ω_p as

$$H = \hbar\omega_0 a^\dagger a + \frac{\hbar K}{2}a^{\dagger 2}a^2 + \frac{\hbar}{2}(\epsilon e^{i\omega_p t}a^2 + \epsilon^* e^{-i\omega_p t}a^{\dagger 2}), \tag{A.8}$$

where $\epsilon = \frac{1}{2}\frac{\partial\omega_0}{\partial\Phi_{\text{ext}}}\delta\Phi e^{i\Phi_p}$

We can now transform to the frame rotating at $\omega_p/2$ using the relations

$$H' \to U^\dagger H U - i\hbar U\partial_t U^\dagger \tag{A.9}$$

$$\implies H' \to U^\dagger H U - \frac{\hbar\omega_p}{2}a^\dagger a \tag{A.10}$$

$$a \to U^\dagger a U = a e^{\frac{-i\omega_p t}{2}} \tag{A.11}$$

$$a^\dagger \to U^\dagger a^\dagger U = a^\dagger e^{\frac{i\omega_p t}{2}}, \tag{A.12}$$

where $U = e^{\frac{-i\omega_p t}{2}a^\dagger a}$. Using these in (A.8) yields the rotating frame Hamiltonian

$$H_{\text{cCPT}}^{\text{rot}} = \hbar\Delta a^\dagger a + \frac{\hbar K}{2}a^{\dagger 2}a^2 + \frac{\hbar}{2}(\epsilon a^2 + \epsilon^* a^{\dagger 2}), \tag{A.13}$$

where we define the detuning, $\Delta = \omega_0 - \frac{\omega_p}{2}$.

Writing down the quantum Langevin equations for Hamiltonian (A.13) yields

$$\begin{aligned}\dot{a} &= \frac{-i}{\hbar}\left[a, H_{\mathrm{cCPT}}^{\mathrm{rot}}\right] - \left[a, a^\dagger\right]\left[\frac{\kappa_{\mathrm{tot}}}{2}a - \sqrt{\kappa_{\mathrm{int}}}b_{\mathrm{in}} - \sqrt{\kappa_{\mathrm{ext}}}a_{\mathrm{in}}\right], \\ &= -i(\Delta + Ka^\dagger a)a - i\epsilon^* a^\dagger - \frac{\kappa_{\mathrm{tot}}}{2}a + \sqrt{\kappa_{\mathrm{int}}}b_{\mathrm{in}} + \sqrt{\kappa_{\mathrm{ext}}}a_{\mathrm{in}} \qquad \text{(A.14)} \\ \dot{a}^\dagger &= \frac{-i}{\hbar}\left[a^\dagger, H_{\mathrm{cCPT}}^{\mathrm{rot}}\right] + \left[\frac{\kappa_{\mathrm{tot}}}{2}a^\dagger - \sqrt{\kappa_{\mathrm{int}}}b_{\mathrm{in}}^\dagger - \sqrt{\kappa_{\mathrm{ext}}}a_{\mathrm{in}}^\dagger\right]\left[a^\dagger, a\right] \\ &= i(\Delta + Ka^\dagger a)a^\dagger + i\epsilon a - \frac{\kappa_{\mathrm{tot}}}{2}a^\dagger + \sqrt{\kappa_{\mathrm{int}}}b_{\mathrm{in}}^\dagger + \sqrt{\kappa_{\mathrm{ext}}}a_{\mathrm{in}}^\dagger, \qquad \text{(A.15)}\end{aligned}$$

where κ_{ext} is the decay constant associated with the capacitive coupling of the cavity to the probe transmission line, κ_{int} accounts for internal cavity losses and $\kappa_{\mathrm{tot}} = \kappa_{\mathrm{ext}} + \kappa_{\mathrm{int}}$. We have neglected a term $-Ka^\dagger a$ in eqn. (A.15) since the single photon Kerr shift in our system is typically of the order of $K = 0.5\mathrm{MHz} < \kappa_{tot}/2$ and produces negligible effect on the detuning.

Taking the Fourier transform of Eqns. (A.14) and (A.15), we obtain

$$\begin{aligned}-i\omega a(\omega) &= -i(\Delta + Ka^\dagger a)a(\omega) - i\epsilon^* a^\dagger(-\omega) - \frac{\kappa_{\mathrm{tot}}}{2}a(\omega) + \sqrt{\kappa_{\mathrm{int}}}b_{\mathrm{in}}(\omega) + \sqrt{\kappa_{\mathrm{ext}}}a_{\mathrm{in}}(\omega) \\ \Rightarrow a(\omega) &= \frac{1}{\frac{\kappa_{\mathrm{tot}}}{2} - i(\omega - (\Delta + Ka^\dagger a))}\left[-i\epsilon^* a^\dagger(-\omega) + (\sqrt{\kappa_{\mathrm{int}}}b_{\mathrm{in}}(\omega) + \sqrt{\kappa_{\mathrm{ext}}}a_{\mathrm{in}}(\omega)\right],\end{aligned} \qquad \text{(A.16)}$$

and

$$\begin{aligned}-i\omega a^\dagger(-\omega) &= i(\Delta + Ka^\dagger a)a^\dagger(-\omega) + i\epsilon a(\omega) - \frac{\kappa_{\mathrm{tot}}}{2}a^\dagger(-\omega) + \sqrt{\kappa_{\mathrm{int}}}b_{\mathrm{in}}^\dagger(-\omega) + \sqrt{\kappa_{\mathrm{ext}}}a_{\mathrm{in}}^\dagger(-\omega) \\ \Rightarrow a^\dagger(-\omega) &= \frac{1}{\frac{\kappa_{\mathrm{tot}}}{2} - i(\omega + (\Delta + Ka^\dagger a))}\left[i\epsilon a(\omega) + (\sqrt{\kappa_{\mathrm{int}}}b_{\mathrm{in}}^\dagger(-\omega) + \sqrt{\kappa_{\mathrm{ext}}}a_{\mathrm{in}}^\dagger(-\omega))\right].\end{aligned} \qquad \text{(A.17)}$$

Simultaneously solving Eqns. (A.16) and (A.17), we obtain,

$$a(\omega) = \frac{1}{\left((\frac{\kappa_{\text{tot}}}{2} - i\omega)^2 + (\Delta + Ka^\dagger a)^2 - |\epsilon|^2\right)} \times \left[-i\epsilon^*(\sqrt{\kappa_{\text{int}}}b_{\text{in}}^\dagger(-\omega) + \sqrt{\kappa_{\text{ext}}}a_{\text{in}}^\dagger(-\omega)) + \left(\frac{\kappa_{\text{tot}}}{2} - i(\omega + \Delta + Ka^\dagger a)\right)(\sqrt{\kappa_{\text{int}}}b_{\text{in}}(\omega) + \sqrt{\kappa_{\text{ext}}}a_{\text{in}}(\omega))\right], \tag{A.18}$$

$$a^\dagger(-\omega) = \frac{1}{\left((\frac{\kappa_{\text{tot}}}{2} - i\omega)^2 + (\Delta + Ka^\dagger a)^2 - |\epsilon|^2\right)} \times \left[i\epsilon(\sqrt{\kappa_{\text{int}}}b_{\text{in}}(\omega) + \sqrt{\kappa_{\text{ext}}}a_{\text{in}}(\omega)) + \left(\frac{\kappa_{\text{tot}}}{2} - i(\omega - (\Delta + Ka^\dagger a))\right)\left(\sqrt{\kappa_{\text{int}}}b_{\text{in}}^\dagger(-\omega) + \sqrt{\kappa_{\text{ext}}}a_{\text{in}}^\dagger(-\omega)\right)\right]. \tag{A.19}$$

To extract the output field operators, we use the input-output relation [74], [75],

$$a_{\text{out}}(\omega) = a_{\text{in}}(\omega) - \sqrt{\kappa_{\text{ext}}}a(\omega). \tag{A.20}$$

Using Eqns. (A.18) and (A.19) in eqn. (A.20) and its complex conjugate, we have

$$a_{\text{out}}(\omega) = \frac{1}{\left(\frac{\kappa_{\text{tot}}}{2} - i\omega\right)^2 + (\Delta + Ka^\dagger a)^2 - |\epsilon|^2} \times \left[\left(\frac{\kappa_{\text{tot}}^2}{4} - \omega^2 - i\omega\kappa_{\text{tot}} + \left(\Delta + Ka^\dagger a\right)^2 - |\epsilon|^2 - \frac{\kappa_{\text{ext}}\kappa_{\text{tot}}}{2} + i\kappa_{\text{ext}}(\omega + \Delta + Ka^\dagger a)a_{\text{in}}(\omega)\right) - \left(\frac{\kappa_{\text{tot}}}{2} - i(\omega + \Delta + Ka^\dagger a)\right)\sqrt{\kappa_{\text{int}}\kappa_{\text{ext}}}b_{\text{in}}(\omega) + i\epsilon^*\left(\kappa_{\text{ext}}a_{\text{in}}^\dagger(-\omega) + \sqrt{\kappa_{\text{int}}\kappa_{\text{ext}}}b_{\text{in}}^\dagger(-\omega)\right)\right], \tag{A.21}$$

$$a^\dagger_{\rm out}(-\omega) = \frac{1}{\left(\frac{\kappa_{\rm tot}}{2} - i\omega\right)^2 + (\Delta + Ka^\dagger a)^2 - |\epsilon|^2} \times \left[\left(\frac{\kappa_{\rm tot}^2}{4} - \omega^2 - i\omega\kappa_{\rm tot} + \left(\Delta + Ka^\dagger a\right)^2 - |\epsilon|^2 - \frac{\kappa_{\rm ext}\kappa_{\rm tot}}{2} + i\kappa_{\rm ext}(\omega - (\Delta + Ka^\dagger a))a^\dagger_{\rm in}(-\omega) \right) - \left(\frac{\kappa_{\rm tot}}{2} - i(\omega - (\Delta + Ka^\dagger a)) \right) \sqrt{\kappa_{\rm int}\kappa_{\rm ext}} b^\dagger_{\rm in}(-\omega) - i\epsilon \left(\kappa_{\rm ext} a_{\rm in}(\omega) + \sqrt{\kappa_{\rm int}\kappa_{\rm ext}} b_{\rm in}(\omega) \right) \right]. \tag{A.22}$$

When we set $\Delta = 0$ for the above case of a phase-coherent degenerate parametric amplifier, and when $K = 0$, Eqn. (A.21) reduces to Eqn. (10.2.21) in [75] up to signs arising from a slightly different definition of constants in the Hamiltonian.

To connect with [54], Eqns. (A.21) and (A.22) can be rewritten as

$$\begin{bmatrix} a_{\rm out}(\omega) \\ a^\dagger_{\rm out}(-\omega) \\ b_{\rm out}(\omega) \\ b^\dagger_{\rm out}(-\omega) \end{bmatrix} = \begin{bmatrix} G_{\rm ext}(\omega) & M_{\rm ext}(\omega) & G_{\rm int}(\omega) & M_{\rm int}(\omega) \\ M^*_{\rm ext}(-\omega) & G^*_{\rm ext}(-\omega) & M^*_{\rm int}(-\omega) & G^*_{\rm int}(-\omega) \\ X_{\rm ext}(\omega) & Y_{\rm ext}(\omega) & X_{\rm int}(\omega) & Y_{\rm int}(\omega) \\ Y^*_{\rm ext}(-\omega) & X^*_{\rm ext}(-\omega) & Y^*_{\rm int}(\omega) & X^*_{\rm int}(-\omega) \end{bmatrix} \begin{bmatrix} a_{\rm in}(\omega) \\ a^\dagger_{\rm in}(-\omega) \\ b_{\rm in}(\omega) \\ b^\dagger_{\rm in}(-\omega) \end{bmatrix} \tag{A.23}$$

where

$$G_{\rm ext}(\omega) = \frac{\frac{\kappa_{\rm tot}^2}{4} - \omega^2 + (\Delta + Ka^\dagger a)^2 - |\epsilon|^2 - \frac{\kappa_{\rm ext}\kappa_{\rm tot}}{2} - i\omega\kappa_{\rm tot} + i\kappa_{\rm ext}(\omega + \Delta + Ka^\dagger a)}{\left(\frac{\kappa_{\rm tot}}{2} - i\omega\right)^2 + (\Delta + Ka^\dagger a)^2 - |\epsilon|^2}, \tag{A.24}$$

$$M_{\rm ext}(\omega) = \frac{i\epsilon^*\kappa_{\rm ext}}{\left(\frac{\kappa_{\rm tot}}{2} - i\omega\right)^2 + (\Delta + Ka^\dagger a)^2 - |\epsilon|^2}, \tag{A.25}$$

$$M_{\text{int}}(\omega) = \frac{i\epsilon^* \sqrt{\kappa_{\text{ext}}\kappa_{\text{int}}}}{\left(\frac{\kappa_{\text{tot}}}{2} - i\omega\right)^2 + (\Delta + Ka^\dagger a)^2 - |\epsilon|^2}, \tag{A.26}$$

$$G_{\text{int}}(\omega) = \frac{-\left(\frac{\kappa_{\text{tot}}}{2} - i(\omega + \Delta + Ka^\dagger a)\right)\sqrt{\kappa_{\text{int}}\kappa_{\text{ext}}}}{\left(\frac{\kappa_{\text{tot}}}{2} - i\omega\right)^2 + (\Delta + Ka^\dagger a)^2 - |\epsilon|^2}. \tag{A.27}$$

We can verify that

$$\begin{aligned} &\left|G_{\text{ext}}^2\right| - \left|M_{\text{ext}}^2\right| + |G_{\text{int}}|^2 - |M_{\text{int}}|^2 = 1, \\ &G_{\text{ext}}(\omega)M_{\text{ext}}(-\omega) - M_{\text{ext}}(\omega)G_{\text{ext}}(-\omega) + G_{\text{int}}(\omega)M_{\text{int}}(-\omega) - M_{\text{int}}(\omega)G_{\text{int}}(-\omega) = 0, \end{aligned} \tag{A.28}$$

which preserve the commutation relations of the output operators. Since the b_{out} and $b_{\text{out}}^\dagger$ fields are experimentally inaccessible, we don't concern ourselves with the expressions for X_{ext}, X_{int}, Y_{int} and Y_{ext}. When the input is a signal of power $|\alpha_{\text{in}}|^2$ at $\omega_s = \frac{\omega_p}{2} + \omega = \omega_0 + \omega$, where ω is comparable to κ_{tot}, $G_{\text{ext}}(\omega)$ is the amplitude gain at the signal frequency, and $M_{\text{ext}}(-\omega)$ is the amplitude conversion gain (idler gain) at $\omega_I = \frac{\omega_p}{2} - \omega = \omega_0 - \omega$. This describes the process of three-wave mixing, where one photon at the pump frequency ω_p gives rise to one photon each at ω_s and ω_I. To simplify notation in what follows, we have set $\Delta = 0$. All of the following equations hold for $\Delta \neq 0$ with the substitution $\omega_0 \to \omega_0 - \Delta$ (or $\omega \to \omega + \Delta$ since $\omega \ll \omega_0$).

Using the definitions of the transmission line current in appendix C of [76] and section II of [30], as we did in section 2.2.1), we identify the output current at the RF port of the subsequent mixer $I_{\text{out}}(x,t)$ as the left travelling component of the current in the transmission line and write it in terms of the output operators as

$$\begin{aligned} I_{\text{out}}(x,t) = i\sqrt{\frac{\hbar}{4\pi Z_0}} \int_{-\infty}^{\infty} d\omega' \sqrt{\omega' + \omega_0} \\ \times \left[e^{-i(\omega'+\omega_0)(\frac{x}{v_p}+t)} a_{\text{out}}(\omega' + \omega_0) + e^{i(\omega'+\omega_0)(\frac{x}{v_p}+t)} a_{\text{out}}^\dagger(\omega' + \omega_0)\right], \end{aligned} \tag{A.29}$$

$$I^{\dagger}_{\rm out}(x,t) = -i\sqrt{\frac{\hbar}{4\pi Z_0}}\int_{-\infty}^{\infty} d\omega' \sqrt{\omega' + \omega_0} \times \left[e^{-i(\omega'+\omega_0)(\frac{x}{v_p}+t)} a_{\rm out}(\omega'+\omega_0) + e^{i(\omega'+\omega_0)(\frac{x}{v_p}+t)} a^{\dagger}_{\rm out}(\omega'+\omega_0)\right], \tag{A.30}$$

where v_p is the microwave propagation velocity in the transmission line, and the mixer is located at $x \to \infty$ - the furthest extreme from the coupling capacitor on the sample chip. $Z_0 = 50\Omega$ is the characteristic impedance of the transmission line.

We now perform a homodyne measurement of the output field, by mixing the output signal with a strong local oscillator (LO) at frequency $\omega_0 = \frac{\omega_p}{2}$ and a phase $\Phi_{\rm LO}$. Both the signal and idler tones mix with this LO to produce a signal at $+\omega$. For an LO of the form

$$I_{\rm LO}(t) = 2|\alpha_{\rm LO}|\cos(\omega_0 t + \Phi_{\rm LO}) = |\alpha_{\rm LO}|[e^{i(\omega_0 t + \Phi_{\rm LO}} + e^{-i(\omega_0 t + \Phi_{\rm LO})}], \tag{A.31}$$

the current output at the IF port of the mixer $I_{\rm IF}(x,t)$ is given by the product of Eqns. (A.29) and (A.31)

$$\begin{aligned} I_{\rm IF}(x,t) = 2i\sqrt{\frac{\hbar}{4\pi Z_0}}|\alpha_{\rm LO}|\sqrt{\omega_0}\int_0^{\infty} d\omega'' \Bigg[& e^{-i(\omega''+\omega_0)\frac{x}{v_p}} e^{-i\omega'' t} e^{i\Phi_{\rm LO}} a_{\rm out}(\omega''+\omega_0) \\ & + e^{-i(\omega_0-\omega'')\frac{x}{v_p}} e^{i\omega'' t} e^{i\Phi_{\rm LO}} a_{\rm out}(\omega_0-\omega'') \\ & + e^{i(\omega_0+\omega'')\frac{x}{v_p}} e^{i\omega'' t} e^{-i\Phi_{\rm LO}} a^{\dagger}_{\rm out}(\omega_0+\omega'') \\ & + e^{i(\omega_0-\omega'')\frac{x}{v_p}} e^{-i\omega'' t} e^{-i\Phi_{\rm LO}} a^{\dagger}_{\rm out}(\omega_0-\omega'')\Bigg], \end{aligned} \tag{A.32}$$

$$\begin{aligned} I^{\dagger}_{\rm IF}(x,t) = -2i\sqrt{\frac{\hbar}{4\pi Z_0}}|\alpha_{\rm LO}|\sqrt{\omega_0}\int_0^{\infty} d\omega' \Bigg[& e^{i(\omega'+\omega_0)\frac{x}{v_p}} e^{i\omega' t} e^{-i\Phi_{\rm LO}} a_{\rm out}(\omega'+\omega_0) \\ & + e^{i(\omega_0-\omega')\frac{x}{v_p}} e^{-i\omega' t} e^{-i\Phi_{\rm LO}} a_{\rm out}(\omega_0-\omega') \end{aligned}$$

$$+ e^{-i(\omega_0+\omega')\frac{x}{v_p}} e^{-i\omega' t} e^{i\Phi_{\rm LO}} a^\dagger_{\rm out}(\omega_0+\omega')$$
$$+ e^{-i(\omega_0-\omega')\frac{x}{v_p}} e^{i\omega'' t} e^{i\Phi_{\rm LO}} a^\dagger_{\rm out}(\omega_0-\omega')\Big], \quad \text{(A.33)}$$

where we have made the approximations $\omega', \omega'' \ll \omega_0$ and neglected the terms oscillating at $2\omega_0 \pm \omega$ since these are low pass filtered. We have also explicitly indicated that the output operators oscillate at frequencies around ω_0 unlike in the rotating frame version of (A.23).The lower limits of the integral have changed to 0 because we have explicitly written out the negative frequency output operators to make connection with the idler gain.

As in [128], [54] and [30], the power spectrum $P(\omega)$ of the homodyne detector output detected by a spectrum analyzer measuring with a resolution bandwidth $\Delta\omega$ about the center frequency $\omega = \omega_s - \omega_0$ averaged over a measurement time T_M is

$$P_{\rm SA}(\omega, \Delta\omega) = \langle \overline{I^\dagger_{\rm IF}(x,t|\omega,\Delta\omega) I_{\rm IF}(x,t|\omega,\Delta\omega)} \rangle Z_0 \quad \text{(A.34)}$$
$$= \frac{1}{T_M} \int_{-\frac{T_M}{2}}^{\frac{T_M}{2}} dt \langle {I_{\rm IF}}^\dagger(x,t|\omega,\Delta\omega) I_{\rm IF}(x,t|\omega,\Delta\omega) \rangle Z_0, \quad \text{(A.35)}$$

where $I_{\rm IF}(x,t|\omega,\Delta\omega)(I^\dagger_{\rm IF}(x,t|\omega,\Delta\omega))$ refers to Eqns.(A.32) and (A.33) but with the limits of the frequency integral running from $\omega_s - \frac{\Delta\omega}{2}$ to $\omega_s + \frac{\Delta\omega}{2}$.

We then have for the output power

$$P_{\rm SA}(\omega) = \frac{\hbar\omega_0}{\pi} |\alpha_{\rm LO}|^2 \int_{\omega_s-\frac{\Delta\omega}{2}}^{\omega_s+\frac{\Delta\omega}{2}} \int_{\omega_s-\frac{\Delta\omega}{2}}^{\omega_s+\frac{\Delta\omega}{2}} d\omega' d\omega''$$
$$\times \Bigg\{ \frac{2\sin\left[(\omega'-\omega'')T_M/2\right]}{(\omega'-\omega'')T_M} \Big[\langle e^{i(\omega'-\omega'')\frac{x}{v_p}} a^\dagger_{\rm out}(\omega') a_{\rm out}(\omega'') \rangle$$
$$+ \langle e^{i(2\omega_0+\omega'-\omega'')\frac{x}{v_p}} e^{-2i\Phi_{\rm LO}} a^\dagger_{\rm out}(\omega') a^\dagger_{\rm out}(-\omega'') \rangle$$
$$+ \langle e^{i(\omega''-\omega')\frac{x}{v_p}} a^\dagger_{\rm out}(-\omega') a_{\rm out}(-\omega'') \rangle$$
$$+ \langle e^{i(2\omega_0+\omega''-\omega')\frac{x}{v_p}} e^{-2i\Phi_{\rm LO}} a^\dagger_{\rm out}(-\omega') a^\dagger_{\rm out}(\omega'') \rangle$$

$$
\begin{aligned}
&+ \langle e^{-i(2\omega_0+\omega'-\omega'')\frac{x}{v_p}} e^{2i\Phi_{\mathrm{LO}}} a_{\mathrm{out}}(\omega') a_{\mathrm{out}}(-\omega'')\rangle \\
&+ \langle e^{-i(\omega'-\omega'')\frac{x}{v_p}} a_{\mathrm{out}}(\omega') a^{\dagger}_{\mathrm{out}}(\omega'')\rangle \\
&+ \langle e^{-i(2\omega_0+\omega''-\omega')\frac{x}{v_p}} e^{2i\Phi_{\mathrm{LO}}} a_{\mathrm{out}}(-\omega') a_{\mathrm{out}}(\omega'')\rangle \\
&+ \langle e^{-i(\omega''-\omega')\frac{x}{v_p}} a_{\mathrm{out}}(-\omega') a^{\dagger}_{\mathrm{out}}(-\omega'')\rangle \Big] \\
&+ \frac{2\sin\left[(\omega'+\omega'')T_M/2\right]}{(\omega'+\omega'')T_M} \Big[\langle e^{i(\omega'+\omega'')\frac{x}{v_p}} a^{\dagger}_{\mathrm{out}}(\omega') a_{\mathrm{out}}(-\omega'')\rangle \\
&+ \langle e^{i(2\omega_0+\omega'+\omega'')\frac{x}{v_p}} e^{-2i\Phi_{\mathrm{LO}}} a^{\dagger}_{\mathrm{out}}(\omega') a^{\dagger}_{\mathrm{out}}(\omega'')\rangle \\
&+ \langle e^{-i(\omega'+\omega'')\frac{x}{v_p}} a^{\dagger}_{\mathrm{out}}(-\omega') a_{\mathrm{out}}(\omega'')\rangle \\
&+ \langle e^{i(2\omega_0-\omega'-\omega'')\frac{x}{v_p}} e^{-2i\Phi_{\mathrm{LO}}} a^{\dagger}_{\mathrm{out}}(-\omega') a^{\dagger}_{\mathrm{out}}(-\omega'')\rangle \\
&+ \langle e^{-i(2\omega_0+\omega'+\omega'')\frac{x}{v_p}} e^{2i\Phi_{\mathrm{LO}}} a_{\mathrm{out}}(\omega') a_{\mathrm{out}}(\omega'')\rangle \\
&+ \langle e^{-i(\omega'+\omega'')\frac{x}{v_p}} a_{\mathrm{out}}(\omega') a^{\dagger}_{\mathrm{out}}(-\omega'')\rangle \\
&+ \langle e^{-i(2\omega_0-\omega'-\omega'')\frac{x}{v_p}} e^{2i\Phi_{\mathrm{LO}}} a_{\mathrm{out}}(-\omega') a_{\mathrm{out}}(-\omega'')\rangle \\
&+ \langle e^{i(\omega'+\omega'')\frac{x}{v_p}} a_{\mathrm{out}}(-\omega') a^{\dagger}_{\mathrm{out}}(\omega'')\rangle \Big] \Big\},
\end{aligned}
\tag{A.36}
$$

The input for the external probe line is a single coherent tone at frequency ω_s and the internal loss channel has a noisy thermal input. The input correlations are

$$\langle b^{\dagger}_{\mathrm{in}}(\omega'') b_{\mathrm{in}}(\omega')\rangle = \frac{1}{e^{\beta\hbar(\omega_0+\omega')}-1}\delta(\omega''-\omega') = \frac{1}{e^{\beta\hbar\omega_0}-1}\delta(\omega''-\omega') \tag{A.37}$$

$$\langle a_{\mathrm{in}}(\omega') a_{\mathrm{in}}(\omega'')\rangle = \langle a^{\dagger}_{\mathrm{in}}(\omega') a^{\dagger}_{\mathrm{in}}(\omega'')\rangle = \langle b^{\dagger}_{\mathrm{in}}(\omega') b^{\dagger}_{\mathrm{in}}(\omega'')\rangle = \langle b_{\mathrm{in}}(\omega') b_{\mathrm{in}}(\omega'')\rangle = 0 \tag{A.38}$$

$$\langle a_{\mathrm{in}}(\omega') b_{\mathrm{in}}(\omega'')\rangle = \langle a^{\dagger}_{\mathrm{in}}(\omega') b_{\mathrm{in}}(\omega'')\rangle = \langle a_{\mathrm{in}}(\omega') b^{\dagger}_{\mathrm{in}}(\omega'')\rangle = \langle a^{\dagger}_{\mathrm{in}}(\omega') b^{\dagger}_{\mathrm{in}}(\omega'')\rangle = 0 \tag{A.39}$$

$$\langle a^{\dagger}_{\mathrm{in}}(\omega'') a_{\mathrm{in}}(\omega')\rangle = |\alpha(\omega')|^2 \delta(\omega'-\omega''), \tag{A.40}$$

where for a single input coherent tone at $\omega_s = \omega_0 + \omega$, $|\alpha(\omega)|^2 = |\alpha_{\rm in}|^2 \delta(\omega_0 + \omega - \omega_s)$

$$\langle a_{\rm in}(\omega') a^\dagger_{\rm in}(\omega'')\rangle = \langle a^\dagger_{\rm in}(\omega'') a_{\rm in}(\omega') + \delta(\omega' - \omega'')\rangle = (|\alpha(\omega')|^2 + 1)\delta(\omega' - \omega'') \quad \text{(A.41)}$$

and similarly,

$$\langle b_{\rm in}(\omega') b^\dagger_{\rm in}(\omega'')\rangle = \frac{e^{\beta\hbar\omega_0}}{e^{\beta\hbar\omega_0} - 1}\delta(\omega' - \omega'') \quad \text{(A.42)}$$

Using the above expressions, eqn.(A.36) and since our input tone is a coherent single frequency signal at ω_s, using eqn.(A.40), and the fact that at the base temperature of our dilution fridge of 30mK, for $\omega_0 \approx 2\pi \times 5.5$GHz, $\frac{1}{e^{\beta\hbar\omega_0 - 1}} \approx 0$ and $\frac{e^{\beta\hbar\omega_0}}{e^{\beta\hbar\omega_0 - 1}} \approx 1$, we have

$$P_{\rm SA}(\omega, \Delta\omega) = \frac{4\hbar\omega_0}{\pi}|\alpha_{\rm LO}|^2|\alpha_{\rm in}|^2\Big[|G_{\rm ext}(\omega)|^2 + e^{2i\omega_0\frac{x}{v_p}}e^{-2i\Phi_{\rm LO}}G^*_{\rm ext}(\omega)M^*_{\rm ext}(-\omega) + |M_{\rm ext}(-\omega)|^2 + e^{-2i\omega_0\frac{x}{v_p}}e^{2i\Phi_{\rm LO}}G_{\rm ext}(\omega)M_{\rm ext}(-\omega)\Big], \quad \text{(A.43)}$$

where we have neglected the coupling to the internal thermal bath because $\int d\omega' \frac{e^{\beta\hbar\omega_0}}{e^{\beta\hbar\omega_0 - 1}}$ and $\int d\omega' \frac{1}{e^{\beta\hbar\omega_0 - 1}} \ll |\alpha_{\rm in}|^2$ when $\Delta\omega$, the resolution bandwidth of the spectrum analyzer is of the order of Hz, or even kHz. Meanwhile, the coherent drive contains a photon flux of $\sim 10^6$ photons/s for our typical cavity occupations of a few photons (see eqn.(B5) in [33]). For the same reasons, we neglect the +1 terms in the correlations arising from the commutation relations of the input operator. We also draw the position dependant phase factor, which is a constant for a given pump frequency and experimental setup, into the definition of the pump amplitude, ϵ, and we finally

have eqn.(2.12) in [54]

$$P_{\mathrm{SA}}(\omega,\Delta\omega)=\frac{4\hbar\omega_0}{\pi}|\alpha_{\mathrm{LO}}|^2|\alpha_{\mathrm{in}}|^2\Big[|G_{\mathrm{ext}}(\omega)|^2+e^{-2i\Phi_{\mathrm{LO}}}G^*_{\mathrm{ext}}(\omega)M^*_{\mathrm{ext}}(-\omega)$$
$$+|M_{\mathrm{ext}}(-\omega)|^2+e^{2i\Phi_{\mathrm{LO}}}G_{\mathrm{ext}}(\omega)M_{\mathrm{ext}}(-\omega)\Big]. \quad \text{(A.44)}$$

We can then define $P^0_{\mathrm{SA}}(\omega,\Delta\omega)$ to be the output power in the absence of a flux pump which is given by

$$P^0_{\mathrm{SA}}(\omega,\Delta\omega)=\frac{4\hbar\omega_0}{\pi}|\alpha_{\mathrm{LO}}|^2|\alpha_{\mathrm{in}}|^2\Big|G^{(\epsilon=0)}_{\mathrm{ext}}(\omega)\Big|^2, \quad \text{(A.45)}$$

since the idler gains go to zero in the absence of the flux pump.

The gain in the output spectrum due to the pump is then given by

$$G(\omega)=\frac{P_{\mathrm{SA}}(\omega,\Delta\omega)}{P^0_{\mathrm{SA}}(\omega,\Delta\omega)}, \quad \text{(A.46)}$$

which depends on the pump detuning Δ, the pump phase Φ_{p} relative to the phase of the input tone, the phase of the local oscillator Φ_{LO} with respect to the phase of the input tone, the pumping power $|\epsilon|$ and the input detuning ω ($\omega+\Delta$ in reality).

Section A.2

Experiments

We first operate the parametric amplifier in the phase-coherent degenerate mode [152] by pumping the the flux line at exactly $2\omega_0$ for a cCPT bias $(n_g,\Phi_{\mathrm{ext}})=(0,0.125\Phi_0)$, and look at the reflected signal from a single intracavity photon level input tone at ω_0. Fig. (A.1) shows the variation of the gain as a function of the phase of the pump tone and the input tone, each showing the expected period of 2π and π respectively.

This phase dependence of the gain with attenuation for some phases is a clear sign of a phase sensitive amplifier operating in a three-wave mixing mode [55, 135].

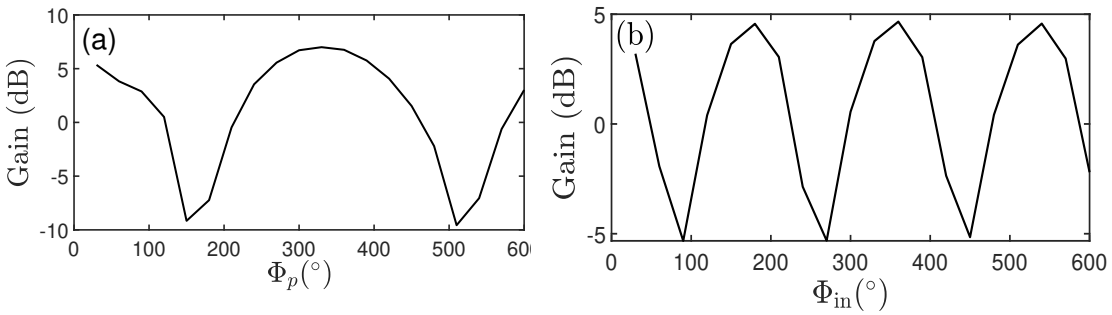

Figure A.1: Gain of an input tone on resonance with the cavity for a flux pump at $\omega_p/2\pi = 2\omega_0/2\pi = 11.554$ GHz for a cCPT bias of $(n_g, \Phi_{\text{ext}}) = (0, 0.125\Phi_0)$, with a flux pump tone strength of -10 dBm at the signal generator, and an input tone $P_{\text{in}} = -60$ dBm.

However, we see very little to no gain for an input detuned from $\omega_p/2$, which is what we hoped to exploit to perform an on-chip enhanced charge sensing scheme. We do observe the typical signs when performing this phase-incoherent degenerate parametric amplification. We see an idler tone (and hence idler gain) at $\omega_I = \omega_p/2 - \omega_s$ where $\omega_{I(s)}$ are the idler (signal) frequencies. Though we cannot explain this, we envision performing the charge sensing experiment as in [1] with a single photon level input tone at $\omega_0 \pm \omega_g$, while modulating the gate line with a frequency ω_g of the order of a few hundred kHz, and then flux pumping the cavity at $2(\omega_0)$, such that one of the sidebands from the gate modulation gets amplified by the phase-coherent degenerate operation.

A.2.1. Subharmonic oscillations, multi-photon resonances and phase space crystals

Looking at the cCPT Hamiltonian eqn.(2.125), we see that by pumping the flux line at close to $3\omega_0$, we drive the $a^3 + a^{\dagger 3}$ term into resonance, and can follow the same procedure in section A.1 to find a region in flux pump parameters where we expect

to generate oscillations close to ω_0. Fig. A.2 shows a plot of the output spectrum in flux pump parameter space ($\delta\Phi - \Delta$), and the corresponding phase space histograms for three pump parameters. We see the expected three equi-amplitude stable states separated by a phase of $2\pi/3$ and sometimes with a stable zero amplitude state. The subharmonic oscillation region doesn't agree with the theoretical expectation for reasons we don't understand.

By flux pumping the cCPT close to $n\omega_0$, we can study multi-photon resonances [156] and the n-fold discrete symmetry in phase space that emerges as pictured for n = 3 in fig.(A.2) [153], can be used in the study of phase space crystals [155, 157].

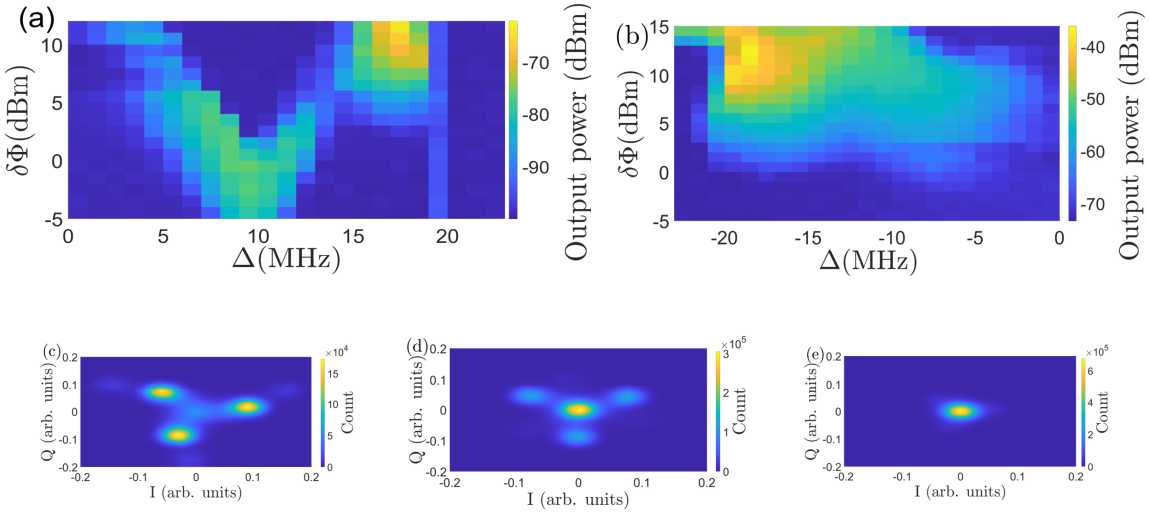

Figure A.2: Output spectrum with no input tone, pumping the flux line of the cCPT at $3(\omega_0 - \Delta)$ with $(n_g, \Phi_{\text{ext}}) =$ (a) $(0, \frac{3\Phi_0}{8})$, (b) $(0, \frac{\Phi_0}{8})$. (c), (d), (e) are heterodyne measurement histograms at different regions in (b).

Bibliography

[1] B. Brock, J. Li, S. Kanhirathingal, B. Thyagarajan, M. Blencowe, A. Rimberg, Fast and ultrasensitive electrometer operating at the single-photon level, Phys. Rev. Applied 16 (2021) L051004. doi:10.1103/PhysRevApplied.16.L051004.
URL https://link.aps.org/doi/10.1103/PhysRevApplied.16.L051004

[2] M. F. Tompsett, G. F. Amelio, G. E. Smith, Charge coupled 8-bit shift register, Applied Physics Letters 17 (3) (1970) 111–115. arXiv:https://doi.org/10.1063/1.1653327, doi:10.1063/1.1653327.
URL https://doi.org/10.1063/1.1653327

[3] R. P. Feynman, Simulating physics with computers, International journal of theoretical physics 21 (6/7) (1982) 467–488.

[4] S. Lloyd, Universal quantum simulators, Science 273 (5278) (1996) 1073–1078. arXiv:https://www.science.org/doi/pdf/10.1126/science.273.5278.1073, doi:10.1126/science.273.5278.1073.
URL https://www.science.org/doi/abs/10.1126/science.273.5278.1073

[5] F. Arute, K. Arya, R. Babbush, D. Bacon, J. C. Bardin, R. Barends, R. Biswas, S. Boixo, F. G. S. L. Brandao, D. A. Buell, B. Burkett, Y. Chen, Z. Chen, B. Chiaro, R. Collins, W. Courtney, A. Dunsworth, E. Farhi, B. Foxen,

A. Fowler, C. Gidney, M. Giustina, R. Graff, K. Guerin, S. Habegger, M. P. Harrigan, M. J. Hartmann, A. Ho, M. Hoffmann, T. Huang, T. S. Humble, S. V. Isakov, E. Jeffrey, Z. Jiang, D. Kafri, K. Kechedzhi, J. Kelly, P. V. Klimov, S. Knysh, A. Korotkov, F. Kostritsa, D. Landhuis, M. Lindmark, E. Lucero, D. Lyakh, S. Mandrà, J. R. McClean, M. McEwen, A. Megrant, X. Mi, K. Michielsen, M. Mohseni, J. Mutus, O. Naaman, M. Neeley, C. Neill, M. Y. Niu, E. Ostby, A. Petukhov, J. C. Platt, C. Quintana, E. G. Rieffel, P. Roushan, N. C. Rubin, D. Sank, K. J. Satzinger, V. Smelyanskiy, K. J. Sung, M. D. Trevithick, A. Vainsencher, B. Villalonga, T. White, Z. J. Yao, P. Yeh, A. Zalcman, H. Neven, J. M. Martinis, Quantum supremacy using a programmable superconducting processor, Nature 574 (7779) (2019) 505–510. doi:10.1038/s41586-019-1666-5.
URL https://doi.org/10.1038/s41586-019-1666-5

[6] J. Koch, T. M. Yu, J. Gambetta, A. A. Houck, D. I. Schuster, J. Majer, A. Blais, M. H. Devoret, S. M. Girvin, R. J. Schoelkopf, Charge-insensitive qubit design derived from the cooper pair box, Phys. Rev. A 76 (2007) 042319. doi:10.1103/PhysRevA.76.042319.
URL https://link.aps.org/doi/10.1103/PhysRevA.76.042319

[7] B. E. Kane, A silicon-based nuclear spin quantum computer, Nature 393 (6681) (1998) 133–137. doi:10.1038/30156.
URL https://doi.org/10.1038/30156

[8] M. Fuechsle, J. A. Miwa, S. Mahapatra, H. Ryu, S. Lee, O. Warschkow, L. C. L. Hollenberg, G. Klimeck, M. Y. Simmons, A single-atom transistor, Nature Nanotechnology 7 (4) (2012) 242–246. doi:10.1038/nnano.2012.21.
URL https://doi.org/10.1038/nnano.2012.21

[9] M. A. Broome, T. F. Watson, D. Keith, S. K. Gorman, M. G. House, J. G. Keizer, S. J. Hile, W. Baker, M. Y. Simmons, High-fidelity single-shot singlet-triplet readout of precision-placed donors in silicon, Phys. Rev. Lett. 119 (2017) 046802. doi:10.1103/PhysRevLett.119.046802.
URL https://link.aps.org/doi/10.1103/PhysRevLett.119.046802

[10] Y. He, S. K. Gorman, D. Keith, L. Kranz, J. G. Keizer, M. Y. Simmons, A two-qubit gate between phosphorus donor electrons in silicon, Nature 571 (7765) (2019) 371–375. doi:10.1038/s41586-019-1381-2.
URL https://doi.org/10.1038/s41586-019-1381-2

[11] J. R. Petta, A. C. Johnson, J. M. Taylor, E. A. Laird, A. Yacoby, M. D. Lukin, C. M. Marcus, M. P. Hanson, A. C. Gossard, Coherent manipulation of coupled electron spins in semiconductor quantum dots, Science 309 (5744) (2005) 2180–2184. arXiv:https://www.science.org/doi/pdf/10.1126/science.1116955, doi:10.1126/science.1116955.
URL https://www.science.org/doi/abs/10.1126/science.1116955

[12] A. Morello, J. J. Pla, F. A. Zwanenburg, K. W. Chan, K. Y. Tan, H. Huebl, M. Möttönen, C. D. Nugroho, C. Yang, J. A. van Donkelaar, A. D. C. Alves, D. N. Jamieson, C. C. Escott, L. C. L. Hollenberg, R. G. Clark, A. S. Dzurak, Single-shot readout of an electron spin in silicon, Nature 467 (7316) (2010) 687–691. doi:10.1038/nature09392.
URL https://doi.org/10.1038/nature09392

[13] J. T. Muhonen, J. P. Dehollain, A. Laucht, F. E. Hudson, R. Kalra, T. Sekiguchi, K. M. Itoh, D. N. Jamieson, J. C. McCallum, A. S. Dzurak, A. Morello, Storing quantum information for 30 seconds in a nanoelectronic device, Nature Nanotechnology 9 (12) (2014) 986–991. doi:10.1038/nnano.

2014.211.

URL https://doi.org/10.1038/nnano.2014.211

[14] T. Fujisawa, T. Hayashi, S. Sasaki, Time-dependent single-electron transport through quantum dots, Reports on Progress in Physics 69 (3) (2006) 759–796. doi:10.1088/0034-4885/69/3/r05.

URL https://doi.org/10.1088/0034-4885/69/3/r05

[15] R. Hanson, L. H. W. van Beveren, I. T. Vink, J. M. Elzerman, W. J. M. Naber, F. H. L. Koppens, L. P. Kouwenhoven, L. M. K. Vandersypen, Single-shot readout of electron spin states in a quantum dot using spin-dependent tunnel rates, Phys. Rev. Lett. 94 (2005) 196802. doi:10.1103/PhysRevLett.94.196802.

URL https://link.aps.org/doi/10.1103/PhysRevLett.94.196802

[16] D. Keith, M. G. House, M. B. Donnelly, T. F. Watson, B. Weber, M. Y. Simmons, Single-shot spin readout in semiconductors near the shot-noise sensitivity limit, Phys. Rev. X 9 (2019) 041003. doi:10.1103/PhysRevX.9.041003.

URL https://link.aps.org/doi/10.1103/PhysRevX.9.041003

[17] L. Barak, I. M. Bloch, M. Cababie, G. Cancelo, L. Chaplinsky, F. Chierchie, M. Crisler, A. Drlica-Wagner, R. Essig, J. Estrada, E. Etzion, G. F. Moroni, D. Gift, S. Munagavalasa, A. Orly, D. Rodrigues, A. Singal, M. S. Haro, L. Stefanazzi, J. Tiffenberg, S. Uemura, T. Volansky, T.-T. Yu, Sensei: Direct-detection results on sub-gev dark matter from a new skipper ccd, Phys. Rev. Lett. 125 (2020) 171802. doi:10.1103/PhysRevLett.125.171802.

URL https://link.aps.org/doi/10.1103/PhysRevLett.125.171802

[18] D. M. T. van Zanten, D. Sabonis, J. Suter, J. I. Väyrynen, T. Karzig, D. I. Pikulin, E. C. T. O'Farrell, D. Razmadze, K. D. Petersson, P. Krogstrup, C. M.

Marcus, Photon-assisted tunnelling of zero modes in a majorana wire, Nature Physics 16 (6) (2020) 663–668. doi:10.1038/s41567-020-0858-0.
URL https://doi.org/10.1038/s41567-020-0858-0

[19] W. Lu, Z. Ji, L. Pfeiffer, K. W. West, A. J. Rimberg, Real-time detection of electron tunnelling in a quantum dot, Nature 423 (6938) (2003) 422–425. doi:10.1038/nature01642.
URL https://doi.org/10.1038/nature01642

[20] D. V. Averin, K. K. Likharev, Coulomb blockade of single-electron tunneling, and coherent oscillations in small tunnel junctions, Journal of Low Temperature Physics 62 (3) (1986) 345–373. doi:10.1007/BF00683469.
URL https://doi.org/10.1007/BF00683469

[21] T. A. Fulton, G. J. Dolan, Observation of single-electron charging effects in small tunnel junctions, Phys. Rev. Lett. 59 (1987) 109–112. doi:10.1103/PhysRevLett.59.109.
URL https://link.aps.org/doi/10.1103/PhysRevLett.59.109

[22] P. D. Dresselhaus, L. Ji, S. Han, J. E. Lukens, K. K. Likharev, Measurement of single electron lifetimes in a multijunction trap, Phys. Rev. Lett. 72 (1994) 3226–3229. doi:10.1103/PhysRevLett.72.3226.
URL https://link.aps.org/doi/10.1103/PhysRevLett.72.3226

[23] M. J. Yoo, T. A. Fulton, H. F. Hess, R. L. Willett, L. N. Dunkleberger, R. J. Chichester, L. N. Pfeiffer, K. W. West, Scanning single-electron transistor microscopy: Imaging individual charges, Science 276 (5312) (1997) 579–582. arXiv:https://www.science.org/doi/pdf/10.1126/science.276.5312.579, doi:10.1126/science.276.5312.579.
URL https://www.science.org/doi/abs/10.1126/science.276.5312.579

[24] P. Lafarge, H. Pothier, E. R. Williams, D. Esteve, C. Urbina, M. H. Devoret, Direct observation of macroscopic charge quantization, Zeitschrift für Physik B Condensed Matter 85 (3) (1991) 327–332. doi:10.1007/BF01307627.
URL https://doi.org/10.1007/BF01307627

[25] H. Grabert, M. H. Devoret, N. A. T. Organization., N. A. S. I. on Single Charge Tunneling, Single charge tunneling : Coulomb blockade phenomena in nanostructures / edited by Hermann Grabert and Michel H. Devoret, Plenum Press New York, 1992.

[26] R. J. Schoelkopf, P. Wahlgren, A. A. Kozhevnikov, P. Delsing, D. E. Prober, The radio-frequency single-electron transistor (rf-set): A fast and ultrasensitive electrometer, Science 280 (5367) (1998) 1238–1242. arXiv:https://www.science.org/doi/pdf/10.1126/science.280.5367.1238, doi:10.1126/science.280.5367.1238.
URL https://www.science.org/doi/abs/10.1126/science.280.5367.1238

[27] H. Brenning, S. Kafanov, T. Duty, S. Kubatkin, P. Delsing, An ultrasensitive radio-frequency single-electron transistor working up to 4.2k, Journal of Applied Physics 100 (11) (2006) 114321. arXiv:https://aip.scitation.org/doi/pdf/10.1063/1.2388134, doi:10.1063/1.2388134.
URL https://aip.scitation.org/doi/abs/10.1063/1.2388134

[28] P. Joyez, P. Lafarge, A. Filipe, D. Esteve, M. H. Devoret, Observation of parity-induced suppression of josephson tunneling in the superconducting single electron transistor, Phys. Rev. Lett. 72 (1994) 2458–2461. doi:10.1103/PhysRevLett.72.2458.
URL https://link.aps.org/doi/10.1103/PhysRevLett.72.2458

[29] O. Naaman, J. Aumentado, Poisson transition rates from time-domain measurements with a finite bandwidth, Phys. Rev. Lett. 96 (2006) 100201. doi:10.1103/PhysRevLett.96.100201.
URL https://link.aps.org/doi/10.1103/PhysRevLett.96.100201

[30] S. Kanhirathingal, B. L. Brock, A. J. Rimberg, M. P. Blencowe, Charge sensitivity of a cavity-embedded cooper pair transistor limited by single-photon shot noise, Journal of Applied Physics 130 (11) (2021) 114401. arXiv:https://doi.org/10.1063/5.0062421, doi:10.1063/5.0062421.
URL https://doi.org/10.1063/5.0062421

[31] M. A. Sillanpää, L. Roschier, P. J. Hakonen, Charge sensitivity of the inductive single-electron transistor, Applied Physics Letters 87 (9) (2005) 092502. arXiv:https://doi.org/10.1063/1.2034096, doi:10.1063/1.2034096.
URL https://doi.org/10.1063/1.2034096

[32] M. A. Sillanpää, L. Roschier, P. J. Hakonen, Inductive single-electron transistor, Phys. Rev. Lett. 93 (2004) 066805. doi:10.1103/PhysRevLett.93.066805.
URL https://link.aps.org/doi/10.1103/PhysRevLett.93.066805

[33] B. Brock, J. Li, S. Kanhirathingal, B. Thyagarajan, W. F. Braasch, M. Blencowe, A. Rimberg, Nonlinear charge- and flux-tunable cavity derived from an embedded cooper-pair transistor, Phys. Rev. Applied 15 (2021) 044009. doi:10.1103/PhysRevApplied.15.044009.
URL https://link.aps.org/doi/10.1103/PhysRevApplied.15.044009

[34] R. Vijay, M. H. Devoret, I. Siddiqi, Invited review article: The josephson bifurcation amplifier, Review of Scientific Instruments 80 (11) (2009) 111101. arXiv:https://doi.org/10.1063/1.3224703, doi:10.1063/1.3224703.
URL https://doi.org/10.1063/1.3224703

[35] I. Siddiqi, R. Vijay, F. Pierre, C. M. Wilson, L. Frunzio, M. Metcalfe, C. Rigetti, R. J. Schoelkopf, M. H. Devoret, D. Vion, D. Esteve, Direct observation of dynamical bifurcation between two driven oscillation states of a josephson junction, Phys. Rev. Lett. 94 (2005) 027005. doi:10.1103/PhysRevLett.94.027005.

URL https://link.aps.org/doi/10.1103/PhysRevLett.94.027005

[36] C. K. Andersen, A. Kamal, N. A. Masluk, I. M. Pop, A. Blais, M. H. Devoret, Quantum versus classical switching dynamics of driven dissipative kerr resonators, Phys. Rev. Applied 13 (2020) 044017. doi:10.1103/PhysRevApplied.13.044017.

URL https://link.aps.org/doi/10.1103/PhysRevApplied.13.044017

[37] J. Bourassa, F. Beaudoin, J. M. Gambetta, A. Blais, Josephson-junction-embedded transmission-line resonators: From kerr medium to in-line transmon, Phys. Rev. A 86 (2012) 013814. doi:10.1103/PhysRevA.86.013814.

URL https://link.aps.org/doi/10.1103/PhysRevA.86.013814

[38] F. Mallet, F. R. Ong, A. Palacios-Laloy, F. Nguyen, P. Bertet, D. Vion, D. Esteve, Single-shot qubit readout in circuit quantum electrodynamics, Nature Physics 5 (11) (2009) 791–795. doi:10.1038/nphys1400.

URL https://doi.org/10.1038/nphys1400

[39] M. Metcalfe, E. Boaknin, V. Manucharyan, R. Vijay, I. Siddiqi, C. Rigetti, L. Frunzio, R. J. Schoelkopf, M. H. Devoret, Measuring the decoherence of a quantronium qubit with the cavity bifurcation amplifier, Phys. Rev. B 76 (2007) 174516. doi:10.1103/PhysRevB.76.174516.

URL https://link.aps.org/doi/10.1103/PhysRevB.76.174516

[40] T. Peyronel, O. Firstenberg, Q.-Y. Liang, S. Hofferberth, A. V. Gorshkov, T. Pohl, M. D. Lukin, V. Vuletić, Quantum nonlinear optics with single photons enabled by strongly interacting atoms, Nature 488 (7409) (2012) 57–60. doi:10.1038/nature11361.
URL https://doi.org/10.1038/nature11361

[41] R. E. Slusher, L. W. Hollberg, B. Yurke, J. C. Mertz, J. F. Valley, Observation of squeezed states generated by four-wave mixing in an optical cavity, Phys. Rev. Lett. 55 (1985) 2409–2412. doi:10.1103/PhysRevLett.55.2409.
URL https://link.aps.org/doi/10.1103/PhysRevLett.55.2409

[42] P. A. Franken, A. E. Hill, C. W. Peters, G. Weinreich, Generation of optical harmonics, Phys. Rev. Lett. 7 (1961) 118–119. doi:10.1103/PhysRevLett.7.118.
URL https://link.aps.org/doi/10.1103/PhysRevLett.7.118

[43] R. A. Fisher, P. L. Kelley, T. K. Gustafson, Subpicosecond pulse generation using the optical kerr effect, Applied Physics Letters 14 (4) (1969) 140–143. arXiv:https://doi.org/10.1063/1.1652749, doi:10.1063/1.1652749.
URL https://doi.org/10.1063/1.1652749

[44] M. Gullans, D. E. Chang, F. H. L. Koppens, F. J. G. de Abajo, M. D. Lukin, Single-photon nonlinear optics with graphene plasmons, Phys. Rev. Lett. 111 (2013) 247401. doi:10.1103/PhysRevLett.111.247401.
URL https://link.aps.org/doi/10.1103/PhysRevLett.111.247401

[45] P. Grangier, J. A. Levenson, J.-P. Poizat, Quantum non-demolition measurements in optics, Nature 396 (6711) (1998) 537–542. doi:10.1038/25059.
URL https://doi.org/10.1038/25059

[46] N. A. Masluk, I. M. Pop, A. Kamal, Z. K. Minev, M. H. Devoret, Microwave characterization of josephson junction arrays: Implementing a low loss superinductance, Phys. Rev. Lett. 109 (2012) 137002. doi:10.1103/PhysRevLett.109.137002.
URL https://link.aps.org/doi/10.1103/PhysRevLett.109.137002

[47] P. R. Muppalla, O. Gargiulo, S. I. Mirzaei, B. P. Venkatesh, M. L. Juan, L. Grünhaupt, I. M. Pop, G. Kirchmair, Bistability in a mesoscopic josephson junction array resonator, Phys. Rev. B 97 (2018) 024518. doi:10.1103/PhysRevB.97.024518.
URL https://link.aps.org/doi/10.1103/PhysRevB.97.024518

[48] G. Kirchmair, B. Vlastakis, Z. Leghtas, S. E. Nigg, H. Paik, E. Ginossar, M. Mirrahimi, L. Frunzio, S. M. Girvin, R. J. Schoelkopf, Observation of quantum state collapse and revival due to the single-photon kerr effect, Nature 495 (7440) (2013) 205–209. doi:10.1038/nature11902.
URL https://doi.org/10.1038/nature11902

[49] M. A. Castellanos-Beltran, K. D. Irwin, G. C. Hilton, L. R. Vale, K. W. Lehnert, Amplification and squeezing of quantum noise with a tunable josephson metamaterial, Nature Physics 4 (12) (2008) 929–931. doi:10.1038/nphys1090.
URL https://doi.org/10.1038/nphys1090

[50] M. A. Castellanos-Beltran, K. W. Lehnert, Widely tunable parametric amplifier based on a superconducting quantum interference device array resonator, Applied Physics Letters 91 (8) (2007) 083509. arXiv:https://doi.org/10.1063/1.2773988, doi:10.1063/1.2773988.
URL https://doi.org/10.1063/1.2773988

[51] R. Vijayaraghavan, Josephson bifurcation amplifier [electronic resource] : Amplifying quantum signals using a dynamical bifurcation., Ph.D. thesis, available at https://qulab.eng.yale.edu/category/theses/ (2008).

[52] C. Macklin, K. O'Brien, D. Hover, M. E. Schwartz, V. Bolkhovsky, X. Zhang, W. D. Oliver, I. Siddiqi, A near–quantum-limited josephson traveling-wave parametric amplifier, Science 350 (6258) (2015) 307–310. arXiv:https://www.science.org/doi/pdf/10.1126/science.aaa8525, doi:10.1126/science.aaa8525.
URL https://www.science.org/doi/abs/10.1126/science.aaa8525

[53] T. Yamaji, S. Kagami, A. Yamaguchi, T. Satoh, K. Koshino, H. Goto, Z. R. Lin, Y. Nakamura, T. Yamamoto, Spectroscopic observation of the crossover from a classical duffing oscillator to a kerr parametric oscillator, Phys. Rev. A 105 (2022) 023519. doi:10.1103/PhysRevA.105.023519.
URL https://link.aps.org/doi/10.1103/PhysRevA.105.023519

[54] B. Yurke, L. R. Corruccini, P. G. Kaminsky, L. W. Rupp, A. D. Smith, A. H. Silver, R. W. Simon, E. A. Whittaker, Observation of parametric amplification and deamplification in a josephson parametric amplifier, Phys. Rev. A 39 (1989) 2519–2533. doi:10.1103/PhysRevA.39.2519.
URL https://link.aps.org/doi/10.1103/PhysRevA.39.2519

[55] T. Yamamoto, K. Inomata, M. Watanabe, K. Matsuba, T. Miyazaki, W. D. Oliver, Y. Nakamura, J. S. Tsai, Flux-driven josephson parametric amplifier, Applied Physics Letters 93 (4) (2008) 042510. arXiv:https://doi.org/10.1063/1.2964182, doi:10.1063/1.2964182.
URL https://doi.org/10.1063/1.2964182

[56] Z. R. Lin, K. Inomata, W. D. Oliver, K. Koshino, Y. Nakamura, J. S. Tsai, T. Yamamoto, Single-shot readout of a superconducting flux qubit with a flux-driven josephson parametric amplifier, Applied Physics Letters 103 (13) (2013) 132602. arXiv:https://doi.org/10.1063/1.4821822, doi:10.1063/1.4821822.

URL https://doi.org/10.1063/1.4821822

[57] C. M. Wilson, T. Duty, M. Sandberg, F. Persson, V. Shumeiko, P. Delsing, Photon generation in an electromagnetic cavity with a time-dependent boundary, Phys. Rev. Lett. 105 (2010) 233907. doi:10.1103/PhysRevLett.105.233907.

URL https://link.aps.org/doi/10.1103/PhysRevLett.105.233907

[58] P. Krantz, Y. Reshitnyk, W. Wustmann, J. Bylander, S. Gustavsson, W. D. Oliver, T. Duty, V. Shumeiko, P. Delsing, Investigation of nonlinear effects in josephson parametric oscillators used in circuit quantum electrodynamics, New Journal of Physics 15 (10) (2013) 105002. doi:10.1088/1367-2630/15/10/105002.

URL https://doi.org/10.1088/1367-2630/15/10/105002

[59] C. M. Wilson, G. Johansson, A. Pourkabirian, M. Simoen, J. R. Johansson, T. Duty, F. Nori, P. Delsing, Observation of the dynamical casimir effect in a superconducting circuit, Nature 479 (7373) (2011) 376–379. doi:10.1038/nature10561.

URL https://doi.org/10.1038/nature10561

[60] P. Lähteenmäki, G. S. Paraoanu, J. Hassel, P. J. Hakonen, Dynamical casimir effect in a josephson metamaterial, Proceedings of the National Academy of Sciences 110 (11) (2013) 4234–4238. arXiv:https://www.pnas.org/doi/pdf/

10.1073/pnas.1212705110, doi:10.1073/pnas.1212705110.
URL https://www.pnas.org/doi/abs/10.1073/pnas.1212705110

[61] P. Krantz, A. Bengtsson, M. Simoen, S. Gustavsson, V. Shumeiko, W. D. Oliver, C. M. Wilson, P. Delsing, J. Bylander, Single-shot read-out of a superconducting qubit using a josephson parametric oscillator, Nature Communications 7 (1) (2016) 11417. doi:10.1038/ncomms11417.
URL https://doi.org/10.1038/ncomms11417

[62] A. Aassime, G. Johansson, G. Wendin, R. J. Schoelkopf, P. Delsing, Radio-frequency single-electron transistor as readout device for qubits: Charge sensitivity and backaction, Phys. Rev. Lett. 86 (2001) 3376–3379. doi:10.1103/PhysRevLett.86.3376.
URL https://link.aps.org/doi/10.1103/PhysRevLett.86.3376

[63] A. Dash, S. K. More, N. Arora, A. K. Naik, Ultra-sensitive charge detection and latch memory using mos2-nanoresonator-based bifurcation amplifiers, Applied Physics Letters 118 (5) (2021) 053105. arXiv:https://doi.org/10.1063/5.0031890, doi:10.1063/5.0031890.
URL https://doi.org/10.1063/5.0031890

[64] M. I. Dykman, C. M. Maloney, V. N. Smelyanskiy, M. Silverstein, Fluctuational phase-flip transitions in parametrically driven oscillators, Phys. Rev. E 57 (1998) 5202–5212. doi:10.1103/PhysRevE.57.5202.
URL https://link.aps.org/doi/10.1103/PhysRevE.57.5202

[65] J. Li, Near quantum-limited charge detector and beyond, Ph.D. thesis, available at https://cpb-us-e1.wpmucdn.com/sites.dartmouth.edu/dist/5/2221/files/2021/02/juliangli_thesis.pdf (2018).

[66] J. Aumentado, M. W. Keller, J. M. Martinis, M. H. Devoret, Nonequilibrium quasiparticles and $2e$ periodicity in single-cooper-pair transistors, Phys. Rev. Lett. 92 (2004) 066802. doi:10.1103/PhysRevLett.92.066802.
URL https://link.aps.org/doi/10.1103/PhysRevLett.92.066802

[67] B. Brock, Ultrasensitive electrometry at the single-photon level, Ph.D. thesis, available at https://cpb-us-e1.wpmucdn.com/sites.dartmouth.edu/dist/5/2221/files/2021/09/bbrock_thesis.pdf (2021).

[68] P. Joyez, The single cooper pair transistor : a macroscopic quantum system, Ph.D. thesis, available at https://tel.archives-ouvertes.fr/tel-00534358 (1994).

[69] A. Cottet, Implementation of a quantum bit in a superconducting circuit, Ph.D. thesis, available at http://www.phys.ens.fr/~cottet/ACottetThesis.pdf (2002).

[70] D. M. Pozar, Microwave engineering, Fourth edition. Hoboken, NJ : Wiley, [2012] ©2012, [2012], includes bibliographical references and index.
URL https://search.library.wisc.edu/catalog/9910153599402121

[71] M. Sillanpää, Quantum device applications of mesoscopic superconductivity, Ph.D. thesis, available at http://lib.tkk.fi/Diss/2005/isbn9512275686/ (2005).

[72] P. Krantz, The joshpson parametric oscillator - from microscopic studies to single-shot qubit readout, Ph.D. thesis, available at https://publications.lib.chalmers.se/records/fulltext/235791/235791.pdf (2016).

[73] B. L. Brock, M. P. Blencowe, A. J. Rimberg, Frequency fluctuations in tunable and nonlinear microwave cavities, Phys. Rev. Applied 14 (2020) 054026. doi:

10.1103/PhysRevApplied.14.054026.

URL https://link.aps.org/doi/10.1103/PhysRevApplied.14.054026

[74] C. W. Gardiner, M. J. Collett, Input and output in damped quantum systems: Quantum stochastic differential equations and the master equation, Phys. Rev. A 31 (1985) 3761–3774. doi:10.1103/PhysRevA.31.3761.

URL https://link.aps.org/doi/10.1103/PhysRevA.31.3761

[75] C. Gardiner, P. Zoller, Quantum Noise: A Handbook of Markovian and Non-Markovian Quantum Stochastic Methods with Applications to Quantum Optics, Springer Series in Synergetics, Springer, 2004.

URL https://books.google.com/books?id=a_xsT8oGhdgC

[76] A. A. Clerk, M. H. Devoret, S. M. Girvin, F. Marquardt, R. J. Schoelkopf, Introduction to quantum noise, measurement, and amplification, Rev. Mod. Phys. 82 (2010) 1155–1208. doi:10.1103/RevModPhys.82.1155.

URL https://link.aps.org/doi/10.1103/RevModPhys.82.1155

[77] M. O. Hecht, A. J. Cobarrubia, K. M. Sundqvist, An engineer's brief introduction to microwave quantum optics and a single-port state-space representation, IEEE Transactions on Quantum Engineering 2 (2021) 1–8. doi:10.1109/TQE.2021.3054041.

[78] U. Vool, M. Devoret, Introduction to quantum electromagnetic circuits, International Journal of Circuit Theory and Applications 45 (7) (2017) 897–934. doi:10.1002/cta.2359.

URL https://doi.org/10.1002%2Fcta.2359

[79] M. G. J. Bowen, Warwick P., Quantum optomechanics, CRC Press, Boca Raton, 2016.

[80] K. K. Likharev, Superconducting weak links, Rev. Mod. Phys. 51 (1979) 101–159. doi:10.1103/RevModPhys.51.101.
URL https://link.aps.org/doi/10.1103/RevModPhys.51.101

[81] M. Tinkham, Introduction to superconductivity, Courier Corporation, 2004.

[82] V. Ambegaokar, A. Baratoff, Tunneling between superconductors, Phys. Rev. Lett. 10 (1963) 486–489. doi:10.1103/PhysRevLett.10.486.
URL https://link.aps.org/doi/10.1103/PhysRevLett.10.486

[83] W. Wustmann, V. Shumeiko, Nondegenerate parametric resonance in a tunable superconducting cavity, Phys. Rev. Applied 8 (2017) 024018. doi:10.1103/PhysRevApplied.8.024018.
URL https://link.aps.org/doi/10.1103/PhysRevApplied.8.024018

[84] A. Bengtsson, P. Krantz, M. Simoen, I.-M. Svensson, B. Schneider, V. Shumeiko, P. Delsing, J. Bylander, Nondegenerate parametric oscillations in a tunable superconducting resonator, Phys. Rev. B 97 (2018) 144502. doi:10.1103/PhysRevB.97.144502.
URL https://link.aps.org/doi/10.1103/PhysRevB.97.144502

[85] C. Eichler, A. Wallraff, Controlling the dynamic range of a josephson parametric amplifier, EPJ Quantum Technology 1 (1) (2014) 2. doi:10.1140/epjqt2.
URL https://doi.org/10.1140/epjqt2

[86] G. Liu, T.-C. Chien, X. Cao, O. Lanes, E. Alpern, D. Pekker, M. Hatridge, Josephson parametric converter saturation and higher order effects, Applied Physics Letters 111 (20) (2017) 202603. arXiv:https://doi.org/10.1063/1.5003032, doi:10.1063/1.5003032.
URL https://doi.org/10.1063/1.5003032

[87] L. Planat, R. Dassonneville, J. P. Martínez, F. Foroughi, O. Buisson, W. Hasch-Guichard, C. Naud, R. Vijay, K. Murch, N. Roch, Understanding the saturation power of josephson parametric amplifiers made from squid arrays, Phys. Rev. Applied 11 (2019) 034014. doi:10.1103/PhysRevApplied.11.034014.
URL https://link.aps.org/doi/10.1103/PhysRevApplied.11.034014

[88] N. E. Frattini, V. V. Sivak, A. Lingenfelter, S. Shankar, M. H. Devoret, Optimizing the nonlinearity and dissipation of a snail parametric amplifier for dynamic range, Phys. Rev. Applied 10 (2018) 054020. doi:10.1103/PhysRevApplied.10.054020.
URL https://link.aps.org/doi/10.1103/PhysRevApplied.10.054020

[89] V. Sivak, N. Frattini, V. Joshi, A. Lingenfelter, S. Shankar, M. Devoret, Kerr-free three-wave mixing in superconducting quantum circuits, Phys. Rev. Applied 11 (2019) 054060. doi:10.1103/PhysRevApplied.11.054060.
URL https://link.aps.org/doi/10.1103/PhysRevApplied.11.054060

[90] D. I. Schuster, Circuit quantum electrodynamics, Ph.D. thesis (2007).

[91] R. Holm, W. Meissner, Messungen mit hilfe von flüssigem helium. xiii, Zeitschrift für Physik 74 (11) (1932) 715–735. doi:10.1007/BF01340420.
URL https://doi.org/10.1007/BF01340420

[92] N. A. Court, Quasiparticle dynamics in a single cooper-pair transistor, Ph.D. thesis, available at https://unsworks.unsw.edu.au/entities/publication/4980e7d4-8829-4848-8a07-7d1646c4aa6b (2008).

[93] N. A. Court, A. J. Ferguson, R. G. Clark, Energy gap measurement of nanostructured aluminium thin films for single cooper-pair devices, Superconductor Science and Technology 21 (1) (2007) 015013. doi:10.1088/0953-2048/21/

01/015013.

URL https://doi.org/10.1088/0953-2048/21/01/015013

[94] A. J. Ferguson, S. E. Andresen, R. Brenner, R. G. Clark, Spin-dependent quasiparticle transport in aluminum single-electron transistors, Phys. Rev. Lett. 97 (2006) 086602. doi:10.1103/PhysRevLett.97.086602.

URL https://link.aps.org/doi/10.1103/PhysRevLett.97.086602

[95] Z. Xin, S. Xiao-Hui, Z. Dian-Lin, Thickness dependence of grain size and surface roughness for dc magnetron sputtered au films, Chinese Physics B 19 (8) (2010) 086802. doi:10.1088/1674-1056/19/8/086802.

URL https://doi.org/10.1088/1674-1056/19/8/086802

[96] M. Castellanos-Beltran, Development of a josephson parametric amplifier for the preparation and detection of nonclassical states of microwave fields, Ph.D. thesis, Boulder (2010).

[97] J. B. Hertzberg, Back-action evading measurements of nanomechanical motion approaching quantum limits, Ph.D. thesis, available at https://drum.lib.umd.edu/handle/1903/9830 (2009).

[98] F. Chen, The cavity-embedded cooper pair transistor, Ph.D. thesis, available at https://sites.dartmouth.edu/rimberglab/theses/ (2013).

[99] R. Barends, J. Wenner, M. Lenander, Y. Chen, R. C. Bialczak, J. Kelly, E. Lucero, P. O'Malley, M. Mariantoni, D. Sank, H. Wang, T. C. White, Y. Yin, J. Zhao, A. N. Cleland, J. M. Martinis, J. J. A. Baselmans, Minimizing quasiparticle generation from stray infrared light in superconducting quantum circuits, Applied Physics Letters 99 (11) (2011) 113507. doi:10.1063/1.3638063.

URL https://doi.org/10.1063/1.3638063

[100] J. B. Johnson, Thermal agitation of electricity in conductors, Phys. Rev. 32 (1928) 97–109. doi:10.1103/PhysRev.32.97.
URL https://link.aps.org/doi/10.1103/PhysRev.32.97

[101] H. Nyquist, Thermal agitation of electric charge in conductors, Phys. Rev. 32 (1928) 110–113. doi:10.1103/PhysRev.32.110.
URL https://link.aps.org/doi/10.1103/PhysRev.32.110

[102] . Ott, Henry W., Noise reduction techniques in electronic systems, Second edition. New York : Wiley, 1988., 1988, "A Wiley-interscience publication.";Includes bibliographies.
URL https://search.library.wisc.edu/catalog/999586078302121

[103] C. M. Caves, Quantum limits on noise in linear amplifiers, Phys. Rev. D 26 (1982) 1817–1839. doi:10.1103/PhysRevD.26.1817.
URL https://link.aps.org/doi/10.1103/PhysRevD.26.1817

[104] A. Fukushima, A. Sato, A. Iwasa, Y. Nakamura, T. Komatsuzaki, Y. Sakamoto, Attenuation of microwave filters for single-electron tunneling experiments, IEEE Transactions on Instrumentation and Measurement 46 (2) (1997) 289–293. doi:10.1109/19.571834.

[105] S. Kafanov, H. Brenning, T. Duty, P. Delsing, Charge noise in single-electron transistors and charge qubits may be caused by metallic grains, Phys. Rev. B 78 (2008) 125411. doi:10.1103/PhysRevB.78.125411.
URL https://link.aps.org/doi/10.1103/PhysRevB.78.125411

[106] E. Paladino, Y. M. Galperin, G. Falci, B. L. Altshuler, $1/f$ noise: Implications for solid-state quantum information, Rev. Mod. Phys. 86 (2014) 361–418. doi:

10.1103/RevModPhys.86.361.

URL https://link.aps.org/doi/10.1103/RevModPhys.86.361

[107] P. Kumar, S. Sendelbach, M. A. Beck, J. W. Freeland, Z. Wang, H. Wang, C. C. Yu, R. Q. Wu, D. P. Pappas, R. McDermott, Origin and reduction of $1/f$ magnetic flux noise in superconducting devices, Phys. Rev. Applied 6 (2016) 041001. doi:10.1103/PhysRevApplied.6.041001.

URL https://link.aps.org/doi/10.1103/PhysRevApplied.6.041001

[108] M. S. Khalil, M. J. A. Stoutimore, F. C. Wellstood, K. D. Osborn, An analysis method for asymmetric resonator transmission applied to superconducting devices, Journal of Applied Physics 111 (5) (2012) 054510. arXiv:https://doi.org/10.1063/1.3692073, doi:10.1063/1.3692073.

URL https://doi.org/10.1063/1.3692073

[109] J. Aumentado, The Cooper Pair Transistor, The Handbook of Nanophysics, Taylor and Francis, New York, NY, 2010.

[110] A. D. Córcoles, J. M. Chow, J. M. Gambetta, C. Rigetti, J. R. Rozen, G. A. Keefe, M. Beth Rothwell, M. B. Ketchen, M. Steffen, Protecting superconducting qubits from radiation, Applied Physics Letters 99 (18) (2011) 181906. arXiv:https://doi.org/10.1063/1.3658630, doi:10.1063/1.3658630.

URL https://doi.org/10.1063/1.3658630

[111] M. I. Dykman, M. A. Krivoglaz, Fluctuations in nonlinear systems near bifurcations corresponding to the appearance of new stable states, Physica 104A (1980) 480.

[112] M. I. Dykman, Critical exponents in metastable decay via quantum activation, Phys. Rev. E 75 (2007) 011101. doi:10.1103/PhysRevE.75.011101.
URL https://link.aps.org/doi/10.1103/PhysRevE.75.011101

[113] M. I. Dykman, M. A. Krivoglaz, Theory of fluctuational transitions between stable states of a nonlinear oscillator, Zh. Eksp. Teor. Fiz. 77 (1979) 60.

[114] H. B. Chan, M. I. Dykman, C. Stambaugh, Paths of fluctuation induced switching, Phys. Rev. Lett. 100 (2008) 130602. doi:10.1103/PhysRevLett.100.130602.
URL https://link.aps.org/doi/10.1103/PhysRevLett.100.130602

[115] H. Kramers, Brownian motion in a field of force and the diffusion model of chemical reactions, Physica 7 (4) (1940) 284–304. doi:https://doi.org/10.1016/S0031-8914(40)90098-2.
URL https://www.sciencedirect.com/science/article/pii/S0031891440900982

[116] M. I. D. A. P. Dmitriev, A. F. Ioffe, Activated and tunneling transitions between the two forced-oscillation regimes of an anharmonic oscillator, Zh. Eksp. Teor. Fiz. 90 (1986) 1430.

[117] M. I. Dykman, V. N. Smelyanskii, Quantum theory of transitions between stable states of a nonlinear oscillator interacting with a medium in a resonant field, Zh. Eksp. Teor. Fiz. 94 (1988) 61.

[118] M. Dykman, Fluctuating nonlinear oscillators : from nanomechanics to quantum superconducting circuits, Oxford University Press, Oxford, 2012.

[119] a. Strogatz, Steven, Nonlinear dynamics and chaos : with applications to physics, biology, chemistry, and engineering, Second edition. Boulder, CO :

Westview Press, a member of the Perseus Books Group, [2015], [2015], includes bibliographical references and index.

URL https://search.library.wisc.edu/catalog/9910223127702121

[120] O. Kogan, Controlling transitions in a duffing oscillator by sweeping parameters in time, Phys. Rev. E 76 (2007) 037203. doi:10.1103/PhysRevE.76.037203.

URL https://link.aps.org/doi/10.1103/PhysRevE.76.037203

[121] S. Zaitsev, O. Shtempluck, E. Buks, O. Gottlieb, Nonlinear damping in a micromechanical oscillator, Nonlinear Dynamics 67 (1) (2012) 859–883. doi:10.1007/s11071-011-0031-5.

URL https://doi.org/10.1007/s11071-011-0031-5

[122] S. R. K. Rodriguez, W. Casteels, F. Storme, N. Carlon Zambon, I. Sagnes, L. Le Gratiet, E. Galopin, A. Lemaître, A. Amo, C. Ciuti, J. Bloch, Probing a dissipative phase transition via dynamical optical hysteresis, Phys. Rev. Lett. 118 (2017) 247402. doi:10.1103/PhysRevLett.118.247402.

URL https://link.aps.org/doi/10.1103/PhysRevLett.118.247402

[123] C. Stambaugh, H. B. Chan, Noise-activated switching in a driven nonlinear micromechanical oscillator, Phys. Rev. B 73 (2006) 172302. doi:10.1103/PhysRevB.73.172302.

URL https://link.aps.org/doi/10.1103/PhysRevB.73.172302

[124] J. Johansson, P. Nation, F. Nori, Qutip 2: A python framework for the dynamics of open quantum systems, Computer Physics Communications 184 (4) (2013) 1234–1240. doi:https://doi.org/10.1016/j.cpc.2012.11.019.

URL https://www.sciencedirect.com/science/article/pii/S0010465512003955

[125] M. I. Dykman, D. G. Luchinsky, R. Mannella, P. V. E. McClintock, N. D. Stein, N. G. Stocks, Supernarrow spectral peaks and high-frequency stochastic resonance in systems with coexisting periodic attractors, Phys. Rev. E 49 (1994) 1198–1215. doi:10.1103/PhysRevE.49.1198.
URL https://link.aps.org/doi/10.1103/PhysRevE.49.1198

[126] H. B. Chan, C. Stambaugh, Fluctuation-enhanced frequency mixing in a nonlinear micromechanical oscillator, Phys. Rev. B 73 (2006) 224301. doi:10.1103/PhysRevB.73.224301.
URL https://link.aps.org/doi/10.1103/PhysRevB.73.224301

[127] G. Tancredi, G. Ithier, P. J. Meeson, Bifurcation, mode coupling and noise in a nonlinear multimode superconducting microwave resonator, Applied Physics Letters 103 (6) (2013) 063504. arXiv:https://doi.org/10.1063/1.4818123, doi:10.1063/1.4818123.
URL https://doi.org/10.1063/1.4818123

[128] B. Yurke, E. Buks, Performance of cavity-parametric amplifiers, employing kerr nonlinearites, in the presence of two-photon loss, J. Lightwave Technol. 24 (12) (2006) 5054–5066.
URL http://jlt.osa.org/abstract.cfm?URI=jlt-24-12-5054

[129] J. S. Aldridge, A. N. Cleland, Noise-enabled precision measurements of a duffing nanomechanical resonator, Phys. Rev. Lett. 94 (2005) 156403. doi:10.1103/PhysRevLett.94.156403.
URL https://link.aps.org/doi/10.1103/PhysRevLett.94.156403

[130] J. Zou, S. Buvaev, M. Dykman, H. B. Chan, Poisson noise induced switching in driven micromechanical resonators, Phys. Rev. B 86 (2012) 155420. doi:

10.1103/PhysRevB.86.155420.

URL https://link.aps.org/doi/10.1103/PhysRevB.86.155420

[131] M. Marthaler, M. I. Dykman, Switching via quantum activation: A parametrically modulated oscillator, Phys. Rev. A 73 (2006) 042108. doi:10.1103/PhysRevA.73.042108.

URL https://link.aps.org/doi/10.1103/PhysRevA.73.042108

[132] L. J. Lapidus, D. Enzer, G. Gabrielse, Stochastic phase switching of a parametrically driven electron in a penning trap, Phys. Rev. Lett. 83 (1999) 899–902. doi:10.1103/PhysRevLett.83.899.

URL https://link.aps.org/doi/10.1103/PhysRevLett.83.899

[133] Y. Yuzhelevski, M. Yuzhelevski, G. Jung, Random telegraph noise analysis in time domain, Review of Scientific Instruments 71 (4) (2000) 1681–1688. arXiv:https://doi.org/10.1063/1.1150519, doi:10.1063/1.1150519.

URL https://doi.org/10.1063/1.1150519

[134] I. Siddiqi, R. Vijay, F. Pierre, C. M. Wilson, L. Frunzio, M. Metcalfe, C. Rigetti, M. H. Devoret, The josephson bifurcation amplifier for quantum measurements (2005). doi:10.48550/ARXIV.COND-MAT/0507248.

URL https://arxiv.org/abs/cond-mat/0507248

[135] W. Wustmann, V. Shumeiko, Parametric resonance in tunable superconducting cavities, Phys. Rev. B 87 (2013) 184501. doi:10.1103/PhysRevB.87.184501.

URL https://link.aps.org/doi/10.1103/PhysRevB.87.184501

[136] A. J. Rimberg, M. P. Blencowe, A. D. Armour, P. D. Nation 16 (5) (2014) 055008. doi:10.1088/1367-2630/16/5/055008, [link].

URL https://doi.org/10.1088/1367-2630/16/5/055008

[137] M. Aspelmeyer, T. J. Kippenberg, F. Marquardt, Cavity optomechanics, Rev. Mod. Phys. 86 (2014) 1391–1452. doi:10.1103/RevModPhys.86.1391.
URL https://link.aps.org/doi/10.1103/RevModPhys.86.1391

[138] A. Nunnenkamp, K. Børkje, S. M. Girvin, Single-photon optomechanics, Phys. Rev. Lett. 107 (2011) 063602. doi:10.1103/PhysRevLett.107.063602.
URL https://link.aps.org/doi/10.1103/PhysRevLett.107.063602

[139] W. H. Zurek, Decoherence, einselection, and the quantum origins of the classical, Rev. Mod. Phys. 75 (2003) 715–775. doi:10.1103/RevModPhys.75.715.
URL https://link.aps.org/doi/10.1103/RevModPhys.75.715

[140] J. D. Teufel, T. Donner, D. Li, J. W. Harlow, M. S. Allman, K. Cicak, A. J. Sirois, J. D. Whittaker, K. W. Lehnert, R. W. Simmonds, Sideband cooling of micromechanical motion to the quantum ground state, Nature 475 (7356) (2011) 359–363. doi:10.1038/nature10261.
URL https://doi.org/10.1038/nature10261

[141] J. B. Hertzberg, T. Rocheleau, T. Ndukum, M. Savva, A. A. Clerk, K. C. Schwab, Back-action-evading measurements of nanomechanical motion, Nature Physics 6 (3) (2010) 213–217. doi:10.1038/nphys1479.
URL https://doi.org/10.1038/nphys1479

[142] T. Rocheleau, T. Ndukum, C. Macklin, J. B. Hertzberg, A. A. Clerk, K. C. Schwab, Preparation and detection of a mechanical resonator near the ground state of motion, Nature 463 (7277) (2010) 72–75. doi:10.1038/nature08681.
URL https://doi.org/10.1038/nature08681

[143] T. T. Ndukum, Detecting motion of a nanomechanical resonator near the quantum ground state, Ph.D. thesis, available at https://ecommons.cornell.edu/handle/1813/33637?show=full (2011).

[144] M. Thalakulam, Development and study of charge sensors for fast charge detection in quantum dots, Ph.D. thesis, available at https://sites.dartmouth.edu/rimberglab/theses/ (2007).

[145] R. M. Ranade, S. S. Ang, W. D. Brown, Reactive ion etching of thin gold films, Journal of The Electrochemical Society 140 (12) (1993) 3676–3678. doi:10.1149/1.2221148.
URL https://doi.org/10.1149/1.2221148

[146] S. Rips, I. Wilson-Rae, M. J. Hartmann, Nonlinear nanomechanical resonators for quantum optoelectromechanics, Phys. Rev. A 89 (2014) 013854. doi:10.1103/PhysRevA.89.013854.
URL https://link.aps.org/doi/10.1103/PhysRevA.89.013854

[147] D. H. Santamore, A. C. Doherty, M. C. Cross, Quantum nondemolition measurement of fock states of mesoscopic mechanical oscillators, Phys. Rev. B 70 (2004) 144301. doi:10.1103/PhysRevB.70.144301.
URL https://link.aps.org/doi/10.1103/PhysRevB.70.144301

[148] L. Tosi, D. Vion, H. le Sueur, Design of a cooper-pair box electrometer for application to solid-state and astroparticle physics, Phys. Rev. Applied 11 (2019) 054072. doi:10.1103/PhysRevApplied.11.054072.
URL https://link.aps.org/doi/10.1103/PhysRevApplied.11.054072

[149] S. Kanhirathingal, B. Thyagarajan, B. L. Brock, J. Li, E. Jeffrey, M. P. Blencowe, J. Y. Mutus, A. J. Rimberg, Feedback stabilization of the resonant

frequency in tunable microwave cavities with single-photon occupancy (2022). doi:10.48550/ARXIV.2202.04227.
URL https://arxiv.org/abs/2202.04227

[150] P. D. Nation, M. P. Blencowe, E. Buks, Quantum analysis of a nonlinear microwave cavity-embedded dc squid displacement detector, Phys. Rev. B 78 (2008) 104516. doi:10.1103/PhysRevB.78.104516.
URL https://link.aps.org/doi/10.1103/PhysRevB.78.104516

[151] D. Zoepfl, M. L. Juan, N. Diaz-Naufal, C. M. F. Schneider, L. F. Deeg, A. Sharafiev, A. Metelmann, G. Kirchmair, Kerr enhanced backaction cooling in magnetomechanics (2022). doi:10.48550/ARXIV.2202.13228.
URL https://arxiv.org/abs/2202.13228

[152] J. Aumentado, Superconducting parametric amplifiers: The state of the art in josephson parametric amplifiers, IEEE Microwave Magazine 21 (8) (2020) 45–59. doi:10.1109/MMM.2020.2993476.

[153] I.-M. Svensson, A. Bengtsson, P. Krantz, J. Bylander, V. Shumeiko, P. Delsing, Period-tripling subharmonic oscillations in a driven superconducting resonator, Phys. Rev. B 96 (2017) 174503. doi:10.1103/PhysRevB.96.174503.
URL https://link.aps.org/doi/10.1103/PhysRevB.96.174503

[154] I.-M. Svensson, A. Bengtsson, J. Bylander, V. Shumeiko, P. Delsing, Period multiplication in a parametrically driven superconducting resonator, Applied Physics Letters 113 (2) (2018) 022602. arXiv:https://doi.org/10.1063/1.5026974, doi:10.1063/1.5026974.
URL https://doi.org/10.1063/1.5026974

[155] L. Guo, M. Marthaler, G. Schön, Phase space crystals: A new way to create a quasienergy band structure, Phys. Rev. Lett. 111 (2013) 205303. doi:10.1103/PhysRevLett.111.205303.
URL https://link.aps.org/doi/10.1103/PhysRevLett.111.205303

[156] B. Lang, A. D. Armour, Multi-photon resonances in josephson junction-cavity circuits, New Journal of Physics 23 (3) (2021) 033021. doi:10.1088/1367-2630/abe483.
URL https://doi.org/10.1088/1367-2630/abe483

[157] J. Gosner, B. Kubala, J. Ankerhold, Relaxation dynamics and dissipative phase transition in quantum oscillators with period tripling, Phys. Rev. B 101 (2020) 054501. doi:10.1103/PhysRevB.101.054501.
URL https://link.aps.org/doi/10.1103/PhysRevB.101.054501